Laboratory Astrophysics:
Spectroscopy and Instrumentation for the Gas Phase and the Solid State

Habilitationsschrift

vorgelegt am 18.06.2018

der Physikalisch-Astronomischen Fakultät
der Friedrich-Schiller-Universität Jena

von
Dr. Alexey Potapov
aus Moskau

Gutachter:

1. Prof. Dr. Thomas Henning, Max-Planck-Institut für Astronomie
2. Prof. Dr. Harold Linnartz, Leiden Observatory
3. Prof. Dr. Melanie Schnell, Christian-Albrechts-Universität zu Kiel

Erteilung der Lehrbefähigung am 06.12.2018

for my children, Tanja and Andrey

Contents

1. Introduction

Laboratory astrophysics is bridging the studies of atomic and molecular species in the interstellar medium (ISM) that we can probe remotely by means of astronomy, and the studies of these species or their analogues that we can create in the laboratory and probe in-situ. Laboratory astrophysics provides spectroscopic passports of species that are necessary for the decoding of astronomical spectra and allows us the modelling of physical-chemical processes at the conditions of the ISM. It helps to understand these processes in their completeness and to build reliable astrochemical models that, being supported by astronomical observations, can reveal our astrochemical past and future. The spectroscopic part of the laboratory astrophysics "bridge" is schematically represented in Figure 1.

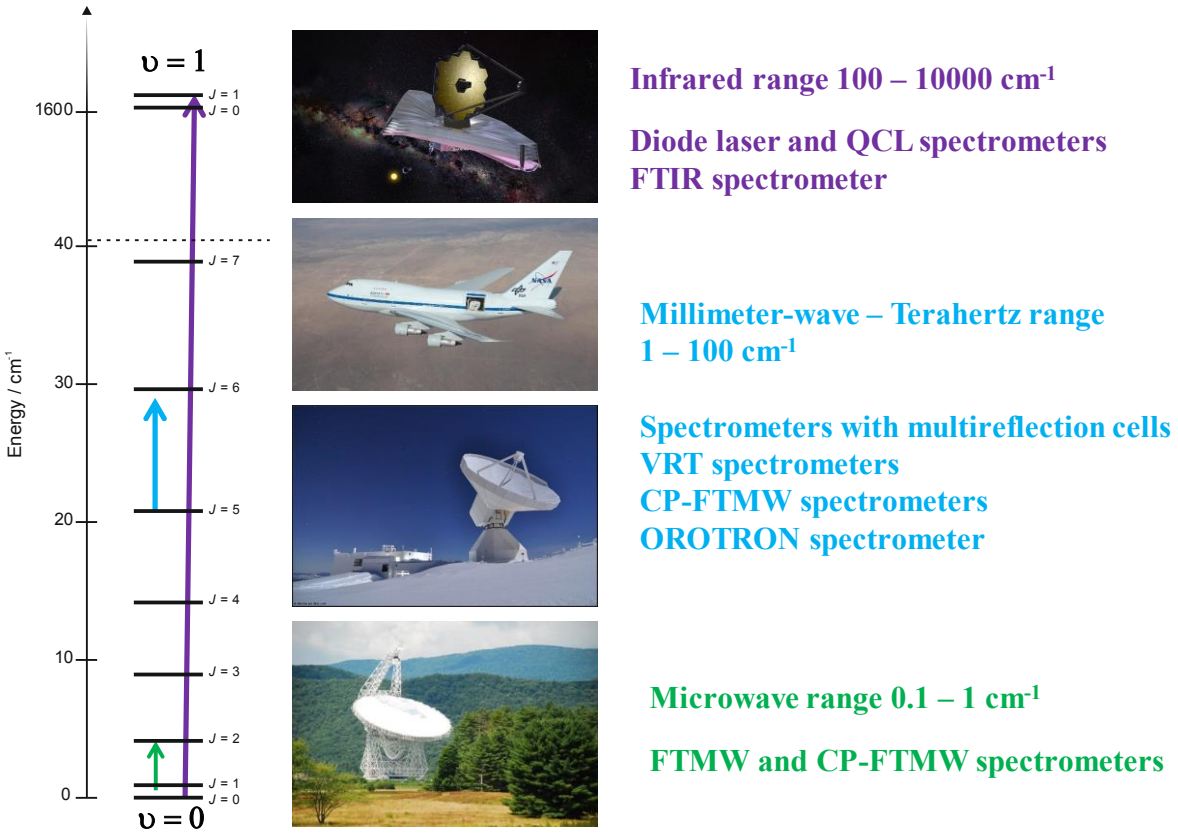

Figure 1. Rotational and rovibrational energy levels of the H_2-H_2O van der Waals complex and transitions between them (J is the total angular momentum of the complex, υ is the vibrational quantum number), corresponding spectral ranges and laboratory techniques, and corresponding observatories (photos): Green Bank Telescope, IRAM 30 m telescope, SOFIA observatory, and James Webb Space Telescope (from bottom to top).

The interstellar medium, the space between the stars, is one of the most attractive and fascinating environments for research due to our interest in the appearance of the universe, galaxies, formation of stars, planets, and our solar system, and the origin of life on Earth. As we hope, answers to all these exciting questions are hidden in the information, which we obtain or can obtain from the ISM. The ISM is filled with a tenuous range of material, such as gas and dust. The gas, about 99% by mass, is predominantly hydrogen (70%), followed by helium (28%) and heavier elements, and the dust, about 1% by mass, consists mainly of carbon- and silicate-based compounds. For a detailed description of the ISM we refer to recent reviews (Tielens 2013; Herbst 2014; van Dishoeck 2014) and books by Tielens (Tielens 2005) and Draine (Draine 2011). Different physical conditions in the ISM and the interactions among atomic and molecular species as well as with UV photons and cosmic rays determine the interstellar chemistry that leads to the formation of simple and complex molecular species, dust and ice grains, and, finally, stars, comets, planetesimals, and planets. In turn, these objects are tracers for processes that occurred in the past and, thus, for our astrochemical history.

One of the most fascinating questions arising from the studies of our planet and the universe is the origin of life on Earth. There are two main hypotheses about the source of the organic compounds that could serve as the basis of life. The first is their formation in the primitive Earth atmosphere (Oparin 1938; Bernal 1951; Urey 1952). In 1953 Stanley Miller demonstrated the production of amino acids from simple molecules, such as CH_4, NH_3, H_2O, and H_2 (major compounds of a possible primitive Earth atmosphere) after exposing the gas mixture to an electrical discharge that was used to form free radicals (Miller 1953; Miller & Urey 1959). Amino acids can be considered to be the most important prebiotic molecules, because they are the building blocks of proteins and, thus, are critical to life on Earth (Lattelais et al. 2011). Amino acids were produced in the gas phase also through the action of X-rays on various mixtures of CH_4, CO_2, NH_3, N_2, H_2O, and H_2 (Dose & Rajewsky 1957). Miller-type experiments have been realized in a number of groups leading to the production of amino acids and other biomolecules (Abelson 1956; Oro 1963; Sanchez, Ferris, & Orgel 1966a; Sanchez, Ferris, & Orgel 1966b; Parker et al. 2011; Scherer et al. 2016; Wollrab et al. 2016).

The second hypothesis is the formation of prebiotic molecules in the ISM and their delivery to Earth on board of meteorites (Oro 1961; Cronin & Chang 1993; Brack 1999; Pearce et al. 2017). The proposed mechanisms for the formation of amino acids in the ISM include reactions on interstellar grains and gas-phase reactions [see, for example, (Martins & Sephton 2009)]. Amino acids have been searched in a variety of locations in the ISM. Several attempts to identify the simplest amino acid, glycine, were made in molecular clouds without being

successful. However, some of the chemical precursors of amino acids, such as glycolaldehyde (Halfen et al. 2006; Beltran et al. 2009; Jorgensen et al. 2012), formamide (Motiyenko et al. 2012), methanol (Tafalla et al. 2006; Bizzocchi et al. 2014; Potapov et al. 2016), and methylamine (Kaifu et al. 1974), have been identified in different objects of the ISM, and glycine has been detected in comets (Elsila, Glavin, & Dworkin 2009; Altwegg & al. 2016). Following the hypothesis of the formation of prebiotic molecules on the surface of interstellar grains, a number of laboratory experiments have demonstrated the formation of simple and complex molecules, including amino acids, in interstellar ice analogues containing similar to Miller-type experiments sets of molecules by UV photolysis (Bernstein et al. 2002; Muñoz Caro et al. 2002; Nuevo et al. 2006). These results have shown that the spontaneous generation of amino acids in the ISM is possible.

One of the fundamental questions we have regarding the interstellar medium is the nature and abundance of detected molecular species. To answer this question, there are three main tasks:

(i) to search and identify species present in the ISM,

(ii) to develop theoretical models that explain the synthesis of the observed objects, and

(iii) to measure crucial parameters to substantiate the models, such as dynamical and structural parameters of species and rate coefficients for chemical reactions between them.

The present work is devoted to the first and third of these challenging tasks. The main objects for the studies were:

1) weakly bound molecular complexes produced in the low temperature environment of a supersonic molecular jet, and

2) interstellar laboratory grain analogues produced at low temperatures and pressures.

Molecular complexes are considered to play a large role in the chemistry of the ISM, in particular in dense and cold molecular clouds, and also at the higher density and higher temperatures found in planetary atmospheres, where they can contribute to the atmospheric chemistry (Klemperer & Vaida 2006; Vaida 2011). Weakly bound complexes are intermediate species in chemical reactions in the gas phase as well as on the surface of grains. Investigations of weakly bound complexes allow us to study molecular interactions between important astronomical species.

Dust grains play a central role in the physics and chemistry of practically all astrophysical environments. They influence the thermodynamic properties of the medium and provide a surface for very efficient chemical reactions responsible for the synthesis of a major part of

important astronomical molecules (Henning 1998; Draine 2003). Interstellar and circumstellar dust grains are of great interest as building blocks of planets in protoplanetary disks. Knowing the properties of grains, we can follow their pathways to larger astronomical bodies and trace back the history of planetary systems.

High-resolution spectra of weakly bound complexes involving abundant astronomical molecules can be used directly as reference spectra to match data in radioastronomical searches for ISM species and also give unambiguous information on the dynamics, composition, and structure of the complex. They are the best data to use for testing intermolecular potential energy surfaces that are a prerequisite for understanding collision processes between sub-units of the complex.

Studies of the formation of molecules on the surface of interstellar grain analogues lead to a better understanding of routes of the formation of complex organic molecules (COMs) in the ISM. New optical and structural data on the grain analogues can be used in models describing different environments of the ISM and for predictions of observables and provide a link between the structure and morphology of small cosmic bodies and their physical and chemical properties.

The Habilitation is organized as follows. In chapters 2 and 3 state-of-the-art and main results of the studies on weakly bound molecular complexes and interstellar grain analogues are discussed. Chapter 4 presents new directions for research and technical developments. Chapter 5 contains the summary of the Habilitation in German. Then, after bibliography and acknowledgments, chapter 6 contains the original publications on weakly bound complexes and interstellar grain analogues, which form the core of this Habilitation.

List of integrated papers commented with own contributions

6.1.1 **Rotational spectroscopy of the CO–paraH_2 molecular complex**
Potapov A.V., Surin L.A., Panfilov V.A., Dumesh B.S., Giesen T.F., Schlemmer S., Raston P.L., and Jäger W.
The Astrophysical Journal, 2009, v.703, p.2108

Contribution: experiments, analysis, interpretation, writing

6.1.2 **A comprehensive experimental and theoretical study of H_2-CO Spectra**
Jankowski P., Surin L.A., Potapov A., Schlemmer S., McKellar A.R.W., Szalewicz K.
Journal of Chemical Physics, 2013, v.138, p.084307

Contribution: experiments, analysis, interpretation

6.1.3 **First observation of the rotational spectrum of the HD–CO weakly bound complex**
Potapov A., Surin L., Schlemmer S.
Journal of Molecular Spectroscopy, 2015, v.307, p.18

Contribution: experiments, analysis, interpretation, writing

6.1.4 **The CO-H_2 van der Waals complex and complex organic molecules in cold molecular clouds: a TMC-1C survey**
Potapov A., Sanchez-Monge A., Schilke P., Graf U.U., Möller Th., Schlemmer S.
Astronomy & Astrophysics, 2016, v.594, A117

Contribution: idea, observations, analysis, interpretation, writing

6.1.5 **Submillimetre-wave spectroscopy of the K = 2 – 1 subband of the Ne–CO complex**
Potapov A.V., Surin L.A., Schlemmer S., and Giesen T.F.
Journal of Molecular Spectroscopy, 2011, v.270, p.116

Contribution: idea, spectrometer development, experiments, analysis, interpretation, writing

6.1.6 **Conformational landscape of the SF_6 dimer as revealed by high-resolution infrared spectroscopy and complexation with rare gas atoms**
Asselin P., Potapov A., Turner A., Boudon V., Bruel L., Gaveau M. A., and Mons M.
Physical Chemistry Chemical Physics, 2017, v.19, p.17224

Contribution: idea, spectrometer development, experiments, interpretation

6.2.1 **The formation of formaldehyde on interstellar carbonaceous grain analogs by O and H atom addition**
Potapov A., Jäger C., Henning T., Jonusas M., Krim L.
The Astrophysical Journal, 2017, v.846, p.131

Contribution: idea, experiments, analysis, interpretation, writing

6.2.2 **Low temperature optical properties of interstellar and circumstellar icy silicate grain analogues in the mid-infrared spectral region**
Potapov A., Mutschke H., Seeber P., Henning T., Jäger C.
The Astrophysical Journal, 2018, v.861, p.84

Contribution: experiments, analysis, interpretation, writing

6.2.3 **Temperature programed desorption of water ice mixed with amorphous carbon and silicate grains as related to planet-forming disks**
Potapov A., Jäger C., Henning T.
The Astrophysical Journal, 2018, v.865, p.58

Contribution: idea, experiments, analysis, interpretation, writing

6.2.4 **Total power millimetre-wave spectrometer for measurements of dust opacity at cryogenic temperatures**

Potapov A., Lewen F., Mutschke H., Mohr P., Schlemmer S.
Review of Scientific Instruments, 2014, v.85, p.073102

Contribution: spectrometer development, experiments, analysis, interpretation, writing

2. Weakly bound molecular complexes

2.1. State-of-the-art

To understand the evolution of the ISM and planet-forming regions, and finally the origin of life it is necessary to expand our knowledge of the dynamics of the relevant processes, physical chemistry, and biological processes as they happen on different time and size scales. Weakly bound molecular complexes are considered to be a bridge between individual isolated molecules and the bulk phase, a bridge along which properties of matter change dramatically. Intermolecular interactions in molecular complexes affect optical properties and reaction dynamics and, thus, are of a general importance beyond astrochemical applications.

Weakly bound complexes are discussed below in the context of spectroscopic studies and include hydrogen bonded and van der Waals complexes. Strongly bound molecular aggregates involving ions are also of great interest and importance for astrophysics and astrochemistry [see, for example (Herbst 1985; Klemperer & Vaida 2006)] but are beyond the scope of this work. Molecular complexes are considered to play a large role in the chemistry of the ISM, in particular in dense and cold molecular clouds, and also at the higher density and higher temperatures found in planetary atmospheres, where they can contribute to atmospheric chemistry (Vaida & Headrick 2000; Klemperer & Vaida 2006; Vaida 2011). Weakly bound complexes are intermediate species in chemical reactions in the gas phase as well as on the surface of grains. It has been demonstrated that gas phase reactions at temperatures of interstellar clouds go through a formation of weakly bound complexes that are sufficiently long-lived to undergo quantum-mechanical tunnelling to form reaction products (Herbst et al. 1991; Georgievskii & Klippenstein 2007; Shannon et al. 2013; Gómez Martín et al. 2014; Sleiman et al. 2016).

Molecular dimers have been proposed to be a major constituent of cometary matter (Krasnopolsky et al. 1988) and to be contained in interstellar grain mantles (Scherer et al. 1998). The formation of complexes between H_2O and CO_2, CH_3OH and CO_2, H_2O and CH_3OH, and H_2O and CO in laboratory interstellar ices during heating has been shown by analysing the IR spectra of ice mixtures (Ehrenfreund et al. 1998; Dartois et al. 1999; Ehrenfreund et al. 1999; Burke & Brown 2010; Pirim & Krim 2014). It was discussed that the CH_3OH-CO_2 complexes can be formed in interstellar ices during heating events on the long timescales of the ISM (Ehrenfreund, et al. 1999). The formation of the CH_3OH-CO_2 complex was proposed to explain the substructure of the 15.2 μm CO_2 bending mode observed in different astronomical objects (Dartois, et al. 1999). It is worth mentioning the model devised by Ruaud et al. that can explain

recent observations of COMs in the gas phase at temperatures of 10 K (Ruaud et al. 2015). The authors propose the formation of COMs on grain surfaces through the formation of short-lived van der Waals complexes of adsorbing gas-phase carbon atoms with a number of major ice compounds, such as H_2O, NH_3, CO_2, CH_4, and CH_3OH.

At relatively high densities and low temperatures of planetary atmospheres, the formation of weakly bound complexes can be expected. These complexes involving abundant molecules, such as H_2, O_2, NH_3, CH_4, H_2O, can be active in the infrared region and play an important role in atmospheric chemistry by absorption of stellar radiation and as intermediate species in chemical reactions. Molecular complexes of oxygen have been observed on the water-ice covered surfaces of Ganymede and Europa and odd oxygen production from oxygen dimer photolysis in the UV was used to explain ozone formation on these planetary satellites (Klemperer & Vaida 2006). In the Saturnian system, it has been estimated that the initial ice budgets of Titan as well as of the smaller satellites may have contained as much as 15% ammonia-water hydrate (Ellsworth & Schubert 1983). Concerning our planet, weakly bound complexes involving water are suspected to significantly affect Earth's atmospheric chemistry. The water molecule itself contributes significantly to Earth's radiation balance because of the high partial pressure of water in the atmosphere and its large absorption cross-section in the IR (Daniel et al. 1999). Water, interacting with the other atmospheric molecules, affects the absorption of solar and terrestrial radiation (e.g., shift of transition frequencies, change of transition intensities, new absorption bands), participates in photochemical reactions (e.g., destruction of ozone, production of radicals), and behaves as a catalyst (e.g., photodissociation of hydrated H_2SO_4 and HNO_3) (Vaida & Headrick 2000; Pfeilsticker et al. 2003; Vaida, Kjaergaard, & Feierabend 2003; Vaida 2011). Moreover, complexes involving water can be stepping stones in the formation of atmospheric nanoparticles (Murphy, Thomson, & Mahoney 1998; Zhang et al. 2012), strongly influencing climate and human health.

The binding energy of weakly bound complexes is usually much smaller than room temperature thermal energy. For this reason, rare-gas solid matrixes, gas phase supersonic jets, and liquid helium droplets are the environments in which weakly bound complexes are typically studied in the laboratory (Schriver-Mazzuoli 1998; Havenith 2002; Toennies & Vilesov 2004). Low and high-resolution spectroscopy, mainly in the infrared (IR), terahertz (THz), millimetre-wave (MMW), and microwave (MW) spectral regions, has been performed. Interaction between a complex and a rare-gas solid matrix or helium droplet surface leads to inhomogeneous shifts

and broadening of the spectral lines and also hinders free rotation of the complex. Thus, the laboratory data best suited for the development of interaction potentials between species of the complex and for comparison to radioastronomical observations is that determined in the gas phase and at high-resolution. “High” resolution refers to measurements taken at resolution good enough to interpret data from radio telescopes, namely, as defined by the Doppler linewidth, which is hundreds of kHz at a frequency of 100 GHz.

Typically, MW spectroscopy gives access to information about ground state rotational energy levels of the entire complex, MMW to internal rotor states, THz probes intermolecular vibrations, and IR comprises intramolecular vibrations. As one can see, different techniques probe different parts of the intermolecular potential, and, when merged, provide a complete picture of the interaction between sub-units in the complex. Gas phase high-resolution data can be used directly as reference spectra to match data in radio astronomical searches for ISM species, and also give unambiguous information on the dynamics, composition, and structure of the complex. Moreover, they are the best data to use for testing intermolecular potential energy surfaces (PESs). For details about the relation between PES and the spectra of weakly bound complexes, the reader is referred to the review by Wormer and van der Avoird (Wormer & van der Avoird 2000). Examples of testing of PESs for molecular complexes with high-resolution data are available in the literature (Fellers et al. 1999; Potapov et al. 2009a; Potapov et al. 2011; van der Avoird & Nesbitt 2011; Jankowski et al. 2013).

A huge number of weakly bound complexes have been probed spectroscopically in the gas phase [for reviews see (Xu, Van Wijngaarden, & Jäger 2005; Tanaka, Harada, & Yamada 2011; Potapov & Asselin 2014; Herman et al. 2016; Potapov 2017a) and also the bibliography of rotational spectra of weakly bound molecular complexes published by Novick (https://wesfiles.wesleyan.edu/home/snovick/SN_webpage/vdw.pdf)]. In spite of this “huge number” relevant information for many important species is not yet available. The future tasks for complexes involving important astronomical molecules, such as H_2O, NH_3, O_2, PAHs, etc, are: (i) to obtain spectroscopic signatures in different spectral ranges; (ii) to reveal their internal dynamics; (iii) to understand the role of hydrogen and van der Waals bonds in the dynamics, structure, and reactivity of the complexes; (iv) to build reliable interaction potentials; and, (v) finally, to include the new data into state-of-the-art models. A schematic Figure 2 shows the experimentally determined energy level scheme of the CO-paraH_2 van der Waals complex and the ways of further usage of high-resolution data.

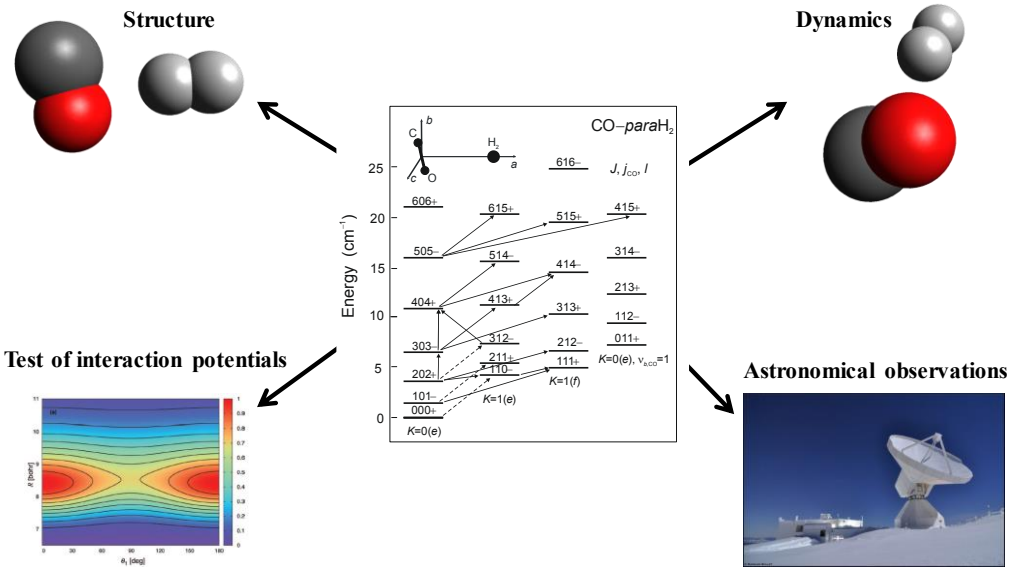

Figure 2. A schematic figure showing the experimentally determined energy level scheme of the CO-paraH_2 van der Waals complex (Potapov, et al. 2009a) and the ways of further usage of high-resolution data.

Up until now only the $(O_2)_2$ and $(H_2)_2$ dimers have been detected in the atmospheres of Earth (Pfeilsticker, Erle, & Platt 1997; Solomon et al. 1998) and Jupiter and Saturn (Mckellar 1988; Trafton & Watson 1992). The rotationally resolved millimetre-wave spectrum of the water dimer has been recorded in the laboratory under atmospheric conditions (Tretyakov et al. 2013). The feasibility of observing weakly bound molecular complexes in the ISM is still debatable because their formation rates at the very low densities in interstellar molecular clouds (below 10^7 cm^{-3}) are low. This is because of the small probability of three-body collisions, needed to stabilize a two-body complex. On the other hand, the large timescale on which these processes occur in the ISM makes radiative association, usually a slow process, feasible (Klemperer & Vaida 2006). In this case the complex would normally be formed in its ground electronic state and stabilized by emission from vibrational-rotational levels above the dissociation limit to stable levels below the dissociation limit (Herbst 1985; Bates & Herbst 1988). Also, non-equilibrium conditions in the ISM may favour formation of weakly bound complexes over longer periods of time on the surfaces of dust grains in shielded regions, at low temperatures, with sudden release occurring by localized heating processes such as turbulence or bipolar flows (Allen et al. 1997). It is possible that under "normal" gas-phase chemistry conditions, the abundances of the complexes are very low, however, non-LTE (Local Thermodynamic Equilibrium) effects may play an important role in enhancing their abundance and detectability. There have been a number of surprising observations (unexpected from

standard models) that brought new insight into the physics and chemistry of the ISM, for example, the detection of complex organic molecules in cold molecular clouds (Bacmann et al. 2012; Vastel et al. 2014; Balucani, Ceccarelli, & Taquet 2015). Finding weakly bound complexes would equally challenge prevailing beliefs about the chemistry of the ISM and planetary atmospheres including their physical (temperature, number density) and chemical (molecular composition, structure) properties.

As molecular hydrogen, H_2, is by far the most abundant molecule in the universe and carbon monoxide, CO, is the second most abundant, the intermolecular forces between them are of fundamental interest. Also, weakly bound complexes involving these two species are the best candidates for detection in interstellar space. Another promising candidate is the water dimer, $(H_2O)_2$, due to the high abundance of water molecules in ices in interstellar clouds and the relatively strong bond of the dimer, which can possibly allow it to survive after sublimation from an ice surface. Also it was hoped that HCN dimers, $(HCN)_2$, would be detected, since the abundance of the monomer is quite high, the binding energy strong, and the dipole moment large. Nevertheless, all astronomical searches for weakly bound complexes in the ISM have been unsuccessful. The first published search was devoted to $(HCN)_2$ (Storey & Cheung 1978). It was followed by a search for the CO dimer, $(CO)_2$, (Vanden Bout et al. 1979), one more try for $(HCN)_2$ (Schenewerk et al. 1985), a try for the CO-*para*H_2 complex (Allen, et al. 1997), and the H_2O dimer search (Scherer, et al. 1998). Later laboratory measurements pointed out that the $(HCN)_2$ and $(CO)_2$ searches were based on frequencies that could not be unambiguously attributed to the dimers (Schenewerk, et al. 1985; Surin et al. 2007). In the case of CO-H_2, the strongest pure rotational transition at low temperatures, originated from the lowest energy level, that would have helped to identify this complex in the ISM was wrongly tuned (fell outside of the search range) (Allen, et al. 1997). Thus, the first detection of a weakly bound complex in the ISM is still a challenging task.

2.2. Main results

We performed a laboratory study and a radioastronomical search of the CO−H_2 van der Waals complex. The rotational spectra of the complex and its isotopologues were measured in the laboratory allowing for a precise determination of the corresponding energy level positions of CO–paraH_2 (Potapov, et al. 2009a), CO-orthoH_2 (Jankowski, et al. 2013), CO-orthoD_2 (Potapov et al. 2009b), and CO-HD (Potapov, Surin, & Schlemmer 2015). The interaction potential for the CO-H_2 complex was tested and improved on the basis of the high-resolution spectra (Potapov, et al. 2009a; Jankowski, et al. 2013), which is a prerequisite for understanding collision processes between hydrogen and carbon monoxide, the most abundant molecules in the universe.

The high-resolution data enabled a radioastronomical search for the CO-H_2 molecular complex in a cold, dense core in TMC-1C (with a temperature of ~10 K) by using the Institute de Radioastronomie Millimétrique (IRAM) 30 m telescope (Potapov, et al. 2016). Unfortunately, we did not detect any lines belonging to the CO-H_2 complex. In our paper we could set up a new, more stringent upper limit for the abundance of the complex. We concluded that it should be possible to detect a weakly bound complex in the ISM, for the first time, by observations with one or two orders higher sensitivity, feasible with the Atacama Large Millimeter/submillimeter Array (ALMA) (Figure 3). A proposal devoted to a radioastronomical search for weakly bound complexes in cold molecular clouds with ALMA is being under preparation.

Figure 3. The Atacama Large Millimeter/submillimeter Array (ALMA). Collage. Photos are taken from the website of the European Southern Observatory (https://www.eso.org/public/). Credits: Clem & Adri Bacri-Normier (wingsforscience.com)/ESO, ALMA (ESO/NAOJ/NRAO).

One more result of our astronomical survey was the detection of 75 lines associated with 41 different species. A number of complex organic species, for example, methyl cyanide, methanol, propyne, and ketene, associated with cold gas were detected, confirming the presence of these complex species not only in warm objects but also in cold regimes and bringing new information for the understanding of astrochemical networks.

A THz spectrometer combining pulsed supersonic expansion, light source, and multi-pass optics was developed. The spectrometer was tested on the pure rotational spectrum of the Ne–CO van der Waals complex in the frequency range of 208–230 GHz (Potapov, et al. 2011). Improved molecular parameters of the complex were obtained which allowed us to perform a sensitive test of the available intermolecular potential energy surfaces of the Ne–CO system. The spectrometer allows systematic measurements of jet-cooled molecules and molecular complexes in the terahertz spectral range.

An IR spectrometer combining pulsed supersonic expansion, light source, and multi-pass optics was developed. The spectrometer was used to revisit the rovibrational absorption spectrum of the SF_6 dimer in the ν_3 mode region (Asselin et al. 2017). For the first time, two conformers of the dimer were unambiguously identified. Furthermore, an additional intense rovibrational band in the spectrum was assigned to the $(SF_6)_2$–He trimer. The spectrometer allows systematic measurements of jet-cooled molecules and molecular complexes in the infrared spectral range. Recently, it was used to study the rovibrational spectrum of the NH_3-Ar complex in the ν_2 umbrella region of NH_3 and test the accuracy of the interaction potential between NH_3 and Ar (Asselin et al. 2018).

3. Interstellar grains

3.1 State-of-the-art

Dust grains play a central role in the physics and chemistry of practically all astrophysical environments where temperatures are low enough for dust grains to exist (Dorschner & Henning 1995; Henning 2010). They influence the thermodynamic properties of the medium and provide a surface for efficient chemical reactions responsible for the synthesis of important astronomical molecules. Circumstellar dust grains are of great interest as building blocks of planets and as a remnant of protoplanetary disks (Krivov 2010; Henning & Semenov 2013). Knowing the properties of grains, we can follow their pathways to larger astronomical bodies and trace back the history of planetary systems.

Carbonaceous materials are a primary component of the interstellar dust and play a key role in many interstellar processes (Henning & Salama 1998; Ehrenfreund & Charnley 2000; van Dishoeck 2014). One more important material is amorphous silicates, and other types of solids, such as iron oxides, carbides, sulphides or metallic iron, are minor components (Henning 2010; van Dishoeck 2014). Circumstellar shells of AGB stars, planetary nebulas, and supernovae, and dense interstellar clouds are well-known sources of cosmic dust grains, but their formation pathways are not yet revealed and it remains a matter of many scientific discussions (Zhukovska, Henning, & Dobbs 2018). The knowledge of the formation process, building blocks, and/or intermediates are indispensable for the definition of the initial dust structure and composition and the understanding of the dust cycle in different astrophysical environments (Draine 2003; Jäger 2015; Jäger & Mutschke 2015). Three main steps of dust formation are the formation of the molecular precursors, the particle nucleation, and the particle growth, where two mechanisms, the growth of particles by addition of gas-phase molecules and coagulation via particle–particle collisions, can be considered. The most controversially discussed phase is the nucleation process (Jäger & Mutschke 2015).

In cold cosmic environments, such as dense molecular clouds and outer parts of circumstellar shells, including envelopes of evolved stars, protoplanetary disks, and debris disks, dust grains are covered by molecular ices (Tielens 2013). Ice-coated grains are expected to stick together much more efficiently. The increase of the mass in solid material in the region where there is ice compared to where there is no ice has been estimated to range from a factor of 1.6 (Min et al. 2011) to a factor of 4.2 (Thommes & Duncan 2006). After coagulation of dust grain monomers, covered by ice, in dense regions, ice can be trapped inside grain aggregates, and, thus, these aggregates might present mixtures of ice and dust. This assumption is supported

by laboratory experiments and theoretical simulations on dust particles aggregation by collisions, where it was shown that final dust aggregates are highly porous (Henning & Stognienko 1996; Wurm & Blum 1998; Krause & Blum 2004; Blum 2018). Ice can stay in the pores on the surface of dust monomers or/and can fill the pores later via adsorption of volatile molecules from the gas phase. As it was shown by the examination of the samples brought by the Stardust mission, there are indications that the dust and water-ice agglomerates were mixed before cometesimals formed in the outer solar system (Brownlee et al. 2006). It was also demonstrated that the nucleus of the comet 67P/Churyumov-Gerasimenko is characterized by an average dust-to-ices mass ratio of 7.5 consistent with a mixture of ices, Fe-sulphides, silicates, and hydrocarbons (Fulle et al. 2017).

Observations and dedicated laboratory experiments have shown that the main constituent of interstellar and circumstellar ices is H_2O with lower fractions of other volatile species, such as CO, CO_2, NH_3, CH_4, and CH_3OH (Allamandola et al. 1999; Burke & Brown 2010; van Dishoeck 2014; Boogert, Gerakines, & Whittet 2015). Water plays an outstanding role in the chemistry of the ISM and is well known as a catalyst for chemical reactions and nucleation of particles (van Dishoeck et al. 2014). Crystalline water ice in protoplanetary disks was tentatively detected (McClure et al. 2012; McClure et al. 2015). Recently, it was unambiguously identified in a disk around the Herbig star HD 142527 (Min et al. 2016). It was shown there that the disk contains a large reservoir of water ice, comparable to the water ice abundance in the outer solar system, comets, and dense interstellar clouds. Thus, the interaction between water ice and dust species and the structural and optical properties of dust/ice mixtures are very important for the understanding of astronomical observations of water vapour in star- and planet-forming regions [for review see (Bergin & van Dishoeck 2012)] and for the revealing of the architecture and evolution of different phases of the ISM.

Dust grains absorb and scatter stellar light and reemit the absorbed energy. To interpret the astronomical spectra of dust grains, spectral data on laboratory dust grain analogues are required. Optical properties of grains in different frequency regions are important for the modelling and understanding of the physics in astrophysical environments. The opacity of grains is the base for the estimation of important astrophysical parameters, such as dust temperatures, mass loss rates of evolved stars, and the total dust mass in circumstellar shells or molecular clouds. Optical properties of pure water ice, silicate and carbon grains have been intensively investigated in the laboratory (Hagen, Tielens, & Greenberg 1981; Kitta & Krätschmer 1983; Smith et al. 1994; Dorschner et al. 1995; Henning & Mutschke 1997; Jäger, Mutschke, & Henning 1998; Jäger et al. 2003; Curtis et al. 2005; Jäger et al. 2008; Mastrapa et

al. 2008; Mastrapa et al. 2009; Allodi et al. 2014; Sabri et al. 2014; Reinert et al. 2015). However, as it was discussed above, dust in cold and dense phases of the ISM is, probably, mixed with molecular ices, that is why there is strong need to study experimentally optical properties of such mixtures, which are not yet known. One can try to obtain optical constants of dust/ice mixtures by mixing of known pure dust and ice constants using a number of theoretical mixing rules, as it was done in a number of works (Mukai & Mukai 1984; Maron & Maron 2008; Min, et al. 2016), but the question is the reliability of such approaches. Recently, for the first time, optical constants of silicate/water ice mixtures were experimentally determined in our laboratory in the mid-infrared spectral region (Potapov et al. 2018a).

The main triggers of grain surface chemistry in the ISM are UV irradiation, cosmic rays, thermal processing, reactions with radicals, and atom addition. A schematic Figure 4 shows cosmic grains covered by molecular ices and the main routes of their processing that takes place in astrophysical environments.

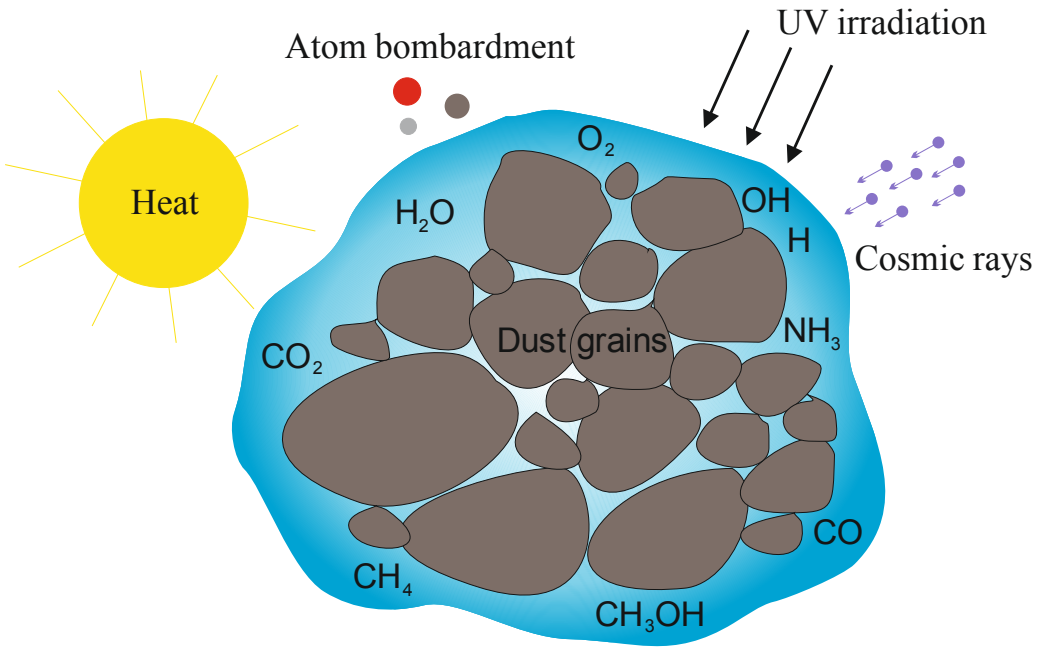

Figure 4. Schematic figure showing cosmic grains covered by molecular ices and the main routes of their processing that takes place in astrophysical environments.

Many laboratory experiments have been performed on the formation of simple and complex molecules, including amino acids, in interstellar ice analogues using the triggers mentioned above [for reviews see (Theule et al. 2013; Linnartz, Ioppolo, & Fedoseev 2015; Öberg 2016)]. A major part of the laboratory work deals with molecular ices covering standard substrates not related to the ISM, such as metals, KBr or HOPG. The dust grain surface can

participate in ice chemistry and can alter the efficiency of the molecular formation. In pioneering experiments on the formation of molecules in grain-ice systems, CO and CO_2 were produced by irradiation of hydrogenated carbon grains covered by water ice by He^+ ions (Mennella, Palumbo, & Baratta 2004) and by Lyα photons (Mennella et al. 2006). These experiments were followed by the synthesis of CO_2 in H_2O ice covering amorphous carbon foils by irradiation with protons (Raut et al. 2012) and in O_2 ice covering amorphous carbon foils by ultraviolet irradiation (Fulvio, Raut, & Baragiola 2012). Finally, the formation of CO and CO_2 in H_2O and O_2 ices on hydrogenated fullerene-like carbon grains after proton bombardment (Sabri et al. 2015) and in H_2O ice on graphite films by Lyα irradiation (Shi, Grieves, & Orlando 2015) were demonstrated. Thus, only CO and CO_2 molecules have been synthesized in interstellar ice-dust analogues up to very recently, when we performed our experiments on the formation of formaldehyde, H_2CO, on hydrogenated fullerene-like carbon grains by O/H atom addition (Potapov et al. 2017b).

Laboratory gas-phase condensation techniques are used to mimic astrophysical condensation processes of cosmic dust grains and to produce cosmic dust analogues. Nanometre-sized dust particles can be produced in two steps. The first step is the formation of grains in the gas phase by laser ablation or pyrolysis techniques. In the second step, the generated grains are deposited as a film on a substrate. The individual particles are very small (less than 3-4 nm) and the largest particle agglomerates are in a range of 15 nm. The morphology of the dust particle agglomerates on the substrate can be understood as a porous layer of rather fractal agglomerates. The porosity of the deposited dust is very high and was found to be about 90% (Sabri, et al. 2015). The surface of the dust is very large, but the area cannot be measured exactly.

The two main laboratory methods for studying COMs forming on laboratory grain analogues are solid state Fourier transform infrared spectroscopy (FTIR) and gas phase mass spectrometry (MS). FTIR spectrometers combine many advantages such as multiplex recording, broadband coverage, and easy wavelength calibration. MS has a very high sensitivity, capable of reading partial pressures down to $5x10^{-13}$ mbar (Fraser, Collings, & McCoustra 2002). MS is often used to follow the kinetics of desorption of molecules from ice analogues. In so-called temperature programmed desorption (TPD) experiments one obtains information on the mass of a desorbed molecule and its desorption temperature and rate, which can be converted into a desorption energy and used in astrochemical models. These methods have limitations, however. At smaller wavenumbers, in the terahertz frequency range, which is the range of many ground-based

observatories (e.g., Nobeyama, LMT, APEX, IRAM, ALMA) the signal to noise of the FTIR spectrometers is limited due to the low power density of the thermal radiation source. The problems of the MS method are low mass resolution of typically used mass spectrometers and the lack of spectral data associated with species observed. Also, in standard MS experiments it is not possible to distinguish between molecules of the same mass. This has been recently overcome by fragment-free tunable single photon vacuum ultraviolet photoionization in combination with reflectron time-of-flight mass spectrometry (Abplanalp, Forstel, & Kaiser 2016), but this method is not widely available. Thus, new laboratory methods overcoming the problems of the standard techniques are highly desired. A new experimental approach will be discussed in this context in section 4.3.

3.2 Main Results

In our study (Potapov, et al. 2017b) a new route of COM formation in the ISM, grain surface processes, was probed experimentally. Our results demonstrate, for the first time, that the bombardment of interstellar carbonaceous grain analogues not covered by molecular ices by O and H atoms at low temperatures causes the formation of CO molecules with their further hydrogenation leading to the formation of solid formaldehyde. Figure 5 shows the infrared (IR) difference spectra of grain analogues before and after atom bombardment, where two absorption signals corresponding to H_2CO are visible. The formation of H_2CO is an indication for a possible methanol formation route in such systems. Methanol is generally taken to be a starting point towards the formation of more complex organic molecules in dense and cold molecular clouds (Öberg et al. 2009; Vasyunin & Herbst 2013; Balucani, et al. 2015). The idea on the further study of this new route of COM formation in the interstellar medium is discussed in chapter 4.

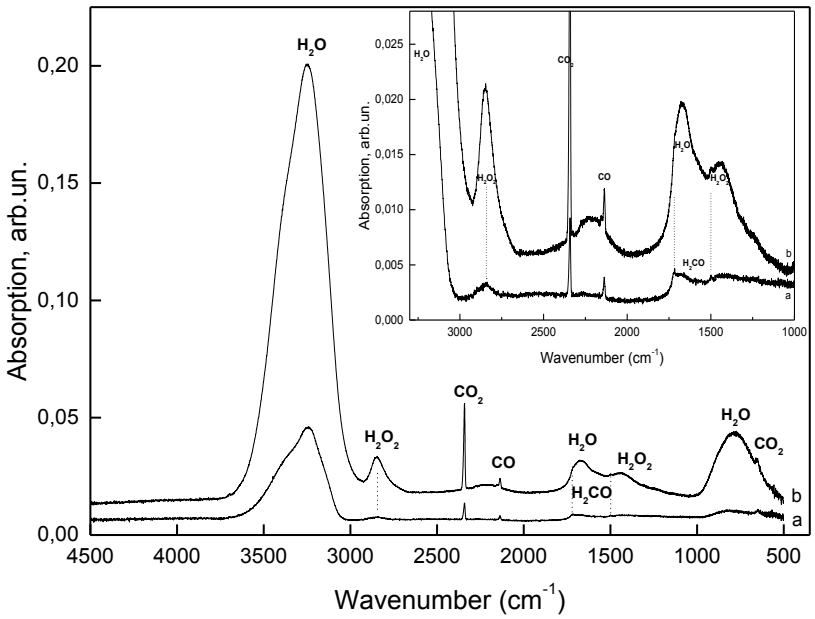

Figure 5. IR difference spectra before and after O/H bombardment of carbon grains for two O_2/H_2 gas mixtures in the atomic source: (a) $[O_2]/[H_2]$ = 1/60, (b) $[O_2]/[H_2]$ = 10/70. Inset: zoom-in in the 3300 – 1000 cm^{-1} spectral range (Potapov, et al. 2017b).

The main purpose of the next study was to produce unique sets of experimental optical data for silicate/water ice mixtures in the mid-IR spectral region at low temperatures. For the first time, optical constants, the real and imaginary parts of the complex refractive index, of such

mixtures were experimentally determined (Potapov, et al. 2018a). In addition, optical constants of pure water ice and pure silicates were derived in the laboratory. Two sets of constants were compared, namely, “measured” constants calculated from the transmission spectra of silicate/water ice samples and “effective” constants calculated from the optical constants of pure silicates and pure water ice samples using different mixing rules (effective medium approaches). Differences between measured and effective constants show that a “theoretical” mixing (averaging) of optical constants of water ice and silicates for the determination of the optical properties of silicate/ice mixtures can lead to incorrect results.

It was also shown in the same study that a part of water ice molecules is trapped in/on silicate grains and does not desorb up to 200 K. Water ice trapped in/on grains and, thus, survived during the transition from a dense molecular cloud to a protoplanetary disk can partly explain large amounts of H_2O ice in disks around young stars (Min, et al. 2016).

The temperature programmed desorption (TPD) of water ice mixed with amorphous carbon and silicate grains was studied in the laboratory (Potapov, Jäger, & Henning 2018b). We showed that variations of the grain/ice mass ratio lead to a transformation of the TPD curve of the H_2O ice, which can be perfectly fitted with the Polanyi-Wigner equation by using fractional desorption orders. For carbon grains, the desorption order of H_2O ice increases from 0 for pure H_2O ice to 1 for the grain/ice ratio of 1.3. For two silicate/ice mixtures, the desorption order of the H_2O ice is 1. This result could be explained by the desorption of water molecules from a large surface of fractal clusters composed of carbon and silicate grains and provides a link between the structure and morphology of small cosmic bodies and the kinetics of desorption of water ice included in them.

A unique highly sensitive total power millimetre-wave spectrometer for investigations of the opacity of solid samples at cryogenic temperatures was developed (Potapov et al. 2014). The spectrometer was benchmarked on the MMW spectra of iron-free silicate samples. It allows systematic measurements of absorption spectra of interstellar dust analogues.

4. New directions for research and technical developments

4.1 Formation of complex organic molecules on interstellar grain analogues

One of the challenging new directions for research is to develop the idea of the formation of COMs on the surface of cold interstellar carbonaceous grains pioneered by our experiments on the formation of H_2CO (Potapov, et al. 2017b). One has to try to synthesize astrochemically relevant COMs by the bombardment of laboratory carbonaceous samples by O, H and N atoms and OH radicals and by UV irradiation of the samples. Such a project can be realized in our laboratory by using a new ultra-high vacuum (UHV) set-up INSIDE (INterStellar Ice Dust Experiment) shown in Figure 6, which allows investigations of interstellar grain analogues as represented by carbon- or silicate-based dust substrates covered or not covered by molecular ices (Potapov 2017c). Using the set-up, we are able to investigate surface chemistry and desorption properties of grain or grain/ice samples at conditions similar to those in dense molecular clouds (temperatures down to 6 K and pressure of 10^{-11} mbar corresponding to a number density of 10^6 molecules/cm^3). The set-up comprises a UHV chamber coupled to an FTIR spectrometer, a quadrupole mass spectrometer, and a UV source. An atomic source can be installed instead of the UV source for the bombardment.

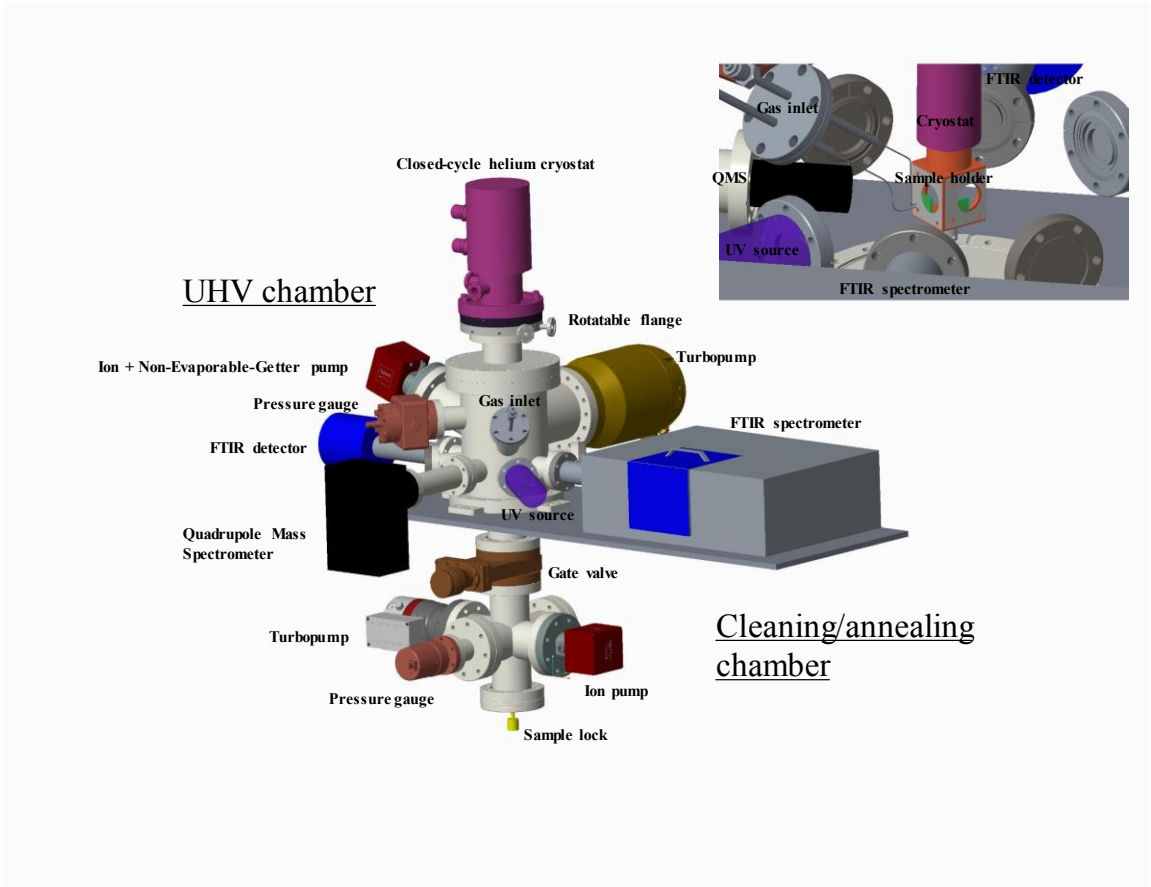

Figure 6. A sketch of INSIDE. Inset: UHV chamber, internal view (Potapov 2017c).

There are a number of important complex organic molecules known as building blocks for prebiotic molecules, such as amino acids, which have been detected in the ISM and are, probably, formed on the surface of interstellar carbon grains, for example, methanol, glycolaldehyde, acetaldehyde, and methylamine. The next step is glycine, the simplest amino acid, which is known to be present in comets (Elsila, et al. 2009; Altwegg & al. 2016). If we synthesize these molecules on the surface of interstellar grain analogues we will take an essential step towards understanding:

i) the molecular complexity and chemical routes in the ISM,

ii) the catalytic effect of interstellar grains on the surface chemistry in the ISM,

iii) the hypothesis of the formation of prebiotic molecules in the interstellar medium.

4.2 Optical and structural properties of dust/ice mixtures

With our pioneering studies of dust/ice mixtures presented in this Habilitation (Potapov, et al. 2018a; Potapov, et al. 2018b) we have opened a new door for future research. Differences between measured and effective optical constants discussed above underline the importance of further investigations of optical and structural properties of grain/ice mixtures. A trapping of a part of water ice in/on dust grains must be investigated in more details and can improve our understanding of the abundance and desorption properties of interstellar and circumstellar ices and can help to develop a link between the dust/ice ratio in a cosmic body and the cosmic environment, from where the body originates. The desorption rates of ices are important for the understanding of the thermal history of dust grains at different astronomical conditions. First stage of molecule formation on cold grain surfaces is dominated by H_2O ice and mixtures with H_2O in all Galactic and extragalactic environments (Boogert, et al. 2015). After the initial ice layers are formed, grain coagulation accelerates by the presence of polar coverage. Thus, an existence of water ice on the grains must be one of the important parameters for the rate and efficiency of the grain growth and this existence is directly related to the desorption properties of ices mixed with dust grains.

Investigations of dust/ice mixtures are just in time with respect to a new challenging space mission, the James Webb Space Telescope, which will be able to bring novel detailed information on interstellar and circumstellar grains, and suitable laboratory data are extremely important for the decoding of astronomical spectra.

4.3 Gas phase spectroscopy of molecules produced on interstellar grain analogues

The problems of the FTIR and MS methods discussed at the end of chapter 3.1 do not exist in high-resolution spectroscopy in the MW, MMW, and THz spectral regions. High-resolution laboratory spectra can be directly compared to spectra observed by ground-based and space-board observatories and give unambiguous information on the molecular composition and structure of molecules.

The idea discussed here is to develop an innovative approach for the laboratory study of COMs produced on interstellar grain analogues - a combination of chemical synthesis in the solid state and gas phase high-resolution spectroscopy. The approach aims at providing unambiguous information on the molecular composition and structure of "new" COMs formed in the solid state and released to the gas phase and at measuring reference microwave, millimetre-wave, and terahertz spectra for their detection in the ISM. It is important to note that we, as astronomers and astrophysicists, are particularly interested in molecules known to be formed only in laboratory interstellar ice analogues, but for which high-resolution spectral data are not yet available.

There are, to the best of my knowledge, only a few examples of gas phase high-resolution spectroscopy techniques used in studies of interstellar ice analogues, all published as conference abstracts (Auriacombe et al. 2014; Mesko et al. 2014; Mesko et al. 2015). They are based on broadband high-resolution THz spectrometers that allow observations of spectra of desorbed molecules directly above the ice surface during thermal- or photo-processing. In our recent experiments the usefulness of combining solid-phase chemistry at low temperatures with gas-phase MW spectroscopy detection in the laboratory using a chirped pulse Fourier transform microwave (CP-FTMW) spectrometer was demonstrated.

The CP-FTMW technique is a very promising spectroscopic technique. It was developed about 10 years ago by Brooks Pate and co-workers (Brown et al. 2008) and has quickly become used worldwide to obtain high-resolution spectra (Jahn et al. 2012; Perez et al. 2013; Medcraft, Wolf, & Schnell 2014) and to study reaction dynamics (Dian et al. 2008; Abeysekera et al. 2014; Prozument et al. 2014; Abeysekera et al. 2015). The abilities of a CP-FTMW spectrometer to create a phase-reproducible chirped excitation pulse of more than 10 GHz linear frequency sweep and microsecond duration with subsequent broadband signal detection make it possible to detect simultaneously many transitions belonging to a single or several species with meaningful relative intensities, thus, allowing one to follow the time evolution of spectra and reaction dynamics. In the last years the spectral range of CP-FTMW spectrometers was

extended to the MMW (Park et al. 2011) and THz regions (Gerecht, Douglass, & Plusquellic 2011; Steber et al. 2012).

Our set-up was tested by looking at the thermal desorption of ammonia ice deposited on the walls of a copper U-shaped waveguide at 20 K. We showed that the sensitivity of the CP-FTMW technique is several orders of magnitude lower than MS, but is enough to detect a sub-monolayer amount of desorbing ice. Within the ideal gas approximation, the detection limit corresponds to a few picomoles of material. This is competitive with the best gas chromatograph-mass spectrometers (Mrad et al. 2014). One ice monolayer coating will provide 100 nanomoles inside the waveguide used in the experiments, which is five orders of magnitude more than the detection limit. Scaling to a smaller dipole moment molecule (e.g. 0.1 D compared to 1.4718 D for NH_3) and taking into account that solid-state reactions usually have a low yield, on the order of a percent, we are still one-two orders of magnitude above the detection limit. Thus, such a set-up should be sensitive enough to study MW spectra of "new" COMs synthesized on interstellar grain analogues.

4.4 Small helium and hydrogen clusters

While He- and H_2-clusters pose no direct relevance to the chemistry and physics of the ISM, certainly understanding their properties as model cluster systems at low temperatures and pressures will allow insight into the behaviour of other clustered or weakly bound species.

Seventy years ago Elephter Andronikashvili was able to demostrate superfluidity by studying the torsional oscillations of a stack of closely spaced thin disks in liquid helium (Andronikashvili 1946). "Drag" from the normal fluid component caused a decrease of the momentum of inertia of the stack, providing evidence for the superfluidity of helium below the λ-point of 2.17 K.

More than 50 years later, the Andronikashvili experiment was repeated on a "microscopic" scale. Spectra of molecules embedded in helium nanodroplets consisting of 10^3–10^4 He atoms were measured, showing the same effect, namely, an increase in the rotational constant (decrease in the moment of inertia) of a probe molecule (Grebenev, Toennies, & Vilesov 1998; Toennies & Vilesov 2004). A fundamental question arose from these nanodroplet studies: how many He atoms are required for the onset of superfluidity?

To answer this question, He_N-molecule clusters with N = 2–80 were explored using high-resolution MW, MMW, and IR spectroscopy. A similar increase in the rotational constant was observed for small clusters with increasing cluster size at a certain N [(Surin et al. 2008; Dumesh, Potapov, & Surin 2009; Potapov et al. 2010) and references therein]. This nonclassical

behavior was interpreted as being a decoupling of part of the He density from the rotational motion of the molecule. It was proposed that this decoupling is a sign of superfluidity at the microscopic level, in analogy to the ‘‘macroscopic’’ Andronikashvili experiment.

Superfluidity of molecular hydrogen, predicted more than 40 years ago (Ginzburg & Sobyanin 1972), was also examined (Moroni et al. 2005; Raston et al. 2012). A microwave study of $(para\text{H}_2)_N$–CO clusters showed the decoupling of a part of the ($para\text{H}_2$) density from the rotational motion of the CO molecule (same as in the case of the He_N–CO clusters) (Raston, et al. 2012). This decoupling was interpreted as being due to the superfluidity of molecular hydrogen.

It is not yet clear whether the behaviour observed in small clusters and attributed to superfluidity results from the same kind of superfluid structure that exists in a bulk liquid. A fundamental question is: what is the relation between “microscopic superfluidity” in the small clusters and macroscopic superfluidity in liquid helium? Spectroscopic investigations of helium and molecular hydrogen clusters involving fermionic particles, i.e., $(^3\text{He})_N$–molecule and $(\text{HD})_N$–molecule clusters, would unambiguously confirm whether the decoupling of helium/hydrogen density is indeed an indicator of superfluidity. A first step, MMW studies of the ^{3}He-CO and HD-CO binary complexes has already been taken (Surin et al. 2000; Potapov, et al. 2015).

5. Deutsche Zusammenfassung

Laborastrophysik ist eine Brücke zwischen Untersuchungen von Atomen und Molekülen im interstellaren Medium, die wir durch astronomische Beobachtungen identifizieren können, und Untersuchungen dieser Spezies oder ihrer Analoga, die wir im Labor erzeugen und in situ vermessen können. Die Laborastrophysik liefert dabei spektroskopische Fingerabdrücke von Spezies, die benötigt werden, um beobachtete astronomische Spektren zu entschlüsseln und erlaubt die Modellierung physikalisch-chemischer Prozesse unter den Bedingungen des interstellaren Mediums. Sie hilft, diese Prozesse in ihrer Gesamtheit zu verstehen und belastbare astrochemische Modelle aufzustellen, die, unterstützt durch astronomische Beobachtungen, unsere astrochemische Vergangenheit und Zukunft enthüllen können.

Eine der grundlegenden Fragen, die sich bezüglich des interstellaren Mediums stellt, ist die nach der Natur und Häufigkeiten der detektierten Spezies. Um diese Frage zu beantworten, sind drei wesentliche Voraussetzungen zu erfüllen: (a) Spezies im interstellaren Medium suchen und identifizieren, (b) theoretische Modelle entwickeln, die die Bildung der beobachteten Spezies erklären und (c) Schlüsselparameter der Modelle bestimmen, wie etwa dynamische und strukturelle Parameter der Spezies und Ratenkoeffizienten der chemischen Netzwerke.

Die vorliegende Arbeit widmet sich dem ersten und dritten dieser Problemkreise. Hauptuntersuchungsobjekte dieser Forschung waren 1) schwach gebundene Molekülcluster, die in den niedrigen Temperaturen eines Überschallmolekularstrahls produziert wurden, und 2) Laboranaloga interstellarer Staubpartikel bei niedrigen Temperaturen und Drücken. Es wird davon ausgegangen, dass Molekülcluster eine große Rolle in der Chemie des ISM spielen, besonders in dichten und kalten Molekülwolken, aber auch bei höheren Dichten und Drücken, wie sie in Planetenatmosphären auftreten und wo sie zur Atmosphärenchemie beitragen (Vaida & Headrick 2000; Klemperer & Vaida 2006; Vaida 2011). Schwach gebundene Molekülcluster sind Zwischenprodukte chemischer Reaktionen in der Gasphase sowie auf der Oberfläche von Staubpartikeln. Untersuchungen an diesen Clustern ermöglichen es uns, die Wechselwirkungen zwischen astronomisch wichtigen Spezies zu verstehen. Staubpartikel sind von zentraler Bedeutung in der Chemie und Physik des interstellaren Mediums und in praktisch allen astrophysikalischen Umgebungen. Sie beeinflussen die thermodynamischen Eigenschaften des Mediums und stellen Oberflächen für sehr effiziente chemische Reaktionen zur Verfügung, welche für die Bildung eines Großteils der astronomisch relevanten Moleküle verantwortlich sind (Henning 1998; Draine 2003; Henning 2010). Interstellare und zirkumstellare Staubpartikel sind außerdem von erheblichem Interesse als Bausteine der Planeten sowie als Überreste protoplanetarer Scheiben. Sind die Eigenschaften der Staubpartikel bekannt, können

wir ihren Weg zur Bildung größerer astronomischer Körper folgen und die Geschichte der Planetensysteme zurückverfolgen.

Laboruntersuchungen und radioastronomische Durchmusterungen nach CO-H_2-van-der-Waals-Clustern wurden durchgeführt. Die Rotationsspektren der Cluster und ihrer Isotopologe wurden im Labor gemessen und ermöglichen die präzise Bestimmung der zugehörigen Energieniveaus von CO–paraH_2 (Potapov, et al. 2009a), CO-orthoH_2 (Jankowski, et al. 2013), CO-orthoD_2 (Potapov, et al. 2009b), and CO-HD (Potapov, et al. 2015). Es wurde gezeigt, dass hochauflösende Spektren die beste Grundlage sind, um intermolekulare Potenzialenergiehyperflächen (PES) zu testen, und damit einen genauen Test für die bereits verfügbare PES des CO-H_2-Clusters zur Verfügung zu stellen, womit die Entwicklung neuer, verlässlicherer PES angeregt wird.

Die hochauflösenden Daten ermöglichten die radioastronomische Suche nach dem CO-H_2-Cluster in einem kalten, dichten Kern in TMC-1C (mit einer Temperatur von ~10 K), unter Verwendung des Institute de Radioastronomie Millimétrique (IRAM) 30 m-Teleskops (Potapov, et al. 2016). Es konnten keine Linien detektiert werden, die zum CO-H_2-Cluster gehören. Wir konnten jedoch eine neue, obere Grenze für die Häufigkeit des Clusters ermitteln. Wir schlussfolgerten, dass es möglich sein müsste, den van-der-Waals-Komplex durch Beobachtungen mit um ein bis zwei Ordnungen besserer Empfindlichkeit, zu detektieren, die mit dem Atacama Large Millimeter/submillimeter Array (ALMA) möglich ist. Ein weiteres Resultat unserer astronomischen Durchmusterung war die Entdeckung von 75 Linien, die 41 verschiedenen Spezies zugeordnet werden konnten. Wir detektierten komplexe organische Moleküle, darunter Methylcyanid, Methanol, Propin und Ethenon, die mit kaltem Gas assoziiert sind, womit die Anwesenheit dieser Moleküle nicht nur in warmen Objekten, sondern auch in kalten Regionen bestätigt wird und neue Informationen bezüglich der zugrundeliegenden astrochemischen Netzwerken gewonnen werden.

Ein THz-Spektrometer, welches gepulste Überschallausdehnung, eine Strahlungsquelle und eine Multi-Pass-Optik kombiniert, wurde entwickelt. Referenzmessungen des Spektrometers wurden an dem bloßen Rotationsspektrum des Ne-CO-van-der-Waals-Clusters in einem Frequenzbereich von 208 bis 230 GHz durchgeführt (Potapov, et al. 2011). Ein verbesserter Parametersatz des Ne-CO-Komplexes wurde bestimmt, welcher einen Test der verfügbaren intermolekularen PES des Ne-CO-Systems ermöglichte.

Ein Infrarotspektrometer, welches gepulste Überschallausdehnung, eine Strahlungsquelle und eine Multi-Pass-Optik kombiniert, wurde entwickelt. Das Spektrometer wurde genutzt, um

das Rotationschwingungsspektrum in der ν_3-Region des SF_6-Dimers erneut zu vermessen (Asselin, et al. 2017). Zum ersten Mal wurden zwei Konformere des Dimers auf der Basis zweier S–S-Abstände, die aus der Rovibrationsanalyse der parallelen Bandenkonturen im Bereich des ν3-Übergangs gewonnen wurden, eindeutig identifiziert. Eine spezifische Dynamik der Bildung für die beiden Konformere wurde basierend auf der Entwicklung ihrer relativen Populationen in kalten/schnellen und langsamen/heißen Expansionen abgeleitet. Weiterhin wurde eine zusätzliche, intensive Rotationschwingungsbande im Spektrum dem $(SF_6)_2$-He-Trimer zugeordnet. Vor kurzem wurde das Infrarotspektrometer genutzt, um das Rotationschwingungsspektrum des NH_3-Ar-Clusters in der ν_2-Inversionsregion von NH_3 zu untersuchen (Asselin, et al. 2018).

In unserer Publikation (Potapov, et al. 2017b) wurde ein neuer Weg zur Bildung komplexer organischer Moleküle im ISM, Staubpartikeloberflächenprozesse, experimentell erforscht. Unsere Resultate zeigen, dass das Bombardement interstellarer kohlenstoffhaltiger Staubpartikelanaloga, welche nicht mit molekularen Eisen bedeckt sind, mit O- und H-Atomen bei niedrigen Temperaturen zur Bildung von CO-Molekülen und ihre darauffolgende Hydrierung zur Bildung von festem Formaldehyd führt. Die Bildung von H_2CO ist ein Indiz für die Bildung von Methanol in derartigen Systemen. Methanol wird allgemeinhin als Ausgangspunkt für die Bildung komplexerer organischer Moleküle angenommen (Öberg, et al. 2009; Vasyunin & Herbst 2013; Balucani, et al. 2015).

Die optischen Eigenschaften von Silikat/Wassereis-Gemischen im mittleren Infraroten bei niedrigen Temperaturen wurden bestimmt (Potapov, et al. 2018a). Zusätzlich wurden außerdem die optischen Konstanten reinen Wassereises und reiner Silikate im Labor bestimmt. Zwei verschiedene Datensätze von optischen Konstanten wurden verglichen, die “gemessenen” Konstanten, berechnet aus den Transmissionsspektren der Silikat/Wassereis-Proben, und “effektive” Konstanten, berechnet aus den optischen Konstanten reiner Silikaten und reinen Wassereises unter Verwendung verschiedener theoretischen Mischungsregeln (effektives Medium-Ansatz). Die Unterschiede zwischen den gemessenen und effektiven Konstanten zeigt, dass ein Mischen (Durchschnittsbildung) der optischen Konstanten von Wassereis und Silikaten für die Bestimmung der optischen Eigenschaften von Silikat/Wassereis-Mischungen zu fehlerhaften Ergebnissen führen kann. Es wurde auch gezeigt, dass Teile des Wassers in/auf Partikeln gefangen werden können und bis zu einer Temperatur von 200 K nicht desorbieren. Wassereis, welches in/auf Partikeln „gefangen“ ist, kann somit den Übergang von einer dichten Molekülwolke zu einer protoplanetaren Scheibe überleben und teilweise die großen Mengen H_2O-Eis in den Scheiben um junge Sterne erklären (Min, et al. 2016).

Erstmalig wurden Temperatur-programmierte Desorptionsexperimente (TPD) an Wassereis in Mischung mit amorphen Kohlenstoff- und Silikatpartikeln durchgeführt (Potapov, et al. 2018b). Wir haben gezeigt, dass Variationen im Partikel/Eis-Massenverhältnis zu einer Transformation der TPD-Kurve von H_2O-Eis führen, für welche eine perfekte Regression mit der Polanyi-Wigner-Gleichung durchgeführt werden kann, wenn nicht-ganzzahlige Desorptionsraten verwendet werden. Im Fall von Kohlenstoffpartikeln erhöht sich die Desorptionsordnung von 0.1 für reines Wassereis auf 1 für Partikel/Eis-Verhältnisse von 1.3. Für zwei Silikat/Eis-Mischungen wurde eine Desorptionsordnung von 1 für Wassereis gefunden. Diese Ergebnisse könnten mit einer Desorption von Wassermolekülen von einer großen Oberfläche fraktaler Cluster, bestehend aus Kohlenstoff- und Silikatpartikeln, erklärt werden und liefern einen Zusammenhang zwischen der Struktur und Morphologie von Staubpartikeln und der Kinetik der Desorption von Wassereis, gemischt mit diesen Partikeln.

Es wurden ein hochempfindliches THz-Spektrometer zur Untersuchung der optischen Eigenschaften interstellarer Staubanaloga im Temperaturbereich von 10 bis 300 K entwickelt (Potapov, et al. 2014). Referenzmessungen im Millimeterwellenbereich mit dem Spektrometer wurden an eisenfreien Silikatproben durchgeführt.

Diese Arbeiten weisen in neue Richtungen der Untersuchungen und technischen Entwicklungen:

- zur Untersuchung der Bildung komplexer organischer Moleküle auf interstellaren Staubpartikeln,
- zur Untersuchung der optischen und strukturellen Eigenschaften von Staub/Eis-Mischungen,
- zur Entwicklung neuer experimenteller Methoden – der Gasphasenspektroskopie von Molekülen, die auf Analoga interstellarer Partikel gebildet wurden.

References

Abelson, P. H. 1956, Science, 124, 935
Abeysekera, C., Joalland, B., Ariyasingha, N., Zack, L. N., Sims, I. R., Field, R. W., & Suits, A. G. 2015, Journal of Physical Chemistry Letters, 6, 1599
Abeysekera, C., et al. 2014, Journal of Chemical Physics, 141, 214203
Abplanalp, M. J., Forstel, M., & Kaiser, R. I. 2016, Chemical Physics Letters, 644, 79
Allamandola, L. J., Bernstein, M. P., Sandford, S. A., & Walker, R. L. 1999, Space Sci Rev, 90, 219
Allen, R. J., Loinard, L., McKellar, A. R. W., & Lequeux, J. 1997, Astrophysical Journal, 489, 102
Allodi, M. A., Ioppolo, S., Kelley, M. J., McGuire, B. A., & Blake, G. A. 2014, Phys Chem Chem Phys, 16, 3442
Altwegg, K., & al., e. 2016, Sci Adv, 2, e1600285
Andronikashvili, E. L. 1946, J Phys USSA, 10, 201
Asselin, P., Belkhodja, Y., Jabri, A., Potapov, A., Loreau, J., & van der Avoird, A. 2018, Molecular Physics, https://doi.org/10.1080/00268976.2018.1471533
Asselin, P., Potapov, A., Turner, A. C., Boudon, V., Bruel, L., Gaveau, M. A., & Mons, M. 2017, Physical Chemistry Chemical Physics, 19, 17224
Auriacombe, O., Fraser, H., Ellison, B., & Rea, S. 2014, Proceedings of the International Symposium on Space Terahertz Technology, Moscow, Russia, 131
Bacmann, A., Taquet, V., Faure, A., Kahane, C., & Ceccarelli, C. 2012, Astron Astrophys, 541
Balucani, N., Ceccarelli, C., & Taquet, V. 2015, Monthly Notices of the Royal Astronomical Society, 449, L16
Bates, D. R., & Herbst, E. 1988, Rate coefficients in astrochemistry, Eds Millar TJ, Williams DA, Kluwer Academic Publishers, 17
Beltran, M. T., Codella, C., Viti, S., Neri, R., & Cesaroni, R. 2009, Astrophysical Journal Letters, 690, L93
Bergin, E. A., & van Dishoeck, E. F. 2012, Philosophical Transactions of the Royal Society a-Mathematical Physical and Engineering Sciences, 370, 2778
Bernal, J. D. 1951, London: Routledge and Kegan Paul
Bernstein, M. P., Dworkin, J. P., Sandford, S. A., Cooper, G. W., & Allamandola, L. J. 2002, Nature, 416, 401
Bizzocchi, L., Caselli, P., Spezzano, S., & Leonardo, E. 2014, Astronomy & Astrophysics, 569
Blum, J. 2018, Space Sci Rev, 214
Boogert, A. C. A., Gerakines, P. A., & Whittet, D. C. B. 2015, Annual Review of Astronomy and Astrophysics, 53, 541
Brack, A. 1999, Life Sciences: New Insights into Complex Organics in Space, 24, 417
Brown, G. G., Dian, B. C., Douglass, K. O., Geyer, S. M., Shipman, S. T., & Pate, B. H. 2008, Review of Scientific Instruments, 79
Brownlee, D., et al. 2006, Science, 314, 1711
Burke, D. J., & Brown, W. A. 2010, Physical Chemistry Chemical Physics, 12, 5947
Cronin, J. R., & Chang, S. 1993, in Chemistry of Life's Origins (NATO ASI) (eds Greenberg, J M, Pirronello, V & Mendoza-Gomez, C), 209
Curtis, D. B., Rajaram, B., Toon, O. B., & Tolbert, M. A. 2005, Appl Optics, 44, 4102
Daniel, J. S., Solomon, S., Sanders, R. W., Portmann, R. W., Miller, D. C., & Madsen, W. 1999, Journal of Geophysical Research-Atmospheres, 104, 16785
Dartois, E., Demyk, K., d'Hendecourt, L., & Ehrenfreund, P. 1999, Astron Astrophys, 351, 1066
Dian, B. C., Brown, G. G., Douglass, K. O., & Pate, B. H. 2008, Science, 320, 924
Dorschner, J., Begemann, B., Henning, T., Jager, C., & Mutschke, H. 1995, Astron Astrophys, 300, 503
Dorschner, J., & Henning, T. 1995, Astronomy and Astrophysics Review, 6, 271
Dose, K., & Rajewsky, B. 1957, Biochimica Et Biophysica Acta, 25, 225
Draine, B. T. 2003, Annual Review of Astronomy and Astrophysics, 41, 241
Draine, B. T. 2011, Princeton University Press, UK
Dumesh, B. S., Potapov, A. V., & Surin, L. A. 2009, Physics-Uspekhi, 52, 294
Ehrenfreund, P., & Charnley, S. B. 2000, Annual Review of Astronomy and Astrophysics, 38, 427

Ehrenfreund, P., Dartois, E., Demyk, K., & d'Hendecourt, L. 1998, Astron Astrophys, 339, L17
Ehrenfreund, P., et al. 1999, Astron Astrophys, 350, 240
Ellsworth, K., & Schubert, G. 1983, Icarus, 54, 490
Elsila, J. E., Glavin, D. P., & Dworkin, J. P. 2009, Meteoritics & Planetary Science, 44, 1323
Fellers, R. S., Leforestier, C., Braly, L. B., Brown, M. G., & Saykally, R. J. 1999, Science, 284, 945
Fraser, H. J., Collings, M. P., & McCoustra, M. R. S. 2002, Rev Sci Instr, 73, 2161
Fulle, M., et al. 2017, MNRAS, 469, S45
Fulvio, D., Raut, U., & Baragiola, R. A. 2012, Astrophysical Journal Letters, 752, L33
Georgievskii, Y., & Klippenstein, S. J. 2007, Journal of Physical Chemistry A, 111, 3802
Gerecht, E., Douglass, K. O., & Plusquellic, D. F. 2011, Optics Express, 19, 8973
Ginzburg, V. L., & Sobyanin, A. A. 1972, Jetp Letters-Ussr, 15, 242
Gómez Martín, J. C., Caravan, R. L., Blitz, M. A., Heard, D. E., & Plane, J. M. C. 2014, Journal of Physical Chemistry A, 118, 2693
Grebenev, S., Toennies, J. P., & Vilesov, A. F. 1998, Science, 279, 2083
Hagen, W., Tielens, A. G. G. M., & Greenberg, J. M. 1981, Chemical Physics, 56, 367
Halfen, D. T., Apponi, A. J., Woolf, N., Polt, R., & Ziurys, L. M. 2006, Astrophysical Journal, 639, 237
Havenith, M. 2002, Infrared Spectroscopy of Molecular Clusters (Springer, Berlin)
Henning, T. 1998, Chemical Society Reviews, 27, 315
---. 2010, Annu Rev Astron Astr, 48, 21
Henning, T., & Mutschke, H. 1997, Astron Astrophys, 327, 743
Henning, T., & Salama, F. 1998, Science, 282, 2204
Henning, T., & Semenov, D. 2013, Chem Rev, 113, 9016
Henning, T., & Stognienko, R. 1996, Astron Astrophys, 311, 291
Herbst, E. 1985, Astrophysical Journal, 291, 226
---. 2014, Physical Chemistry Chemical Physics, 16, 3344
Herbst, E., Defrees, D. J., Talbi, D., Pauzat, F., Koch, W., & Mclean, A. D. 1991, Journal of Chemical Physics, 94, 7842
Herman, M., Foldes, T., Didriche, K., Lauzin, C., & Vanfleteren, T. 2016, International Reviews in Physical Chemistry, 35, 243
https://wesfiles.wesleyan.edu/home/snovick/SN_webpage/vdw.pdf.
https://www.eso.org/public/.
Jäger, C. 2015, in Laboratory Astrochemistry, Wiley-VCH, eds Schlemmer S, Giesen T, Mutschke H, Jäger C 447
Jäger, C., Dorschner, J., Mutschke, H., Posch, T., & Henning, T. 2003, Astron Astrophys, 408, 193
Jäger, C., & Mutschke, H. 2015, in Laboratory Astrochemistry, Wiley-VCH, eds Schlemmer S, Giesen T, Mutschke H, Jäger C 467
Jäger, C., Mutschke, H., & Henning, T. 1998, Astron Astrophys, 332, 291
Jäger, C., Mutschke, H., Henning, T., & Huisken, F. 2008, Astrophys J, 689, 249
Jahn, M. K., Dewald, D. A., Wachsmuth, D., Grabow, J. U., & Mehrotra, S. C. 2012, Journal of Molecular Spectroscopy, 280, 54
Jankowski, P., Surin, L. A., Potapov, A., Schlemmer, S., McKellar, A. R. W., & Szalewicz, K. 2013, Journal of Chemical Physics, 138
Jorgensen, J. K., Favre, C., Bisschop, S. E., Bourke, T. L., van Dishoeck, E. F., & Schmalzl, M. 2012, Astrophysical Journal Letters, 757
Kaifu, N., Morimoto, M., Nagane, K., Akabane, K., Iguchi, T., & Takagi, K. 1974, Astrophysical Journal, L135
Kitta, K., & Krätschmer, W. 1983, Astron Astrophys, 122, 105
Klemperer, W., & Vaida, V. 2006, P Natl Acad Sci USA, 103, 10584
Krasnopolsky, V. A., Tkachuk, A. Y., Moreels, G., & Gogoshev, M. 1988, Astron Astrophys, 203, 175
Krause, M., & Blum, J. 2004, Phys Rev Lett, 93
Krivov, A. V. 2010, Research in Astronomy and Astrophysics, 10, 383
Lattelais, M., Pauzat, F., Pilme, J., Ellinger, Y., & Ceccarelli, C. 2011, Astronomy & Astrophysics, 532

Linnartz, H., Ioppolo, S., & Fedoseev, G. 2015, International Reviews in Physical Chemistry, 34, 205
Maron, N., & Maron, O. 2008, Mon Not R Astron Soc, 391, 738
Martins, Z., & Sephton, M. A. 2009, in „Amino Acids, Peptides and Proteins in Organic Chemistry Ed by A B Hughes, WILEY-VCH Verlag GmbH & Co KGaA, Weinheim, 1
Mastrapa, R. M., Bernstein, M. P., Sandford, S. A., Roush, T. L., Cruikshank, D. P., & Ore, C. M. D. 2008, Icarus, 197, 307
Mastrapa, R. M., Sandford, S. A., Roush, T. L., Cruikshank, D. P., & Ore, C. M. D. 2009, Astrophysical Journal, 701, 1347
McClure, M. K., et al. 2015, Astrophys J, 799
McClure, M. K., et al. 2012, Astrophys J Lett, 759
Mckellar, A. R. W. 1988, Astrophysical Journal, 326, L75
Medcraft, C., Wolf, R., & Schnell, M. 2014, Angewandte Chemie-International Edition, 53, 11656
Mennella, V., Baratta, G. A., Palumbo, M. E., & Bergin, E. A. 2006, Astrophysical Journal, 643, 923
Mennella, V., Palumbo, M. E., & Baratta, G. A. 2004, Astrophysical Journal, 615, 1073
Mesko, A., Weaver, S. L. W., Milam, S. N., & Wagner, I. C. 2014, Proceedings of the International Symposium on Molecular Spectroscopy, Champaign-Urbana, Illinois, USA, , TA04
Mesko, A. J., Wagner, I. C., Smith, H. H., Milam, S. N., & Weaver, S. L. W. 2015, Proceedings of the International Symposium on Molecular Spectroscopy, Champaign-Urbana, Illinois, USA, RI13
Miller, S. L. 1953, Science, 117, 528
Miller, S. L., & Urey, H. C. 1959, Science, 130, 245
Min, M., et al. 2016, Astron Astrophys, 593
Min, M., Dullemond, C. P., Kama, M., & Dominik, C. 2011, Icarus, 212, 416
Moroni, S., Botti, M., De Palo, S., & McKellar, A. R. W. 2005, Journal of Chemical Physics, 122
Motiyenko, R. A., Tercero, B., Cernicharo, J., & Margules, L. 2012, Astronomy & Astrophysics, 548
Mrad, N. A., Duvernay, F., Theule, P., Chiavassa, T., & Danger, G. 2014, Analytical chemistry, 86, 8391
Mukai, T., & Mukai, S. 1984, Adv Space Res, 4, 207
Muñoz Caro, G. M., et al. 2002, Nature, 416, 403
Murphy, D. M., Thomson, D. S., & Mahoney, T. M. J. 1998, Science, 282, 1664
Nuevo, M., et al. 2006, Astron Astrophys, 457, 741
Öberg, K. I. 2016, Chem Rev, 116, 9631
Öberg, K. I., Garrod, R. T., van Dishoeck, E. F., & Linnartz, H. 2009, Astron Astrophys, 504, 891
Oparin, A. I. 1938, New York: Macmillan
Oro, J. 1961, Nature, 190, 389
---. 1963, Nature, 197, 862
Park, G. B., Steeves, A. H., Kuyanov-Prozument, K., Neill, J. L., & Field, R. W. 2011, Journal of Chemical Physics, 135
Parker, E. T., et al. 2011, Proceedings of the National Academy of Sciences of the United States of America, 108, 5526
Pearce, B. K. D., Pudritz, R. E., Semenov, D. A., & Henning, T. K. 2017, P Natl Acad Sci USA, 114, 11327
Perez, C., et al. 2013, Chemical Physics Letters, 571, 1
Pfeilsticker, K., Erle, F., & Platt, U. 1997, Journal of the Atmospheric Sciences, 54, 933
Pfeilsticker, K., Lotter, A., Peters, C., & Bosch, H. 2003, Science, 300, 2078
Pirim, C., & Krim, L. 2014, Rsc Advances, 4, 15419
Potapov, A. 2017a, Molecular Astrophysics, 6, 16
---. 2017c, Workshops "Planet Formation and Evolution 2017", Jena, Germany
Potapov, A., & Asselin, P. 2014, International Reviews in Physical Chemistry, 33, 275
Potapov, A., Jäger, C., & Henning, T. 2018b, Astrophysical Journal, submitted, http://arxivorg/abs/180607673
Potapov, A., Jager, C., Henning, T., Jonusas, M., & Krim, L. 2017b, Astrophysical Journal, 846, 131
Potapov, A., Lewen, F., Mutschke, H., Mohr, P., & Schlemmer, S. 2014, Rev Sci Instrum, 85, 073102
Potapov, A., Mutschke, H., Seeber, P., Henning, T., & Jäger, C. 2018a, Astrophysical Journal, in press, http://arxivorg/abs/180305810

Potapov, A., Sanchez-Monge, A., Schilke, P., Graf, U. U., Moller, T., & Schlemmer, S. 2016, Astron Astrophys, 594, A117
Potapov, A., Surin, L., & Schlemmer, S. 2015, Journal of Molecular Spectroscopy, 307, 18
Potapov, A. V., Panfilov, V. A., Dolgov, A. A., Surin, L. A., & Dumesh, B. S. 2009b, Optics and Spectroscopy, 106, 655
Potapov, A. V., Panfilov, V. A., Surin, L. A., & Dumesh, B. S. 2010, Journal of Experimental and Theoretical Physics, 111, 770
Potapov, A. V., et al. 2009a, Astrophysical Journal, 703, 2108
Potapov, A. V., Surin, L. A., Schlemmer, S., & Giesen, T. F. 2011, Journal of Molecular Spectroscopy, 270, 116
Prozument, K., et al. 2014, Physical Chemistry Chemical Physics, 16, 15739
Raston, P. L., Jager, W., Li, H., Le Roy, R. J., & Roy, P. N. 2012, Physical Review Letters, 108
Raut, U., Fulvio, D., Loeffler, M. J., & Baragiola, R. A. 2012, Astrophysical Journal, 752, 159
Reinert, C., Mutschke, H., Krivov, A. V., Lohne, T., & Mohr, P. 2015, Astron Astrophys, 573, A29
Ruaud, M., Loison, J. C., Hickson, K. M., Gratier, P., Hersant, F., & Wakelam, V. 2015, Monthly Notices of the Royal Astronomical Society, 447, 4004
Sabri, T., Baratta, G. A., Jäger, C., Palumbo, M. E., Henning, T., Strazzulla, G., & Wendler, E. 2015, Astron Astrophys, 575, A76
Sabri, T., Gavilan, L., Jager, C., Lemaire, J. L., Vidali, G., Mutschke, H., & Henning, T. 2014, Astrophys J, 780, 180
Sanchez, R., Ferris, J., & Orgel, L. E. 1966a, Science, 153, 72
Sanchez, R. A., Ferris, J. P., & Orgel, L. E. 1966b, Science, 154, 784
Schenewerk, M. S., Jewell, P. R., Snyder, L. E., Buxton, L. W., Campbell, E. J., & Flygare, W. H. 1985, Astrophysical Journal, 296, 218
Scherer, M., Havenith, M., Mauersberger, R., & Wilson, T. L. 1998, Astron Astrophys, 335, 1070
Scherer, S., et al. 2016, Orig Life Evol Biosph, doi:10.1007/s11084
Schriver-Mazzuoli, L. 1998, in Molecular Complexes in Earth's Planetary, Cometary and Interstellar Atmospheres, edited by A Vigasin and Z Slanina (World scientific, Singapore)
Shannon, R. J., Blitz, M. A., Goddard, A., & Heard, D. E. 2013, Nature Chemistry, 5, 745
Shi, J., Grieves, G. A., & Orlando, T. M. 2015, Astrophysical Journal, 804, 24
Sleiman, C., González, S., Klippenstein, S. J., Talbi, D., El Dib, G., & Canosa, A. 2016, Physical Chemistry Chemical Physics, 18, 15118
Smith, R. G., Robinson, G., Hyland, A. R., & Carpenter, G. L. 1994, Mon Not R Astron Soc, 271, 481
Solomon, S., Portmann, R. W., Sanders, R. W., & Daniel, J. S. 1998, Journal of Geophysical Research-Atmospheres, 103, 3847
Steber, A. L., Harris, B. J., Neill, J. L., & Pate, B. H. 2012, Journal of Molecular Spectroscopy, 280, 3
Storey, J. W. V., & Cheung, A. C. 1978, Astrophysical Letters & Communications, 19, 89
Surin, L. A., et al. 2007, Journal of Physical Chemistry A, 111, 12238
Surin, L. A., Potapov, A. V., Dumesh, B. S., Schlemmer, S., Xu, Y., Raston, P. L., & Jager, W. 2008, Physical Review Letters, 101
Surin, L. A., Roth, D. A., Pak, I., Dumesh, B. S., Lewen, F., & Winnewisser, G. 2000, Journal of Chemical Physics, 112, 4064
Tafalla, M., Santiago-Garcia, J., Myers, P. C., Caselli, P., Walmsley, C. M., & Crapsi, A. 2006, Astronomy & Astrophysics, 455, 577
Tanaka, K., Harada, K., & Yamada, K. M. T. 2011, In: Quack, M, Merkt, F (Eds), Hand- book of High-Resolution Spectroscopy John Wiley & Sons, Ltd
Theule, P., et al. 2013, Advances in Space Research, 52, 1567
Thommes, E. W., & Duncan, M. J. 2006, in Planet Formation, The accretion of giant-planet cores, eds H Klahr, & W Brandner (Cambridge University Press), 129
Tielens, A. G. G. M. 2005, The physics and chemistry of the interstellar medium Cambridge University Press
Tielens, A. G. G. M. 2013, Reviews of Modern Physics, 85, 1021

Toennies, J. P., & Vilesov, A. F. 2004, Angewandte Chemie-International Edition, 43, 2622
Trafton, L. M., & Watson, J. K. G. 1992, Astrophysical Journal, 385, 320
Tretyakov, M. Y., Serov, E. A., Koshelev, M. A., Parshin, V. V., & Krupnov, A. F. 2013, Physical Review Letters, 110
Urey, H. C. 1952, P Natl Acad Sci USA, 38, 351
Vaida, V. 2011, Journal of Chemical Physics, 135
Vaida, V., & Headrick, J. E. 2000, Journal of Physical Chemistry A, 104, 5401
Vaida, V., Kjaergaard, H. G., & Feierabend, K. J. 2003, International Reviews in Physical Chemistry, 22, 203
van der Avoird, A., & Nesbitt, D. J. 2011, Journal of Chemical Physics, 134
van Dishoeck, E. F. 2014, Faraday Discussions, 168, 9
van Dishoeck, E. F., Bergin, E. A., Lis, D. C., & Lunine, J. I. 2014, arXiv:14018103 [astro-phGA]
Vanden Bout, P. A., Steed, J. M., Lawrence, J. M. S., Bernstein, S., & Klemperer, W. 1979, ApJ, 234, 504
Vastel, C., Ceccarelli, C., Lefloch, B., & Bachiller, R. 2014, Astrophysical Journal Letters, 795
Vasyunin, A. I., & Herbst, E. 2013, Astrophysical Journal, 769
Wollrab, E., Scherer, S., Aubriet, F., Carre, V., Carlomagno, T., Codutti, L., & Ott, A. 2016, Origins of Life and Evolution of Biospheres, 46, 149
Wormer, P. E. S., & van der Avoird, A. 2000, Chem Rev, 100, 4109
Wurm, G., & Blum, J. 1998, Icarus, 132, 125
Xu, Y. J., Van Wijngaarden, J., & Jäger, W. 2005, International Reviews in Physical Chemistry, 24, 301
Zhang, R. Y., Khalizov, A., Wang, L., Hu, M., & Xu, W. 2012, Chem Rev, 112, 1957
Zhukovska, S., Henning, T., & Dobbs, C. 2018, Astrophysical Journal, 857

Acknowledgments

First of all, I would like to thank all my co-authors as well as my collaborators, which contributed to this work. Special thanks to my supervisors of the past 6 years: Prof. Dr. Stephan Schlemmer, Dr. Cornelia Jäger, and Prof. Dr. Thomas Henning. Special thanks also to Pierre Asselin, André Canosa, Thomas Giesen, Elena Jiménez, Christoph Konietzko, Lahouari Krim, Frank Lewen, Álvaro Sánchez-Monge, Harald Mutschke, Victor Panfilov, Bertrand Rowe, Leonid Surin, and Patrice Theulé. It was a great pleasure for me to work with them. I am grateful to Prof. Dr. Boris Dumesh, who supervised my research after my PhD. I like to acknowledge the reviewers of the Habilitation for their work.

I appreciate also the contributions of the technicians of the workshops and the work of the secretaries. I thank all these persons at the I. Physical Institute of the University of Cologne and at the Institute of Solid State Physics of the Friedrich-Schiller University Jena, who made my work much easier.

Finally, I would like to thank my wife, Natasha, for her love and permanent support. I dedicate this Habilitation to my children, Tanja and Andrey, who always are a source of light, which shows me the way in dark moments.

6. Integrated papers

6.1.1. **Rotational spectroscopy of the CO–paraH_2 molecular complex**
Potapov A.V., Surin L.A., Panfilov V.A., Dumesh B.S., Giesen T.F., Schlemmer S., Raston P.L., and Jäger W.
The Astrophysical Journal, 2009, v.703, p.2108

6.1.2. **A comprehensive experimental and theoretical study of H_2-CO Spectra**
Jankowski P., Surin L.A., Potapov A., Schlemmer S., McKellar A.R.W., Szalewicz K.
Journal of Chemical Physics, 2013, v.138, p.084307

6.1.3. **First observation of the rotational spectrum of the HD–CO weakly bound complex**
Potapov A., Surin L., Schlemmer S.
Journal of Molecular Spectroscopy, 2015, v.307, p.18

6.1.4. **The CO-H_2 van der Waals complex and complex organic molecules in cold molecular clouds: a TMC-1C survey**
Potapov A., Sanchez-Monge A., Schilke P., Graf U.U., Möller Th., Schlemmer S.
Astronomy & Astrophysics, 2016, v.594, A117

6.1.5. **Submillimetre-wave spectroscopy of the K = 2 – 1 subband of the Ne–CO complex**
Potapov A.V., Surin L.A., Schlemmer S., and Giesen T.F.
Journal of Molecular Spectroscopy, 2011, v.270, p.116

6.1.6. **Conformational landscape of the SF_6 dimer as revealed by high-resolution infrared spectroscopy and complexation with rare gas atoms**
Asselin P., Potapov A., Turner A., Boudon V., Bruel L., Gaveau M. A., and Mons M.
Physical Chemistry Chemical Physics, 2017, v.19, p.17224

6.2.1 **The formation of formaldehyde on interstellar carbonaceous grain analogs by O and H atom addition**
Potapov A., Jäger C., Henning T., Jonusas M., Krim L.
The Astrophysical Journal, 2017, v.846, p.131

6.2.2 **Low temperature optical properties of interstellar and circumstellar icy silicate grain analogues in the mid-infrared spectral region**
Potapov A., Mutschke H., Seeber P., Henning T., Jäger C.
The Astrophysical Journal, 2018, 2018, v.861, p.84

6.2.3 **Temperature programed desorption of water ice mixed with amorphous carbon and silicate grains as related to planet-forming disks**
Potapov A., Jäger C., Henning T.
The Astrophysical Journal, v.865, p.58

6.2.4 **Total power millimetre-wave spectrometer for measurements of dust opacity at cryogenic temperatures**
Potapov A., Lewen F., Mutschke H., Mohr P., Schlemmer S.
Review of Scientific Instruments, 2014, v.85, p.073102

The Astrophysical Journal, 703:2108–2112, 2009 October 1 doi:10.1088/0004-637X/703/2/2108

ROTATIONAL SPECTROSCOPY OF THE CO–PARA-H_2 MOLECULAR COMPLEX

A. V. Potapov[1,2], L. A. Surin[1,2], V. A. Panfilov[2], B. S. Dumesh[2], T. F. Giesen[1], S. Schlemmer[1], P. L. Raston[3], and W. Jäger[3]

[1] I. Physikalisches Institut, University of Cologne, Zülpicher Str. 77, 50937 Cologne, Germany; potapov@ph1.uni-koeln.de
[2] Institute of Spectroscopy, Russian Academy of Sciences, 142190 Troitsk, Moscow Region, Russia
[3] Department of Chemistry, University of Alberta, Edmonton, Alberta T6G 2G2, Canada
Received 2009 June 24; accepted 2009 August 20; published 2009 September 16

ABSTRACT

The rotational spectrum of the CO–para-H_2 van der Waals complex, produced using a molecular jet expansion, was observed with two different techniques: OROTRON intracavity millimeter-wave spectroscopy and pulsed Fourier transform microwave spectroscopy. Thirteen transitions in the frequency range from 80 to 130 GHz and two transitions in the 14 GHz region were measured and assigned, allowing for a precise determination of the corresponding energy level positions of CO–para-H_2. The data obtained enable further radio astronomical searches for this molecular complex and provide a sensitive test of the currently best available intermolecular potential energy surface for the CO–H_2 system.

Key words: ISM: molecules – molecular data – techniques: spectroscopic

1. INTRODUCTION

Considerable interest in spectroscopic studies of the CO–H_2 van der Waals (vdW) complex has been stimulated by its astrophysical significance As dihydrogen, H_2, is by far the most abundant molecule in the universe, followed by carbon monoxide, CO, the intermolecular forces between these two species are of fundamental interest. High-resolution spectroscopic measurements of the CO–H_2 complex can provide valuable information about both transition frequencies for a reliable search by means of radiotelescopes (Allen et al. 1997) and the intermolecular potential of the complex, which is a prerequisite for understanding collision processes in interstellar molecular clouds (Green & Thaddeus 1976).

There have been several attempts to detect complexes containing CO and H_2 molecules in the interstellar medium (ISM). The detection of the H_2 dimer, $(H_2)_2$, in the atmosphere of Jupiter has been reported by McKellar (1988), while searches for the CO dimer, $(CO)_2$ (Vanden Bout et al. 1979), and for the CO–para-H_2 complex (Allen et al. 1997) in galactic molecular clouds were not successful thus far. There is still an open debate about the feasibility of observing such weakly bound species because their formation rates at the very low densities in interstellar molecular clouds (below 10^7 cm^{-3}) are low because of the small probability of three-body collisions. On the other hand, the large timescale on which these processes occur in interstellar space makes radiative association, which is usually a slow process, quite feasible. The relation between radiative association and three-body association rates has been discussed repeatedly (see, e.g., Klemperer & Vaida 2006).

Laboratory data on precisely measured transition frequencies of vdW complexes of astrophysical interest, especially in the microwave (MW) and millimeter-wave (MMW) ranges are prerequisite for further searches and their possible detection in the ISM. The lack of precise data might result in some confusion. For example, the recent extensive MMW studies of the CO dimer (Surin et al. 2007) have shown that the only reported radio astronomical search of this complex in the past (Vanden Bout et al. 1979) was based on frequencies which cannot be unambiguously attributed to the CO dimer, $(CO)_2$. In the particular case of the CO–para-H_2 complex, the interstellar search (Allen et al. 1997) was outside the correct line position of the most promising $R(0)$ line, as later identifie by the f rst MMW study of CO–para-H_2 (Pak et al. 1999).

In the present paper we report the spectroscopic study of pure rotational transitions of CO–para-H_2, significantl increasing the number of lines with precisely known frequencies (50 kHz and better). These measurements allowed us to determine the positions of many energy levels of CO–para-H_2 in the ground vibrational state with "MW accuracy." This is especially important because the energy level positions cannot be obtained directly from the previous infrared (IR) spectra of CO–para-H_2 (McKellar 1991, 1998), since the rotation–vibration transitions combine the levels in the ground and excited vibrational states of opposite parity. Further, the level energies determined in this work are compared with those from the most recent potential energy surfaces of Jankowski & Szalewicz (1998, 2005). These surfaces have been used for calculations of state-to-state cross sections and rate coefficient for CO–H_2 collisions (Mengel et al. 2000; Yang et al. 2006), which are crucial input parameters for numerical astrophysical models. Our results provide a large amount of very precise data, which can be used to check the quality of the existing intermolecular potential energy surfaces or to construct empirical ones.

2. EXPERIMENTAL DETAILS

Two instruments, an OROTRON intracavity MMW spectrometer and a pulsed Fourier transform microwave (FTMW) spectrometer, were used for observation of the rotational spectrum of CO–para-H_2, produced in a molecular jet expansion. Both FTMW and OROTRON spectrometers use a resonant cavity as a sample cell, thereby providing extremely high sensitivity which is crucial for the detection of such very weakly bound species. The principle of FTMW spectroscopy is based on the excitation of a molecular ensemble with a pulse of coherent radiation and the subsequent detection of the molecular emission signal (Schmalz & Flygare 1978). The OROTRON spectrometer measures direct absorption and is based on an intracavity operation principle (Dumesh & Surin 1996).

2.1. OROTRON Experiment

The spectra of CO–para-H_2 in the frequency range from 80 to 130 GHz were measured using the OROTRON spectrometer. Details of the spectrometer have been described elsewhere (Surin et al. 2001). In brief, the MMW generator OROTRON and a supersonic jet apparatus are installed into a vacuum chamber. The molecular beam is produced by a pulsed solenoid valve with an opening diameter of 1.0 mm and a pulse duration of 500 μs, operating at a repetition rate of 5–10 Hz. The molecular beam is injected into the OROTRON cavity perpendicularly to the cavity axis. The high Q-factor of the cavity results in ≈100 effective passes of the radiation through the jet. The absorption of radiation in the cavity causes a change of collector current, which is used for sensitive detection.

To increase the sensitivity, the frequency of the OROTRON was modulated at 25 kHz. The collector signal was demodulated by a digital lock-in amplifie operated in second derivative mode with a time constant of 160 μs. The output of the lock-in amplifie was then processed by a boxcar integrator with a time constant of 1 s. For frequency determination, a small part of the radiation was coupled out of the cavity and compared to some higher harmonics of a MW synthesizer. The measured width of the lines is caused by the Doppler broadening in the supersonic jet and by the frequency modulation of the OROTRON. For most of the measurements, the full linewidth at half-height is about 500 kHz and the accuracy of the line center positions is about 50 kHz.

At room temperature, 25% of hydrogen molecules are in the para form and 75% in the ortho form. In order to assign transitions to either the CO–para-H_2 or CO–ortho-H_2 spin modification and to increase the strength of the CO–para-H_2 lines, a catalytic ortho-to-para hydrogen converter was used to enhance the para-H_2 fraction in the sample. The converter consists of a steel tube fitte with hermetically sealed in- and out-let ports to enable a constant hydrogen fl w, and is fille with a paramagnetic salt as a catalyst. The device is inserted in a transport dewar with liquid helium and cooled to about 30 K. The temperature can be regulated by adjusting how far the converter is located from the surface of liquid helium and by additional heating. We estimate that para-H_2 gas with a purity level of greater than 95% reaches the exit of the converter at a constant fl w rate of 10^{-4} mol s^{-1}. Figure 1 shows a comparison of the (J, j_{CO}, l) = (1 1 1) ← (1 0 1) transition of CO–para-H_2 measured using enriched and normal hydrogen gas.

A gas mixture consisting of 2%–5% CO in normal H_2 or enriched para-H_2 at backing pressures of about 4–5 bar was used for the production of the CO–H_2 complexes. In addition to CO–H_2 lines, transitions of the CO dimer were also observed in the spectrum but they could be easily distinguished from CO–H_2 lines based on our previous MMW survey (Surin et al. 2007).

2.2. FTMW Experiment

The lines of CO–para-H_2 at 14 GHz were measured with an FTMW spectrometer, the details of which are available elsewhere (Schmalz & Flygare 1978; Xu & Jäger 1997). The sample gas is pulsed through a pinhole nozzle and injected into an evacuated Fabry–Perot resonator. It is polarized with a $\pi/2$ MW pulse, and the subsequent coherent emission signal is recorded and then Fourier transformed to give the frequency domain spectrum. The CO–para-H_2 spectra were averaged over 100,000 cycles at a repetition rate of 1 Hz. A Doppler pair is observed for each transition since the molecular beam travels parallel to the resonator axis. The full width at half-height for each line is 15 kHz, and the uncertainty in the line positions is estimated to be ∼1 kHz. The sample consisted of about 1% CO and 10% enriched para-H_2 in 3–6 bar of helium. The enriched para-H_2 was prepared by liquefying normal H_2 at <20 K in the presence of a paramagnetic salt for about 1 hr.

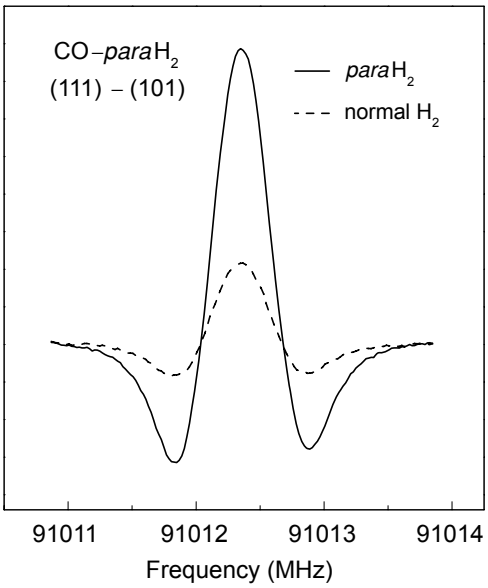

Figure 1. Example of the recorded (J, j, l) = (1 1 1) ← (1 0 1) line of CO–para-H_2 with and without ortho-to-para hydrogen conversion.

3. THE ENERGY LEVEL SCHEME FOR CO–PARA-H_2

As was shown in previous studies (McKellar 1991, 1998), it is useful to consider the CO–H_2 complex in terms of almost free internal rotation of its subunits. The level energies for the complex in the free rotation limit will be the sum of the individual CO and H_2 monomer rotational energies and the *end-over-end* rotational energy of the complex. The energy levels are labeled by quantum numbers j_{CO}, j_{H2}, l, and J, where j_{CO} and j_{H2} refer to the rotation of the CO and H_2 subunits, respectively, l refers to the *end-over-end* rotation of the complex, and J corresponds to the total angular momentum, $\boldsymbol{J} = \boldsymbol{j}_{CO} + \boldsymbol{j}_{H2} + \boldsymbol{l}$.

The existence of two equivalent H atoms and nearly free rotation of H_2 within the CO–H_2 complex results in two distinct groups of energy levels corresponding to two different spin modifications CO–para-H_2, with total nuclear spin of H_2, I = 0, and CO–ortho-H_2, with I = 1. For symmetry reasons, the states with j_{H2} = 0, 2, 4 ... are associated with para-H_2 and states with j_{H2} = 1, 3, 5, ... correspond to ortho-H_2. Transitions between these two modification are forbidden in general, and the allowed transitions obey selection rules $\Delta j_{CO} = 0, \pm 1$, and $\Delta j_{H2} = 0$. In the molecular beam environment, only the lowest states, i.e., j_{H2} = 0 for para-H_2 and j_{H2} = 1 for ortho-H_2 are significantl populated.

Each (j_{CO}, j_{H2}) state forms the foundation for a number of stacks of *end-over-end* rotational levels. Since free H_2 with j_{H2} = 0 is spherical, the spectrum of CO–para-H_2 somewhat resembles those of the CO–rare gas complexes, in particular the He–CO complex, which has been studied in detail in the infrared, MW, and MMW regions (McKellar et al. 1999; Surin et al. 2000b). By analogy, the energy levels of CO–para-H_2 can be labeled by quantum numbers J, j (= j_{CO}), and l as shown in the energy level diagram in Figure 2.

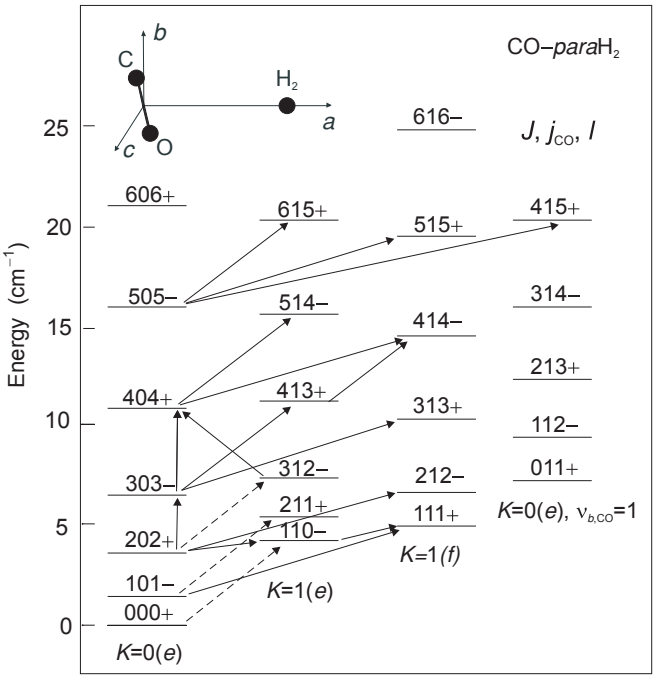

Figure 2. Energy level diagram for CO–para-H_2. The energy levels are labeled by quantum numbers J, j_{CO}, and l where j_{CO} refers to the rotation of the CO subunit, l refers to the *end-over-end* rotation of complex, and J to the total angular momentum. Alternative labeling by values of K, which corresponds to the projection of total angular momentum J onto the intermolecular axis, is also given. Newly measured transitions are indicated by solid arrows; previously measured transitions (Pak et al. 1999) are indicated by dashed arrows. The inset shows the approximate geometrical structure of the CO–H_2 complex.

The different stacks of levels in Figure 2 can also be labeled by values of K, which corresponds to the projection of total angular momentum J onto the intermolecular axis, a more conventional label appropriate for a semirigid molecule. The lowest stack with $K = 0$ represents the ground state of CO–para-H_2, a pair of stacks with $K = 1$ corresponds to the rotation of the CO unit about the intermolecular axis which approximately coincides with the inertial a-axis, and one stack with $K = 0$ has the nature of a CO bending vibration. The labels e and f indicate the parity of the J levels within a given stack. The parity of an even-J level is "+" for stacks labeled by e and "−" for f, while the parity of an odd-J level is "−" for e and "+" for stacks labeled by f.

The strongest pure rotational transitions are those with a b-type character ($\Delta K = \pm 1$), rather than a-type ($\Delta K = 0$). This is a result of the T-shape of the dimer, in which the CO dipole moment lies approximately parallel to the b-axis (see the inset in Figure 2). Three previously measured transitions of CO–para-H_2 (Pak et al. 1999) are indicated by dashed lines in the diagram of Figure 2. The newly observed transitions are shown by solid lines.

4. RESULTS AND DISCUSSION

The search for rotational transitions of the CO–para-H_2 complex was based on the data from an earlier IR study (McKellar 1998). The most prominent and complete series of observed MMW lines include $K = 1 - 0$, b-type, R-branch transitions, $(J, j, l) = (J{+}1, 1, J) \leftarrow (J, 0, J)$, with J from 3 to 5 and Q-branch transitions, $(J, 1, J) \leftarrow (J, 0, J)$, with J from 1 to 5. One $R(3)$ transition of the $K = 0 - 1$ sub-band, (4 0 4) ← (3 1 2) was also observed. Moreover, the a-type $R(2)$ and $R(3)$ transitions within the ground $K = 0$ state, $(J{+}1, 0, J{+}1) \leftarrow (J, 0, J)$, the $Q(4)$ transition between $K = 1$ stacks, (4 1 4) ← (4 1 3), and the $P(5)$ transition, (4 1 5) ← (5 0 5), to the excited CO bending state, i.e., $\nu_b = 1 - 0$, were measured. The lower frequency MW measurements include two transitions, $P(2)$ $K = 1 - 0$, (1 1 0) ← (2 0 2) and $Q(1)$ $K = 1 - 1$, (1 1 1) ← (1 1 0) in the 14 GHz region. Spectra of these lines are presented in Figure 3. All measured rotational transitions of CO–para-H_2 are indicated by arrows in Figure 2. The total number of newly detected lines is 15. These measurements significantl extend the previous results (Pak et al. 1999), where only three $K = 1 - 0$ R-branch transitions were observed.

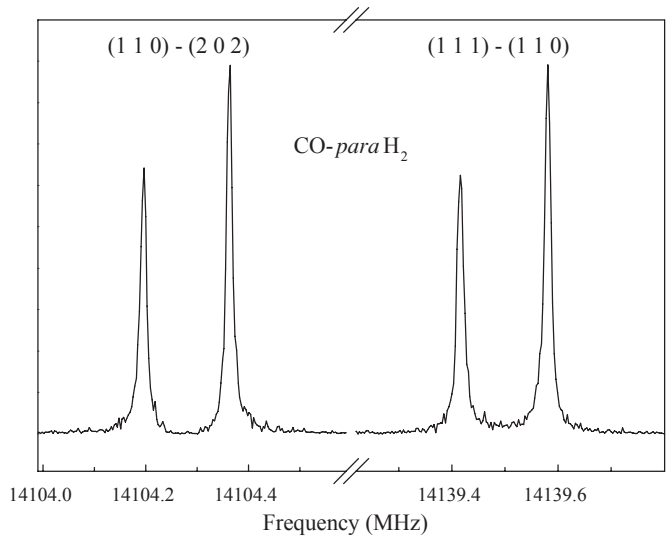

Figure 3. Recorded $(J, j, l) = (1\,1\,0) \leftarrow (2\,0\,2)$ and $(1\,1\,1) \leftarrow (1\,1\,0)$ MW transitions of CO–para-H_2.

The assignment of the observed transitions to CO–para-H_2 was based on close coincidence of the measured frequencies with those predicted from the IR data (McKellar 1998). The use of highly enriched samples of para-H_2 was very useful to distinguish lines belonging to the CO–para-H_2 spin modification which were located very close to CO–ortho-H_2 lines in a few cases.

The measured frequencies and their deviations from the predictions based on the IR data (McKellar 1998) are listed in Table 1. Most of the differences are in the order of a few MHz, with the largest being 17.9 MHz for the $(J, j, l) = (1\,1\,0) \leftarrow (0\,0\,0)$ transition (see Table 1). Such reasonably good coincidence with the IR prediction could initially not be expected because of the fundamental problems in determining the CO–para-H_2 energy levels, as mentioned earlier. In the IR work (McKellar 1998), it was not possible to accurately determine the relative positions of energy levels with positive and negative parity since the vibrational transitions connect states with positive (negative) parity in the ground state with those with negative (positive) parity in the excited state. McKellar determined the relative positions of "+" and "−" levels, and thus predicted MW and MMW transition frequencies, by requiring that the differences between corresponding energy levels in the CO ground and excited states be a smooth function of J (McKellar 1998). The data in Table 1 indicate that this approach yielded transition frequencies with "IR accuracy." However, from the astrophysical point of view information about the line positions with accuracy of a few kHz is desired.

The newly measured transitions were combined with three previously observed MMW lines (Pak et al. 1999) to construct

Table 1
Measured Rotational Transitions of CO–para-H_2

$(J'j'l') \leftarrow (J''j''l'')$	$\nu_{measured}$ (MHz)	$\Delta\nu_{IR}$ (MHz)
1 1 0 ← 0 0 0	108480.857[a]	−17.9
2 1 1 ← 1 0 1	118725.491[a]	6.5
3 1 2 ← 2 0 2	124271.567[a]	−10.6
4 1 3 ← 3 0 3	127985.517	1.5
5 1 4 ← 4 0 4	127479.175	1.8
6 1 5 ← 5 0 5	123738.713	3.3
1 1 1 ← 1 0 1	91012.364	13.6
2 1 2 ← 2 0 2	93471.460	0.5
3 1 3 ← 3 0 3	97186.009	−2.0
4 1 4 ← 4 0 4	103044.545	3.5
5 1 5 ← 5 0 5	106665.833	6.2
3 0 3 ← 2 0 2	92953.433	−5.4
4 0 4 ← 3 0 3	120623.172	−1.2
4 0 4 ← 3 1 2	89305.052	3.0
4 1 4 ← 4 1 3	95682.097	−0.1
4 1 5 ← 5 0 5	124050.211	9.8
1 1 0 ← 2 0 2	14104.2776	−11.3
1 1 1 ← 1 1 0	14139.4953	16.5

Notes.
For comparison, differences between transitions frequencies predicted from the IR data (McKellar 1998) and measured values are given in the third column.
[a] Measured by Pak et al. (1999).

Table 2
Level Energies for CO–para-H_2

$(J\ j\ l)$	E_{exp} (cm^{-1})	ΔE_{V04} (cm^{-1})	$\lvert\Delta E_{V04}\rvert/E_{exp}$ (%)
0 0 0	0	0	0
1 0 1	1.0543290(24)	0.002	0.16
2 0 2	3.1480638(17)	0.004	0.13
3 0 3	6.2486570(22)	0.006	0.10
4 0 4	10.2722123(23)	−0.003	0.03
5 0 5	15.27360(28)	0.041	0.27
6 0 6	20.92922(38)	0.047	0.22
1 1 0	3.6185319(17)	−0.001	0.01
2 1 1	5.0145851(29)	0.014	0.29
3 1 2	7.2933168(22)	0.031	0.42
4 1 3	10.5177952(25)	0.062	0.59
5 1 4	14.5244599(29)	0.045	0.31
6 1 5	19.40108(28)	0.074	0.38
1 1 1	4.0901747(17)	−0.009	0.22
2 1 2	6.2659361(24)	−0.004	0.06
3 1 3	9.4904333(28)	0.004	0.04
4 1 4	13.7094074(26)	0.016	0.11
5 1 5	18.83159(28)	0.031	0.17
6 1 6	24.68381(90)	0.055	0.22
0 1 1	7.07959(45)	0.094	1.33
1 1 2	8.48560(37)	0.088	1.03
2 1 3	11.09726(31)	0.06	0.54
3 1 4	14.82184(30)	0.083	0.56
4 1 5	19.41147(28)	0.087	0.45

Note. For comparison, differences and percentage differences between level energies calculated from the last available potential (Jankowski & Szalewicz 2005) and the experimental values are given in the third and fourth columns, respectively.

the energy level scheme of CO–para-H_2 with the aid of a least-squares term value program. A number of energy levels, namely levels in the $K = 0$ (e) stack with J up to 4, in the $K = 1$ (e) stack up to $J = 5$, and in the $K = 1$ (f) stack up to $J = 4$, were derived directly from the measured transition frequencies forming closed loops (see Figure 2). The obtained energy values are presented in Table 2. From these values it is possible to determine the frequencies of other, still not measured transitions. For example, the frequency of the (1 0 1) ← (0 0 0) transition from the lowest energy level (the most populated at low temperatures) can be predicted very precisely to be 31607.990 ± 0.05 MHz.

The energies of CO–para-H_2 levels not involved in closed loops were determined by including the available IR data (McKellar 1998) in the analysis. In the fittin procedure, the frequencies of the IR, MMW, and MW transitions were given weights of 1, 300, 15,000, according to the corresponding measurement accuracies. The resulting level energies are given in Table 2 relative to the $(J, j, l) = (0\,0\,0)$ level.

Further, the determined energy level positions can be compared with those derived from the most recent potential energy surfaces of CO–H_2, referred to as V_{98} (Jankowski & Szalewicz 1998) and V_{04} (Jankowski & Szalewicz 2005), respectively. The V_{98} surface was obtained treating the CO and H_2 molecules as rigid and using symmetry-adapted perturbation theory (SAPT) with high-level electron correlation effects. The V_{04} surface was obtained by averaging over the intramolecular vibration of H_2 using the coupled-cluster method with single, double, and noniterative triple excitations (CCSD(T)) and the supermolecular approach. The superior quality of the V_{04} potential was already established before (Jankowski & Szalewicz 2005), essentially on the basis of the IR measurements (McKellar 1998). The largest discrepancy in energy level positions was found to be smaller than 0.1 cm^{-1} for V_{04} surface compared to nearly 1 cm^{-1} for the previous V_{98} surface. Our analysis of the IR data in Table 1 indicates that those "experimental" energy levels really reflec "IR accuracy." Table 2 shows the differences between our experimental values and those calculated from the most advanced V_{04} surface. The percentage differences in Table 2 indicate that the V_{04} potential is of rather high quality. The differences are well below 1% for all levels, except the $(J, j, l) = (0\,1\,1)$ and $(1\,1\,2)$ levels. However, a tuning of the V_{04} potential to the precise experimental data reported here for CO–para-H_2 and obtained earlier for the isotopic modifica tion CO–ortho-D_2 (McKellar 2000; Surin et al. 2000a; Potapov et al. 2009a) could be useful for further improvement of the intermolecular potential energy surface for CO–H_2.

It is reasonable to compare the obtained energy level positions of CO–para-H_2 with those of the CO–He complex (McKellar et al. 1999; Surin et al. 2000b; Potapov et al. 2009b), which is also of astrophysical significanc (Green & Thaddeus 1976). The binding energy of CO–H_2 is about 22 cm^{-1} (McKellar 1998) as compared to 7 cm^{-1} for CO–He (McKellar et al. 1999). CO–H_2 has therefore a much higher number of bound states, even with $j_{CO} = 2$ and 3, in contrast to CO–He with only a few bound states. Nevertheless, both complexes may be discussed in the limits of a rigid model and the free rotor model considered in Section 3. In a rigidly T-shaped CO rare gas (or spherical para-H_2) complex, the separation between the $K = 0$ and 1 stacks of levels, i.e., the energy of the $(J, j, l) = (1\,1\,0)$ level, would be 1.92 cm^{-1} (the CO monomer B value), whereas in the case of free internal rotation of CO, the separation would be $2B$, or 3.84 cm^{-1}. Analyses of the measured spectra give values of 3.99 cm^{-1} for CO–He (McKellar et al. 1999) and 3.62 cm^{-1} for CO–para-H_2, indicating an almost unhindered out-of-plane rotation ($K = 1$) of the CO unit. The in-plane rotation ($K = 0$, $v_{b,CO} = 1$) of the CO monomer in the CO rare gas complexes is normally rather hindered by the angular anisotropy of the

interaction potential. With increasing anisotropy it becomes an intermolecular bending vibration and approaches the semi-rigid rotor limit. In the limit of free in-plane rotation, the energy of the lowest $(J, j, l) = (0\,1\,1)$ level of the $K = 0$ ($v_{b,\mathrm{CO}} = 1$) stack is equal to the energy of the (1 1 1) and (2 1 1) levels (identical j and l) of the $K = 1$ stack. The corresponding experimental values are 7.08, 4.09, and 5.01 cm^{-1} for CO–para-H_2, and 5.39, 4.27, and 4.73 cm^{-1} for CO–He (McKellar et al. 1999). The slightly higher energy of the in-plane rotation (or bending vibration) of CO in CO–para-H_2 compared to CO–He is a result of a greater angular anisotropy in the interaction potential of CO–para-H_2.

Evidently, CO–H_2 is a more complicated system than CO–He and exhibits more complex spectra revealing also internal motion of the H_2 unit. However, since the interaction potential is nearly isotropic with regard to H_2 rotation, the present results contain essentially no information about the orientation of the H_2 unit. Such information can be obtained from the spectra of CO–ortho-H_2. Although the infrared spectrum of CO–ortho-H_2 was recorded (McKellar 1998) and MW and MMW spectra are currently under investigation in our laboratories, a complete assignment has not been achieved yet, because of the more complicated structure of these spectra compared to the CO–para-H_2 system. The assistance of theoretical calculations will certainly help to better understand the CO–ortho-H_2 spectra.

5. CONCLUSIONS

Fifteen new transitions of the CO–para-H_2 vdW complex were measured and assigned with an intracavity jet spectrometer OROTRON in the frequency range of 80–130 GHz and with a pulsed-jet cavity FTMW spectrometer in the 14 GHz region, thus giving reliable data for radio astronomical searches for the CO–H_2 molecular complex in the ISM. The measurements extend significantl the previous data set of only three MMW transitions and allow us to determine a large number of energy levels of CO–para-H_2 with an accuracy of 50 kHz. Comparison with results from available ab initio calculations points to the need for improvement of the intermolecular potential energy surface for CO–H_2. Even if the number densities of weakly bound complexes in space are too low for spectroscopic identification the CO–H_2 spectrum is still of astrophysical significanc as it enables an accurate determination of the potential energy surface, which, in turn, provides information about the collisional processes between hydrogen and carbon monoxide molecules.

This work was supported by the Deutsche Forschungsgemeinschaft (grants 436 RUS 113/946, SU 579/1) and by the Natural Sciences and Engineering Research Council of Canada. A.V.P., V.A.P., and B.S.D. acknowledge the support by the Russian Foundation for Basic Research (grants 08-02-91966 and 09-02-00813).

REFERENCES

Allen, R. J., Loinard, L., McKellar, A. R. W., & Lequeux, J. 1997, ApJ, 489, 102
Dumesh, B. S., & Surin, L. A. 1996, Rev. Sci. Instrum., 67, 3458
Green, S., & Thaddeus, P. 1976, ApJ, 205, 766
Jankowski, P., & Szalewicz, K. 1998, J. Chem. Phys., 108, 3554
Jankowski, P., & Szalewicz, K. 2005, J. Chem. Phys., 123, 104301
Klemperer, W., & Vaida, V. 2006, Proc. Natl. Acad. Sci. USA, 103, 10584
McKellar, A. R. W. 1988, ApJ, 326, L75
McKellar, A. R. W. 1991, Chem. Phys. Lett., 186, 58
McKellar, A. R. W. 1998, J. Chem. Phys., 108, 1811
McKellar, A. R. W. 2000, J. Chem. Phys., 112, 9282
McKellar, A. R. W., Xu, Y., Jäger, W., & Bissonnette, C. 1999, J. Chem. Phys., 110, 10766
Mengel, M., Flatin, D. C., & De Lucia, F. C. 2000, J. Chem. Phys., 112, 4069
Pak, I., Surin, L. A., Dumesh, B. S., Roth, D. A., Lewen, F., & Winnewisser, G. 1999, Chem. Phys. Lett., 304, 145
Potapov, A. V., Panfil v, V. A., Dolgov, A. A., Surin, L. A., & Dumesh, B. S. 2009a, Opt. Spectrosc., 106, 655
Potapov, A. V., Surin, L. A., Panfil v, V. A., & Dumesh, B. S. 2009b, Opt. Spectrosc., 106, 183
Schmalz, T. G., & Flygare, W. H. 1978, in Laser and Coherence Spectroscopy, ed. J. I. Steinfeld (New York: Plenum), 125
Surin, L. A., Dumesh, B. S., Lewen, F., Roth, D. A., Kostromin, V. P., Rusin, F. S., Winnewisser, G., & Pak, I. 2001, Rev. Sci. Instrum., 72, 2535
Surin, L. A., Dumesh, B. S., Winnewisser, G., & Pak, I. 2000a, J. Chem. Phys., 113, 9351
Surin, L. A., Roth, D. A., Pak, I., Dumesh, B. S., Lewen, F., & Winnewisser, G. 2000b, J. Chem. Phys., 112, 4064 (erratum 112, 9190)
Surin, L. A., et al. 2007, J. Phys. Chem. A, 111, 12238
Vanden Bout, P. A., Lawrence, J. M. S., Bernstein, S., & Klemperer, W. 1979, ApJ, 234, 504
Xu, Y., & Jäger, W. 1997, J. Chem. Phys., 106, 7968
Yang, B., Stancil, P. S., Balakrishnan, N., & Forrey, R. S. 2006, J. Chem. Phys., 124, 104304

A comprehensive experimental and theoretical study of H2−CO spectra

Piotr Jankowski, L. A. Surin, A. Potapov, S. Schlemmer, A. R. W. McKellar et al.

Citation: J. Chem. Phys. **138**, 084307 (2013); doi: 10.1063/1.4791712
View online: http://dx.doi.org/10.1063/1.4791712
View Table of Contents: http://jcp.aip.org/resource/1/JCPSA6/v138/i8
Published by the American Institute of Physics.

A comprehensive experimental and theoretical study of H_2-CO spectra

Piotr Jankowski,[1] L. A. Surin,[2,3] A. Potapov,[2] S. Schlemmer,[2] A. R. W. McKellar,[4] and Krzysztof Szalewicz[5]

[1]*Department of Quantum Chemistry, Faculty of Chemistry, Nicolaus Copernicus University, Gagarina 7, 87-100 Toruń, Poland*
[2]*I. Physikalisches Institut, University of Cologne, Zülpicher Str. 77, 50937 Cologne, Germany*
[3]*Institute of Spectroscopy, Russian Academy of Sciences, 142190 Troitsk, Moscow Region, Russia*
[4]*National Research Council of Canada, Ottawa, Ontario K1A 0R6, Canada*
[5]*Department of Physics and Astronomy, University of Delaware, Newark, Delaware 19716, USA*

(Received 10 December 2012; accepted 29 January 2013; published online 27 February 2013)

A detailed description of a new *ab initio* interaction potential energy surfaces for the H_2-CO complex computed on a six-dimensional grid (i.e., including the dependence on the H−H and C−O separations) is presented. The interaction energies were firs calculated using the coupled-cluster method with single, double, and noniterative triple excitations and large basis sets, followed by an extrapolation procedure. Next, a contribution from iterative triple and noniterative quadruple excitations was added from calculations in smaller basis sets. The resulting interaction energies were then averaged over the ground-state and both ground- and first- xcited-states vibrational wave functions of H_2 and CO, respectively. The two resulting four-dimensional potential energy surfaces were fitte by analytic expressions. Theoretical infrared spectra calculated from these surfaces have already been shown [P. Jankowski, A. R. W. McKellar, and K. Szalewicz, Science **336**, 1147 (2012)] to agree extremely well, to within a few hundredth of wavenumber, with the experimental spectra of the *para* and *ortho*H_2-CO complex. In the latter case, this agreement enabled an assignment of the experimental spectrum, ten years after it had been measured. In the present paper, we provide details concerning the development of the surfaces and the process of spectral line assignment. Furthermore, we assign some transitions for *para*H_2-CO that have not been assigned earlier. A completely new element of the present work are experimental investigations of the *ortho*H_2-CO complex using microwave spectroscopy. Vast parts of the measured spectrum have been interpreted by comparisons with the infrared experiments, including new low-temperature ones, and theoretical spectrum. Better understanding of the spectra of both *para* and *ortho*H_2-CO complexes provides a solid foundation for a new search of the bound H_2-CO complex in space. © *2013 American Institute of Physics*. [http://dx.doi.org/10.1063/1.4791712]

I. INTRODUCTION

In the past three decades, the van der Waals interactions between the H_2 and CO molecules have been the subject of considerable experimental and theoretical efforts, primarily due to their astrophysical importance.[1] The main reason is that collisional excitations of CO by H_2 in space determine the populations of the CO energy levels which are reflecte in easy to observe CO spectra. If the collisional excitation rates are known, this in turn allows indirect measurement of the abundances of H_2, the main component of molecular clouds, and therefore mapping of interstellar matter.[2–4] On the other hand, searches for the bound H_2-CO complex in space[5] have not been successful yet. Despite significan efforts, not all of the mysteries of the H_2-CO interaction have been resolved. The infrared spectrum of *para*H_2-CO was recorded and assigned by one of the present authors (Ref. 6). Also the rovibrational energy-level patterns for that complex, with CO in its ground and firs excited vibrational states, were proposed.[6] In parallel, the same spectrum has been computed based on an *ab initio* potential energy surface (PES).[7] The results of Ref. 6 provided guidance needed for a more precise determination of several rovibrational states from the microwave measurements.[8,9] The advantage of using microwave spectroscopy is that the microwave transitions provide much more precise values of energy differences than the corresponding infrared transitions. Analogous infrared measurements were performed and spectra assigned for the *ortho*D_2-CO complex.[10] Also these measurements were followed by microwave ones.[11,12] The spectra contain indirect information about the PES and an empirical surface can be fitte to such spectra provided that the spectra were assigned. However, due to the nearly spherical character of the rotational wavefunction of the hydrogen molecule in *para*H_2-CO and *ortho*D_2-CO, information about the dependence of PES on the orientation of these monomers is limited. This anisotropy is much more extensively probed in the *ortho*H_2-CO or *para*D_2-CO spectrum since the motion of hydrogen is not spherical anymore. The former spectrum has been recorded more than ten years ago,[10] but due to its complexity has never been assigned (nor published) until very recently.[13]

Although most assignments of measured spectra are done using spectroscopic models, one can also achieve such assignments by comparisons with theoretically predicted

spectra based on *ab initio* PESs. Two earlier such surfaces[7,14] were found, however, insufficientl accurate to achieve an assignment for the *ortho*H_2-CO, even after an empirical tuning on *para*H_2-CO spectrum. Only very recently, three of the present authors have assigned *ortho*H_2-CO infrared spectrum[13] using a new *ab initio* PES.

The plan of this paper is as follows. The development of the potential energy surface will be presented in Sec. II. The methods used in calculations of rovibrational spectra will be briefl discussed in Sec. III. The two new spectroscopic experiments for the *ortho*H_2-CO complex are described in Sec. IV. In the firs experiment, the infrared measurements were performed for several values of temperatures around 2 K, much lower than the 49 K experiments reported earlier.[10,13] In the second experiment, microwave spectra were measured for the firs time for this complex. The general features of the interaction energy surfaces are discussed and compared to literature in Sect. V A. The reliability of the surfaces has been firs tested by checking their performance in reproducing the empirical pattern of the rovibrational energy levels for *para*H_2-CO in Sec. V B. This comparison allowed us also to assign a few lines hitherto unassigned. Section V C includes detailed comparisons of theoretically predicted and measured infrared spectra for *ortho*H_2-CO. Finally, similar comparisons for microwave spectra are presented in Sec. V D. Section VI contains conclusions.

II. CALCULATIONS OF PES

There exists a number of published PESs for H_2-CO, including surfaces computed by two of the present authors[7,14] which will be denoted by V_{98} and V_{04}, respectively. The agreement of the theoretical infrared spectra of *para*H_2-CO with experiment improved from about 1 cm^{-1} discrepancies in values of spectral lines achieved in Ref. 7 to 0.1 cm^{-1} in Ref. 14. Nevertheless, even the latter accuracy was not sufficien to assign the *ortho*H_2-CO spectrum, as the lines are often spaced by a fraction of wavenumber. Also tuning of the potential of Ref. 14 to experimental transition energies for *para*H_2-CO did not resolve the problem, probably since the *ortho*H_2-CO spectrum is more sensitive to the anisotropy of H_2 motion than the *para*H_2-CO one. Clearly, to realize the goal of assigning the *ortho*H_2-CO spectrum, a further increase in accuracy of PES was necessary. Such a surface has been developed recently and a successful assignment of the *ortho*H_2-CO spectrum based on the new surface was presented in Ref. 13. In this section, we describe the *ab initio* calculations and the f t-ting procedure used in this development in more detail than in Ref. 13.

A. Coordinates

For a full description of the H_2-CO complex, one needs six coordinates. In the present work, the Jacobi coordinates are used. The intermolecular coordinates include three angles θ_1, θ_2, and ϕ, and the variable R denoting the separation between the center of the mass of H_2, $CM(H_2)$ and the center of the mass of CO, CM(CO). To defin the angles θ_1, θ_2, and ϕ, one can choose the z axis pointing from $CM(H_2)$ to CM(CO). The parameter ϕ denotes then the dihedral angle between the two half-planes extending from the z axis to the chosen H atom (H1) and to the C atom. The angle between the z axis and the vector pointing from $CM(H_2)$ (CM(CO)) to H1 (C) is denoted θ_1 (θ_2). A set of these four coordinates will be denoted further as $\boldsymbol{X} = \{R, \theta_1, \theta_2, \phi\}$. To describe the intramolecular distances, one has to use two more parameters, r and s, which are the CO and H_2 bond lengths, respectively. Thus, the surface is a function of six variables $V(R, \theta_1, \theta_2, \phi, r, s)$.

B. Relation between six- and four-dimensional PESs

Although most of theoretical investigations of nuclear dynamics in van der Waals clusters still use PESs with rigid monomers, when very high accuracy is required, one has to eventually take into account the dependence of interaction energy on intramolecular degrees of freedom.[15–18] Full dimensionality is also required for properties that explicitly depend on intramonomer motion such as shifts of intramonomer transitions due to intermolecular interactions.[19,20] Although ultimately all steps of calculations leading to predictions of observables have to be performed at the full dimensionality, there exists an intermediate approach, proposed in Ref. 15, consisting in computing a full-dimensional PES, averaging it over monomers' nuclear motion in specifi monomers' rovibrational states, and using only the reduced dimensionality averaged surface in calculations of dimer spectra or of scattering cross-sections. For Ar−HF,[15] the dimer rovibrational energy levels computed using the two-dimensional (2D) potential obtained by averaging a 3D potential over the HF ground state vibration were only 0.1 cm^{-1} different than these from the fully 3D calculations, whereas energies computed using the 2D potential with the H−F separation f xed at its average value gave errors of 1.1 cm^{-1}. Since the former accuracy of energy levels should be sufficien for our purposes, we have used here the approach of Ref. 15. This approach has several computational advantages: (a) although it still requires calculations of interaction energies on a grid of coordinates in 6D space, if averaging is performed only over the lowest vibrational functions of monomers, one can use less points in r and s that would have been required to f t a complete analytic 6D potential valid in a broad range of intramonomer coordinates; (b) fittin of a 6D surface can actually be avoided, only 4D fit are performed; (c) 4D rovibrational calculations are much easier than 6D ones. Of course, if higher excited states of monomers are of interest, the advantage (a) does not hold anymore, but (b) and (c) still do.

In the present work, we express the 6D surface at each set of values of intermonomer coordinates $\boldsymbol{X}$ as the second-order Taylor expansion with respect to r and s around some reference intramolecular configuration r_c and s_c,[16]

$$\begin{aligned} V(\boldsymbol{X}, r, s) \approx\ & f^c_{00}(\boldsymbol{X}) \\ & + f^c_{10}(\boldsymbol{X})(r - r_c) + f^c_{01}(\boldsymbol{X})(s - s_c) \\ & + f^c_{11}(\boldsymbol{X})(r - r_c)(s - s_c) \\ & + \frac{1}{2} f^c_{20}(\boldsymbol{X})(r - r_c)^2 + \frac{1}{2} f^c_{02}(\boldsymbol{X})(s - s_c)^2. \end{aligned} \quad (1)$$

The derivatives f^c_{ij} are calculated numerically with steps h_r and h_s from the following formulas:

$$f^c_{00}(\boldsymbol{X}) = V(\boldsymbol{X}, r_c, s_c), \tag{2}$$

$$f^c_{10}(\boldsymbol{X}) = \left.\frac{\partial V}{\partial r}\right|_{r=r_c} \simeq \frac{V(\boldsymbol{X}, r_c + h_r, s_c) - V(\boldsymbol{X}, r_c - h_r, s_c)}{2h_r}, \tag{3}$$

$$f^c_{01}(\boldsymbol{X}) = \left.\frac{\partial V}{\partial s}\right|_{s=s_c} \simeq \frac{V(\boldsymbol{X}, r_c, s_c + h_s) - V(\boldsymbol{X}, r_c, s_c - h_s)}{2h_s}, \tag{4}$$

$$f^c_{20}(\boldsymbol{X}) = \left.\frac{\partial^2 V}{\partial r^2}\right|_{r=r_c} \simeq \frac{V(\boldsymbol{X}, r_c + h_r, s_c) - 2V(\boldsymbol{X}, r_c, s_c) + V(\boldsymbol{X}, r_c - h_r, s_c)}{h_r^2}, \tag{5}$$

$$f^c_{02}(\boldsymbol{X}) = \left.\frac{\partial^2 V}{\partial s^2}\right|_{s=s_c} \simeq \frac{V(\boldsymbol{X}, r_c, s_c + h_s) - 2V(\boldsymbol{X}, r_c, s_c) + V(\boldsymbol{X}, r_c, s_c - h_s)}{h_s^2}, \tag{6}$$

$$\begin{aligned} f^c_{11}(\boldsymbol{X}) &= \left.\frac{\partial^2 V}{\partial s \partial r}\right|_{r=r_c, s=s_c} \\ &\simeq \frac{V(\boldsymbol{X}, r_c + h_r, s_c + h_s) - V(\boldsymbol{X}, r_c + h_r, s_c) - V(\boldsymbol{X}, r_c, s_c + h_s) + V(\boldsymbol{X}, r_c, s_c)}{h_r h_s}. \end{aligned} \tag{7}$$

If the full-dimensional PES is define by the expansion (1), it is easy to calculate a surface vibrationally averaged over the vibrational wave functions of a molecule A, χ_v, and B, $\chi'_{v'}$,

$$\begin{aligned} \langle V\rangle_{vv'}(\boldsymbol{X}) &= \langle \chi_v(r)\chi'_{v'}(s)|V(\boldsymbol{X}, r, s)|\chi_v(r)\chi'_{v'}(s)\rangle \\ &\approx f^c_{00}(\boldsymbol{X}) + f^c_{10}(\boldsymbol{X})(\langle r\rangle_v - r_c) + f^c_{01}(\boldsymbol{X})(\langle s\rangle_{v'} - s_c) \\ &\quad + f^c_{11}(\boldsymbol{X})(\langle r\rangle_v - r_c)(\langle s\rangle_{v'} - s_c) \\ &\quad + \frac{1}{2} f^c_{20}(\boldsymbol{X})\left(\langle r^2\rangle_v - 2r_c\langle r\rangle_v - r_c^2\right) \\ &\quad + \frac{1}{2} f^c_{02}(\boldsymbol{X})\left(\langle s^2\rangle_{v'} - 2s_c\langle s\rangle_{v'} - s_c^2\right), \end{aligned} \tag{8}$$

where $\langle r^n\rangle_v = \langle \chi_v(r)|r^n|\chi_v(r)\rangle$ ($\langle s^n\rangle_{v'} = \langle \chi'_{v'}(s)|s^n|\chi'_{v'}(s)\rangle$) denote vibrationally averaged values of powers of intramonomer distances. Thus, a vibrationally averaged value of the interaction energy at a point $\boldsymbol{X}$ can be obtained if one knows the f^c_{nm} coefficient and the averaged values of low powers of r and s. In the present work, we used the following values for the latter quantities: $\langle s\rangle_0 = 1.44874$ bohrs, $\langle s^2\rangle_0 = 2.12705$ bohrs^2, $\langle r\rangle_0 = 2.13989$ bohrs, $\langle r^2\rangle_0 = 4.58320$ bohrs^2, $\langle r\rangle_1 = 2.15543$ bohrs, $\langle r^2\rangle_1 = 4.65817$ bohrs^2, taken from Ref. 21 for H_2 and calculated by us using an empirical potential from Ref. 22 for CO. The rovibrational wave functions used in the averaging are rotationless, i.e., correspond to the rotational quantum numbers $j_1 = 0$ and $j_2 = 0$ for H_2 and CO, respectively.

The procedure presented above gives values of $V(\boldsymbol{X})$ for all the points of the 4D grid in $\boldsymbol{X}$. This set of interaction energies is subsequently fitte by an analytic function as described in Sec. II F. Thus, no 6D f tting is performed. If an explicit 6D surface is needed, this can be achieved by fittin separately (in 4D) each of the six functions $f^c_{nm}(\boldsymbol{X})$ and using Eq. (1).

C. Calculations of interaction energies

1. Basis sets

Values of the interaction energies of the H_2-CO complex have been obtained using the supermolecular approach. The Boys and Bernardi counterpoise scheme[23,24] has been applied in all calculations, i.e., the quantities $V(R, \theta_1, \theta_2, \phi, r, s)$ were computed as

$$V \equiv E_{\rm int} = E^{\rm H_2-CO}_{\rm tot} - E^{\rm H_2}_{\rm tot} - E^{\rm CO}_{\rm tot}, \tag{9}$$

where all total energies on the right-hand side are computed in the same basis set, the monomer bond lengths are the same in monomer and dimer calculations, and in monomer calculations the positions of "ghost" functions are determined by (R, $\theta_1, \theta_2, \phi, r, s$).

The total interaction energy $E_{\rm int}$ can be expressed as a sum $E_{\rm int} = E^{\rm HF}_{\rm int} + E^{\rm corr}_{\rm int}$ of the Hartree-Fock ($E^{\rm HF}_{\rm int}$) and of the correlation ($E^{\rm corr}_{\rm int}$) components. We discuss below types of basis sets and the level of correlation treatment which is needed to achieve the goal of improving accuracy of the potential by about an order of magnitude relative to Ref. 14.

The basis set performance for the series of Dunning-type basis supplemented by midbond functions has been comprehensively discussed in Ref. 14, see also Refs. 25–27. We return to this issue since it has to be reexamined for larger basis set used in the present study. We independently analyze the convergence of $E^{\rm HF}_{\rm int}$ and $E^{\rm corr}_{\rm int}$ with respect to basis-set size, since the two components have different patterns of convergence. The convergence tests have been performed for the H_2 and CO molecules with bond lengths equal to 1.449 bohrs and 2.140 bohrs, respectively, which correspond to the roundings of the H−H and C−O distances vibrationally averaged

TABLE I. Comparison of basis-set convergence for the $E_{\rm int}^{\rm HF}$ component of H_2-CO interaction energy. The calculations have been performed for the specifie sets of intermolecular coordinates (θ_1,θ_2,ϕ) and two values of intermolecular distance R. The intramolecular separations in H_2 and CO are set to 1.449 bohrs and 2.140 bohrs, respectively. The bases aug-cc-pVXZ are denoted by X = T, Q, 5, 6. The entries including the symbol "b69" use the aug-cc-pVXZ bases supplemented with a 69-function midbond set from Ref. 26. The energies are given in cm^{-1}.

Basis set	(0°, 0°, 0°)	(0°, 90°, 0°)	(0°, 180°, 0°)	(45°, 45°, 45°)
		R = 7.0 bohrs		
T	22.627	58.324	297.590	50.396
Q	23.350	58.190	296.786	50.378
5	22.994	58.157	296.857	50.316
6	22.965	58.139	296.807	50.315
Tb69	23.309	58.335	297.534	50.401
Qb69	23.062	58.213	296.962	50.337
5b69	22.978	58.147	296.813	50.312
6b69	22.968	58.137	296.805	50.309
		R = 8.0 bohrs		
T	−20.709	18.214	17.301	11.027
Q	−19.929	18.132	17.202	10.966
5	−19.959	18.178	17.190	11.004
6	−19.982	18.166	17.189	11.001
Tb69	−19.898	18.242	17.174	11.010
Qb69	−19.930	18.192	17.209	11.011
5b69	−19.977	18.169	17.186	11.000
6b69	−19.980	18.164	17.188	10.999

over the lowest vibrational states of these molecules (note that these values are different from the values of s_c and r_c).

a. Hartree-Fock level: Table I presents the performance of various basis sets in calculation of the $E_{\rm int}^{\rm HF}$ component of the interaction energy for a few configuration of the complex. A sequence of aug-cc-pVXZ basis sets, up to the cardinal number X = 6, have been tested. Moreover, in additional tests these bases have been augmented with the set of 69 bond functions from Ref. 26. The converged energies are, of course, not known, but one can assume that the results for the bases of the X = 6 quality can be regarded as the reference. From Table I, one can see that the energies calculated in the aug-cc-pV5Z basis set do not differ from the X = 6 results by more than 0.05 cm^{-1} for the eight tested geometries. In particular, for the geometry corresponding to the global minimum of the interaction energy surface, (θ_1,θ_2,ϕ)= (0°, 180°, 0°) and R = 8.0 bohrs, the X = 5, 5b69, 6, and 6b69 results are the same to within 0.004 cm^{-1}. These observations suggest that the calculations of $E_{\rm int}^{\rm HF}$ in the aug-cc-pV5Z basis set, feasible for generation of the whole surface, should be accurate enough for our purposes. There exist extrapolation schemes applicable to the Hartree-Fock energies, most often the three-point exponential extrapolation[28] is used. However, since the convergence of $E_{\rm int}^{\rm HF}$ is somewhat erratic, we have decided not to use any extrapolation in the calculations of $E_{\rm int}^{\rm HF}$. This energy is anyway sufficientl accurate in bases with X = 5.

b. CCSD(T) level: The supermolecular approach based on the coupled-cluster method with single, double, and nonit-

TABLE II. Comparison of basis-set convergence including CBS extrapolations for the H_2-CO correlation component of interaction energy, $\delta E_{\rm int}^{\rm CCSD(T)}$. The calculations have been performed for the same set of intermolecular coordinates (R,θ_1,θ_2,ϕ) and the same intramonomer separations as in Table I. X = T, Q, 5, 6 denotes bases aug-cc-pVXZ. The results denoted by TQ, Q5, and 56 are extrapolations based on X = T and Q, X = Q and 5, and X = 5 and 6, respectively. The symbol "b69" has the same meaning as it Table I. The energies are given in cm^{-1}. All electrons were included in calculations.

Basis set	(0°, 0°, 0°)	(0°, 90°, 0°)	(0°, 180°, 0°)	(45°, 45°, 45°)
		R = 7.0 bohrs		
T	−88.545	−84.260	−260.100	−82.474
Q	−92.625	−86.628	−269.522	−85.263
5	−93.768	−87.476	−272.390	−86.299
6	−94.275	−87.886	−273.613	−86.785
TQ	−95.603	−88.356	−276.398	−87.300
Q5	−94.968	−88.366	−275.399	−87.386
56	−94.972	−88.449	−275.293	−87.453
Tb69	−94.362	−88.297	−272.027	−87.174
Qb69	−94.371	−88.126	−273.180	−87.070
5b69	−94.525	−88.187	−273.844	−87.131
6b69	−94.643	−88.239	−274.246	−87.194
TQb69	−94.378	−88.001	−274.021	−86.994
Q5b69	−94.686	−88.250	−274.541	−87.195
56b69	−94.806	−88.310	−274.797	−87.282
Best est.	−94.889	−88.380	−275.045	−87.3675
Uncertainty	0.43	0.32	1.12	0.38
		R = 8.0 bohrs		
T	−32.485	−36.658	−104.196	−34.815
Q	−33.781	−37.416	−106.588	−35.608
5	−34.180	−37.699	−107.481	−35.963
6	−34.358	−37.849	−107.836	−36.123
TQ	−34.726	−37.969	−108.334	−36.187
Q5	−34.599	−37.995	−108.417	−36.337
56	−34.602	−38.054	−108.324	−36.342
Tb69	−34.658	−38.190	−108.763	−36.448
Qb69	−34.535	−38.039	−108.163	−36.333
5b69	−34.517	−38.014	−108.163	−36.308
6b69	−34.539	−38.021	−108.174	−36.313
TQb69	−34.445	−37.928	−107.724	−36.249
Q5b69	−34.497	−37.988	−108.163	−36.282
56b69	−34.569	−38.030	−108.190	−36.320
Best est.	−34.586	−38.042	−108.257	−36.331
Uncertainty	0.14	0.11	0.25	0.11

erative triple excitations, CCSD(T), provides reliable values of the interaction energy and has been used in the present work to calculate the major component of the correlation part of interaction energy. We have performed basis-set convergence tests for the $E_{\rm int}^{\rm corr}$ component calculated at the CCSD(T) level of theory, $\delta E_{\rm int}^{\rm CCSD(T)} = E_{\rm int}^{\rm CCSD(T)} - E_{\rm int}^{\rm HF}$, and the results are presented in Table II. For the selected configuration included in the table, we were able to use bases of X = 6 quality, too expensive for the calculations of the whole surface. Basis-set convergence of correlated contributions can be accelerated by extrapolation techniques and the results obtained with the $1/X^3$ extrapolation algorithm[29] are also given in Table II. The values of the correlation part of interaction energies obtained from extrapolations based on the consecutive X and Y cardinal numbers will be denoted by XY. As in the case of $E_{\rm int}^{\rm HF}$, the quality of a basis set in calculations of correlated parts of

interaction energies can be significantl improved by addition of midbond functions, in fact, such addition is more important in the latter case.[25] Such an approach was used in the calculation of V_{04}, Ref. 14, where the aug-cc-pVDZ and aug-cc-pVTZ basis sets were supplemented by midbond functions (different from the b69 set used here).

The extrapolated 56 and 56b69 results agree to within 0.5 cm^{-1} (0.2%) for $R = 7$ bohrs and 0.13 cm^{-1} (0.1%) for $R = 8$ bohrs. Examination of the results in Table II does not allow one to conclude which of these results are more reliable. The convergence with midbond functions is much faster than without but it is less regular. Therefore, we have taken the averages of the largest basis set extrapolated results as our best estimates of $\delta E_{\rm int}^{\rm CCSD(T)}$. One possible way to compute an estimate of the uncertainties of these values is to the average of the magnitudes of the difference between the extrapolated and the largest basis set $\delta E_{\rm int}^{\rm CCSD(T)}$ quantities for calculation with and without midbond functions. As one can see in Table II, the uncertainties are below 1.1 cm^{-1} (0.4%) for $R = 7$ bohrs and 0.25 cm^{-1} (0.4%) for $R = 8$ bohrs. Although these uncertainties are small compared to the estimated uncertainty of V_{04}, Ref. 14, amounting to about 2%, analysis of the convergence patterns of the extrapolated results, in particular the closeness of Q5 and 56 values with and without bond functions, suggests that our current estimates are too conservative, perhaps even by a factor of two. For example, for $(\theta_1,\theta_2,\phi) = (0^\circ, 180^\circ, 0^\circ)$ and $R = 7.0$ bohrs, the change of the value of $\delta E_{\rm int}^{\rm CCSD(T)}$ when proceeding from Q5 to 56 amounts to 0.1 cm^{-1}, the corresponding value for Q5b69 and 56b69 is equal to 0.25 cm^{-1}, and the difference between 56 and 56b69 values is 0.5 cm^{-1}, whereas the estimated uncertainty is 1.1 cm^{-1}. Similarly, for the same angles and $R = 8.0$ bohrs, the analogous changes are 0.09, 0.03, and 0.1 cm^{-1}, whereas the estimated uncertainty is 0.25 cm^{-1}. Thus, we will somewhat arbitrarily assume that the uncertainties of the best estimates are 0.3%.

The largest practical basis sets for the calculations of the whole PES are of the $X = 5$ or 5b69 quality. The comparison of these results to our best estimates will allow us to choose one of these bases and determine the relevant uncertainties. The deviations of the Q5 and Q5b69 extrapolations from the best estimates are about 0.1%–0.2%. Because the Q5 results are slightly closer to the benchmarks than the Q5b69 ones and the latter calculations are two times more time consuming, we decided to use the Q5 approach in the calculations of the new surface. Another argument supporting the choice of the Q5 level rather than the Q5b69 one is that for small intermolecular distances the calculations in the aug-cc-pV5Z basis set with midbond functions do not converge in some cases. Since our benchmarks are accurate to about 0.3%, one can estimate the overall uncertainty of our correlated interaction energies at the CCSD(T) level as equal to about 0.5% in most regions of PES (except, of course, near points where PES crosses zero) or about 0.4 cm^{-1} in the well region.

The diminishing role of midbond basis sets as the monomer-located basis sets increase is, of course, expected since the latter sets become near-complete. We just concluded that with CBS extrapolations the midbond functions are not needed anymore at the Q5 level of basis sets (however, should definitel be used even at the $X = 5$ level if extrapolations are not applied). At the TQ level of CBS extrapolations, the question of which method is more accurate is open, but if computer time argument is taken into account, again our results would favor the approach without bond functions. These conclusions should be applicable to other van der Waals molecules.

TABLE III. Evaluation of performance of the frozen-core approximation in calculations of the H_2-CO correlation component of interaction energy, $\delta E_{\rm int}^{\rm CCSD(T)}$. X (= T, Q, 5) denotes bases aug-cc-pVXZ, whereas Xcv denotes bases aug-cc-pCVXZ. The intramonomer separations are the same as in Table I. The energies are given in cm^{-1}.

Basis set	(0°, 0°, 0°)	(0°, 90°, 0°)	(0°, 180°, 0°)	(45°, 45°, 45°)
		Frozen-core approximation		
		$R = 7.0$ bohrs		
T	−88.975	−84.290	−259.493	−82.472
Q	−92.756	−86.691	−268.633	−85.288
5	−93.930	−87.559	−271.314	−86.342
TQ	−95.787	−88.442	−275.302	−87.343
Q5	−95.162	−88.470	−274.126	−87.447
		$R = 8.0$ bohrs		
T	−32.529	−36.693	−103.951	−34.831
Q	−33.888	−37.474	−106.303	−35.642
5	−34.315	−37.773	−107.184	−36.012
TQ	−34.880	−38.044	−108.020	−36.234
Q5	−34.764	−38.087	−108.108	−36.399
		All electrons		
		$R = 7.0$ bohrs		
Tcv	−88.692	−84.276	−260.667	−82.522
Qcv	−92.638	−86.633	−269.943	−85.269
5cv	−93.780	−87.490	−272.626	−86.314
TQcv	−95.518	−88.352	−276.711	−87.274
Q5cv	−94.979	−88.390	−275.441	−87.410
		$R = 8.0$ bohrs		
Tcv	−32.500	−36.634	−104.073	−34.804
Qcv	−33.744	−37.403	−106.511	−35.592
5cv	−34.161	−37.697	−107.411	−35.960
TQcv	−34.651	−37.964	−108.291	−36.167
Q5cv	−34.599	−38.006	−108.356	−36.347

c. Frozen-core effects: The frozen-core (FC) approximation is often used in calculations of interaction energies, even for the complexes of the size of H_2-CO. The number of orbitals which could be frozen for H_2-CO is very limited, but even then savings of the central processing unit (CPU) time might reach 40%. Therefore, we have performed tests to check a potential inaccuracy introduced by the FC approximation and the results are given in Table III. One can see that although the FC effect is not large, it amounts to 0.3 cm^{-1} at the Q5 extrapolation level, for the geometry corresponding to the global minimum of the interaction energy surface $(R, \theta_1,\theta_2,\phi) = (8.0, 0^\circ, 180^\circ, 0^\circ)$, whereas for smaller intermolecular distance $R = 7.0$ bohrs it can be as large as 1 cm^{-1}. In both cases, the FC effect is comparable to the basis-set-truncation error. Thus, we have decided to correlate all electrons (AE) in the calculations of the $\delta E_{\rm int}^{\rm CCSD(T)}$ energies in the present study. Despite this choice, we have used the basis sets aug-cc-pVXZ which were optimized for frozen-core calculations. To validate the latter choice, we have checked

TABLE IV. Comparison of basis-set convergence including CBS extrapolations for the H_2-CO total interaction energy, $E_{int} = E_{int}^{HF} + \delta E_{int}^{CCSD(T)}$. The intramonomer distances and the symbols of basis sets used are the same as those in Tables I and II. The energies denoted by cardinal numbers *XY* has been obtained as a sum of E_{int}^{HF} calculated in the aug-cc-pV*YZ* basis set and the value of $\delta E_{int}^{CCSD(T)}$ extrapolated from the results of calculations in the bases aug-cc-pV*XZ* and aug-cc-pV*YZ*. The energies are given in cm^{-1}. All calculations included all electrons.

Basis set	(0°, 0°, 0°)	(0°, 90°, 0°)	(0°, 180°, 0°)	(45°, 45°, 45°)
		$R = 7.0$ bohrs		
TQ	−72.253	−30.166	20.388	−36.922
Q5	−71.974	−30.209	21.458	−37.070
56	−72.007	−30.310	21.514	−37.139
TQb69	−71.316	−29.788	22.941	−36.657
Q5b69	−71.708	−30.103	22.272	−36.883
56b69	−71.838	−30.173	22.008	−36.972
Best est.	−71.923	−30.242	21.761	−37.056
Q5−best est.	−0.052	0.033	−0.30	−0.015
		$R = 8.0$ bohrs		
TQ	−54.655	−19.837	−91.132	−25.221
Q5	−54.558	−19.817	−91.227	−25.333
56	−54.584	−19.888	−91.135	−25.341
TQb69	−54.375	−19.736	−90.515	−25.238
Q5b69	−54.474	−19.819	−90.977	−25.282
56b69	−54.549	−19.866	−91.002	−25.321
Best est.	−54.5665	−19.877	−91.0685	−25.331
Q5−best est.	0.009	0.06	−0.16	−0.002

TABLE V. Performance of various basis sets and extrapolation schemes in calculation of the total interaction energy, $E_{int} = E_{int}^{HF} + \delta E_{int}^{CCSD(T)}$, of the H_2-CO complex. The intramolecular geometries of H_2 and CO are the same as in Table I. The energy denoted by *X*mb has been obtained with the basis aug-cc-pV*XZ* supplemented by the *X*-dependent midbond functions in the way described in Ref. 14. The energy denoted by *XY*mb has been obtained as a sum of E_{int}^{HF} calculated in the *Y*mb basis set and the value of $\delta E_{int}^{CCSD(T)}$ extrapolated from the results of calculations in the bases *X*mb and *Y*mb. The energies are given in cm^{-1}.

Basis set	(0°, 0°, 0°)	(0°, 90°, 0°)	(0°, 180°, 0°)	(45°, 45°, 45°)
		$R = 7.0$ bohrs		
Dmb	−57.693	−25.304	57.925	−29.037
Tmb	−69.342	−28.913	28.597	−35.815
Qmb	−71.228	−29.802	24.280	−36.666
5mb	−71.579	−30.047	22.905	−36.843
DTmb	−71.679	−31.245	18.104	−38.182
TQmb	−72.332	−30.342	21.135	−37.221
Q5mb	−71.862	−30.255	21.595	−37.034
		$R = 8.0$ bohrs		
Dmb	−51.088	−19.180	−80.459	−23.597
Tmb	−53.986	−19.591	−90.190	−25.166
Qmb	−54.453	−19.801	−90.787	−25.307
5mb	−54.509	−19.857	−90.979	−25.322
DTmb	−54.146	−20.211	−92.864	−25.805
TQmb	−54.742	−19.889	−91.301	−25.403
Q5mb	−54.540	−19.884	−91.176	−25.347

how much the interaction energies would change if the core-valence aug-cc-pCV*XZ* basis sets were used. From Table III, one can see that for the test geometries the Q5cv values of $\delta E_{int}^{CCSD(T)}$ differ only slightly, not more than 0.06 cm^{-1}, from their Q5 counterparts from Table II. The nonextrapolated contributions differ more, however, one should remember that for a given cardinal number *X* the aug-cc-pCV*XZ* basis differs from the aug-cc-pV*XZ* one by additional functions enhancing the description of the core-valence effects. The extrapolation diminishes these differences to almost negligible values. Thus, we have used the aug-cc-pV*XZ* bases which result in significantl less expensive calculations.

d. Total CCSD(T) interaction energies: The values of the total interaction energies at the CCSD(T) level for our test geometries are listed in Table IV. The values denoted by *XY* are sums of E_{int}^{HF} calculated in the aug-cc-pV*YZ* basis set and of $\delta E_{int}^{CCSD(T)}$ extrapolated from values obtained in the aug-cc-pV*XZ* and aug-cc-pV*YZ* basis sets. The Q5 values differ from the best estimates by less than 0.16 cm^{-1} or 0.3% except for the positive point where this difference is 0.3 cm^{-1} or 1.4%. The fairly large percentage error in the latter case is due to the fact that this point is close to the region where the potential crosses zero. Thus, 0.2 cm^{-1} or 0.3% should be a reasonable estimate of the maximum discrepancy between the Q5 and the benchmark results. Since the benchmark values have uncertainties of similar magnitude, we estimate that the uncertainty of $E_{int}^{CCSD(T)}$ at the Q5 level, which will be used to compute $V(\boldsymbol{X}, r_c, s_c)$, is about 0.4 cm^{-1} or 0.6%. This estimate is consistent with one obtained for the correlated part of the CCSD(T) energy, the different percentage value reflect the fact that the Hartree-Fock energy is positive for most points.

A similar analysis of convergence of interaction energies with respect to the quality of basis sets was performed in Ref. 14. To obtain the complete PES, CBS extrapolations were applied there to results in aug-cc-pVDZ and aug-cc-pVTZ basis set with added midbond functions dependent on *X*. This level of basis set was denoted as DT in Ref. 14, but we will denote it now as DTmb to distinguish from the current notation. The test calculations were performed in Ref. 14 in bases up to 5mb and Qb69, the latter identical to that used in the current work. It was found that the TQmb level gives interaction energies within 0.5 cm^{-1} off the best estimates from that work computed just for a few points and the TQmb results were then used as benchmarks for a few cross sections of PES. It turned out that the interaction energies computed at the DTmb level behave, somewhat surprisingly, quite differently for different mutual angular orientations of monomers. Whereas for most orientations these energies were about 1−2 cm^{-1} too deep relative to the TQmb ones (in particular, 2 cm^{-1} too deep near the global minimum), for the (0°, 0°, 0°) orientation, corresponding to the local minimum, these energies were about 0.5 cm^{-1} too shallow. With the extended bases used in this work, we can shed more light on the observed behavior. Since the set of test geometries used in Ref. 14 has only one common element with the set of test geometries used earlier in the present work, to facilitate more extended comparison, the calculations with the *X*mb basis sets have been performed at the present test geometries and the results are shown in Table V. As one can see, the Q5mb results agree to about 0.1 (0.2) cm^{-1} with the present best estimates for the test

geometries at $R = 8$ ($R = 7$) bohrs. Thus, these results have sufficientl small uncertainties to be utilized for determining the accuracy of the TQmb predictions and for the subsequent analysis of the accuracy of the DTmb results, as it has been done in Ref. 14. Consequently, the somewhat uneven accuracy of the V_{04} potential is confirmed The CBS extrapolations from small bases are simply not very reliable. If (unextrapolated) Tmb results were used, one would have gotten a PES more uniformly shallow than the exact one and therefore with a better description of the anisotropy of PES. It was also suspected in Ref. 14 that the Q5mb extrapolations may be overshooting and the true limits are between these and the 5mb values. The present test demonstrates that indeed, the best estimates lie almost in the middle of the distance between the 5mb and Q5mb energies for the geometry of the minimum, but we fin that the Q5mb extrapolations overshoot only slightly. As we will discuss later, the fina PES obtained in the present work is sometimes deeper and sometimes shallower than V_{04}. This is a combined effect of the problem discussed here and of the inclusion of the post-CCSD(T) terms.

2. Terms beyond CCSD(T)

Whereas CCSD(T) is the most often used method in electronic structure calculations for systems of the size of H_2-CO, more advanced treatments of electron excitations are possible.[30,31] In fact, Noga *et al.*[32] have shown that such more advanced treatments of electron correlation may be necessary in the case of H_2-CO for a further increase of accuracy. We will now examine this question further on. The inclusion of full triple excitations (CCSDT),[33] of noniterative quadruple excitations [CCSDT(Q)],[34] and of full quadruple excitations (CCSDTQ)[35] are the currently available methods beyond CCSD(T). Let us introduce four quantities related to various levels of excitations in the coupled-cluster method: $\delta E_{\rm int}^{\rm T} = \delta E_{\rm int}^{\rm CCSDT} - \delta E_{\rm int}^{\rm CCSD(T)}$, $\delta E_{\rm int}^{\rm (Q)} = \delta E_{\rm int}^{\rm CCSDT(Q)} - \delta E_{\rm int}^{\rm CCSDT}$, $\delta E_{\rm int}^{\rm T(Q)} = \delta E_{\rm int}^{\rm T} + \delta E_{\rm int}^{\rm (Q)} = \delta E_{\rm int}^{\rm CCSDT(Q)} - \delta E_{\rm int}^{\rm CCSD(T)}$, and $\delta E_{\rm int}^{\rm Q} = \delta E_{\rm int}^{\rm CCSDTQ} - \delta E_{\rm int}^{\rm CCSDT(Q)}$. The values of these quantities are presented in Table VI and compared with the interaction energies calculated at the CCSD(T) level. As one can see, the values of the $\delta E_{\rm int}^{\rm T}$ and $\delta E_{\rm int}^{\rm (Q)}$ terms are small but not negligible, and for some geometries, e.g., (R, θ_1, θ_2, ϕ) = (7.0, 0°, 180°, 0°), their sum, $\delta E_{\rm int}^{\rm T(Q)}$, amounts to a few percent of the total interaction energy. The magnitudes of both $\delta E_{\rm int}^{\rm T}$ and $\delta E_{\rm int}^{\rm (Q)}$ are similar which means that both terms should be taken into account simultaneously if possible. Moreover, the value of $\delta E_{\rm int}^{\rm T(Q)}$ strongly depends on the geometry of the complex, thus can affect the anisotropy of the interaction energy surface, which is of great importance for the spectroscopic predictions. The comparison of the values of $\delta E_{\rm int}^{\rm T(Q)}$ with the values of uncertainties of $\delta E_{\rm int}^{\rm CCSD(T)}$ due to the limited basis set size at the Q5 level (0.4 $\rm cm^{-1}$ or 0.6%) shows that the former quantity is often a few times (sometimes an order of magnitude) larger than the latter. Thus, the $\delta E_{\rm int}^{\rm T(Q)}$ term definitel has to be taken into account if the CCSD(T) energies are computed at the Q5 level.

The values of $\delta E_{\rm int}^{\rm T(Q)}$ change by less than 0.02 $\rm cm^{-1}$ when the frozen-core approximation is used. Thus, this approximation is completely sufficien in the present work. Unfortunately, due to the severe limitations of the size of the bases in CCSDT and CCSDT(Q) calculations, it is difficul to study the convergence of $\delta E_{\rm int}^{\rm T}$ and $\delta E_{\rm int}^{\rm (Q)}$ in basis-set size. We were able to use only the aug-cc-pVDZ and aug-cc-pVTZ basis sets. One can see in Table VI that the values of $\delta E_{\rm int}^{\rm T}$ and $\delta E_{\rm int}^{\rm (Q)}$ depend fairly strongly on the size of basis set. However, the absolute differences between the results in these two basis sets are smaller than about 0.2 $\rm cm^{-1}$, typically around 0.1 $\rm cm^{-1}$. We have also calculated the $\delta E_{\rm int}^{\rm Q}$ term for four configuration in the aug-cc-pVDZ basis set. The results presented in Table VI show that the values of this term are very small in comparison to $\delta E_{\rm int}^{\rm T(Q)}$ and can be safely neglected at the current level of uncertainties. In calculations of $\delta E_{\rm int}^{\rm T(Q)}$ for the whole surface, we could only use the aug-cc-pVDZ

TABLE VI. Values of the $\delta E_{\rm int}^{\rm T}$, $\delta E_{\rm int}^{\rm (Q)}$, $\delta E_{\rm int}^{\rm T(Q)}$, and $\delta E_{\rm int}^{\rm Q}$ contributions compared to the total supermolecular interaction energy, $E_{\rm int}^{\rm CCSD(T)}$. The calculations have been performed with all electron correlated and within the frozen-core approximation, as noted. The intramonomer distances are the same as in Table I. Two basis sets, aug-cc-pVDZ and aug-cc-pVTZ, have been used. The energies are given in $\rm cm^{-1}$.

	(0°, 0°, 0°)	(0°, 90°, 0°)	(0°, 180°, 0°)	(45°, 45°, 45°)
		aug-cc-pVDZ, all electrons correlated		
		$R = 7.0$ bohrs		
$\delta E_{\rm int}^{\rm T}$	−0.426	−0.688	−3.877	−0.497
$\delta E_{\rm int}^{\rm (Q)}$	−0.427	−0.644	−2.134	−0.397
$\delta E_{\rm int}^{\rm T(Q)}$	−0.853	−1.332	−6.011	−0.893
$E_{\rm int}^{\rm CCSD(T)}$	−50.003	−18.154	87.217	−20.214
		$R = 8.0$ bohrs		
$\delta E_{\rm int}^{\rm T}$	−0.119	−0.289	−1.726	−0.224
$\delta E_{\rm int}^{\rm (Q)}$	−0.172	−0.310	−0.798	−0.181
$\delta E_{\rm int}^{\rm T(Q)}$	−0.291	−0.599	−2.524	−0.405
$E_{\rm int}^{\rm CCSD(T)}$	−48.375	−16.563	−74.762	−20.365
		aug-cc-pVDZ, frozen core		
		$R = 7.0$ bohrs		
$\delta E_{\rm int}^{\rm T}$	−0.428	−0.692	−3.903	−0.500
$\delta E_{\rm int}^{\rm (Q)}$	−0.430	−0.643	−2.127	−0.397
$\delta E_{\rm int}^{\rm T(Q)}$	−0.857	−1.335	−6.030	−0.896
$\delta E_{\rm int}^{\rm Q}$	−0.017		−0.086	
$E_{\rm int}^{\rm CCSD(T)}$	−50.991	−18.132	87.434	−20.188
		$R = 8.0$ bohrs		
$\delta E_{\rm int}^{\rm T}$	−0.119	−0.291	−1.737	−0.226
$\delta E_{\rm int}^{\rm (Q)}$	−0.174	−0.309	−0.795	−0.181
$\delta E_{\rm int}^{\rm T(Q)}$	−0.293	−0.600	−2.532	−0.406
$\delta E_{\rm int}^{\rm Q}$	−0.003		−0.043	
$E_{\rm int}^{\rm CCSD(T)}$	−48.373	−16.556	−74.664	−20.355
		aug-cc-pVTZ, frozen core		
		$R = 7.0$ bohrs		
$\delta E_{\rm int}^{\rm T}$	−0.477	−0.523	−3.440	−0.343
$\delta E_{\rm int}^{\rm (Q)}$	−0.616	−0.793	−2.684	−0.617
$\delta E_{\rm int}^{\rm T(Q)}$	−1.093	−1.315	−6.124	−0.960
$E_{\rm int}^{\rm CCSD(T)}$	−65.975	−25.966	38.096	−32.077
		$R = 8.0$ bohrs		
$\delta E_{\rm int}^{\rm T}$	−0.184	−0.214	−1.368	−0.154
$\delta E_{\rm int}^{\rm (Q)}$	−0.219	−0.373	−1.055	−0.268
$\delta E_{\rm int}^{\rm T(Q)}$	−0.403	−0.587	−2.423	−0.421
$E_{\rm int}^{\rm CCSD(T)}$	−53.238	−18.479	−86.649	−23.804

basis set. Thus, we increase the uncertainties of our interaction energies at the nonrelativistic Born-Oppenheimer level to 0.5 cm^{-1} or 0.7%. Note that since the excitations beyond CCSDTQ level are certainly negligible, this is an estimate of the basis-set truncation error relative to the exact solution of nonrelativistic clamped-nuclei Schrödinger equation.

In addition to basis-set truncation error, other possible uncertainties are mainly due to the Born-Oppenheimer approximation and to the nonrelativistic approach used by us. In Ref. 32, Noga *et al*. have estimated the magnitudes of these uncertainties by calculating the diagonal Born-Oppenheimer correction[36] and the relativistic mass-velocity-Darwin correction. For the geometry of the complex corresponding to the global minimum, the values of each of these corrections are of the order of 0.1 cm^{-1} for the largest basis set applied. Thus, these terms are smaller than our basis set uncertainties and therefore we have not include them. However, in the future applications, those effects should be taken into account if the basis sets uncertainties are reduced significantl below 0.1 cm^{-1}. At present time, we have just increased our basis set uncertainties to account for these effects, obtaining the total uncertainty of $V(\boldsymbol{X}, r_c, s_c)$ amounting to 0.6 cm^{-1} or 0.8%.

TABLE VII. Comparison of performance of various basis sets in calculation of this part of the vibrationally averaged interaction energy that depends on the vibrational states of the CO (v) and H_2 (v') molecules: $\langle V\rangle_{vv'}(\boldsymbol{X}) - f^c_{00}(\boldsymbol{X})$. The data are provided for two intermolecular geometries of the complex $\boldsymbol{X} = (R, \theta_1, \theta_2, \phi)$. The acronyms definin basis sets are the same as in Table II. The unit of R is bohr, energies are given in cm^{-1}.

(v, v')	(0, 0)	(1, 0)	(0, 1)	(1, 1)
		(7.911, 0°, 180°, 0°)		
D	0.081	1.558	− 4.858	− 3.209
T	0.189	1.581	− 6.088	− 4.540
Q	0.269	1.618	− 6.516	− 5.013
5	0.292	1.633	− 6.567	− 5.073
DT	0.316	1.634	− 6.517	− 5.044
TQ	0.311	1.639	− 6.747	− 5.265
Q5	0.317	1.651	− 6.626	− 5.139
		(7.168, 0°, 0°, 0°)		
D	2.712	2.022	1.963	1.198
T	3.240	2.300	1.330	0.298
Q	3.323	2.324	1.048	− 0.047
5	3.373	2.357	0.964	− 0.149
DT	3.344	2.379	0.944	− 0.115
TQ	3.420	2.376	0.849	− 0.294
Q5	3.416	2.387	0.928	− 0.199

3. Calculations of derivatives

The fairly time-consuming calculations at the levels of theory and basis sets described above have been performed only for the $f^c_{00}(\boldsymbol{X}) = V(\boldsymbol{X}, r_c, s_c)$ term. One does not need to apply such high levels to calculations of interaction energies needed to compute the derivatives f^c_{ij} for $i + j > 0$, given by Eqs. (3)–(8). The reason is that the change of the interaction energy due to the change of the r and s coordinates in the allowed range corresponding to the ground and firs excited vibrational states of monomer is only a relatively small percent of the value of $V(\boldsymbol{X}, r_c, s_c)$, see Fig. 1 in Ref. 14. For the dimer configuratio most dependent on r and s, the relative change is only about 20%. The illustration of this behavior can be found in Table VII, where the performance of various basis sets in calculations of $\langle V\rangle_{vv'}(\boldsymbol{X}) - f^c_{00}(\boldsymbol{X})$ is presented for four pairs of vibrational quantum states (v, v'), where v and v' correspond to CO and H_2, respectively. The derivatives f^c_{ij}, $i + j > 0$, needed to obtain $\langle V\rangle_{vv'}(\boldsymbol{X}) - f^c_{00}(\boldsymbol{X})$, were calculated at the $E^{\mathrm{HF}}_{\mathrm{int}} + \delta E^{\mathrm{CCSD(T)}}_{\mathrm{int}}$ level of theory with a sequence of basis sets. For the geometry close to the global minimum and for $(v, v') = (0, 0)$, the difference between the TQ and Q5 energies amounts to 0.006 cm^{-1}. Generally, for all tested cases the TQ results are very close to the Q5 ones. Moreover, one can see from Table VII that even the DT extrapolation performs surprising well in all cases, despite the fact that the energies obtained without the extrapolation at the D and T levels are quite far from the most reliable Q5 ones. Thus, our fina choice to compute the f^c_{ij}, $i + j > 0$, derivatives from interaction energies obtained as a sum of $E^{\mathrm{HF}}_{\mathrm{int}}$/aug-cc-pVQZ and $\delta E^{\mathrm{CCSD(T)}}_{\mathrm{int}}$/TQ/AE produces negligible uncertainties compared to same level calculations in much larger basis sets. The remaining question is the neglect of the $\delta E^{\mathrm{T(Q)}}_{\mathrm{int}}$ term. It will be demonstrated in Sec. V A that this approximation produces uncertainty below 0.08 cm^{-1} for the geometry of the global minimum and therefore works very well. Table VIII summarizes information about the theory level and basis set used for all f^c_{ij} terms.

Since the additional uncertainty due to the averaging over monomer coordinates is small, our estimate of uncertainty of $V(\boldsymbol{X}, r_c, s_c)$, 0.6 cm^{-1}, or 0.8%, carries over to $V(\boldsymbol{X}, r, s)$. In the region of the potential well, the uncertainties should be around 0.6 cm^{-1}. In the asymptotic region, one should apply the relative estimate of 0.8% which will result in absolute errors smaller than 0.6 cm^{-1}. On the repulsive walls near the region where the potential crosses zero, the estimate of 0.6 cm^{-1} should still be valid. For larger values on the positive part of the repulsive wall, the relative estimate should be applied.

D. Grid points

We have performed Taylor expansions around the points $s_c = 1.474$ and $r_c = 2.165$ bohrs for H_2 and CO, respectively.

TABLE VIII. Description of the levels of theory and basis sets used to calculate the f^c_{ij} coefficient which defin the interaction potential energy surface [see Eqs. (1)–(8)].

	f^c_{00}
Theory level	$E_{\mathrm{int}} = E^{\mathrm{HF}}_{\mathrm{int}} + \delta E^{\mathrm{CCSD(T)}}_{\mathrm{int}} + \delta E^{\mathrm{T(Q)}}_{\mathrm{int}}$
Basis set	$E^{\mathrm{HF}}_{\mathrm{int}}$: aug-cc-pV5Z
	$\delta E^{\mathrm{CCSD(T)}}_{\mathrm{int}}$: aug-cc-pVQZ + aug-cc-pV5Z + extrapolation, all electrons correlated
	$\delta E^{\mathrm{T(Q)}}_{\mathrm{int}}$: aug-cc-pVDZ, frozen core
	$f^c_{ij}, i + j > 0$
Theory level	$E_{\mathrm{int}} = E^{\mathrm{HF}}_{\mathrm{int}} + \delta E^{\mathrm{CCSD(T)}}_{\mathrm{int}}$
Basis set	$E^{\mathrm{HF}}_{\mathrm{int}}$: aug-cc-pVQZ
	$\delta E^{\mathrm{CCSD(T)}}_{\mathrm{int}}$: aug-cc-pVTZ + aug-cc-pVQZ + extrapolation, all electrons correlated

These points are not any vibrationally averaged values but are judiciously chosen to lie between $\langle s\rangle_0$ and $\langle s\rangle_1$ and similarly for r. It would have been more appropriate to use two different Taylor expansions for $v = 0$ and 1, centered at $\langle s\rangle_0$ and $\langle s\rangle_1$, respectively, but this option would lead to a significantl larger numerical effort while giving negligible improvements of results.[16] Note that although we averaged only over $v = 0$ state for H_2, the value of r_c was chosen to enable future effective averaging also for $v = 1$. To calculate the leading f_{00}^c term of expansion (1), one has to perform calculations for (r_c, s_c), while to compute the other f_{ij}^c coefficient one has to use all six grid points in (r, s), as shown in Eqs. (3)–(8). These six points are define by the values of the steps $h_r = h_s = 0.025$ bohr.

To design a grid for the intermolecular coordinates $\boldsymbol{X} = (R, \theta_1, \theta_2, \phi)$, one should keep in mind that the main goal of the present calculations is to obtain a surface which would be accurate enough to predict the *ortho*H_2-CO spectra. It is clear that in nuclear motion leading to the *ortho*H_2-CO spectrum, the anisotropy of the potential energy surface is extensively probed, much more than in the *para*H_2-CO case.[10] Thus, the angular part of the fi should be based on as many grid points as possible. To fulfil this requirement, the angular grid points have been chosen to be relatively dense for selected values of the intermolecular distance. Our regular angular grid is define as in V_{04}[14] by the set of 33 unique combinations of the following angles: 0°, 45°, 90°, 135° for θ_1; 0°, 45°, 90°, 135°, 180° for θ_2; 0°, 45°, 90° for ϕ. This angular grid is combined with the following values of R (in bohr): 5.5, 6.0, 6.5, 7.0, 7.5, 8.0, 8.5, 9.0, 10.0, 12.0, 15.0, 17.5, 20.0. For four intermolecular distances, 7.0, 8.0, 10.0, and 15.0 bohrs, the angular grid was made twice as dense in each of the θ_1, θ_2, and ϕ coordinates, which resulted in 208 additional angular configurations The coverage of the intermonomer coordinate space by these additional grid points is more extensive than in the case of V_{04}, where only 112 geometries out of the regular grid have been used. Our present choice results in the total of 1261 grid points in the $\boldsymbol{X}$ coordinates. It should be stressed here that majority of the additional grid points correspond to the C_1 symmetry of the complex and are, therefore, more time consuming to compute than symmetric points. All calculations were performed using the MOLPRO package[37] and the MRCC program of Kállay.[38]

E. Construction of the vibrationally averaged interaction energy surface

To obtain the vibrationally averaged PES, for any point of the grid $\boldsymbol{X}$ in the intermolecular coordinates, the interaction energy was integrated over the intramolecular coordinates r and s according to the formula (8). Two sets of averaged values of interaction energies were obtained: firs for the ground vibrational states of both CO and H_2 molecules, and second for the ground vibrational state of H_2 and the f rst excited of CO. For each of these two sets of points, four-dimensional interaction energy surfaces were fitte using the analytical form presented in Sec. II F. The two resulting surfaces will be further denoted as V_0 and V_1, where $V_v(R, \theta_1, \theta_2, \phi) = \langle V\rangle_{vv'}(R, \theta_1, \theta_2, \phi)$, i.e., we will drop subscript v' since it is always zero.

F. Analytic fi

The analytic representation of the potential energy surface has been chosen in the form[7,39]

$$V(R, \theta_1, \theta_2, \phi) = V_{\rm sh}(R, \theta_1, \theta_2, \phi) + V_{\rm as}(R, \theta_1, \theta_2, \phi), \tag{10}$$

where $V_{\rm sh}$ and $V_{\rm as}$ are the short-range and long-range components, respectively. The short-range part of the potential is define exactly in the same way as in Ref. 7, i.e.,

$$V_{\rm sh}(R, \theta_1, \theta_2, \phi) = G(R, \theta_1, \theta_2, \phi)\mathrm{e}^{D(\theta_1,\theta_2,\phi)-B(\theta_1,\theta_2,\phi)R}, \tag{11}$$

where G is a polynomial in R with angle-dependent coefficient

$$G(R, \theta_1, \theta_2, \phi) = \sum_{i=0}^{3} R^i C_i(\theta_1, \theta_2, \phi). \tag{12}$$

The angular coefficient in Eqs. (11) and (12) are define as

$$C_i(\theta_1, \theta_2, \phi) = \sum_{l_1,l_2,l} g_i^{l_1 l_2 l} A_{l_1 l_2 l}(\theta_1, \theta_2, \phi), \tag{13}$$

$$B(\theta_1, \theta_2, \phi) = \sum_{l_1,l_2,l} b^{l_1 l_2 l} A_{l_1 l_2 l}(\theta_1, \theta_2, \phi), \tag{14}$$

and D is analogous to B. The definition of the angular functions $A_{l_1 l_2 l}(\theta_1, \theta_2, \phi)$ can be found in Ref. 7. The sum in Eq. (13) runs over (l_1, l_2, l) indices in the set of 25 arrangements [(0,0,0), (0,1,1), (0,2,2), (0,3,3), (0,4,4), (2,0,2), (2,1,1), (2,1,3), (2,2,0), (2,2,2), (2,2,4), (2,3,1), (2,3,3), (2,3,5), (2,4,2), (2,4,4), (4,0,4), (4,2,2), (4,2,4), (4,3,1), (4,3,3), (4,3,5), (4,4,0), (4,4,2),(4,4,4)], whereas the sum in Eq. (14) runs over 8 such set [(0,0,0), (0,1,1), (0,2,2), (2,0,2), (2,1,1), (2,2,0), (2,2,2), (2,3,1)]. Both sets were arbitrarily chosen in the optimization procedure. Note that the individual terms of our potential surface do not separate the radial and angular dependence. This feature leads to better f ts with less terms in the expansion compared the standard "partial wave" potential form. In calculations of rovibrational spectra, our potential is refitte by a potential of latter form via a numerical projection.

The $V_{\rm as}$ component of the surface is slightly modifie in comparison with the one from Ref. 7 by introduction of a factor γ_n,

$$V_{\rm as}(R, \theta_1, \theta_2, \phi) = \sum_{l_1,l_2,l,n} f_n[B(\theta_1, \theta_2, \phi)R] \times \frac{C_n^{l_1 l_2 l}}{R^n}\gamma_n A_{l_1 l_2 l}(\theta_1, \theta_2, \phi), \tag{15}$$

where f_n are Tang-Toennies damping functions[40] and B is the same as in Eq. (11). The $C_n^{l_1 l_2 l}$ asymptotic parameters collect information about the electrostatic, induction, and dispersion components of the interaction energy. The value of n runs from 4 to 12, where the $n = 4$ term originates from the quadrupole-dipole electrostatic interaction of the H_2 and CO

TABLE IX. Comparison of theory levels, basis sets, and other details characterizing *ab initio* potential energy surfaces for the H_2−CO complex: V_{98},[7] V_{04},[14] and V_0 and V_1 obtained in the present work. Only the largest basis sets used in calculations on the whole grid are listed.

	Theory level	Basis set	CBS extrapolation	*Ab initio* grid	Final potential fi
V_{98}	SAPT[a]: $E_{\rm int} = E_{\rm int}^{\rm HF} + E_{\rm int,resp}^{\rm corr} E_{\rm int,resp}^{\rm corr}$ $= \epsilon_{\rm elst,resp}^{(1)}(3) + \epsilon_{\rm exch}^{(1)}({\rm CCSD}) +^t E_{\rm ind}^{(22)}$ $+^t E_{\rm exch-ind}^{(22)} + E_{\rm disp}^{(20)} + \epsilon_{\rm disp}^{(2)}(2)$ $+ E_{\rm exch-disp}^{(20)}$	MC$^+$BS[b] composed of [3*s*2*p*2*d*2*f*] for H [5*s*3*p*3*d*2*f*1*g*] for C and O [3*s*2*p*1*d*] for midbond[c]	No	4D with monomers at $\langle r\rangle_0$ and $\langle s\rangle_0$ separations	4D, f tted directly to computed points
V_{04}	CCSD(T)/AE	aug-cc-pVTZ + midbond	Yes	5D with CO separation f xed at $\langle r\rangle_0$	4D, f tted to energies averaged over $\chi_0(s)$
Present	CCSDT(Q)/AE&FC	See Table VIII	Yes	6D	Two 4D surfaces fitte to vibrationally averaged energies

[a]See Refs. 41–43 for definition of SAPT components.
[b]MC$^+$BS is a monomer-centered basis set extended by midbond functions and a subset of functions on the interacting partner, see Ref. 25.
[c]For details of this basis set, see Ref. 7.

molecules. In the present work, the values of $C_n^{l_1 l_2 l}$ and the parameters definin the B function have been taken from Ref. 7. All the $C_n^{l_1 l_2 l}$ coefficient were computed *ab initio* in Ref. 7 at the level of theory consistent with the symmetry-adapted perturbation theory (SAPT)[41–43] calculations used there and the basis sets of the [3*s*2*p*2*d*2*f*] quality for H_2 and [5*s*3*p*3*d*2*f*1*g*] for CO. The computations were performed for the frozen geometries of the H_2 and CO molecules. Since the present basis set sizes are larger, level of theory higher, and treatment of intramonomer coordinates different, we have introduced the scaling parameters γ_n. Values of seven γ_n parameters, $n = 4, \ldots, 10$ have been obtained by least squares fittin $V_{\rm as}$ to the 647 *ab initio* energies for $R \geq 10$ bohrs. The γ_n parameters for $n > 10$ have been set to 1. In the least squares fittin of $V_{\rm as}$, the interaction energies were weighted by a factor $w = (\frac{R}{R_w})^8$, where $R_w = 10$ bohrs. The fina fi was performed to interaction energies at all grid points using the functional form of Eq. (10) with the asymptotic part frozen except for the parameters $b^{l_1 l_2 l}$. A FORTRAN program computing the fitte surfaces is available from the authors upon request.

G. Comparisons with V_{98} and V_{04}

We have already performed some comparisons of the present PESs with V_{98} and V_{04} and more such comparisons will be presented later in the paper. Understanding the relation between the increasing levels of *ab initio* treatment in the sequence of potentials V_{98}, V_{04}, and the present ones and the corresponding improvements of agreement with experiment provides important information on the interplay between theory and experiment in the fiel of van der Waals clusters. To make the distinctions between the potentials clear, we present a summary of the main features of these three potentials in Table IX. One can see that in all discussed categories represented in separate columns, levels of theory gradually increase starting from V_{98}, through V_{04}, to the present surface. We have observed that all these factors have their contributions to the improvement of agreement with experiment.

III. ROVIBRATIONAL CALCULATIONS

All the rovibrational calculations presented in this paper have been performed with the BOUND package[44] using the coupled-channel method within the space-fi ed coordinate formalism. The details of present calculations are the same as of those in Ref. 7. However, some basic information will be presented below to make the further discussion more transparent.

A bound-state wave function can be written using the versors $\hat{\boldsymbol{R}}_1$ and $\hat{\boldsymbol{R}}_2$ for orientation of H_2 and CO, respectively, and $\hat{\boldsymbol{R}}$ for the angular coordinates describing vector $\boldsymbol{R}$,[45]

$$\Psi(\hat{\boldsymbol{R}}_1, \hat{\boldsymbol{R}}_2, \boldsymbol{R}) = \sum_{\Lambda} R^{-1} f_\Lambda(R) I_\Lambda(\hat{\boldsymbol{R}}_1, \hat{\boldsymbol{R}}_2, \hat{\boldsymbol{R}}), \tag{16}$$

where $\Lambda \equiv \{JMj_1 j_2 j_{12} l\}$ denotes the set of indices definin normalized angular basis functions I_Λ. The consecutive indices are related to the eigenvalues of the total angular momentum operator $\boldsymbol{J}$, its projection $\boldsymbol{J}_z$, the angular momenta $\boldsymbol{j}_1$ and $\boldsymbol{j}_2$ of H_2 and CO, respectively, the sum of these momenta $\boldsymbol{j}_1 + \boldsymbol{j}_2$, and the end-over-end angular momentum $\boldsymbol{l}$. The angular basis functions I_Λ are the following expansions in radial harmonics:

$$\begin{aligned} I_\Lambda(\hat{\boldsymbol{R}}_1, \hat{\boldsymbol{R}}_2, \hat{\boldsymbol{R}}) &= \sum_{m_{12} m} (j_{12} m_{12} l m | J M) Y_{lm}(\hat{\boldsymbol{R}}) \\ &\times \sum_{m_1 m_2} (j_1 m_1 j_2 m_2 | j_{12} m_{12}) Y_{j_1 m_1}(\hat{\boldsymbol{R}}_1) Y_{j_2 m_2}(\hat{\boldsymbol{R}}_2), \end{aligned} \tag{17}$$

where m, m_1, m_2, and m_{12} are quantum numbers of the projections of the operators $\boldsymbol{l}$, $\boldsymbol{j}_1$, $\boldsymbol{j}_2$, and $\boldsymbol{j}_1 + \boldsymbol{j}_2$, respectively, and $(l_1 m_1 l_2 m_2 | l m)$ are the Clebsch-Gordan coefficients

The total angular momentum J and the spectroscopic parity, define as $P = (-1)^{J + j_1 + j_2 + l}$, are good quantum numbers for H_2−CO and therefore the system of coupled differential equations, obtained by the substitution of Ψ into the Schrödinger equation and integration over angular coordinates, can be solved within the subset of the given values

of J and P. Moreover, the subsystem of equations for a given J does not depend on M, so the radial function $f_\Lambda(R)$ with indices differing only by the values of M are the same. Thus, for each subsystem of rovibrational equations, a reduced number of parameters $\{j_1 j_2 j_{12} l\}$ is sufficien to label the angular basis set functions I_Λ.

Further, although approximate, reduction of the parameter set can be done if one takes into account that the values of j_1 are even for the *para* form and odd for the *ortho* form. Moreover, due to the fact that the rotational constant of H_2 is large relative to the depth of the PES, the rovibrational wave functions Ψ are dominated by the I_λ components with $j_1 = 0$ for *para*H_2-CO and with $j_1 = 1$ for *ortho*H_2-CO. In the former case, this implies $j_{12} = j_2$ which further reduces the set of indices needed for labeling the wave function components to $\{j_2 l\}$. In the case of *ortho*H_2-CO, the reduction is not that significan since the angular momentum $\boldsymbol{j}_1$ with the eigenvalue $j_1 = 1$ can be coupled with $\boldsymbol{j}_2$ in up to three different ways characterized by j_{12}, so the set of indices can be reduced only to $\{j_2 j_{12} l\}$.

From the results of rovibrational calculations presented in Refs. 7 and 14, one can learn that for *para*H_2-CO and in particular for *ortho*H_2-CO, there are many eigenfunctions Ψ which are composed of more than one significan I_Λ components, so that more than one set of $\{j_2 j_{12} l\}$ is relevant. We still will use the $\{j_2 j_{12} l\}$ set of the dominating component to denote the wave function. To fin out such components, one can use the values of the $\lambda(\Lambda)$ coefficien measuring the relative contribution of the basis function I_Λ,[7]

$$\lambda(\Lambda) = \frac{\sum_i f_\Lambda^2(R_i)}{\sum_i \sum_{\Lambda'} f_{\Lambda'}^2(R_i)}, \tag{18}$$

where i runs over all grid points used to evaluate the radial coefficien f_Λ[46,47] and Λ' runs over the components of the angular basis set.

It has been shown in Ref. 14 that to reproduce the experimental spectra of *para*H_2-CO one has to take into account the resonance states of this complex. An inclusion of resonance states in theoretical predictions is even more important for the *ortho*H_2-CO complex.[13] In this case, due to the nuclear symmetry of H_2, any state with the value of energy larger than the dissociation limit of $H_2(j_1 = 1)-$CO, is a resonance. Thus, this energy threshold, E_{thr}^{ortho}, is equal to twice the value of the rotational constant B for H_2, i.e., $E_{\text{thr}}^{ortho} = 118.644\ \text{cm}^{-1}$. The BOUND package, used for bound states, has been utilized also to fin resonance states. In each calculation, BOUND generates many discrete energy levels above the E_{thr}^{ortho} threshold and these levels generally represent the continuum states. Values of these levels vary when boundary conditions or angular basis sets are changed. Some of the levels, corresponding to the resonance states, remain relatively constant and can be identifie in this way. Such a simple approach is sometimes called the stabilization method. This method has an important advantage that the resonance states are treated in a consistent way with the bound states and the transition matrix elements for both types of states can be calculated using a simple procedure[48] interfaced with BOUND.

IV. EXPERIMENTAL METHODS

A. The infrared experiment

Details of the *para*H_2-CO and *ortho*H_2-CO infrared experiments performed at the temperatures $T = 49$ K and 47.5 K have been described previously.[6,13] Briefl , a mixture of CO and H_2 gas with a total pressure of a few Torr was contained in a long-path (200 m) low-temperature absorption cell. The cell was interfaced to a Bomem DA3.002 Fourier transform spectrometer, and spectra were recorded with a typical spectral resolution of 0.005 cm^{-1}. Nearly pure *para*H_2 (>99%) was prepared in a batch process by liquefying normal H_2 (75% ortho, 25% para) in the presence of a catalyst. A good approximation of the spectrum of *ortho*H_2-CO was obtained by subtracting a scaled *para*H_2-CO spectrum from one obtained using a normal H_2 plus CO mixture.

The low temperature (~1−2 K) infrared experiments for *ortho*H_2-CO were performed using a tunable infrared diode laser spectrometer to probe a pulsed supersonic jet expansion.[49] A typical gas mixture was 1% CO plus 15% normal H_2 in helium, but mixtures without helium were also used. The effective rotational temperatures were in the range of about 0.9−2.5 K, which means that the spectra were very sparse, in contrast to the rich 49 K spectrum. The results are important because they give information on the very lowest energy levels of *ortho*H_2-CO.

B. The microwave experiment

The microwave measurements for *ortho*H_2-CO in the frequency range of 80−150 GHz (2.67–5.00 cm^{-1}) were performed with the intracavity OROTRON spectrometer combined with a molecular jet expansion. A detailed description of the spectrometer can be found in Ref. 50.

Briefl , the millimeter-wave generator OROTRON is placed in a vacuum chamber together with the supersonic jet apparatus. In OROTRON, the millimeter-wave radiation is produced by interaction of an electron beam with the electromagnetic fiel of an open Fabry-Perot cavity which consists of movable spherical and fi ed plane mirrors with a periodical structure implanted on the surface of the latter. The high-vacuum part of the generator containing an electron beam source (cathode) and plane mirror (anode) is separated by a thin mica window from the remaining part of the resonator which is used as an absorption cell. The molecular jet enters into the resonator perpendicularly to its axis. A high Q-factor (~10^4) of the cavity results in 100 effective passes of the radiation through the jet. Absorption in the cavity causes changes of the electron current in the collector circuit placed beyond the periodical structure and is detected with high sensitivity by measuring these current changes. The frequency tuning of the OROTRON radiation is realized by movements of spherical mirror and corresponding adjustments of accelerating voltage for the electron beam. A small part of the radiation is taken out of the cavity through the coupling openings in a spherical mirror and mixed with the radiation of the microwave synthesizer for precise frequency determination.

In the present experiments, two OROTRON tubes were used to cover completely the 80−150 GHz frequency range with two very small gaps: 128.9−129.7 and 132.9−134.0 GHz. Generally, a gas mixture of 5% of CO in H_2 at backing pressure of 4−5 bar was used for the production of complexes. The gas mixture adiabatically expanded into the OROTRON cavity through the pulsed pin nozzle with an opening diameter of 1 mm operated at a repetition rate of 10−15 Hz. We estimate the rotational temperature of the jet at such conditions to be about 2−4 K.

The supplementary measurements in dilute gas mixture of CO (1%) and H_2 (5%) in helium (corresponding to a colder molecular jet) were made for the purpose of establishing the transitions originating from the lowest energy levels of *ortho*H_2−CO. In some cases, in order to distinguish closely located transitions belonging to two different spin modifi cations of the H_2−CO complex, an ortho-to-para converter was used, as described in a preceding microwave study of *para*H_2−CO.[9]

In addition to the H_2−CO lines, a lot of transitions of the CO dimer were also observed in the spectrum, but most of them could be easily separated from H_2−CO lines using frequency list of previous millimeter-wave surveys of $(CO)_2$.[51,52]

TABLE X. The positions (R_{min}) and values (E_{min}) of the global and local minima on the V_0 and V_1 surfaces and the corresponding values from V_{04}.[14] In addition, the values of the interaction energies at these minima, $E_{int,0}$ and $E_{int,1}$, computed *ab initio* with the same approach as used to generate the V_0 and V_1 surfaces. The energies $E'_{int,v}$ and $E^{best}_{int,v}$ have been calculated in the same way as $E_{int,v}$, but using larger basis sets, see footnotes. The distances are given in bohr and energies in cm^{-1}. The angle $\phi = 0°$.

	$(\theta_1,\theta_2)=(0°,180°)$		$(\theta_1,\theta_2)=(0°,0°)$	
	R_{min}	E_{min}	R'_{min}	E'_{min}
		$v=0$		
V_{04}	7.918	−93.049	7.171	−72.741
V_0	7.911	−94.096	7.168	−73.738
$E_{int,0}$		−94.077		−73.741
$E'_{int,0}$ [a]		−94.001		−73.789
$E^{best}_{int,0}$ [b]		−93.651		−73.929
		$v=1$		
V_1	7.925	−92.775	7.169	−74.769
$E_{int,1}$		−92.755		−74.787
$E'_{int,1}$ [a]		−92.694		−74.764
$E^{best}_{int,1}$ [b]		−92.414		−74.902

[a]Computed using the following levels of theory and basis sets for all f^c_{ij}: E^{HF}_{int}/aug-cc-pV5Z, $\delta E^{CCSD(T)}_{int}$/Q5/AE, $\delta E^{T(Q)}_{int}$/aug-cc-pVDZ/FC.
[b]Computed using the following levels of theory and basis sets for f^c_{00}: E^{HF}_{int}/6b69, $\delta E^{CCSD(T)}_{int}$/56b69/AE, $\delta E^{T(Q)}_{int}$/aug-cc-pVTZ/FC; and for f^c_{ij}, $i+j>0$: E^{HF}_{int}/5b69, $\delta E^{CCSD(T)}_{int}$/Q5b69/AE, $\delta E^{T(Q)}_{int}$/aug-cc-pVDZ/FC.

V. RESULTS AND DISCUSSION

A. Features of potential energy surface

We will analyze here the interaction energies at two most important points on PES, namely, at the global and local minima. The minimum geometries in Table X were obtained from our fits As expected, the geometries obtained from the V_0 potential are only negligibly different from those given by V_{04}. Since this is the f rst time the v-specifi surfaces have been obtained, it is interesting to compare V_0 and V_1 minima: V_1 has the global minimum 1.3 cm^{-1} shallower than V_0, whereas the secondary one is 1.0 cm^{-1} deeper. This means that the anisotropy of the PES changes qualitatively with v. Thus, differences in the patterns of the rovibrational energy levels calculated from the V_0 and V_1 surfaces should be related to this feature, as it will be discussed later.

Compared to V_{04}, the V_0 surface is deeper by about 1 cm^{-1} or 1% at both minima (however, this is not true for the whole surface, see below). Interestingly enough, the reasons for these nearly identical shifts are quite different. At the global minimum, V_{04} is too deep due to the overshooting of the DTmb CBS extrapolations at the CCSD(T) level, so at this level alone, our surface would have been shallower by about 1.6 cm^{-1}. However, the $\delta E^{T(Q)}_{int}$ term amounts to about −2.5 cm^{-1} at this point, which leads to the observed lowering. In contrast, the local minimum is at the orientation where the DTmb extrapolations worked well, and the lowering is due almost entirely due to the $\delta E^{T(Q)}_{int}$ term.

To check the quality of the f t at the positions of the global and local minima, we have calculated directly the interaction energy for the values of θ_1, θ_2, ϕ, and R corresponding to those positions, using the same level of approximation as in the calculations for the surface. The resulting energies $E_{int,v}$ are very close to the values of the energies obtained from the fit the discrepancies do not exceed 0.02 cm^{-1}, which shows the high quality of the f t (which will be discussed in more global way later on).

We have also included in Table X interaction energies computed at a higher level of theory than used for the whole surface. The quantities denoted by $E'_{int,v}$ were computed using the same level of theory and basis sets for f^c_{ij} with $i+j>0$ as for f^c_{00} and were properly averaged over the monomer vibrations. The improvement relative to $E_{int,v}$ is smaller than 0.08 cm^{-1}. Since it has been demonstrated in Sec. II C 3 that the reduced (relative to the calculations of f^c_{00}) quality of the basis set used to calculate f^c_{ij}, $i+j>0$, affects the results only slightly, by about 0.006 cm^{-1} at the global minimum, it is the inclusion of the $\delta E^{T(Q)}_{int}$ component in the calculation of $E'_{int,0}$ that is mainly responsible for the 0.08 cm^{-1} difference mentioned above.

Another quantity given in Table X is $E^{best}_{int,v}$, the interaction energy calculated using the same prescription as in the case of $E_{int,v}$, including averaging over the vibration of the monomers, but all the coefficient f^c_{ij}, including f^c_{00}, have been computed using the largest basis sets we could afford. Moreover, in the calculation of the $f^c_{ij}, i+j>0$, coeffi cients, the $\delta E^{T(Q)}_{int}$ component, computed in the frozen-core approximation for the aug-cc-pVDZ basis set, has been also taken into account. The comparison of $E^{best}_{int,v}$ and $E_{int,v}$ shows that the largest discrepancy amounts to about 0.4 cm^{-1}, with the global minimum shallower and the local one deeper (but only by about 0.2 cm^{-1}). The change at the global minimum is consistent with the estimated uncertainty due to all basis set effects equal to 0.5 cm^{-1}, as obtained earlier.

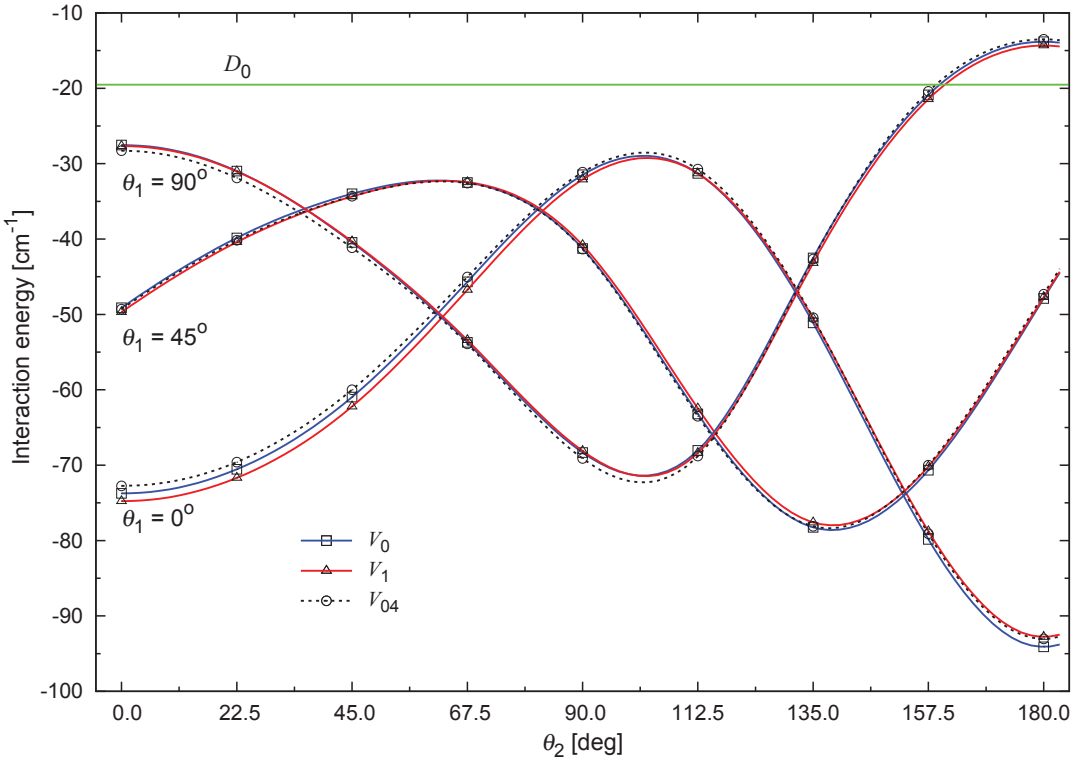

FIG. 1. Minimum-energy path for V_{04}, V_0, and V_1 PES's. For each value of θ_1, θ_2, and ϕ, the displayed interaction energy corresponds to the radial minimum in this angular configuration D_0 is the dissociation energy of V_0.

A broader picture of the PES is present in Fig. 1. We show there interaction energies at radial minima for various angular orientations. The $\theta_1 = 0°$ and 90° curves are symmetric in the range of θ_2 from 180° to 360°. The $\theta_1 = 45°$ curve is not, but it is fairly similar to that displayed. One can see that deepening of V_0 relative to V_{04} discussed above holds only for the $\theta_1 = 0°$ curve, for the two other curves the shifts can be in both directions. This is due the interplay of the anisotropy of the basis set truncation error in V_{04} and of $\delta E_{\rm int}^{\rm T(Q)}$, discussed above.

B. Rovibrational energies and spectra of *para*H_2-CO

1. Comparison of energy levels

The experimental *para*H_2-CO infrared spectrum has been measured and assigned in Ref. 6. The assignments allowed a deduction of the patterns of rovibrational energy levels of this complex for both $v = 0$ and $v = 1$ states of CO[6] which constitute a set of very reliable benchmarks for theory. Results of our calculations of these levels have been presented in Table S1 of Ref. 13. This table shows that the discrepancy between the calculated and empirical rovibrational energies vary from -0.011 cm^{-1} to 0.013 cm^{-1} for the $v = 0$ case and from -0.015 cm^{-1} to 0.009 cm^{-1} for $v = 1$. Thus, the maximum magnitude of the discrepancy is equal to 0.015 cm^{-1}. The root-mean-square errors (rmse) are equal to 0.006 cm^{-1} and 0.007 cm^{-1} for the $v = 0$ and $v = 1$ cases, respectively. These values can be compared to the previous most accurate theoretical results obtained with the V_{04} surface given in Ref. 16, where the maximum magnitude was 0.095 cm^{-1}, whereas the rmses were 0.05 cm^{-1} and 0.04 cm^{-1} for $v = 0$ and $v = 1$, respectively. Thus, the present surfaces provides a 6−8-fold improvement in accuracy of predictions.

2. Dissociation energies and virial coefficient

The calculated ground state energies give us also new theoretical values of the dissociation energies; 19.440 cm^{-1} and 19.616 cm^{-1} for $v = 0$ and $v = 1$, respectively. The difference between these values is the origin of the redshift of the $v = 1 \leftarrow 0$ vibrational transition in the CO molecule in complex with H_2 relative to an isolated CO. The calculated redshift amounts to -0.176 cm^{-1} and is in a very good agreement with the experimental value equal to -0.179 cm^{-1}.[6] It is important to note that the ability of current theory to predict this shift is due to our separate averaging of the six-dimensional surface over the CO $v = 0$ and 1 vibrations. Such averaging was not used in Ref. 14 and the dissociation energies given by the V_{04} surface, 19.527 cm^{-1} and 19.532 cm^{-1} for $v = 0$ and 1, respectively, do not contain information about the redshift (the tiny difference comes from the different rotational constants for CO in $v = 0$ and 1 states used in the rovibrational calculations).

One surprising feature of the dissociation energies given above is that the value from the V_0 surface is 0.09 cm^{-1} smaller than that from V_{04} despite the fact that V_0 is by 1 cm^{-1} deeper at both minima. This findin can be rationalized by analyzing Fig. 1. This figur shows that the lowest rovibrational level is located above most barriers on PES, therefore its wave function samples not only the local and

global minima, but a rather broad region of the configuratio space. In many such regions V_0 is actually above V_{04}, which explains the very small change of the dissociation energy.

The relatively small difference between the V_0 and V_1 dissociation energies is expected based on the different ordering of the two surfaces at the global and local minima. This is confirme by results shown in Fig. 1 where the two potentials produce minimum energy curves which are very close to each other and differ mostly near the minima.

Our dissociation energy is significantl different from the experimental estimate of 22 cm^{-1} given in Ref. 6. It was suggested in Ref. 14 that the experimental estimate is too high due to mistaking some resonances for bound states. The present set of authors upholds this opinion.

Another issue discussed in Ref. 14 was that in order to further improve agreement with experiment for the interaction second virial coefficient the V_{04} potential had to be scaled by a factor of 1.042. This fact, together with the difference between the experimental and theoretical dissociation energies, was suggestive that despite all the estimates based on basis-set and theory-level convergence patterns, the V_{04} potential was by about 2−4 cm^{-1} too shallow. The calculations and estimates of the present work show that this was not the case.

The present PES gives practically the same interaction second virial coefficient as V_{04}. At $T = 77.30$ K, our value is −64.346 cm^3/mol, whereas the value from V_{04} is −64.283 cm^3/mol. The agreement with the experimental value from Ref. 53, equal to -73 ± 5 cm^3/mol, improved negligibly. For other temperatures, the V_0 and V_{04} values of the virial coefficient are within 0.015 cm^3/mol of each other. Therefore, a scaling of V_0 would also improve agreement with experiment. However, we now believe that the remaining discrepancies with experiment are not due to inaccuracies of PES. As Fig. 3 of Ref. 14 shows, the V_{04} predictions are well within experimental error bars for $T > 100$ K and only the experimental value at $T = 77.30$ K is about two sigma below the theoretical prediction. Most likely the reason is that the theoretical value was computed at a semiclassical level which includes only leading order quantum corrections. As shown for the H_2–H_2 dimer in Ref. 54, at 75 K the fully quantum result is by a factor 1.25 larger in magnitude than the semiclassical one.

Very recently, Chefdeville *et al.*[55] studied both theoretically and experimentally low-energy resonances in *para*H_2−CO scattering. Theoretical work used the V_{04} potential and to achieve agreement with experiment, the authors had to scale the surface by a factor of 1.05. In view of our current results, such scaling cannot be justifie and there must be other reasons for the discrepancies between theory and experiment.

3. Theoretical spectra

Although the accuracy of our potential has been already critically evaluated by comparisons to empirical energy levels and to the redshift, direct comparisons the theoretical and experimental *para*H_2−CO spectra will be useful for our goal of assigning the spectra of *ortho*H_2−CO. To calculate the intensities, the rovibrational wave functions computed by BOUND were used in a procedure developed in the group of one of us (P.J.)[48] to calculate the matrix elements of the dipole moment operator of the complex. This dipole moment was approximated by the dipole moment of the CO molecule, so that the comparison of spectra can be treated also as a test of reliability of this assumption.

To make comparison with the observed spectra easier, the computed "stick" spectrum has been transferred into a continuous one by replacing each transition by a Lorentzian-shape function of frequency. A single empirical parameter definin the half-width was used in this transformation. It was obtained by fittin the Lorentzian function to a selected set of well-isolated experimental lines assigned as bound-bound transitions. The integral under each Lorentzian curve was made equal to the calculated value of intensity.

To obtain the theoretical infrared spectrum, an energy equal to 2143.272 cm^{-1}, corresponding to the band origin $Q_1(0)$ in an *isolated* CO molecule, should be added to all theoretical transition energies computed as differences between the rovibrational energy levels from the V_1 and V_0 potentials. Since the redshifts are already included in these differences, this procedure leads to complete agreement with observed line frequencies. However, to make the energy scale of the figur easier to read, we have applied the *reverse* procedure and have subtracted the energy of 2143.272 cm^{-1} from the experimental transition frequencies. Since both experimental and theoretical intensities are relative ones, we have normalized both spectra to have intensities equal to 1 at 3.04 cm^{-1}.

4. Comparison of theoretical and experimental spectra

The computed infrared spectrum for *para*H_2−CO was already compared to the experimental data[6] in Fig. S1 of Ref. 13. In the present work, we have enhanced this comparison by extending the range of experimental frequencies relative to that shown in Fig. S1 of Ref. 13, which included only spectra taken in Ref. 6 at the gas pressure of 3.5 Torr at 49 K. Another spectrum published in Ref. 6 was recorded at 1.1 Torr and 47.5 K. The latter spectrum has a worse signal to noise ratio than the former one, but also narrower lines. Furthermore, the latter spectrum partly fill the gaps in the former one in the regions where *para*H_2−CO transitions are obscured by the strong $^{12}C^{16}O$ monomer absorption lines. Moreover, transitions in the vicinity of these gaps are sometimes distorted. The widths of the gaps depend on pressure and in lower pressures new lines of the complex are revealed. Thus, we have supplemented the 3.5 Torr spectrum by the 1.1 Torr one by fillin the gaps and replacing the lines from the former spectrum by those from the latter one in a narrow region around each gap. The resulting combined spectrum is presented in Fig. 2. The two spectra are distinguished by different colors. One can see in the plot that the 1.1 Torr transitions provide information in quite a few regions of energy not available in the higher pressure measurements.

As one can see in Fig. 2, the predicted spectrum is stunningly close to the experimental one. To achieve such an agreement, it was critical to compute resonance states. The

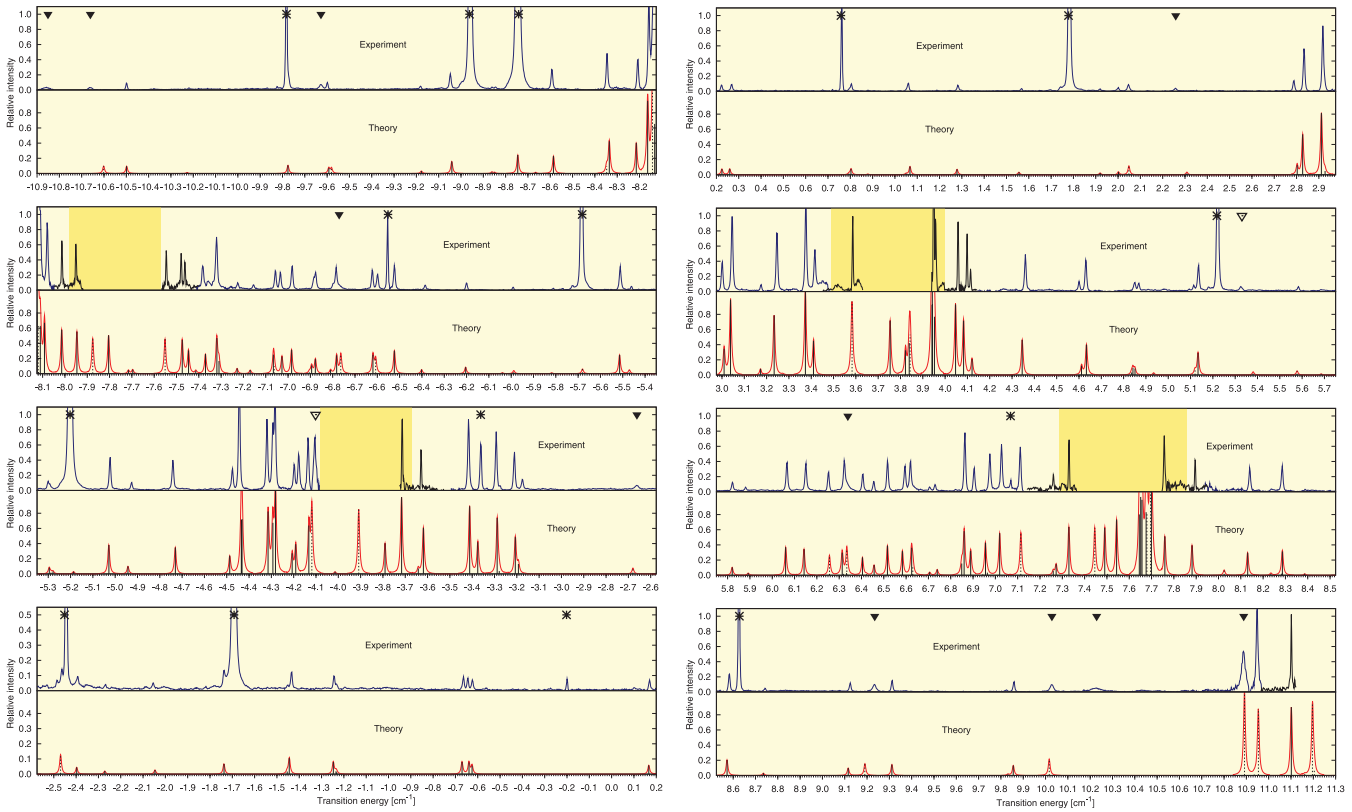

FIG. 2. Comparison of the infrared spectra of *para*H_2–CO calculated from the V_0 and V_1 surfaces for $T = 49$ K (bottom part of each panel) with the experimental data from Ref. 6 (upper part). The experimental spectrum is shifted by the value of the $v = 1 \leftarrow 0$ transition in the isolated CO equal to 2143.272 cm^{-1}. The experimental spectrum recorded at the gas pressure of 3.5 Torr and $T = 49$ K (blue line) was merged with the spectrum recorded at 1.1 Torr and 47.5 K (black line). The dashed lines on the theoretical side of the plot denote transitions which involve at least one resonance state. Transitions indicated by full triangles have not been assigned in Ref. 6. Open triangles mark the transitions not considered before and assigned in the present paper. The calculated transitions with relative intensities larger than 0.01 are plotted. The yellow rectangles indicate gaps in the experimental data at 3.5 Torr and 49 K due to the strong CO monomer lines: $P(2)$, $P(1)$, $R(0)$, and $R(1)$, whereas the transition indicated by asterisks are the R-branch transitions of the $^{13}C^{16}O$, $^{12}C^{17}O$, and $^{12}C^{18}O$ isotopologues in natural abundance.

transitions marked by dashed lines indicate involvement of at least one resonance state. In the case of such transitions, the theoretical widths do not always match the experimental counterparts. This indicates that the resonance state is wider than the average discrete transitions width used by us. The method used by us for identifying resonance states does not allow a rigorous computation of their widths, however, approximate widths can be obtained by observing the changes of the resonant energy levels upon variations of stabilization parameters. Such approximate widths are roughly in agreement with the experimental ones. The shapes of the two spectra shown in Fig. 2 are very similar, which demonstrates that the approximations used in calculations of intensities work very well.

5. New assignments

There are a few *para*H_2−CO spectral lines that have been recorded but not assigned in Ref. 6. These transitions are marked with the full triangles in Fig. 2. Since the lines are rather wide, these transitions must involve at least one resonance state. Since resonances that wide were not considered in the previous work, we have performed a new search for resonances in the range of energies up to 15 cm^{-1}. Compared to an analogous search done in Ref. 14, we have appropriately relaxed the criterion deciding whether a resonance is found or not. In addition to the resonances identifie in Ref. 14 and later recomputed more accurately in Ref. 13 (see Table S1), a few new ones have been found. Their energies are listed in Table XI, accompanied by information about the structure of the related wave functions. The transitions involving these states have already been taken into account in the theoretical part of Fig. 2 and the analysis of this figur enables assignment of most of the transitions not assigned earlier. Moreover, two other transitions not considered earlier, marked with open triangles, have been assigned. The results are presented in Table XII. The maximum difference between the observed and calculated transitions analysed in previous studies was equal to 0.021 cm^{-1} and the rmse for all those transitions amounted to 0.008 cm^{-1}. In the case of some of new lines, the differences are much larger, up to 0.06 cm^{-1} in the worst case. This fact is most likely caused by an inaccuracy in calculations of the positions of the new, wide resonance states. Our procedure of computing such resonance levels does not allow us to determine these levels as precisely as for the bound states or narrow resonances. Concluding, ten new infrared transitions have been assigned, but there are still two transitions that remain unassigned.

TABLE XI. Calculated values of the new resonance states for the *para*H_2−CO complex. The $\mathcal{E}_v$ (E_v) energies (in cm^{-1}) are calculated for the $v = 0$ and 1 vibrational states of CO and are given relatively to the dissociation limit (ground rovibrational level). The corresponding energies in the two sets differ therefore by −19.440 and −19.616 cm^{-1} for $v = 0$ and 1, respectively. $n_{J,P}$ is a consecutive number of the state for the given values of J and P. Other symbols are define in the text.

$n_{J,P}$	J^P	j_2	l	λ(Λ)	$\mathcal{E}_0$	E_0	λ(Λ)	$\mathcal{E}_1$	E_1
6	2^e	1	1	0.40	3.538	22.977	0.49	3.408	23.024
		3	1	0.09			0.16		
		0	2	0.28			0.21		
		2	4	0.21			0.13		
3	4^f	3	2	0.54	6.151	25.590	0.91	5.833	25.449
		1	4	0.43			0.06		
5	4^e	2	4	0.80	1.955	21.394	0.86	1.717	21.333
		0	4	0.15			0.10		
6	4^e	3	1	0.74	4.714	24.154	0.81	4.385	24.001
		1	3	0.20			0.13		
1	7^e	1	6	0.83	5.463	24.902	0.45	5.342	24.958
		0	7	0.13			0.53		

TABLE XII. The list of the experimental values of the infrared transitions, ΔE_{obs}, in the *para*H_2–CO complex which have been recorded but not assigned in Ref. 6. Here an assignment of these transitions is proposed based on theoretical results. The symbol $\Delta E'_{obs}$ denotes the experimental transition energies given relative to the $v = 1 \leftarrow 0$ transition in the isolated CO equal to 2143.272 cm^{-1}. These energies are compared with the ΔE_{theo} theoretical energies. The lower and upper states involved in the transitions are numbered with the set of parameters (J, P, $n_{J,P}$). The unit of energy is cm^{-1}.

ΔE_{obs}	$\Delta E'_{obs}$	Upper	Lower	ΔE_{theo}	$\Delta E'_{obs} - \Delta E_{theo}$
2132.42	− 10.852				
2132.61	− 10.662	(4,*e*,3)	(4,*f*,3)[a]	− 10.601	− 0.061
2133.6433	− 9.6287	(1,*e*,4)	(2,*e*,6)[a]	− 9.581	− 0.048
2136.50	− 6.772	(3,*e*,4)	(4,*e*,5)[a]	− 6.764	− 0.008
2139.1660	− 4.1020	(6,*e*,2)	(7,*e*,1)[a]	− 4.119	0.017
2140.6093	− 2.6627	(6,*e*,3)	(7,*e*,1)[a]	− 2.680	0.017
2145.5294	2.2574	(7,*e*,1)[a]	(6,*e*,3)	2.308	− 0.033
2148.597	5.325	(7,*e*,1)[a]	(6,*e*,1)	5.380	− 0.055
2149.61	6.338	(4,*e*,5)[a]	(3,*e*,4)	6.334	0.004
2152.5054	9.2334	(2,*e*,6)[a]	(1,*e*,4)	9.190	0.043
2153.2995	10.0275	(4,*f*,3)[a]	(4,*e*,3)	10.017	0.011
2153.50	10.228				
2154.1590	10.8870	(4,*e*,6)[a]	(3,*e*,3)	10.892	− 0.005

[a]New resonance state found in this work, see Table XI.

C. Infrared spectra of *ortho*H_2−CO

1. 49 K spectrum

In Ref. 13, a new experimental infrared spectrum of the *ortho*H_2−CO complex in the region of the CO fundamental band has been presented. This spectrum has been recorded earlier but remained unpublished since, as discussed in the Introduction, it was impossible to assign it on the basis of experiment due to the fact that it is congested and without obvious spectral patterns. To solve this problem, the theoretical infrared spectrum for *ortho*H_2−CO has been generated using

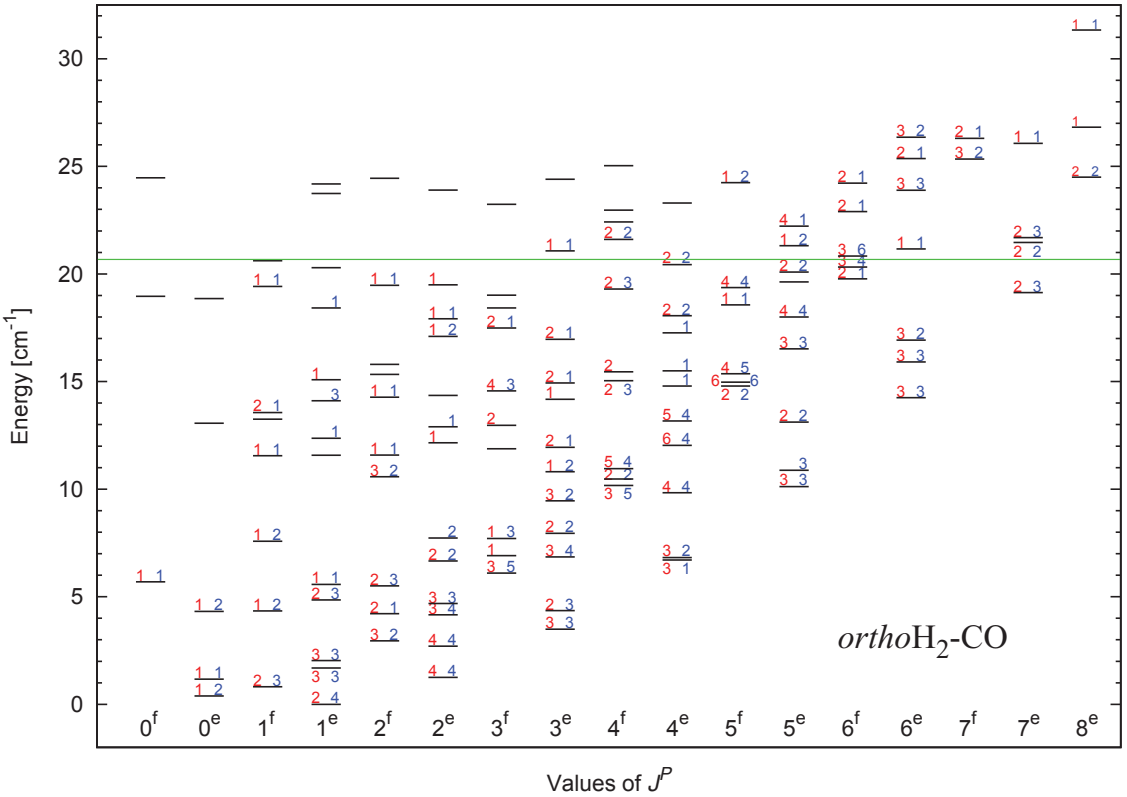

FIG. 3. Energy levels of *ortho*H_2−CO computed from the V_0 surface (V_1 levels would be almost indistinguishable). The energies are given relative to the energy of the lowest rovibrational state lying 97.967 cm^{-1} above the dissociation limit of *para*H_2−CO. The green line corresponds to the *ortho*H_2−CO dissociation threshold at 118.644 cm^{-1} above the dissociation limit of *para*H_2−CO. The numbers indicate how many times a particular state is present in the transitions assigned in Ref. 13. The left-hand-side (red) number corresponds to the V_0 surface, while the right-hand-side (blue) number corresponds to V_1.

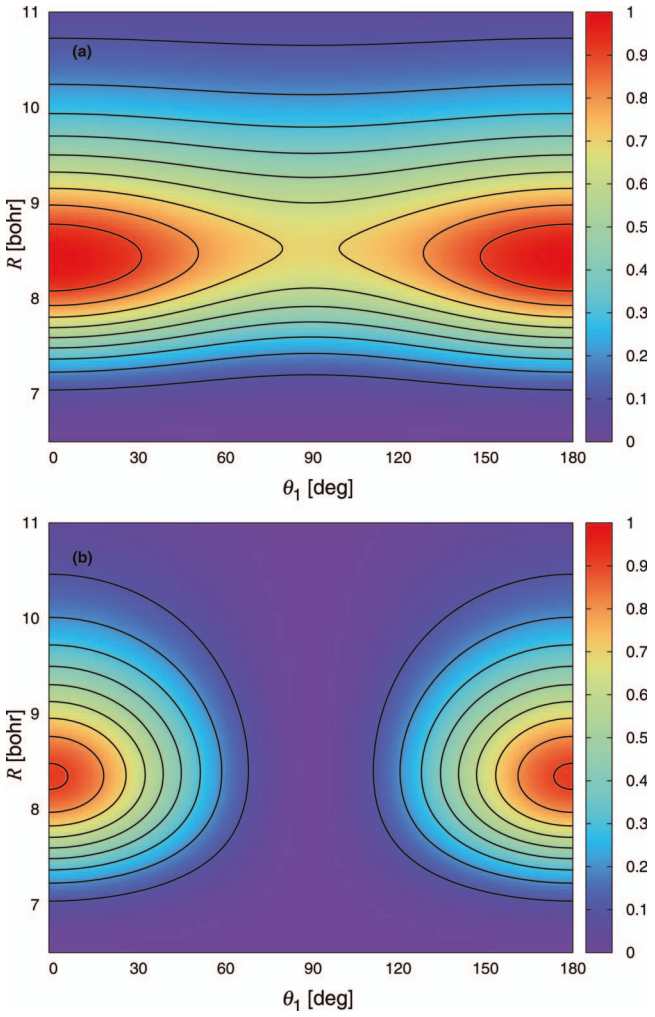

FIG. 4. Contour plot of the (R, θ_1) dependence of the square of the rovibrational wave function $|\Psi|^2$. Panels (a) and (b) correspond to the ground rovibrational states of the *para*H_2-CO and *ortho*H_2-CO systems, respectively. The remaining variables are set to $\theta_2 = 180^\circ$ and $\phi = 0^\circ$. The largest amplitude of $|\Psi|^2$ in each panel is set to 1.

the V_0 and V_1 surfaces. The comparison of this spectrum to the experimental one has enabled an assignment of most of the spectral lines.[13] The largest discrepancy between experimental and theoretical line positions was 0.06 cm^{-1}, while rmse was equal to 0.017 cm^{-1}. It has been also possible to explain some subtle features of the spectra, including a key role of the resonance states. For several lines, only theory can show that a given transition involves one or two resonance states. In particular, one can fin if a broad line is a superposition of several transitions or the width results from a resonance character.

2. Energy-level diagram

Although the spectrum of *ortho*H_2-CO has been assigned in Ref. 13, it was not possible to determine an experimental diagram of energy levels for this system in the same way as it was done for *para*H_2-CO in Ref. 6. Since the line positions in the experimental spectrum of *ortho*H_2-CO have been measured with the same accuracy as for *para*H_2-CO, the experimental energy levels could potentially be determined with an accuracy better 0.001 cm^{-1}, surpassing the accuracy of theoretical values. In the present work, we tried again to deduce such a diagram using the additional information from the 2 K infrared and from the microwave spectra that will be described below. Unfortunately, this task could not be completed. To see why, we show in Fig. 3 the

TABLE XIII. The values of the experimental transition energies, $\Delta E_{\text{cold, obs}}$, for the *ortho*$H_2-$CO complex measured at $T = 2$ K and the assignment of these transitions made by comparisons with the theoretical predictions, ΔE_{theo}. The $\Delta E'_{\text{cold,obs}}$ symbol denotes the experimental transition energies given relative to the $v = 1 \leftarrow 0$ transition in the isolated CO equal to 2143.272 cm^{-1}. Transitions which have not been observed in the 49 K infrared spectrum are denoted by asterisks. The lower and upper states involved in the transitions are numbered with the set of parameters $(J, P, n_{J,P})$. The unit of energy is cm^{-1}.

$\Delta E_{\text{cold,obs}}$	$\Delta E'_{\text{cold,obs}}$	Upper	Lower	ΔE_{theo}	$\Delta E'_{\text{cold,obs}} - \Delta E_{\text{theo}}$
2144.4320	1.1600	(1,e,2)	(0,e,1)	1.2058	0.046
2145.6058	2.3338	(2,e,3)	(1,e,2)	2.3596	− 0.026
2145.7229	2.4509	(2,e,4)	(1,e,3)	2.4222	0.029
2145.8462	2.5742	(2,e,2)	(1,e,1)	2.5674	0.007
2146.0650	2.7930	(2,f,2)	(2,e,1)	2.7912	0.002
2146.2500	2.9780	(3,e,2)	(2,e,1)	2.9635	0.015
2146.4984	3.2264	(2,f,2)	(1,f,1)	3.2228*	0.004
2146.5056	3.2336	(4,e,2)	(3,e,1)	3.2029	0.031
2146.5186	3.2466	(3,f,2)	(3,e,1)	3.2423*	0.004
2147.1145	3.8425	(1,e,4)	(1,f,1)	3.8328*	0.010
2147.3244	4.0524	(3,e,3)	(2,e,2)	4.0465*	0.006
2147.3470	4.0750	(2,f,3)	(2,e,1)	4.0649*	0.010
2147.4200	4.1480	(1,f,2)	(1,e,1)	4.1381	0.010
2147.4343	4.1623	(0,e,3)	(1,e,1)	4.1467*	0.016
2147.5300	4.2580	(1,e,4)	(0,e,1)	4.2652	− 0.007
2147.7163	4.4443	(2,e,5)	(1,e,3)	4.4219	0.022
2147.7222	4.4502	(2,e,4)	(1,e,1)	4.4583*	− 0.008
2147.7337	4.4617	(1,f,3)	(2,f,1)	4.4349*	0.027
2147.7798	4.5078	(2,f,3)	(1,f,1)	4.4965	0.011
2147.8521	4.5801	(3,f,3)	(2,f,1)	4.5688	0.011
2147.9773	4.7053	(0,f,1)	(1,f,1)	4.6955*	0.010

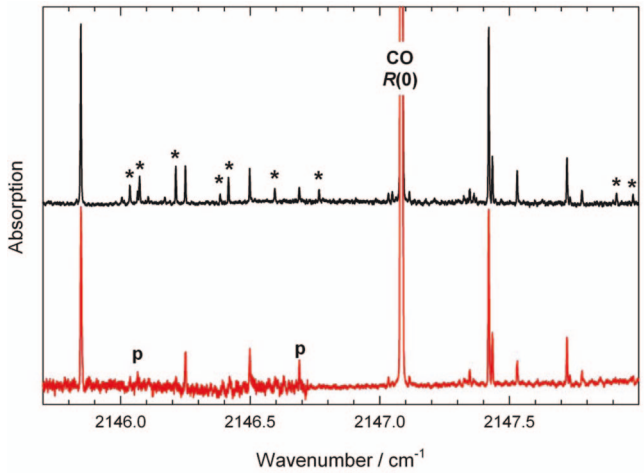

FIG. 5. Part of an experimental infrared supersonic jet spectrum of *ortho*H_2-CO in the region around the CO monomer $R(0)$ line (jet backing pressure 14 atm, jet temperature −30 °C). Asterisks indicate CO dimer transitions,[56] and "p" indicates *para*H_2-CO transitions. The remaining lines are due to *ortho*H_2-CO, notably the strong transitions near 2145.85 and 2147.42 cm^{-1}. The lower trace was obtained with a more dilute gas mixture (less CO), which reduces the CO dimer contribution. Comparison with theory indicates an effective rotational temperature of about 0.9 K for both spectra.

TABLE XIV. The theoretical microwave transition energies, ΔE_{theo}, for the *ortho*H_2-CO complex, computed from the V_0 surface. The intensities calculated at $T = 2$ K are listed in the column denoted by I_{theo} and are given relative to the strongest one whose intensity is set to one. The transitions with $I_{\text{theo}} \geq 0.01$ are given with one exception indicated by an asterisk. The lower and upper states involved in the transitions are numbered with the set of parameters $(J, P, n_{J,P})$. The unit of energy is cm^{-1}.

Upper	Lower	ΔE_{theo}	I_{theo}	Upper	Lower	ΔE_{theo}	I_{theo}
(1,e,3)	(0,e,2)	0.866	0.023	(3,e,3)	(2,e,1)	5.597	0.049
(1,e,2)	(1,f,1)	0.867	0.028	(1,f,4)	(0,f,1)	5.862	0.015
(0,e,2)	(1,e,1)	1.171	0.017	(1,f,3)	(1,e,2)	5.890	0.027
(1,e,3)	(1,f,1)	1.217	0.016	(5,e,3)	(4,e,2)	6.290	0.047
(1,e,2)	(0,e,1)	1.299	0.047	(4,e,5)	(3,e,3)	6.319	0.016
(2,e,4)	(2,f,1)	1.730	0.047	(4,e,3)	(3,e,1)	6.337	0.011
(2,e,3)	(1,e,2)	2.471	0.161	(2,f,4)	(2,e,3)	6.422	0.030
(2,e,4)	(1,e,3)	2.647	0.078	(2,e,7)	(1,e,5)	6.584	0.011
(2,e,2)	(1,e,1)	2.701	0.804	(2,e,7)	(2,f,3)	6.648	0.010
(2,f,2)	(2,e,1)	2.966	0.177	(2,e,5)	(1,e,1)	6.665	0.011
(3,e,2)	(2,e,1)	3.102	0.622	(3,e,4)	(2,e,1)	6.698	0.050
(4,e,2)	(3,e,1)	3.330	0.176	(1,e,6)	(1,f,2)	7.239	0.025
(2,f,2)	(1,f,1)	3.397	0.501	(2,f,5)	(1,f,2)	7.247	0.116
(3,f,2)	(3,e,1)	3.413	0.089	(1,e,6)	(0,e,3)	7.256	0.019
(5,e,1)	(4,e,1)	3.415	0.023	(3,e,7)	(2,e,4)	7.260	0.103
(2,e,5)	(2,f,1)	3.711	0.055	(2,e,7)	(1,e,4)	7.303	0.035
(4,f,2)	(4,e,1)	3.766	0.018	(2,e,8)	(2,f,3)	7.392	0.023
(3,e,4)	(2,e,3)	3.792	0.025	(3,f,5)	(2,f,3)	7.456	0.076
(3,f,2)	(2,f,1)	3.955	0.108	(0,e,4)	(1,e,5)	7.488	0.014
(1,e,4)	(1,f,1)	4.035	0.220	(3,e,8)	(2,e,5)	7.509	0.021
(3,e,6)	(4,e,1)	4.102	0.017	(3,f,4)	(3,e,2)	7.527	0.018
(3,e,3)	(2,e,2)	4.147	0.251	(4,e,7)	(3,e,4)	7.552	0.013
(2,e,3)	(1,e,1)	4.157	0.138	(3,f,4)	(2,f,2)	7.664	0.215
(3,f,3)	(3,e,1)	4.216	0.084	(1,f,5)	(1,e,5)	7.679	0.027
(2,e,6)	(3,e,1)	4.236	0.126	(4,e,4)	(3,e,2)	7.683	0.012
(4,f,3)	(4,e,1)	4.250	0.004*	(2,e,6)	(1,e,1)	7.730	0.020
(2,f,3)	(2,e,1)	4.258	0.454	(4,f,5)	(3,f,3)	7.746	0.020
(0,e,3)	(1,e,1)	4.322	0.301	(3,e,7)	(2,e,3)	7.787	0.035
(1,e,5)	(2,e,1)	4.323	0.386	(2,e,7)	(2,f,2)	7.941	0.025
(1,f,2)	(1,e,1)	4.339	1.000	(1,e,7)	(1,f,2)	8.025	0.020
(1,e,4)	(0,e,1)	4.467	0.529	(1,e,7)	(0,e,3)	8.042	0.037
(1,f,3)	(2,f,1)	4.623	0.071	(2,e,8)	(1,e,4)	8.047	0.074
(2,e,5)	(1,e,3)	4.628	0.268	(4,f,4)	(3,f,2)	8.134	0.024
(2,e,4)	(1,e,1)	4.683	0.197	(4,f,4)	(4,e,2)	8.218	0.014
(2,f,3)	(1,f,1)	4.690	0.312	(3,e,9)	(2,e,5)	8.273	0.020
(3,f,3)	(2,f,1)	4.757	0.162	(4,f,5)	(3,f,2)	8.548	0.010
(3,e,5)	(2,e,4)	4.771	0.011	(3,f,5)	(3,e,2)	8.613	0.058
(4,f,3)	(3,f,1)	4.857	0.033	(1,e,6)	(2,e,2)	8.877	0.012
(0,f,1)	(1,f,1)	4.875	0.177	(2,f,5)	(2,e,2)	8.885	0.149
(2,e,5)	(1,e,2)	4.979	0.088	(3,e,7)	(2,e,2)	9.242	0.110
(4,e,4)	(3,e,3)	5.187	0.013	(3,e,8)	(2,e,4)	9.490	0.016
(3,e,4)	(2,e,2)	5.247	0.028	(1,f,4)	(1,e,3)	9.520	0.081
(3,e,5)	(2,e,3)	5.298	0.096	(2,f,6)	(2,e,4)	9.592	0.028
(4,e,3)	(3,e,2)	5.479	0.169	(1,f,4)	(1,e,2)	9.870	0.117
(1,f,3)	(1,e,3)	5.540	0.064	(1,e,8)	(2,e,3)	9.948	0.020

theoretical rovibrational energy level diagram calculated from V_0 and given relative to the ground rovibrational state (an analogous diagram for V_1 would be almost indistinguishable). The numbers next to the levels indicate how many times a given state was involved in the observed experimental transitions. As one can see, some of the levels are not involved at all, while many other ones are involved in only one transition. If the recorded transitions were marked by arrows, there would be groups of well connected levels separated from other such groups (this separation is unrelated to any symmetries). Thus, even with the assigned experimental spectrum of *ortho*H_2-CO, it has not been possible to deduce a pattern of energy levels. One may ask why such an assignment was possible for *para*H_2-CO. At the same range of energies, there are about three times more levels in the *ortho* than in the *para* case, consistent with the fact that the former spectrum is more congested than the latter. Thus, it is the congestion of spectral lines that makes positive line assignments more difficult Moreover, some weak but important for deduction of the diagram transitions could be masked by stronger transitions or very close transitions with similar intensities can appear as a single line.

The lowest energy level in Fig. 3 corresponds to the dissociation energy of 20.677 cm^{-1}, whereas the value for the V_1 surface is 20.855 cm^{-1}, i.e., the redshift is 0.178 cm^{-1}. Thus, the dissociation energies are somewhat larger than for *para*H_2-CO. The reasons are illustrated in Fig. 4, where the squares of the ground-state rovibrational wave functions for the *para*H_2-CO and *ortho*H_2-CO complexes are plotted. In the case of *para*H_2-CO, the wave function probes fairly uniformly all values of θ_1 for a given value of R, which reflect the nearly spherical character of the motion of H_2 in this complex. On the other hand, for *ortho*H_2-CO the probability is distributed much less uniformly and is the largest for $\theta_1 = 0^\circ$ (and for symmetry equivalent $\theta_1 = 180^\circ$). This means that the H_2 molecule in *ortho*H_2-CO is preferentially oriented along the intermolecular axis, where both the global and local minima are located, which explains the relations between dissociation energies.

3. Low-temperature spectrum

To facilitate determination of rovibrational energy levels from measured *ortho*H_2-CO spectra (which eventually turned out to be not possible) and to help in interpretation of the microwave measurements, we have performed new measurements for this complex for a few temperatures in the range $1 - 2$ K, as described in Sec. IV A. The measured line positions from the spectrum at $T = 2$ K are listed in Table XIII, whereas a portion of the spectrum recorded at $T = 0.9$ K is plotted in Fig. 5. Some of these transitions have been identifie earlier in the 49 K spectrum[13] and the present assignment can be regarded as a confirmatio of previous findings There are also nine transitions not present in previous assignments. This is mainly due to the fact that whereas the position of the spectral lines are the same for $T = 2$ K and 49 K, their intensities are completely different, so some new lines become visible at 2 K.

Comparison with theory indicates that the effective rotational temperature of the spectrum shown in Fig. 5 is about 0.9 K. During the experiments, it was possible to vary this temperature to some extent by varying the supersonic jet backing pressure and gas mixture. In doing so, it was noted that the neighboring *ortho*H_2-CO lines at 2147.420, 2147.434, and 2147.722 cm^{-1} maintained the same relative

TABLE XV. The transition energies from the microwave experiment, ΔE_{obs}^{MW}, for the *ortho*H_2-CO complex and the assignment of these transitions based on theoretical predictions. The observed intensities are listed in the column denoted by I_{obs} and are graded as very weak (vw), weak (w), medium (m), strong (s), and very strong (vs). The lower and upper states involved in the transitions are numbered with the set of parameters (J, P, $n_{J,P}$). The unit of energy is cm^{-1} except as marked.

No.	ΔE_{obs}^{MW} [MHz]	ΔE_{obs}^{MW}	I_{obs}	ΔE_{theo}^{MW}	$\Delta E_{obs}^{MW} - \Delta E_{theo}^{MW}$	Upper	Lower
1	81458.670	2.7172	vs	2.701	0.016	(2,e,2)	(1,e,1)
2	88927.184	2.9663	m	2.966	0.000	(2,f,2)	(2,e,1)
3	93433.726	3.1166	vs	3.102	0.015	(3,e,2)	(2,e,1)
4	100046.231	3.3372	w	3.330	0.007	(4,e,2)	(3,e,1)
5	101907.919	3.3993	vs	3.397	0.002	(2,f,2)	(1,f,1)
6	102834.948	3.4302	vw	3.413	0.017	(3,f,2)	(3,e,1)
7	103050.997	3.4374	vw	3.415	0.022	(5,e,1)	(4,e,1)
8	111273.612	3.7117	w	3.711	0.001	(2,e,5)	(2,f,1)
9	118970.850	3.9685	vw	3.955	0.013	(3,f,2)	(2,f,1)
10	121112.241	4.0399	s	4.035	0.005	(1,e,4)	(1,f,1)
11	124423.440	4.1503	m	4.147	0.003	(3,e,3)	(2,e,2)
12	124979.930	4.1689	w	4.157	0.012	(2,e,3)	(1,e,1)
13	126576.145	4.2221	w	4.216	0.006	(3,f,3)	(3,e,1)
14	127194.190	4.2428	w	4.236	0.007	(2,e,6)	(3,e,1)
15*	127472.980	4.2520	vw	4.250	0.002	(4,f,3)	(4,e,1)
16	127914.461	4.2668	s	4.258	0.009	(2,f,3)	(2,e,1)
17	129731.438	4.3274	m	4.322	0.005	(0,e,3)	(1,e,1)
18	129811.128	4.3300	m	4.323	0.007	(1,e,5)	(2,e,1)
19	130350.560	4.3480	vs	4.339	0.009	(1,f,2)	(1,e,1)
20	133575.990	4.4556	s	4.467	−0.011	(1,e,4)	(0,e,1)
21	138873.887	4.6323	w	4.623	0.009	(1,f,3)	(2,f,1)
22	139771.406	4.6623	m	4.628	0.034	(2,e,5)	(1,e,3)
23	139913.740	4.6670	s	4.683	−0.016	(2,e,4)	(1,e,1)
24	140895.328	4.6998	m	4.690	0.010	(2,f,3)	(1,f,1)
25	146393.470	4.8832	m	4.875	0.008	(0,f,1)	(1,f,1)
26	147791.500	4.9298	w	4.979	−0.049	(2,e,5)	(1,e,2)

intensities, suggesting that these lines originate in the same lower state level. This indeed turns out to be the case (see Table XIII), and the level in question is in fact the lowest rotational level of *ortho*H_2-CO, denoted as (1,e,1). The strong line at 2145.846 cm^{-1} also originates from the same lower state level, but this fact was not so evident in the experiments because of its distance from the other three, which meant that it could not be observed in the same laser scan. A complete list of all assigned experimental transitions obtained from the infrared experiments on *ortho*H_2-CO performed at $T = 49$ K[13] and $T \approx 1$–2 K is given in the supplementary material.[57] The $T \approx 1$–2 K spectrum will be further discussed and compared to theoretical and microwave spectra in Sec. V D.

D. Microwave spectra of *ortho*H_2-CO

The microwave spectra can provide even more accurate values of transition energies than the infrared ones. Similarly as the latter ones, the microwave spectra of the *ortho*H_2-CO complex are impossible to assign based on experiment alone. In fact, the microwave assignments are, in general, even more difficul than infrared ones. In the case of *para*H_2-CO, the microwave spectra were assigned[8,9] based on the infrared experiment of Ref. 6. In the present paper, the interpretation of the microwave spectra for *ortho*H_2-CO has been achieved based mainly on theoretical spectra. The rovibrational calculations have been performed using the V_0 interaction energy surface and the spectra generated at $T = 2$ K. The list of computed transition energies in the range from 0 to 10 cm^{-1} with relative intensities larger than 0.01 is presented in Table XIV. The experimental transition energies from 2.5 to 5 cm^{-1} are given in Table XV and compared to theoretical values (only theoretical lines paired to the corresponding experimental ones are given). All these energies are also shown as the stick spectra in the top panel of Fig. 6 (here all theoretical lines are shown, the paired ones are numbered). The relative intensities of the measured microwave transitions are difficul to determine precisely and thus only a f ve-grade scale is used to defin them (see Table XV) and the assumed numerical heights are define in the captions of Fig. 6.

A direct comparison of the microwave transitions to the infrared ones is not possible because the latter ones involve two different sets of rovibrational states. Even after the subtraction of the $v = 1 \leftarrow 0$ frequency in the isolated CO, the infrared transitions differ from the microwave ones by redshifts which are slightly different for each pair of levels. However, similarities in the spectra are sufficientl strong to fin correlations, in particular if theoretical information is used. Since the experimental microwave lines can be directly related to theoretical microwave ones (i.e., computed using only the V_0 surface), if theoretical accuracy is sufficien to correlate lines, the theoretical information can be used to select

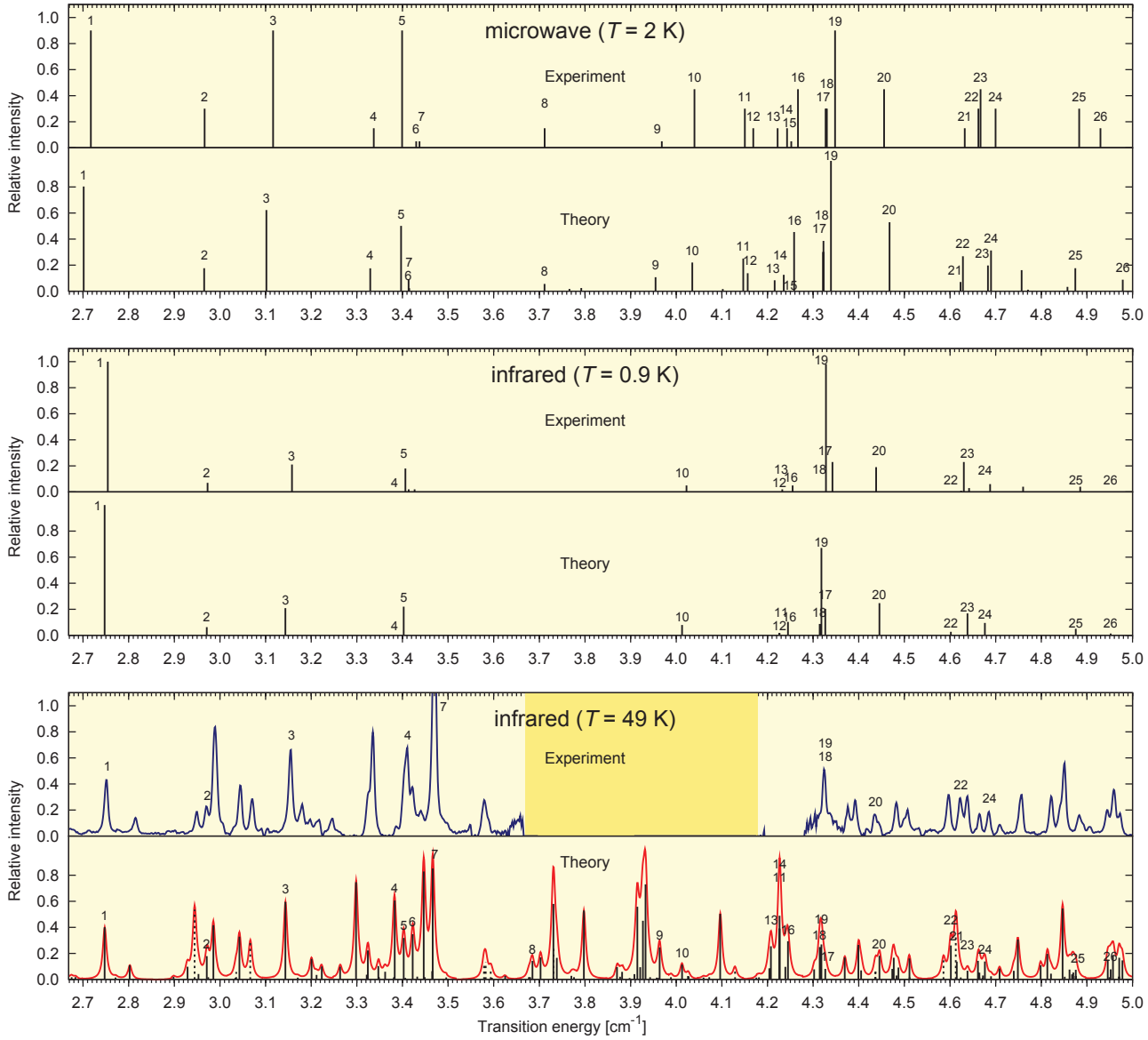

FIG. 6. (Upper panel): Experimental and theoretical microwave spectra at $T = 2$ K for the *ortho*H_2-CO complex. The theoretical spectrum has been calculated from the V_0 surface. The largest calculated intensity is normalized to one and only transitions with intensity larger than 0.01 are presented. The experimental intensities are plotted on a five-grade scale: very weak (0.05), weak (0.15), medium (0.3), strong (0.45), and very strong (0.9). The numbers labeling the transition lines correspond to those given in Table XV. (Middle panel): Experimental and theoretical infrared spectra at $T = 0.9$ K. The experimental one was first shifted by 2143.272 cm^{-1} and then both spectra were shifted by 0.18 cm^{-1}. (Lower panel): Experimental and theoretical infrared spectra at 49 K shifted as in the middle panel (from Ref. 13).

the proper infrared line to be related to the microwave one. For example, one can see in Fig. 6 how this procedure can be used to identify line number 5 in the experimental infrared spectrum in the bottom panel. The procedure becomes much simpler, and often theoretical assistance is not needed, if one compares to the infrared spectrum recorded in the temperature 0.9 K, shown in the middle panel in Fig. 6, since intensities are similar. For example, now line 5 can be unambiguously correlated.

From the top panel of Fig. 6, one can see that several transitions present in the experimental and theoretical spectra are easy to correlate and the experimental microwave lines can be unambiguously assigned, e.g., lines number 1–5, 10, 19, and 20. Assignment of some other transitions is not so obvious, since these transitions are located in more congested parts of the spectrum and the theoretical positions of the lines are not always accurate enough. We then used the chain procedure involving experimental infrared spectra, as described above. In the case of the line number 15, the corresponding theoretical transition is very weak ($I = 0.004$, see Table XIV), but energy fit very well. We have checked that the relative intensity in this case exceeds the 0.01 threshold if calculations are performed at 3 K rather than at 2 K. We therefore assume that this line has been assigned as the estimated temperature in the experiment is 2−4 K. All together, we were able to assign all 26 experimental microwave lines shown in Fig. 6. The complete list of the assignments is given in Table XV. There is only one relatively strong theoretical transition from the range of energies considered in the experiment, at 4.757 cm^{-1} (Table XIV) which has not been found in the experimental

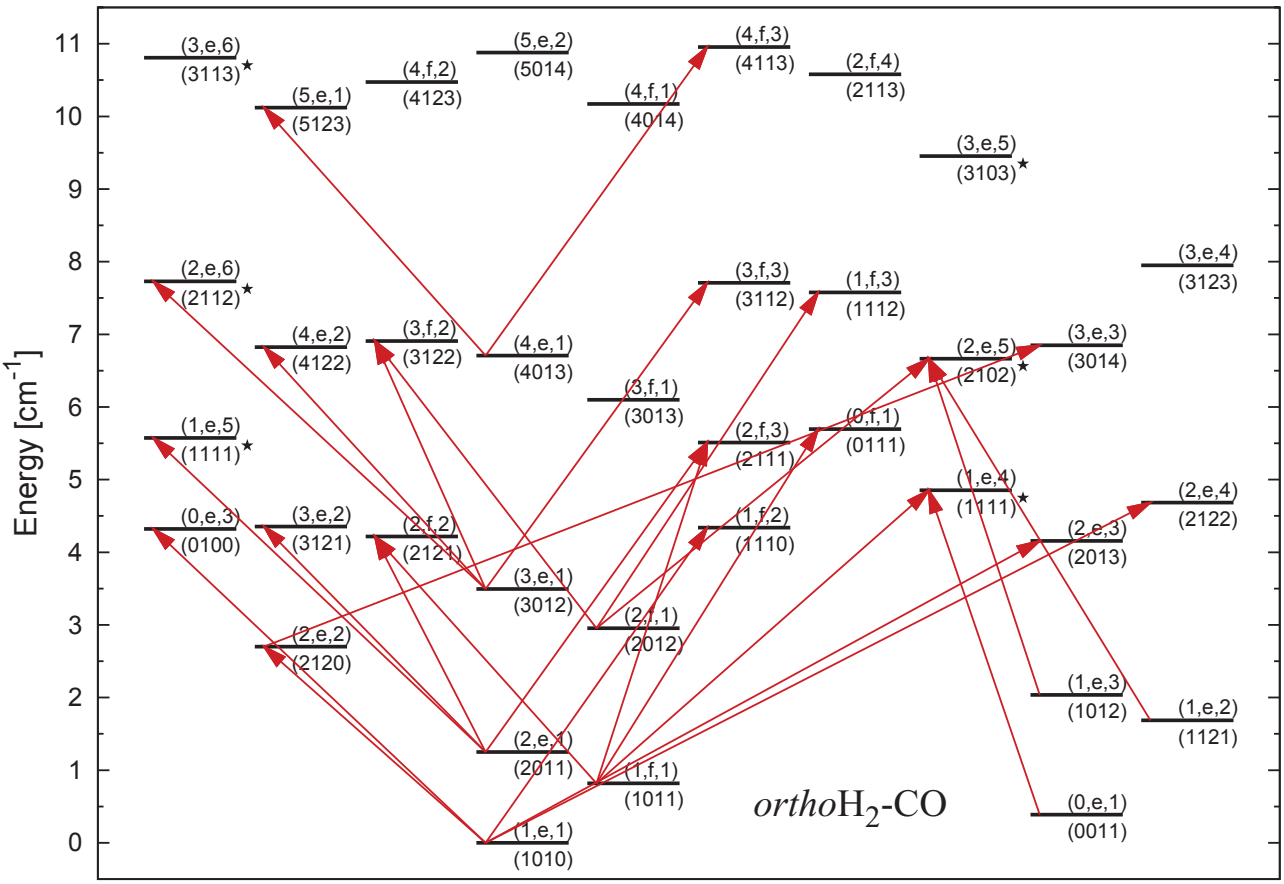

FIG. 7. Energy level diagram for the *ortho*H_2-CO complex computed from the V_0 surface. Each level is labeled by the set of parameters (J, P, $n_{J,P}$) (above the line) and by the other set ($Jj_2j_{12}l$) (below the line). The arrows show all the observed microwave transitions. The ($Jj_2j_{12}l$) states marked with stars cannot be uniquely labeled with one set of such approximate quantum numbers and the set of numbers definin the largest component is given. For example, for the state (3, *e*, 5) the components (3103) and (3113) contribute 51% and 33%, respectively. See Table S2 of Ref. 13 for lists of all major ($Jj_2j_{12}l$) contribution to a given state.

spectrum. Most likely its experimental counterpart exists, but we were not able to properly scan the energy range close to the energy of this transition.

In Fig. 7, we present all the measured microwave transitions on the pattern of a subset of the theoretical energy levels shown in Fig. 3. The energy levels are arranged accordingly to similar rules as the energy levels of *para*H_2-CO in the previous studies.[6,9] The energies in each column have the same value of j_2 and increasing values of l, which is clearly visible if one uses the set of parameters (Jj_2l). The *ortho*H_2-CO case is more complicated than *para*H_2-CO, since the angular momentum of H_2 can be coupled in different ways with the angular momentum of CO, which leads to different values of j_{12} for some states with the same (Jj_2l). Thus, the (Jj_2l) label would be ambiguous for the *ortho*H_2-CO states as the same labels would be present in more than one stack of energies. However, even with the value of j_{12} included, the energy levels still cannot be unambiguously labeled by the resulting ($Jj_2j_{12}l$) set. This is due to the fact that the wave functions of some of the considered states have more than one dominant angular component differing by the value of j_{12}. For instance, from Table S2 of Ref. 13 one can see that the leading component (65%) of the wave function of the (2, *e*, 4) state from the last (tenth) stack has $j_{12} = 2$ [($Jj_2j_{12}l$) = (2122)], while the wave function of the corresponding state (2, *e*, 5) [has the same set of (Jj_2l) = (212)] from the eighth stack has two comparably large components, with $j_{12} = 0$ [(2102), 49%] and $j_{12} = 1$ [(2112), 36%].

VI. CONCLUSIONS

We present here results of a joint experimental and theoretical study of the H_2-CO complex. First, we describe in details the development of a highly accurate potential energy surface for H_2-CO using the CCSDT(Q) method. This surface has recently been used in Ref. 13 to assign the rovibrational spectrum of *ortho*H_2-CO, but was only briefl described in that work. The importance of correlation effects beyond the CCSD(T) level for H_2-CO was previously noticed by Noga *et al.*,[32] but such contributions have been included for the whole surface only here. In fact, this is the firs time that a PES at this level has been computed for a system as large as H_2-CO. The interaction energies have been calculated on a six-dimensional grid, i.e., including the dependence on the H−H and C−O separations. The six-dimensional surface was represented as a second-order Taylor expansion in these separations. The interaction energies have been obtained as a sum of $E_{\rm int}^{\rm HF}$, $\delta E_{\rm int}^{\rm CCSD(T)}$, and $\delta E_{\rm int}^{\rm T(Q)}$ contributions calculated in different-size basis sets up to aug-cc-pV5Z for the grid points corresponding to the reference intermonomer

separations and the CCSD(T)-level results were CBS extrapolated. The inclusion of the $\delta E_{\rm int}^{\rm T(Q)}$ term changes the interaction energies quite substantially, e.g., by about 2.5 $\rm cm^{-1}$ near the global minimum. However, for the energies used for calculations of Taylor-expansion derivatives, the $\delta E_{\rm int}^{\rm T(Q)}$ term could be neglected. For each grid point in intermonomer coordinates, the interaction energies were averaged over the motion of H_2 in the ground vibrational state and of CO in the ground and firs excited vibrational states. The resulting energies were fitte by two four-dimensional interaction energy surfaces V_0 and V_1. For a few selected points, we have performed additional calculations in extended basis sets and using the $\delta E_{\rm int}^{\rm T(Q)}$ term in calculations of derivatives to estimate the uncertainties of our results. In the potential well, the uncertainty at the CCSD(T) level relative to the corresponding true complete basis set limit is 0.4 $\rm cm^{-1}$ and in other regions (except where the PES crosses zero) is should be about 0.6%. At the level including $\delta E_{\rm int}^{\rm T(Q)}$, these estimates increase to 0.5 $\rm cm^{-1}$ and 0.7%. Finally, the neglected post-Born-Oppenheimer and relativistic effects result in a further increase to 0.6 $\rm cm^{-1}$ and 0.8%. The new surfaces have been used in the rovibrational calculations for the *para*H_2-CO and *ortho*H_2-CO complexes.

Two spectroscopic measurements for the *ortho*H_2-CO complex have been performed within the present project. In the f rst experiment, the dimer transitions accompanying the fundamental band of CO have been observed in the infrared region for temperatures around 1–2 K. This experiment is a low-temperature version of the one performed at 49 K and presented in Ref. 13. The second experiment has been performed in the millimeter-wave region and corresponds to the pure dimer spectrum at the temperature of about 2 K.

To estimate accuracy of theoretical spectra, we f rst made comparisons with experiment for *para*H_2-CO. In Ref. 13, such comparisons were made with 3.5 Torr, 49 K measurements. In this work, we constructed a compound experimental spectrum by appropriately merging the 3.5 Torr, 49 K lines with the 1.1 Torr, 47.5 K lines (also measured in Ref. 6). The discrepancies between the calculated rovibrational energy levels and their empirical counterparts[6] are smaller than 0.015 $\rm cm^{-1}$, whereas the discrepancies in positions of spectral lines are smaller than 0.021 $\rm cm^{-1}$ and rmse is equal to 0.008 $\rm cm^{-1}$. Thus, there is clearly a very significan cancellation of errors in calculations of rovibrational energy levels and spectra as these discrepancies are about 50 times smaller than the estimated 0.6 $\rm cm^{-1}$ uncertainty of the PES. The reason is that the difference between our and the exact potential reduces to a fairly uniform shift of the whole well region of our PES, which does not influenc the low lying rovibrational levels. In addition to the excellent agreement in the transitions frequencies, the intensities agree also very well, so that the theoretical and experimental spectra look stunningly similar. There was still a number of transitions measured in Ref. 6 but not assigned before, resulting from transitions involving resonant states. After performing a new computational search for broad resonances, we were able to assign these lines.

For *ortho*H_2-CO, the comparisons of theory with experiment which led to the assignment of the 49 K infrared spectrum in Ref. 13 and resulted in maximum discrepancies in line positions of only 0.06 $\rm cm^{-1}$, with rmse equal to 0.017 $\rm cm^{-1}$, have not been amended in the present work. However, we have used here the V_0 and V_1 surfaces to predict the infrared and microwave spectra at low temperature corresponding to the experiments performed as a part of the present project. The comparisons of these theoretical spectra and of the infrared ones at both temperatures to the microwave spectrum resulted in a nearly complete assignment of the latter spectrum in the range of 80–150 GHz.

Despite virtually all measured spectra of *ortho*H_2-CO being assigned, we were not able to construct an empirical rovibrational energy-level diagram for this complex, whereas such diagram for *para*H_2-CO has been known for a long time.[6] This may seem contradictory in view of the fact that a few times more lines are assigned in the former than in the latter case, however, the former spectrum is also denser, which acts in opposite direction. Moreover, some critical transitions linking groups of energy levels are not visible in the *ortho*H_2-CO spectrum. Fortunately, the present theoretical accuracy is high enough to use the theoretical diagram for all practical purposes.

Compared to the V_{04} surface from Ref. 14, the present surface predicts spectral data nearly an order of magnitude more accurately. This increase of accuracy may seem to be very large taking into account that the differences between V_{04} and V_0 are only of the order of 1 $\rm cm^{-1}$. The reason is that V_{04} was too deep in most regions of the space, but not in some other regions. Thus, it had an imperfect anisotropy which becomes critical when discussing spectra at 0.01 $\rm cm^{-1}$ accuracy level.

Our work resolves some issues that could not be fully explained in Ref. 14. First, we confir the observation from that work that CBS extrapolations from double- and triple-zeta basis sets level overestimate the magnitude of interaction energy by about 1−2 $\rm cm^{-1}$ in most regions of the well, but for a few orientations work very well. This fact is the main reason why the current surface is so close to V_{04} as this overestimate partly cancels with the $\delta E_{\rm int}^{\rm T(Q)}$ term included in the present work. This CBS extrapolation problem does not appear in the present work since the size of the basis set has been increased to quintuple-zeta level. Second, because of some observed discrepancies with experimental results for the dissociation energy and virial coefficients one could not exclude that V_{04} could be too shallow by as much as 4 $\rm cm^{-1}$ in the well region. This possibility is eliminated by the present work. The conclusion of Ref. 14 that the experimental dissociation energy from Ref. 6 is too large is upheld by us. The discrepancy with the measured interaction virial coefficient is present mainly for low temperatures and we argue that it is due to higher level quantum effects neglected in calculations of Ref. 14 (repeated here with V_0).

The new potential energy surfaces as well as new experimental data can fin important use in future investigations. For example, the approach used by us can be utilized for assigning further precise microwave measurements of the spectra. Our results are, however, most important for astrophysics, where the H_2–CO inelastic scattering cross sections are used to get information about the H_2 distribution in interstellar space. Since accurate cross sections of this type are

difficul to measure, this type of investigations have to rely on theory. Our new potentials with their high-accuracy validated by comparisons with spectral data can be used to compute cross sections of ultimate reliability.

We have developed so far 4D potential energy surfaces for $v = 0$ and 1 vibrational states of CO. Our current data should allow extension to $v = 2$. However, PESs corresponding to higher vibrational states would not be described well enough due to our truncation of the Taylor expansion at the second order. One can also develop an analytic 6D potential energy surface based on our data by f tting the derivatives f^c_{ij}. Of course, this surface will work well only for the range of values of r and s corresponding to the f rst three vibrational states of each monomer.

Another possible application of our results is in a search for bound H_2-CO in space. The published search of Ref. 5 was performed at the time when only a few microwave-range transition frequencies were known and the accuracy of these lines was limited. With the very large number of currently known lines, perhaps such searches could be repeated. Our theoretical predictions cover regions of spectra that for various reasons are not accessible to experiments but can be useful for interpretation of astronomical data. There are several transitions for both *para* and *ortho*H_2-CO with energies within the range of the Herschel space observatory far-infrared instruments.

ACKNOWLEDGMENTS

This work was supported by the National Science Foundation (NSF) Grant Nos. CHE-0848589 and CHE-1152899. L.A.S. acknowledges support from DFG (Grant No. SU 579/1) and RFBR (Grant Nos. 12-03-00985 and 12-02-91337).

[1] S. Green and P. Thaddeus, Astrophys. J. **205**, 766 (1976).
[2] M. Wernli, P. Valiron, A. Faure, L. Wiesenfeld, P. Jankowski, and K. Szalewicz, Astron. Astrophys. **446**, 367 (2006).
[3] Y. Yuan and D. A. Neufeld, Astrophys. J. **726**, 76 (2011).
[4] S. C. O. Glover and P. C. Clark, Mon. Not. R. Astron. Soc. **421**, 116 (2012).
[5] R. J. Allen, L. Loinard, A. R. W. McKellar, and J. Lequeux, Astrophys. J. **489**, 102 (1997).
[6] A. R. W. McKellar, J. Chem. Phys. **108**, 1811 (1998).
[7] P. Jankowski and K. Szalewicz, J. Chem. Phys. **108**, 3554 (1998).
[8] I. Pak, L. A. Surin, B. S. Dumesh, D. A. Roth, F. Lewen, and G. Winnewisser, Chem. Phys. Lett. **304**, 145 (1999).
[9] A. V. Potapov, L. A. Surin, V. A. Panf lov, B. S. Dumesh, T. F. Giesen, S. Schlemmer, P. L. Raston, and W. Jäger, Astrophys. J. **703**, 2108 (2009).
[10] A. R. W. McKellar, J. Chem. Phys. **112**, 9282 (2000).
[11] L. A. Surin, B. S. Dumesh, G. Winnewisser, and I. Pak, J. Chem. Phys. **113**, 9351 (2000).
[12] A. V. Potapov, V. A. Panf lov, A. A. Dolgov, L. A. Surin, and B. S. Dumesh, Opt. Spectrosc. **106**, 655 (2009).
[13] P. Jankowski, A. R. W. McKellar, and K. Szalewicz, Science **336**, 1147 (2012).
[14] P. Jankowski and K. Szalewicz, J. Chem. Phys. **123**, 104301 (2005).
[15] M. Jeziorska, P. Jankowski, K. Szalewicz, and B. Jeziorski, J. Chem. Phys. **113**, 2957 (2000).
[16] P. Jankowski, J. Chem. Phys. **121**, 1655 (2004).
[17] P. Jankowski, J. Chem. Phys. **128**, 154311 (2008).
[18] P. Jankowski and K. Szalewicz, Chem. Phys. Lett. **459**, 60 (2008).
[19] K. Szalewicz, G. Murdachaew, R. Bukowski, O. Akin-Ojo, and C. Leforestier, in *Lecture Series on Computer and Computational Science: ICCMSE 2006*, edited by G. Maroulis and T. Simos (Brill Academic, Leiden, 2006), Vol. 6, pp. 482–491.
[20] C. Leforestier, K. Szalewicz, and A. van der Avoird, J. Phys. Chem. **137**, 014305 (2012).
[21] S. Bubin and L. Adamowicz, J. Chem. Phys. **118**, 3079 (2003).
[22] P. Huxley and J. N. Murrel, J. Chem. Soc. Faraday Trans. 2 **79**, 323 (1983).
[23] S. F. Boys and F. Bernardi, Mol. Phys. **19**, 553 (1970).
[24] K. Szalewicz and B. Jeziorski, J. Chem. Phys. **109**, 1198 (1998).
[25] H. L. Williams, E. M. Mas, K. Szalewicz, and B. Jeziorski, J. Chem. Phys. **103**, 7374 (1995).
[26] M. Jeziorska, R. Bukowski, W. Cencek, M. Jaszuński, B. Jeziorski, and K. Szalewicz, Collect. Czech. Chem. Commun. **68**, 463 (2003).
[27] M. Jeziorska, W. Cencek, K. Patkowski, B. Jeziorski, and K. Szalewicz, Int. J. Quantum Chem. **108**, 2053 (2008).
[28] D. G. Truhlar, Chem. Phys. Lett. **294**, 45 (1998).
[29] A. Halkier, W. Klopper, T. Helgaker, P. Jørgensen, and P. R. Taylor, J. Chem. Phys. **111**, 9157 (1999).
[30] A. Tajti, P. G. Szalay, A. G. Császár, M. Kállay, J. Gauss, E. F. Valeev, B. A. Flowers, J. Vázquez, and J. F. Stanton, J. Chem. Phys. **121**, 11599 (2004).
[31] Y. J. Bomble, J. Vázquez, M. Kállay, C. Michauk, P. G. Szalay, A. G. Császár, J. Gauss, and J. F. Stanton, J. Chem. Phys. **125**, 064108 (2006).
[32] J. Noga, M. Kállay, and P. Valiron, Mol. Phys. **104**, 2337 (2006).
[33] J. Noga and R. J. Bartlett, J. Chem. Phys. **86**, 7041 (1987).
[34] Y. J. Bomble, J. F. Stanton, M. Kállay, and J. Gauss, J. Chem. Phys. **123**, 054101 (2005).
[35] S. A. Kucharski and R. J. Bartlett, J. Chem. Phys. **97**, 4282 (1992).
[36] N. C. Handy, Y. Yamaguchi, and H. F. Schaefer III, J. Chem. Phys. **84**, 4481 (1986).
[37] H.-J. Werner, P. J. Knowles, R. Lindh, M. Schütz *et al.*, MOLPRO, version 2006.1, a package of *ab initio* programs 2006, see http://www.molpro.net.
[38] MRCC, a string-based quantum chemical program suite written by M. Kállay, 2005; see also M. Kállay and P. R. Surján, J. Chem. Phys. **115**, 2945 (2001) as well as www.mrcc.hu.
[39] R. Bukowski, J. Sadlej, B. Jeziorski, P. Jankowski, K. Szalewicz, S. A. Kucharski, H. L. Williams, and B. M. Rice, J. Chem. Phys. **110**, 3785 (1999).
[40] K. T. Tang and J. P. Toennies, J. Chem. Phys. **80**, 3726 (1984).
[41] B. Jeziorski, R. Moszynski, and K. Szalewicz, Chem. Rev. **94**, 1887 (1994).
[42] K. Szalewicz, K. Patkowski, and B. Jeziorski, Struct. Bonding **116**, 43 (2005).
[43] K. Szalewicz, Wiley Interdisc. Rev.–Comp. Mol. Sci. **2**, 254 (2012).
[44] J. M. Hutson, BOUND Computer Code, Version 5, distributed by Collaborative Computational Project No. 6 of the UK Science and Engineering Research Council, 1993.
[45] S. Green, J. Chem. Phys. **62**, 2271 (1975).
[46] J. M. Hutson, Comput. Phys. Commun. **84**, 1 (1994).
[47] A. E. Thornley and J. M. Hutson, J. Chem. Phys. **101**, 5578 (1994).
[48] M. Ziolkowski, M. S. thesis, Faculty of Chemistry, Nicolaus Copernicus University, Toruń, Poland, 2006.
[49] A. R. W. McKellar, Appl. Phys. B **90**, 213 (2008).
[50] L. A. Surin, B. S. Dumesh, F. Lewen, D. A. Roth, V. P. Kostromin, F. S. Rusin, G. Winnewisser, and I. Pak, Rev. Sci. Instrum. **72**, 2535 (2001).
[51] J. Tang, A. R. W. McKellar, L. A. Surin, D. N. Fourzikov, B. S. Dumesh, and G. Winnewisser, J. Mol. Spectrosc. **214**, 87 (2002).
[52] L. A. Surin, D. N. Fourzikov, T. F. Giesen, S. Schlemmer, G. Winnewisser, V. A. Panfil v, B. S. Dumesh, G. W. M. Vissers, and A. van der Avoird, J. Phys. Chem. A **111**, 12238 (2007).
[53] B. Schramm, E. Elias, L. Kern, G. Natour, A. Schmitt, and C. Weber, Ber. Bunsenges. Phys. Chem. **95**, 615 (1991).
[54] K. Patkowski, W. Cencek, P. Jankowski, K. Szalewicz, J. B. Mehl, G. Garberoglio, and A. H. Harvey, J. Chem. Phys. **129**, 094304 (2008).
[55] S. Chefdeville, T. Stoecklin, A. Bergeat, K. M. Hickson, C. Nauline, and M. Costes, Phys. Rev. Lett. **109**, 023201 (2012).
[56] M. D. Brookes and A. R. W. McKellar, J. Chem. Phys. **111**, 7321 (1999).
[57] See supplementary material at http://dx.doi.org/10.1063/1.4791712 for the fil containing a complete list of all assigned experimental transitions obtained from the infrared experiments on *ortho*H_2-CO.

Journal of Molecular Spectroscopy 307 (2015) 18–19

Contents lists available at ScienceDirect

Journal of Molecular Spectroscopy

journal homepage: www.elsevier.com/locate/jms

Note

First observation of the rotational spectrum of the HD–CO weakly bound complex

Alexey Potapov [a,*], Leonid Surin [a,b], Stephan Schlemmer [a]

[a] I. Physikalisches Institut, University of Cologne, Zülpicher Str. 77, 50937 Cologne, Germany
[b] Institute of Spectroscopy of RAS, 142190 Troitsk, Moscow, Russia

ARTICLE INFO

Article history:
Received 9 October 2014
In revised form 17 November 2014
Available online 24 November 2014

Keywords:
High resolution molecular spectroscopy
van der Waals complex
Supersonic jet
Orotron

ABSTRACT

In this Note we present the first observation of the rotational spectrum of the HD–CO van der Waals complex. Three *b*-type transitions, namely *R*(1), *R*(2) and *R*(3) corresponding to the rotation of the CO subunit within the complex, were measured in the millimeter-wave region using the orotron jet spectrometer. An approximate low energy level scheme for the HD–CO complex was built on the basis of the previous investigations of the *para*H_2–CO and *ortho*D_2–CO complexes and the presented measurements.

Rovibrational and pure rotational transitions of the H_2–CO and D_2–CO weakly bound complexes have been investigated very intensively during the last quarter of century [1–8]. Considerable interest in spectroscopic studies of these complexes is a result of their physical and astrophysical significance. High-resolution jet-cooled spectroscopic measurements of H_2–CO and its isotopologues can provide valuable information about both the intermolecular potential of the complex, which is a prerequisite for understanding of collision processes in interstellar molecular clouds, and transition frequencies for reliable interstellar searches with radiotelescopes. One of the main motivations from the physical point of view is the investigation of superfluidity of molecular hydrogen, predicted more than 40 years ago [9] and demonstrated in experiments with *para*H_2 clusters in helium nanodroplets [10], through studies on small $(H_2)_N$–CO clusters, $N = 2–20$ [11]. Recent results from a microwave study of $(para H_2)_N$–CO clusters [12] show the decoupling of part of the $(para H_2)$ density from the rotational motion of the CO molecule (similar to the case of ^4He_N–CO clusters [13]) starting from $N = 6$. This decoupling has been interpreted in terms of superfluidity of molecular hydrogen [12]. Spectroscopic investigations of molecular hydrogen containing clusters involving fermionic particles, i.e., $(HD)_N$–CO clusters, would unambiguously confirm if the decoupling of hydrogen density is indeed an indicator of superfluidity. The starting point of these investigations is a study of the $N = 1$ system, i.e. the HD–CO binary complex, which has been never experimentally observed.

In the present Note we report the first observation of rotational transitions of HD–CO produced in a molecular jet expansion. Three *b*-type transitions, *R*(1), *R*(2) and *R*(3) corresponding to the rotation of the CO subunit within the complex, were measured using the orotron intracavity jet spectrometer, which is described in detail elsewhere [14]. A gas mixture consisting of 5% of CO in HD at backing pressures about 4–5 bar was used for production of the HD–CO complexes in a jet. The frequency of the orotron was modulated at $f = 25$ kHz, and a $2f$ demodulation technique was used for the sensitive detection of the absorption signal.

The rotational energy levels for HD–CO can be described using a free rotor basis, with j for the angular momentum of the CO unit, l for the end-over-end rotation of the complex and J for the total angular momentum, $\mathbf{J} = \mathbf{j} + \mathbf{l}$, as it is appropriate for *para*H_2–CO and *ortho*D_2–CO [6,7]. Additionally the "spectroscopic" parity labels $e(+1)$ and $f(-1)$ are used, which are related to the conventional parity p of an individual level by the expression $p(-1)^J$. An approximate rotational energy level scheme for HD–CO is presented in Fig. 1. The level energies were obtained as the mean values of the level energies for *para*H_2–CO and *ortho*D_2–CO.

At the very low effective temperatures of jet experiments all, *para*H_2, *ortho*D_2 and HD molecules have angular momentum equals to 0. We thus might expect similar sequences of transitions for the HD–CO, *para*H_2–CO and *ortho*D_2–CO complexes. Predictions of the measured *b*-type *R*-branch transition frequencies of HD–CO were based on known frequencies for the same lines of *para*H_2–CO [6] and *ortho*D_2–CO [7] and were calculated as the mean values. The following frequencies were obtained:

* Corresponding author.
E-mail address: potapov@ph1.uni-koeln.de (A. Potapov).

http://dx.doi.org/10.1016/j.jms.2014.11.006
0022-2852/

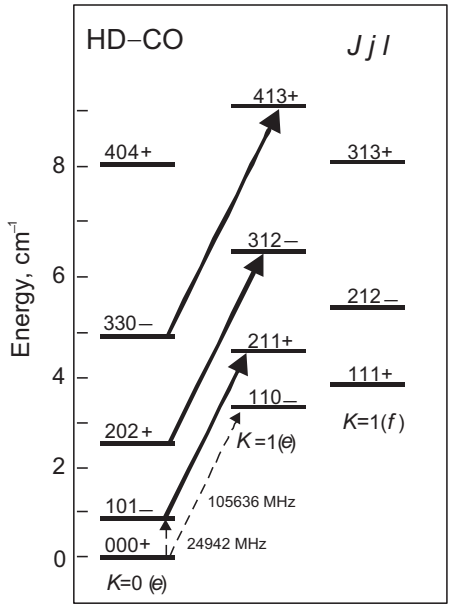

Fig. 1. Approximate low energy level scheme of the HD–CO complex; measured (solid arrows) and predicted (dashed arrows) transitions are shown. K is the projection of J onto the intermolecular axis.

$R(1)$ $(J, j, l) = 2, 1, 1 \leftarrow 1, 0, 1$
Observed: 115509.640(50) MHz
Predicted: 115 766 MHz
$\Delta = -256$ MHz

$R(2)$ $(J, j, l) = 3, 1, 2 \leftarrow 2, 0, 2$
Observed: 122050.023(50) MHz
Predicted: 122 009 MHz
$\Delta = +40$ MHz

$R(3)$ $(J, j, l) = 4, 1, 3 \leftarrow 3, 0, 3$
Observed: 125865.086(50) MHz
Predicted: 126 138 MHz
$\Delta = -272$ MHz

As an example, the spectrum of the $R(1)$ transition is presented in Fig. 2.

There seems to be a trend in the deviations between the observed and predicted frequencies, where the deviations show negative values for the transitions originated from the levels with minus parity and positive values for the transition originated from the levels with plus parity. But to speak about such a trend definitely, more transitions should be measured. Unfortunately the $R(0)$ transition predicted at 105 636 MHz is out of the frequency range of our orotron spectrometer. We also searched for the $R(4)$ transition predicted at 127 185 MHz, but without success, obviously, because of its weakness under our experimental conditions.

Analyses of the transition frequencies for HD–CO, *para*H_2–CO, and *ortho*D_2–CO in pairs show that the frequencies are not simply related to the reduced masses of the complexes or to the masses of the hydrogen units. The different zero-point energies of the complexes play also a significant role. At the same time our simple "mean values" approach gives quite good agreement with the experiment.

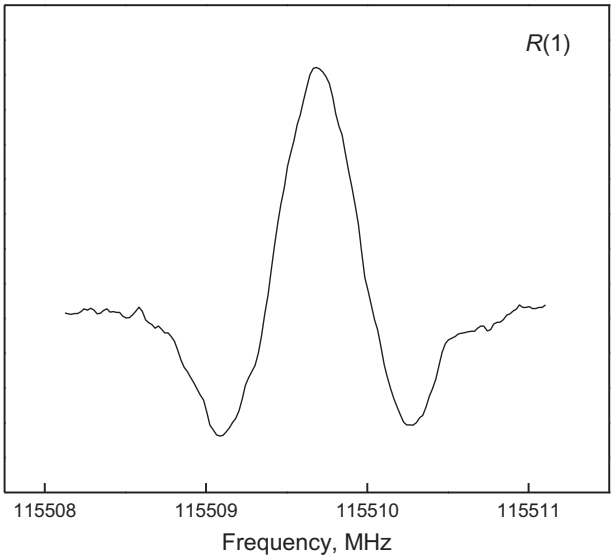

Fig. 2. The $R(1)$ transition of HD–CO measured using 2f demodulation.

The new transition frequencies of HD–CO together with the already available microwave and millimeter-wave data for *para*H_2–CO [6] and *ortho*D_2–CO [7,15] allows for building an approximate low energy level scheme of the HD–CO complex (see Fig. 1) and for predicting the $(1, 1, 0) \leftarrow (0, 0, 0)$, and $(1, 0, 1) \leftarrow (0, 0, 0)$ transition frequencies from the lowest energy level (the most populated one at low temperature). These predictions are also given in Fig. 1.

Acknowledgments

We are grateful to Prof. Wolfgang Jäger for the informal reading of this Note and helpful suggestions on its improvement. The work was supported by Deutsche Forschungsgemeinschaft through grants SFB 956 and SU 579/1. LS also thanks Russian Foundation for Basic Research for support through grant 12-09-91337.

References

[1] A.R.W. McKellar, Chem. Phys. Lett. 186 (1991) 58.
[2] A.R.W. McKellar, J. Chem. Phys. 108 (1998) 1811.
[3] I. Pak, L.A. Surin, B.S. Dumesh, D.A. Roth, F. Lewen, G. Winnewisser, Chem. Phys. Lett. 304 (1999) 145.
[4] A.R.W. McKellar, J. Chem. Phys. 112 (2000) 9282.
[5] L.A. Surin, B.S. Dumesh, G. Winnewisser, I. Pak, J. Chem. Phys. 113 (2000) 9351.
[6] A.V. Potapov, L.A. Surin, V.A. Panfilov, B.S. Dumesh, T.F. Giesen, S. Schlemmer, P.L. Raston, W. Jäger, Astrophys. J. 703 (2009) 2108.
[7] A.V. Potapov, V.A. Panfilov, A.A. Dolgov, L.A. Surin, B.S. Dumesh, Opt. Spectrosc. 106 (2009) 732.
[8] P. Jankowski, L.A. Surin, A. Potapov, S. Schlemmer, A.R.W. McKellar, K. Szalewicz, J. Chem. Phys. 138 (2013) 084307.
[9] V.L. Ginzburg, A.A. Sobyanin, JETP Lett. 15 (1972) 343.
[10] S. Grebenev, B. Sartakov, J.P. Toennies, A.F. Vilesov, Science 289 (2000) 1532.
[11] S. Moroni, M. Botti, S. De Palo, A.R.W. McKellar, J. Chem. Phys. 122 (2005) 094314.
[12] P.L. Raston, W. Jäger, H. Li, R.J. Le Roy, P.-N. Roy, Phys. Rev. Lett. 108 (2012) 253402.
[13] L.A. Surin, A.V. Potapov, B.S. Dumesh, S. Schlemmer, Y. Xu, P.L. Raston, W. Jäger, Phys. Rev. Lett. 101 (2008) 233401.
[14] L.A. Surin, B.S. Dumesh, F. Lewen, D.A. Roth, V.P. Kostromin, F.S. Rusin, G. Winnewisser, I. Pak, Rev. Sci. Instrum. 72 (2001) 2535.
[15] W. Jäger, private communication.

A&A 594, A117 (2016)
DOI: 10.1051/0004-6361/201628426

Astronomy & Astrophysics

The CO-H_2 van der Waals complex and complex organic molecules in cold molecular clouds: A TMC-1C survey[⋆,⋆⋆]

A. Potapov[1,2], Á. Sánchez-Monge[1], P. Schilke[1], U. U. Graf[1], Th. Möller[1], and S. Schlemmer[1]

[1] I. Physikalisches Institut, Universität zu Köln, Zülpicher Str. 77, 50937 Cologne, Germany
[2] Laboratory Astrophysics Group of the Max Planck Institute for Astronomy at the Friedrich Schiller University Jena, Institute of Solid State Physics, Helmholtzweg 3, 07743 Jena, Germany
e-mail: alexey.potapov@uni-jena.de

Received 3 March 2016 / Accepted 7 July 2016

ABSTRACT

Context. Almost 200 different species have been detected in the interstellar medium (ISM) during the last decades, revealing not only simple species but complex molecules with more than six atoms. Other exotic compounds, like the weakly-bound dimer $(H_2)_2$, have also been detected in astronomical sources like Jupiter.
Aims. We aim to detect, for the first time, the CO-H_2 van der Waals complex in the ISM, which could be a sensitive indicator for low temperatures if detected.
Methods. We used the IRAM 30 m telescope, located in Pico Veleta (Spain), to search for the CO-H_2 complex in a cold, dense core in TMC-1C (with a temperature of ∼10 K). All the brightest CO-H_2 transitions in the 3 mm (80–110 GHz) band were observed with a spectral resolution of 0.5–0.7 km s^{-1}, reaching a rms noise level of ∼2 mK. The simultaneous observation of a broad frequency band, 16 GHz, allowed us to conduct a serendipitous spectral line survey.
Results. We did not detected any lines belonging to the CO-H_2 complex. We set up a new, more stringent upper limit for its abundance to be [CO-H_2]/[CO] ∼ 5×10^{-6}, while we expect the abundance of the complex to be in the range ∼10^{-8}–10^{-3}. The spectral line survey has allowed us to detect 75 lines associated with 41 different species (including isotopologues). We detect a number of complex organic species, for example methyl cyanide (CH_3CN), methanol (CH_3OH), propyne (CH_3CCH), and ketene (CH_2CO), associated with cold gas (excitation temperatures ∼7 K), confirming the presence of these complex species not only in warm objects but also in cold regimes.

Key words. astrochemistry – molecular processes – methods: observational – techniques: spectroscopic – radio lines: ISM – ISM: molecules

1. Introduction

In recent decades, the number of atomic and molecular species detected in the interstellar medium (ISM) has increased considerably thanks to the improved sensitivity of facilities like the IRAM 30 m telescope in Spain or the Atacama Large Millimeter/submillimeter array (ALMA) in Chile and new laboratory measurements of transitions of new species included in catalogues, such as the Cologne Database for Molecular Spectroscopy (CDMS). Almost 200 different species have been found in Galactic and extragalactic environments such as cold dense cores, hot molecular cores, circumstellar disks, evolved stars, or large diffuse molecular clouds. These 200 species do not only consist of simple molecules such as the most abundant H_2 and CO, but also include complex species usually defined as molecules with six or more atoms (Herbst & van Dishoeck 2009; see the CDMS database[1] for a summary of detected species in space).

Molecular hydrogen, H_2, is by far the most abundant molecule in the Universe, followed by carbon monoxide, CO. Therefore, the intermolecular forces between these two species are of fundamental interest. If the CO-H_2 van der Waals complex exists in measurable amounts in the ISM, it could be a sensitive indicator for low temperatures. The binding energy of the complex is so small, typically 20 cm^{-1} or 30 K, that the relative abundance of the complex in the gas phase is expected to increase at lower temperatures. We note that this complex does not correspond to the formaldehyde molecule, H_2CO.

There is an open debate about the feasibility of observing such weakly bound species because their formation rates at the very low densities of interstellar molecular clouds (below 10^7 cm^{-3}) are low, because of the small probability of three-body collisions, which is the main formation route of van der Waals complexes in the laboratory. On the other hand, the large timescale on which these processes occur in interstellar space makes radiative association, which is usually a slow process, feasible (e.g. Klemperer & Vaida 2006). Also non-equilibrium conditions in the ISM may strongly favour the formation and concentration of the CO-H_2 complex over time on the surfaces of dust grains in shielded regions at low temperatures, with release to the gas-phase occurring by localized heating processes such as turbulence or jets and outflows (e.g. Allen et al. 1997). However, one also has to consider that CO tends to be frozen out

⋆ Based on observations carried out with the IRAM 30 m Telescope. IRAM is supported by INSU/CNRS (France), MPG (Germany) and IGN (Spain).
⋆⋆ Reduced spectra (FITS files) are only available at the CDS via anonymous ftp to cdsarc.u-strasbg.fr (130.79.128.5) or via http://cdsarc.u-strasbg.fr/viz-bin/qcat?J/A+A/594/A117
[1] http://www.astro.uni-koeln.de/cdms/molecules

onto dust grains in very cold, dense regions, and it seems difficult to release the CO-H_2 complex from grains without destroying it. On the other hand, this is completely unchartered territory, and even sensitive upper limits are useful. A detection of this complex would challenge many beliefs we have about the chemistry of dense molecular clouds.

There have been several attempts to observe complexes containing CO and H_2 molecules. The detection of the H_2 dimer, $(H_2)_2$, in the atmosphere of Jupiter has been reported by McKellar (1988), while searches for the CO dimer, $(CO)_2$ (Vanden Bout et al. 1979), and the CO-paraH_2 complex (Allen et al. 1997) in Galactic molecular clouds were not successful thus far. Laboratory data later clarified a spectroscopic problem of these unsuccessful searches. The extensive millimeter-wave (MMW) studies of the CO dimer (Surin et al. 2007) have shown that the radio astronomical search of this complex was based on frequencies that cannot be unambiguously attributed to $(CO)_2$. In the case of the CO-paraH_2 complex, the interstellar search was outside the correct frequency position of the most promising $R(0)$ line, as later identified by the first MMW study of CO-paraH_2 (Pak et al. 1999), and only the weaker $Q(1)$ line was correctly tuned.

Recent laboratory studies of the CO-H_2 complex have provided precise MMW frequencies with uncertainties of about 50 kHz for the complex in different spin modifications and for its deuterated isotopologues: CO-paraH_2 (Potapov et al. 2009b), CO-orthoH_2 (Jankowski et al. 2013), CO-orthoD_2 (Potapov et al. 2009a), and CO-HD (Potapov et al. 2015). Therefore, the availability of precise rest frequencies and modern astronomical receivers (with a sensitivity several times better than the old receivers used 20 yr ago), combine in a great opportunity to detect a van der Waals complex in the ISM for the first time.

In this paper we present IRAM 30 m observations of a cold region in the Taurus molecular cloud in the search for the CO-H_2 van der Waals complex. In Sect. 2 we describe the observations. In Sect. 3 we present the main results. Unfortunately, we do not have a detection of the CO-H_2 complex but we can set a new limit that can be used in future chemical modelling. In addition to the search for the CO-H_2 complex, the IRAM 30 m observations allowed us to conduct a spectral line survey of a very cold region (~10 K), and we report the detection of complex organic molecules (COMs) as well as first time tentative detections of species in this object. In Sect. 4 we discuss our results, and we end the paper with a summary of the main results in Sect. 5.

2. Observations

The observations were carried out from 2015 May 6 until May 9 at the IRAM 30 m telescope, located in Pico Veleta (Granada, Spain) under the project code 131-14. We have chosen to attempt the detection of the CO-H_2 complex in the nearest star-forming region: the Taurus molecular cloud complex (e.g. Olano et al. 1988; Suzuki et al. 1992; Roberts & Millar 2000). In particular, we performed observations towards a cold, dense condensation nearby TMC-1C, which has measured low excitation temperatures of 3–7 K (Spezzano et al. 2013), and for which a kinetic temperature of 10 K reproduce the observations presented by Spezzano et al. (2016). This object harbours the physical conditions (low temperature and high density, $\sim 4 \times 10^4$ cm^{-3}; Schnee et al. 2007) necessary to search for the CO-H_2 complex. The density is still low enough to not have all the CO frozen out onto the dust grains[2]. The coordinates used for the observations are $\alpha_{2000} = 04^h41^m16\overset{s}{.}1$ and $\delta_{2000} = +25°49'43\overset{''}{.}8$, which is coincident with the coordinates used in Spezzano et al. (2013).

Table 1. Frequencies of the brightest CO-H_2 targeted lines.

	Transition	Frequency (MHz)
CO-paraH_2	(1, 1, 0)–(0, 0, 0)	108 480.857
	(1, 1, 1)–(1, 0, 1)	91 012.364
CO-orthoH_2	(2, f, 2)–(1, f, 1)	101 907.919
	(3, e, 2)–(2, e, 1)	93 433.726
CO-orthoD_2	(1, 1, 0)–(0, 0, 0)	102 791.612
	(1, 1, 1)–(1, 0, 1)	89 483.510
CO-HD	(1, 1, 0)–(0, 0, 0)	105 636

Notes. The uncertainty in the frequency measurements is about 50 kHz for all the transitions, except for CO-HD with a few tens of MHz. The labelling of the quantum numbers of the transitions are explained in detail in Fig. 1.

We tuned the telescope to cover a number of transitions of the CO-H_2 complex and its deuterated isotopologues in the 3 mm band (E090) of the EMIR receiver. All four EMIR sub-bands were connected to the Fast Fourier Transform Spectrometers (FTS), with a spectral resolution of 200 kHz, which results in ~0.5–0.7 km s^{-1} at the corresponding frequencies. In Table 1, we list the most intense transitions of the complex covered in our spectral setup. The frequency coverage was selected in order to optimize the simultaneous search of the strongest CO-paraH_2 and CO-orthoH_2 lines. The energy level diagrams for CO-paraH_2 and CO-orthoH_2 are shown in Fig. 1. In total, our observations cover an effective bandwidth of 16 GHz, ranging from 85.87 to 93.65 GHz in the lower sideband, and from 101.55 to 109.33 GHz in the upper sideband. The total observing time was 20 h. We used the ON-OFF observation mode, with the reference position located at the offset (800″, 600″). The telescope pointing was checked every 1.5 h and was found to be accurate to ~5″, i.e. only a fraction of the beam size of the telescope at these frequencies: ~30″. The weather conditions were stable during the observations with zenith opacities of 0.02–0.07 and system temperatures of 80–100 K. The observed spectra was calibrated following the standard procedures and analysed using the GILDAS[3] software package. We converted the spectra to the main beam temperature scale, using a forward efficiency of 0.95, and a beam efficiency of 0.79 and 0.81 for the upper and the lower sidebands, respectively. The final spectrum has a noise level of ~2 mK.

3. Results and analysis

3.1. The CO-H_2 complex

In Fig. 2 we show, in the top panels, the full spectrum obtained with the IRAM 30 m telescope. A number of bright lines have been detected throughout the covered frequency range and these are discussed in Sect. 3.2. The bottom panels of Fig. 2 show a close-up view of the frequency ranges around the frequencies of the brightest CO-H_2 lines, corresponding to the CO-orthoH_2

[2] Referring to the work of Caselli et al. (1999), a model in which CO is condensed out onto dust grains at densities above 10^5 cm^{-3} and has a roughly canonical abundance at lower hydrogen densities, is supported by the observations of gas-phase depletion in the L1544 cloud core.

[3] The GILDAS software package is developed by the IRAM and Observatoire de Grenoble, and can be downloaded at http://www.iram.fr/IRAMFR/GILDAS

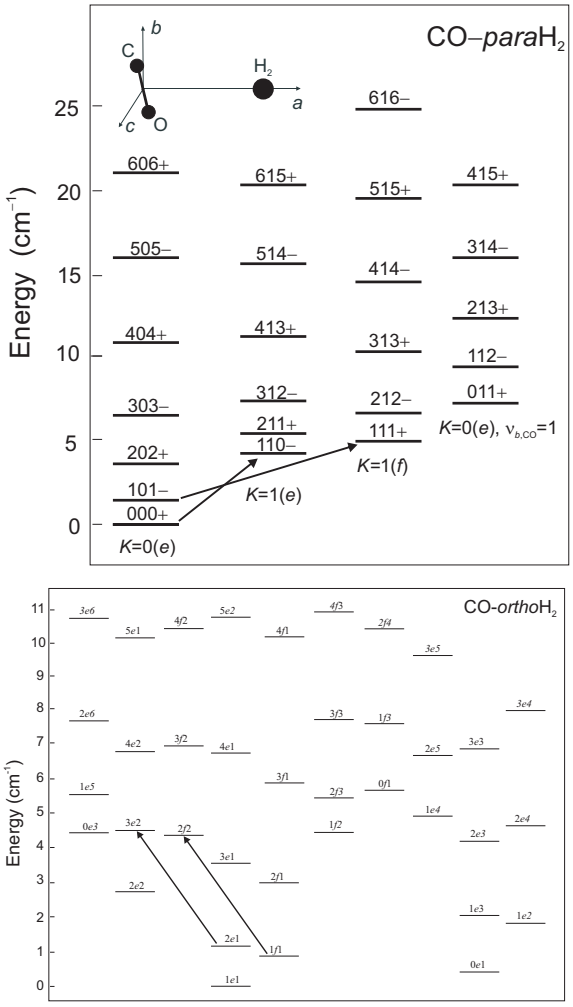

Fig. 1. Energy level diagram for the CO-paraH_2 (*top panel*) and CO-orthoH_2 (*bottom panel*) van der Waals complex. *Top panel*: the energy levels are labelled by quantum numbers J, j_{CO} and l, where J is the total angular momentum; j_{CO} refers to the rotation of the CO sub-unit; and l refers to the end-over-end rotation of the complex. K corresponds to the projection of J onto the intermolecular axis. The labels e and f indicate the parity of the J levels within a given stack. The parity of an even-J level is "+" for stacks labelled with e and "−" for f, while the parity of an odd-J level is "−" for e and "+" for stacks labelled f. The insert shows the approximate geometrical structure of the CO-H_2 complex (see Potapov et al. 2009b, for details). *Bottom panel*: the energy levels are labelled by quantum numbers J, parity P and $n_{J,P}$, a consecutive number of the state for the given values of J and P (see Jankowski et al. 2013 for details). In both panels, the targeted transitions are indicated by arrows.

and CO-paraH_2 transitions listed in Table 1. No lines belonging to the CO-H_2 complex are detected at the corresponding frequencies (indicated in the figure with red dotted vertical lines). The noise at the high-frequency transitions is slightly larger than the average noise of 2 mK. This larger noise is due to ripples in the baseline that were not possible to completely remove. However, since their wavelength is much larger than the expected linewidths, ∼0.3 km s^{-1}, they do not affect the search for the CO-H_2 transitions. None of the four transitions were detected, and therefore we set an upper limit of ∼6 mK (corresponding to 3σ) for the intensities of these lines.

3.2. Spectral line survey

The broad frequency range covered with the IRAM 30 m telescope permits us not only to study the CO-H_2 lines, but also to perform a spectral line survey of this cold dense condensation. It is worth mentioning that the high sensitivity achieved with our observations is adequate to search, for example, for COMs (molecules with six or more atoms) in low-temperature environments. These complex molecules have long been detected in the interstellar medium, especially in hot molecular cores associated with high-mass star-forming regions (e.g. Cummins et al. 1986; Blake et al. 1987; Sánchez-Monge et al. 2013, 2014). The advent of sensitive instruments has also revealed a chemical complexity associated with low-mass hot cores (or hot corinos; e.g. Cazaux et al. 2003) and intermediate-mass hot cores (e.g. Sánchez-Monge et al. 2010). Even though their formation routes remain uncertain, both warm gas-phase and grain-surface reactions have been invoked to account for their presence in low-mass protostars. In this latter scheme, COMs result from radical-radical reactions on the grains as radicals become mobile when the nascent protostar warms up its surroundings and the resulting molecules are subsequently desorbed into the gas phase at higher temperatures or by shock events produced by winds and jets (e.g. Garrod & Herbst 2006). In recent years, the detection of COMs in cold environments (T < 30 K; Bacmann et al. 2012; Vastel et al. 2014) represents a challenge for the chemical models and an opportunity to improve and clarify the role of the grain-surface and gas-phase chemistry.

The top panels of Fig. 2 show the spectral line survey towards the condesation in TMC-1C. We identified 75 lines with an intensity >5σ. The spectral resolution of only 0.5–0.7 km s^{-1} is not enough to resolve most of the lines, suggesting that all they are excited in an environment with a temperature <30 K, i.e. in cold gas. Most of the lines are detected in one single channel. The exceptions are species such as HCN and N_2H^+ due to the hyperfine structure, and $^{13}C^{18}O$ with a weak blueshifted wing. The thermal linewidth for gas at 30 K is 0.23 km s^{-1}, 0.18 km s^{-1} and 0.16 km s^{-1}, for species with mean molecular weights of 25 (e.g. CCH), 40 (e.g. CH_3CCH), and 56 (e.g. CCS), respectively. We identified the lines with the CDMS (Müller et al. 2005) and JPL (Pickett et al. 1998) databases, and later on confirmed these lines by creating synthetic spectra of each species using the XCLASS[4] software (Möller et al. 2015). XCLASS is a toolbox for the Common Astronomy Software Applications (CASA) package containing new functions for modelling interferometric and single-dish data. The included myXCLASS programme calculates synthetic spectra by solving the radiative transfer equation for an isothermal object in one dimension, where the required molecular data are taken from an embedded database containing entries from the CDMS and JPL databases using the Virtual Atomic and Molecular Data Center (VAMDC) portal. The contribution of a molecule is defined by an user-defined number of components where each component is described by four main parameters: excitation temperature, column density, velocity width, and velocity offset. In order to achieve a good description of the data we fit these parameters with the included model optimizer package MAGIX (Möller et al. 2013). By performing an internal resampling, XCLASS makes sure that the line is sampled properly, even if the velocity resolution of the data is coarse.

[4] The eXtended CASA Line Astronomy Software Suite (XCLASS) can be downloaded at https://www.astro.uni-koeln.de/projects/schilke/XCLASSInterface

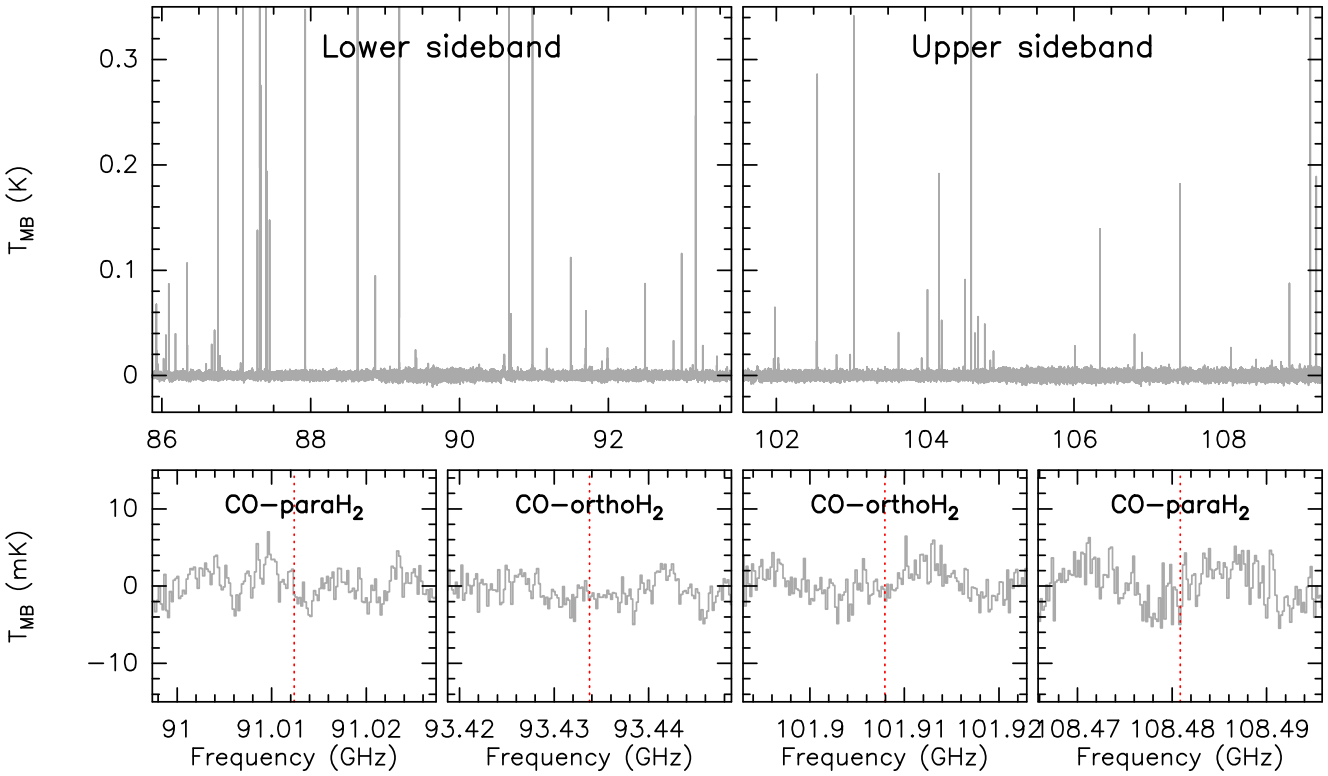

Fig. 2. *Top panels*: full spectrum observed with the IRAM 30 m telescope towards the cold dense core in TMC-1C. The mean rms noise level is ~2 mK. Most of the detected lines emit only in one channel (channel width 0.5–0.7 km s^{-1}), suggesting that the linewidth of the different lines is ≤0.7 km s^{-1} (see Sect. 3.2). *Bottom panels*: close-up views of the frequency ranges around the brightest transitions of the CO-H_2 van der Waals complex. The corresponding frequencies are listed in Table 1, and are shown in the panels with a vertical dotted line. The expected linewidth is ≈0.3 km s^{-1}, as measured in higher spectral resolution observations (e.g. Spezzano et al. 2013).

In Table 2 we list the identified species with the corresponding excitation temperature (Col. 2), column density (Col. 3), and number of transitions above 5σ (Col. 4). The 75 detected lines come from 41 different species (including isotopologues) and four unidentified lines at the frequencies 90.593 GHz, 90.602 GHz, 92.872 GHz, and 101.981 GHz with main beam temperatures of 18 mK, 18 mK, 30 mK, and 15 mK, respectively. For those species with more than one transition, we fitted the excitation temperature and column density simultaneously with XCLASS. For species such as C_3H_2 or CH_3OH, with different spin symmetries ortho and para, the total column density is given. If only one transition is detected above 5σ for a given species, we fit only the column density and fix the excitation temperature to 7 K, which corresponds to the average temperature of the other transitions and is consistent with the value also measured in Spezzano et al. (2013). For the different detected isotopologues, we fixed the excitation temperature to be the same as the main species and we fitted only the column density. In all cases we consider a linewidth of 0.3 km s^{-1}. In Fig. 3 we present the whole spectral survey, indicating the location of the different detected transitions. A number of COMs have been detected in this cold dense core. We discuss the results in Sect. 4.2.

4. Discussion

4.1. Detectability of the CO-H_2 complex

In Sect. 3.1 we report an upper limit of ~6 mK for the CO-H_2 lines. We follow the same approach as in Allen et al. (1997) to establish an upper limit for the column density of the CO-paraH_2 complex. We use the dipole moment of CO and the total partition function of CO-paraH_2 calculated from the now known energy level scheme of the complex (see Fig. 1). Our calculations result in a value of ~3×10^{12} cm^{-2} for the column density of the complex and a fractional abundance of the CO-paraH_2 dimer relative to CO of ~5×10^{-6}. This assumes the CO column density to be 6×10^{17} cm^{-2}, which is derived from the $^{13}C^{18}O$ column density listed in Table 2, and assuming standard $^{12}C/^{13}C$ and $^{16}O/^{18}O$ ratios of 60 and 500, respectively.

In the following, we estimate the number density of the CO-H_2 molecular complex that we expect under the ISM conditions and compare this value to the new upper limit. All the reaction rates used in the following are generic rates, that have not specifically been measured or calculated and are taken from the review paper by van Dishoeck (2014). The given reactions are the basic types of reactions in space. Following van Dishoeck (2014), there are two basic processes by which molecular bonds can be formed in the interstellar molecular clouds: radiative association and formation on grain surface with subsequent release to the gas phase. In the radiative association process, the binding energy of a new molecule or molecular complex is carried out through the emission of a photon, and can be described as

$$H_2 + CO \rightarrow CO\text{-}H_2 + h\nu \quad (1)$$

and proceeds at the rate of a radiative association reaction $k_1 \approx 10^{-17}$–10^{-14} cm^3 s^{-1}. For the case of the formation on grain surfaces, a dust particle accommodates the released energy, and the process can be described as

$$H_2 + \text{CO-grain} \rightarrow CO\text{-}H_2 + \text{grain},$$

which proceeds at a rate of $k_2 \approx 10^{-17}$ cm^3 s^{-1}.

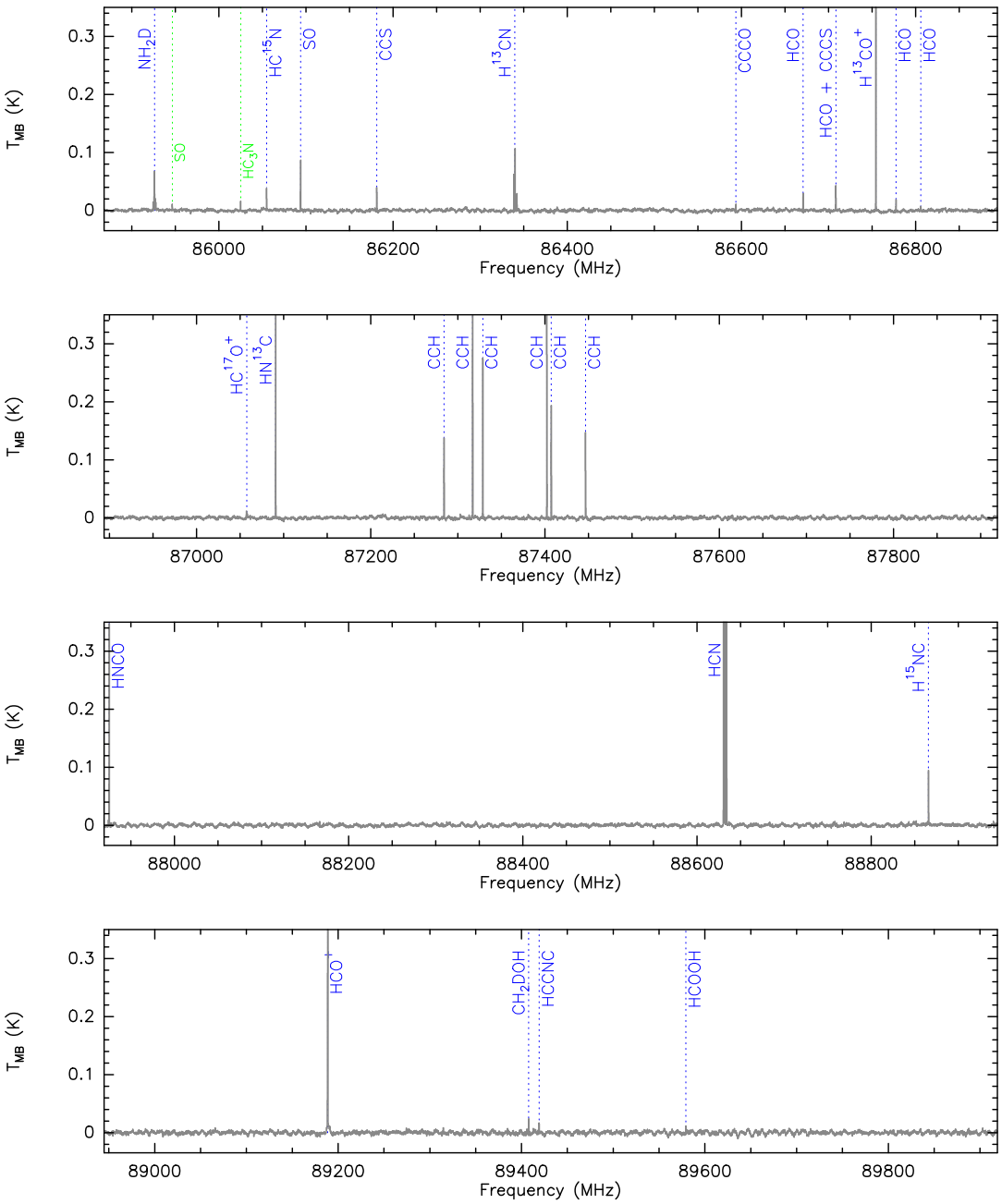

Fig. 3. Spectral line survey towards TMC-1C. Each panel shows about 1 GHz of the total 16 GHz frequency band. The observed spectrum is shown in dark grey. Each identified transition is indicated with a blue dotted line and the name of the corresponding species. The green dotted lines correspond to ghost lines from the image sideband.

On the other side, there are three processes for the destruction of the complex: photodissociation, collisional dissociation and neutral-neutral bond rearrangement. The first process can be described by

$$\text{CO-H}_2 + h\nu \rightarrow \text{products}, \quad (2)$$

with a reaction rate of $k_3 \approx 10^{-10}$–10^{-8} cm^3 s^{-1}. The second and third processes can be given by

$$\text{CO-H}_2 + \text{M} \rightarrow \text{products}, \quad (3)$$

where M is a reaction partner with rates for collisional dissociation of $k_4 \approx 10^{-26}$ cm^3 s^{-1} and for bond rearrangement of $k_5 \approx 10^{-11}$–10^{-9} cm^3 s^{-1}.

We consider a dense condensation with an H_2 density of $[H_2] = 4 \times 10^4$ cm^{-3}, the CO density given by [CO] = [CO-grain] = 10^{-4} [H_2], and assume [M] = [H_2]. Under these conditions, the formation is dominated by radiative association, while the destruction mainly occurs by the bond rearrangement. As stated by van Dishoeck (2014), a collisional dissociation of molecules is only important in regions of very high temperature (>3000 K) and density. Thus, we determine the CO-H_2 abundance in the equilibrium as $[\text{CO-H}_2] = (k_1[H_2][CO])/(k_5[M]) = 4 \times 10^{-8}$–$4 \times 10^{-3}$ cm^{-3} and $[\text{CO-H}_2]/[CO] \sim 10^{-8}$–$10^{-3}$. The obtained range for a possible abundance of CO-H_2 is wide. From the comparison of our estimated $[\text{CO-H}_2]/[CO]$ abundance to the upper detection limit of $[\text{CO-H}_2]/[CO] \sim 5 \times 10^{-6}$, we can conclude that

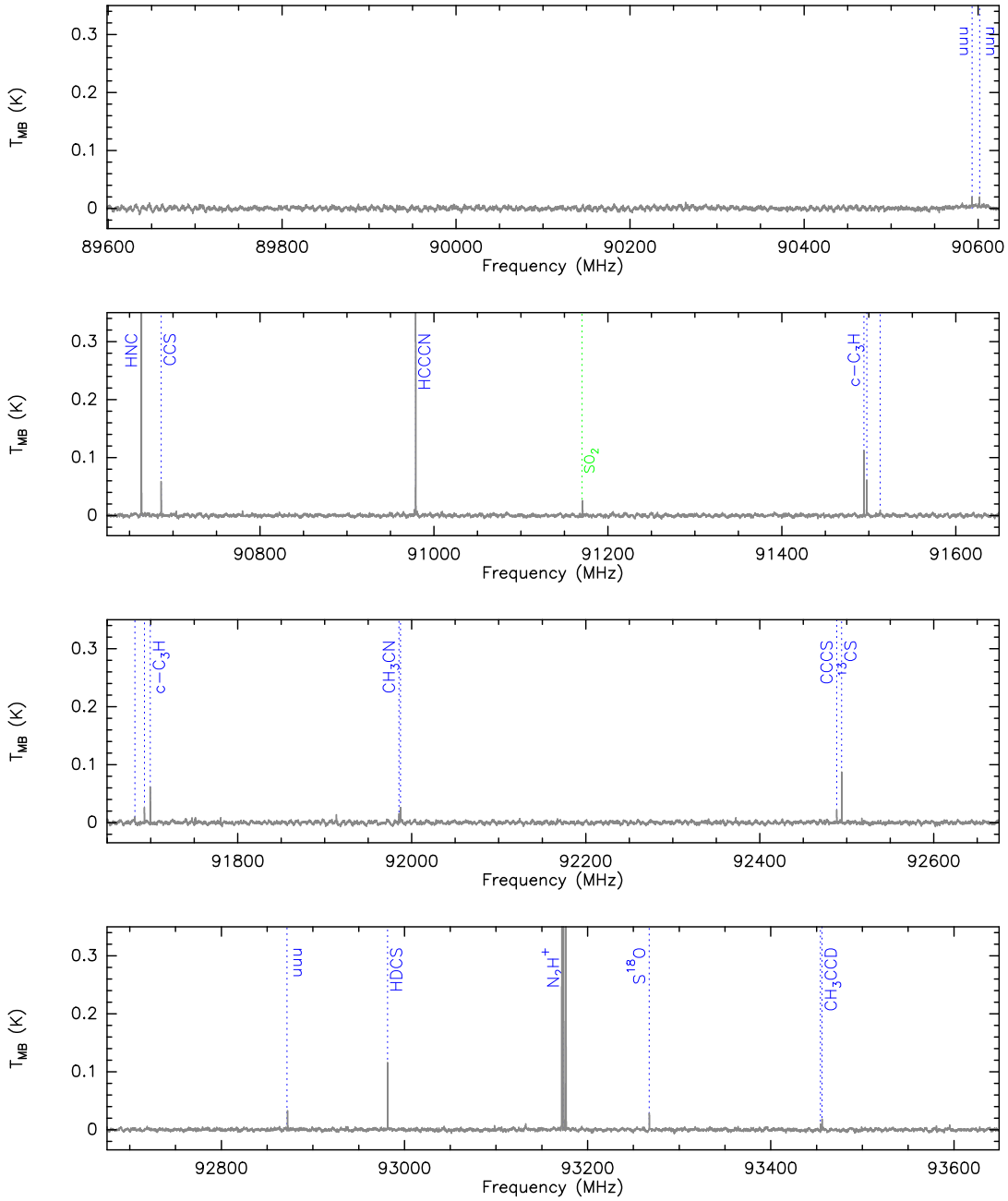

Fig. 3. continued.

the complex might be detected by observations with one or two orders higher sensitivity.

4.2. Molecular inventory in cold regions

Table 2 and Fig. 3 reveal a relatively rich chemistry in the cold dense core TMC-1C. Even though the average excitation temperature is only 7 K, we are able to detect a number of species with six or more atoms: CH_3CN, CH_3OH, and CH_3CCH. The column densities for these species are in the range 10^{11}–10^{13} cm^{-2}, which results in abundances of 10^{-12}–10^{-10} assuming a H_2 column density of 10^{22} cm^{-2} (e.g. Schnee & Goodman 2005). These abundances are about two orders of magnitude lower than the typical abundances found towards more massive hot molecular cores. We searched for more complex species, such as methyl formate (CH_3OCHO) or dimethyl ether (CH_3OCH_3), but we did not detect them with an upper limit on the column density of about 10^{12} cm^{-2}, assuming an excitation temperature of 7 K. Similarly to the cold core L1689B studied by Bacmann et al. (2012) we also detect ketene (CH_2CO), with a column density of $\sim 3 \times 10^{12}$ cm^{-2} in complete agreement with the column densities determined for L1689B. In addition to the main isotopologues of the detected species, we also detect transitions of the deuterated counterparts CH_3CCD and CH_2DOH. The deuteration level is estimated to be about 0.045 for CH_3CCH and 0.055 for CH_3OH, however, this deuteration fractions should be better constrained with future observations of other transitions and with higher spectral resolution (necessary to resolve the lines). The uncertainty of the column density listed in Table 2 does not includes the uncertainty in the linewidth, which cannot be

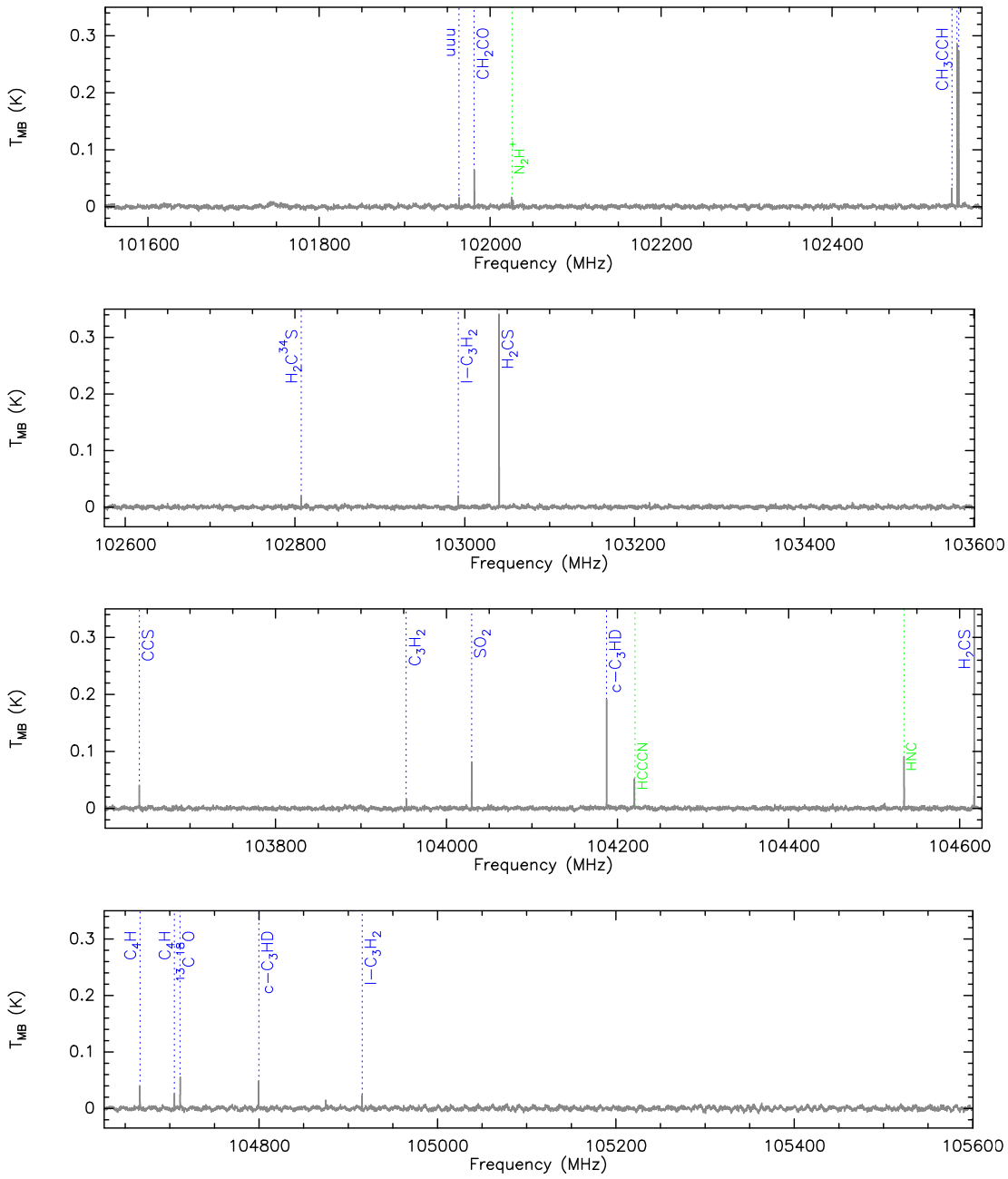

Fig. 3. continued.

measured in our coarse spectral resolution observations. The column densities can differ by 30% if the linewidth is increased or decreased by 0.1 km s^{-1}, or by 50% if the variation is 0.2 km s^{-1}. Therefore, the column densities reported in Table 2 have to be considered with caution. High-spectral resolution observations are necessary to improve the determination of the excitation temperature and column density. Another source of uncertainty in the column density determination is the excitation temperature. Observations of more transitions for the different molecules are required to better constrain the column density and to search for non-LTE effects.

In general, a number of deuterated compounds have been detected: DCS^+, HDCS, NH_2D, c-C_3HD, c-C_3D_2, CH_2DOH, and CH_3CCD. The deuteration fraction is 0.2 for H_2CS, 0.07 for c-C_2HD, and about 0.05 for CH_3CCH and CH_3OH. The column density measured for c-C_3HD and c-C_3D_2 is in agreement with the recent measurements of Spezzano et al. (2013).

Finally, in addition to the COMs discussed above, we highlight the detection of some species: (a) HCS^+ has been observed in previous surveys towards Taurus molecular cores (e.g. Ohishi & Kaifu 1998; Kaifu et al. 2004). Here, we present for the first time, a tentative detection of the deuterated counterpart DCS^+. A detailed study of different deuterated species may help to better understand the routes of deuteration, in particular for those more complex species, and to compare with similar studies conducted in high-mass star-forming regions (e.g. Fontani et al. 2011, 2015); (b) Similarly, we report a tentative detection of $HOCO^+$ in this source for the first time, for which we determine a column density of $\sim 2 \times 10^{11}$ cm^{-2}; and (c) the detection of HCO is common in photon-dominated regions (PDRs; e.g.

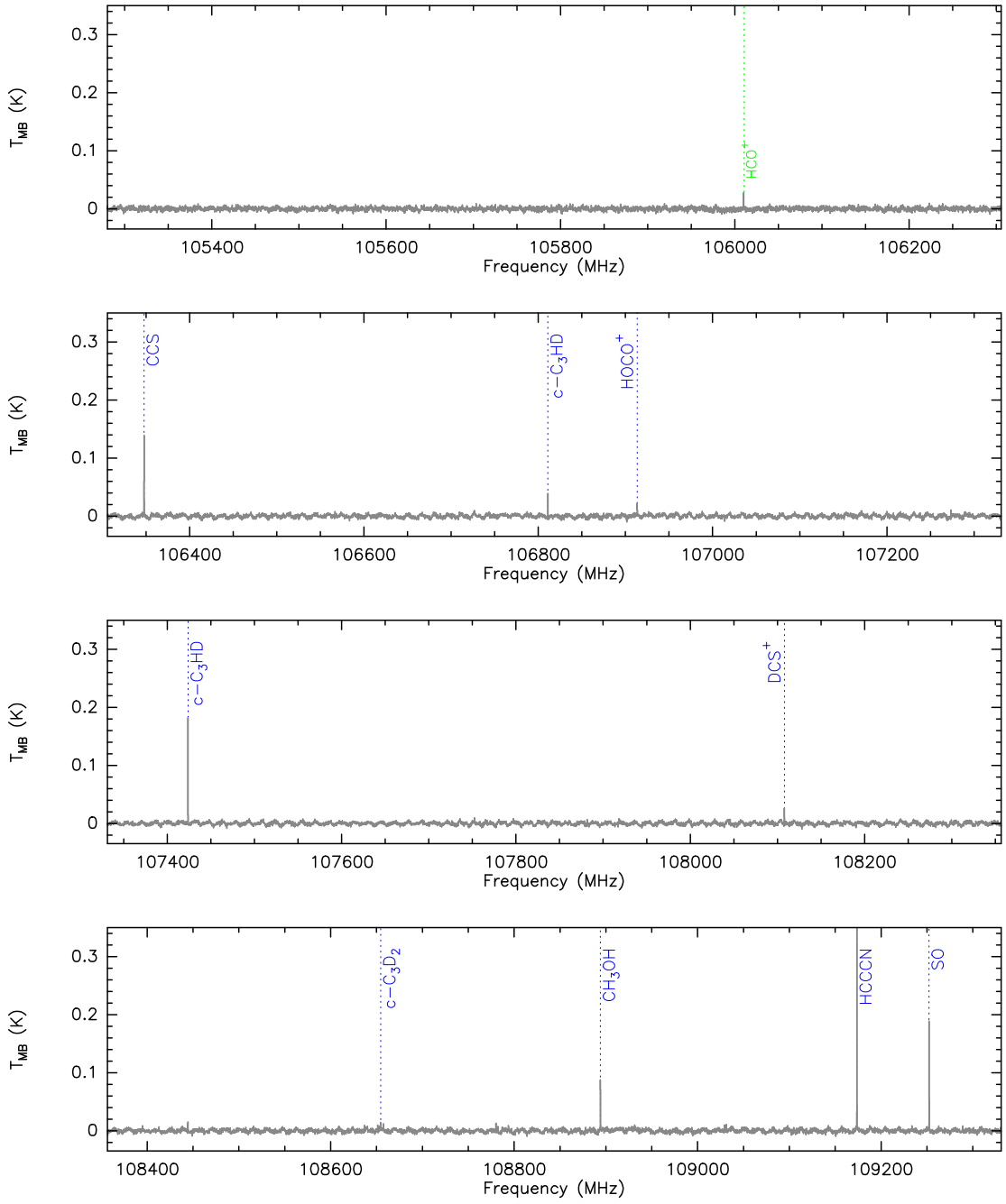

Fig. 3. continued.

Schilke et al. 2001), where the chemistry is dominated by the presence of large amounts of far-UV photons. The Taurus molecular cloud is a low-mass star-forming complex, and therefore there are no high-mass stars in the region able to produce enough UV photons. In this survey we report the detection of HCO in a cold, dense core, not associated with a PDR with a column density of $\sim 10^{12}$ cm^{-2}. Bacmann & Faure (2016) studied HCO in a number of cold prestellar cores, and related its abundance with that of other species such as H_2CO, CH_3O and finally CH_3OH. The authors determine the abundance ratios between the different species to be HCO:H_2CO:CH_3O:CH_3OH ~10:100:1:100, when the formation of methanol occurs via hydrogenation of CO on cold grain surfaces. The observed abundances of the intermediate species HCO and CH_3O suggest they are gas-phase products of the precursors H_2CO and CH_3OH, respectively. We measure an abundance ratio of HCO:CH_3OH ~1:10 for our cold, dense core (see Table 2), which is consistent with the results reported by Bacmann & Faure (2016).

5. Summary

We used the IRAM 30 m telescope to conduct sensitive observations of a cold, dense core in TMC-1C, with the goal of detecting the CO-H_2 van der Waals complex. We did not detect any transition of the CO-paraH_2 and CO-orthoH_2 compounds with a rms noise level of ~2 mK for a spectral resolution of 0.7 km s^{-1}. This sets a new strong upper limit for the abundance of the complex of [CO-H_2]/[CO] $\sim 5 \times 10^{-6}$. We estimate that the expected

Table 2. Species, temperatures, column densities, and number of transitions detected above 5σ towards TMC-1C (see Sect. 3.2 for details).

Species	T (K)	log (N) (log[cm^{-2}])	Transitions
$^{13}C^{18}O$	7.0	13.30 ± 0.50	1
^{13}CS	7.0	11.65 ± 0.26	1
SO	6.2 ± 0.7	13.25 ± 0.28	2
$S^{18}O$	6.2	11.81 ± 0.26	1
CCH	7.0	13.42 ± 0.11	6
CCS	4.7 ± 0.7	12.95 ± 0.38	4
HCN	7.0	12.26 ± 0.18	1
$H^{13}CN$	7.0	11.51 ± 0.29	1
$HC^{15}N$	7.0	10.71 ± 0.21	1
HNC	7.0	12.92 ± 1.01	1
$HN^{13}C$	7.0	11.76 ± 0.13	1
$H^{15}NC$	7.0	11.51 ± 0.30	1
HCO	6.1 ± 1.8	11.03 ± 0.30	4
HCO^+	7.0	12.09 ± 0.35	1
$H^{13}CO^+$	7.0	11.59 ± 0.38	1
$HC^{17}O^+$	7.0	9.97 ± 1.50	1
DCS^+	7.0	10.88 ± 0.24	1
SO_2	7.0	11.95 ± 0.23	1
N_2H^+	7.0	12.42 ± 0.19	1
CCCS	6.2 ± 0.5	12.67 ± 0.31	2
CCCO	7.0	11.26 ± 0.23	1
c-CCCH	6.0 ± 1.9	12.14 ± 0.35	6
H_2CS	14.8 ± 2.1	12.67 ± 0.15	2
HDCS	14.8	12.01 ± 0.98	1
$H_2C^{34}S$	14.8	11.43 ± 1.59	1
$HOCO^+$	7.0	11.25 ± 0.19	1
HNCO	7.0	13.11 ± 0.11	1
NH_2D	7.0	12.59 ± 1.00	1
C_4H	7.8 ± 0.9	13.12 ± 0.26	2
l-C_3H_2	7.2 ± 0.7	11.18 ± 0.31	3
c-C_3HD	6.0 ± 1.8	12.14 ± 0.35	4
c-C_3D_2	6.0	10.99 ± 1.90	1
CH_2CO	7.0	12.42 ± 0.37	1
HC_3N	4.2 ± 0.3	14.62 ± 0.45	2
HCCNC	7.0	11.81 ± 0.15	1
HCOOH	7.0	11.64 ± 0.13	1
CH_3CN	7.1 ± 1.0	11.80 ± 0.45	2
CH_3OH	7.0	12.86 ± 1.27	1
CH_2DOH	7.0	11.60 ± 0.50	1
CH_3CCH	15.0 ± 3.6	13.31 ± 0.13	3
CH_3CCD	15.0	11.97 ± 0.16	2

abundance of the complex with respect to CO in the ISM can be ~10^{-8}–10^{-3}, which suggest that more sensitive observations would be required to search for and detect for the first time the CO-H_2 complex in the ISM.

Our sensitive spectral line survey has revealed the detection of 75 different spectral lines coming from 41 different species (including isotopologues). The excitation temperature is ~7 K, which is consistent with previous estimates. We detect a number of complex organic molecules such as CH_3CN, CH_3OH, CH_3CCH and deuterated isotopologues. The detection of these species in a cold object is consistent with the similar findings in other objects (e.g. L1689B, Bacmann et al. 2012). Future studies of these complex species to better constrain the physical parameters, as well as the study of more rare isotopologues, could help to improve the current understanding of the formation of complex species in the cold ISM.

Acknowledgements. We acknowledge the comments and suggestions of the anonymous referee that helped to improve the manuscript. A.P. would like to thank Nicolas Billot for his help with the observations and data processing and he would also like to thank the IRAM team. This work was supported by Deutsche Forschungsgemeinschaft through grant SFB 956 (subprojects A6, B4 and C3).

References

Allen, R. J., Loinard, L., McKellar, A. R. W., & Lequeux, J. 1997, ApJ, 489, 102
Bacmann, A., & Faure, A. 2016, A&A, 587, A130
Bacmann, A., Taquet, V., Faure, A., Kahane, C., & Ceccarelli, C. 2012, A&A, 541, L12
Blake, G. A., Sutton, E. C., Masson, C. R., & Phillips, T. G. 1987, ApJ, 315, 621
Caselli, P., Walmsley, C. M., Tafalla, M., Dore, L., & Myers, P. C. 1999, ApJ, 523, L165
Cazaux, S., Tielens, A. G. G. M., Ceccarelli, C., et al. 2003, ApJ, 593, L51
Cummins, S. E., Linke, R. A., & Thaddeus, P. 1986, ApJS, 60, 819
Fontani, F., Palau, A., Caselli, P., et al. 2011, A&A, 529, L7
Fontani, F., Busquet, G., Palau, A., et al. 2015, A&A, 575, A87
Garrod, R. T., & Herbst, E. 2006, A&A, 457, 927
Herbst, E., & van Dishoeck, E. F. 2009, ARA&A, 47, 427
Jankowski, P., Surin, L. A., Potapov, A., et al. 2013, J. Chem. Phys., 138, 084307
Kaifu, N., Ohishi, M., Kawaguchi, K., et al. 2004, PASJ, 56, 69
Klemperer, W., & Vaida, V. 2006, Proc. Nat. Acad. Sci., 103, 10584
McKellar, A. R. W. 1988, ApJ, 326, L75
Möller, T., Bernst, I., Panoglou, D., et al. 2013, A&A, 549, A21
Möller, T., Endres, C., & Schilke, P. 2015, ArXiv e-prints [arXiv:1508.04114]
Müller, H. S. P., Schlöder, F., Stutzki, J., & Winnewisser, G. 2005, J. Mol. Struct., 742, 215
Ohishi, M., & Kaifu, N. 1998, Faraday Discussions, 109, 205
Olano, C. A., Walmsley, C. M., & Wilson, T. L. 1988, A&A, 196, 194
Pak, I., Surin, L. A., Dumesh, B. S., et al. 1999, Chem. Phys. Lett., 304, 145
Pickett, H. M., Poynter, R. L., Cohen, E. A., et al. 1998, J. Quant. Spectr. Rad. Transf., 60, 883
Potapov, A. V., Panfilov, V. A., Dolgov, A. A., Surin, L. A., & Dumesh, B. S. 2009a, Opt. Spectr., 106, 655
Potapov, A. V., Surin, L. A., Panfilov, V. A., et al. 2009b, ApJ, 703, 2108
Potapov, A., Surin, L., & Schlemmer, S. 2015, J. Mol. Spectr., 307, 18
Roberts, H., & Millar, T. J. 2000, A&A, 364, 780
Sánchez-Monge, Á., Palau, A., Estalella, R., et al. 2010, ApJ, 721, L107
Sánchez-Monge, Á., Cesaroni, R., Beltrán, M. T., et al. 2013, A&A, 552, L10
Sánchez-Monge, Á., Beltrán, M. T., Cesaroni, R., et al. 2014, A&A, 569, A11
Schilke, P., Pineau des Forêts, G., Walmsley, C. M., & Martín-Pintado, J. 2001, A&A, 372, 291
Schnee, S., & Goodman, A. 2005, ApJ, 624, 254
Schnee, S., Caselli, P., Goodman, A., et al. 2007, ApJ, 671, 1839
Spezzano, S., Brünken, S., Schilke, P., et al. 2013, ApJ, 769, L19
Spezzano, S., Gupta, H., Brünken, S., et al. 2016, A&A, 586, A110
Surin, L. A., Fourzikov, D. N., Giesen, T. F., et al. 2007, J. Phys. Chem. A, 111, 12238
Suzuki, H., Yamamoto, S., Ohishi, M., et al. 1992, ApJ, 392, 551
van Dishoeck, E. F. 2014, Faraday Discussions, 168, 9
Vanden Bout, P. A., Steed, J. M., Bernstein, L. S., & Klemperer, W. 1979, ApJ, 234, 503
Vastel, C., Ceccarelli, C., Lefloch, B., & Bachiller, R. 2014, ApJ, 795, L2

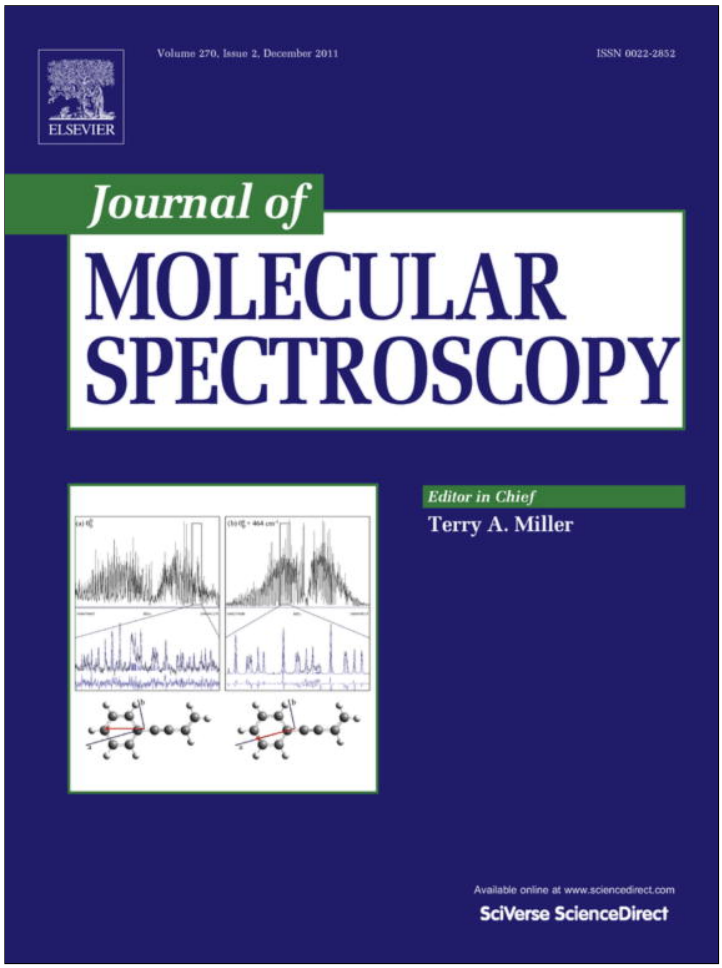

Journal of Molecular Spectroscopy 270 (2011) 116–119

Contents lists available at SciVerse ScienceDirect

Journal of Molecular Spectroscopy

journal homepage: www.elsevier.com/locate/jms

Submillimeter-wave spectroscopy of the $K = 2–1$ subband of the Ne–CO complex

A.V. Potapov [a,b,*], L.A. Surin [a,b], S. Schlemmer [a], T.F. Giesen [a]

[a] I. Physikalisches Institut, University of Cologne, Zülpicher Str. 77, 50937 Cologne, Germany
[b] Institute of Spectroscopy of Russian Academy of Sciences, 142190 Troitsk, Moscow Region, Fizicheskaya Str. 5, Russia

ARTICLE INFO

Article history:
Received 22 August 2011
In revised form 24 September 2011
Available online 4 October 2011

Keywords:
Van der Waals complex
Ne–CO complex
Supersonic jet
Rotational spectra
SuJeSTA

ABSTRACT

The pure rotational spectrum of the Ne–CO van der Waals complex has been measured in the frequency range of 208–230 GHz by using the Cologne supersonic jet spectrometer for terahertz applications (SuJeSTA). Eleven new transitions were assigned as belonging to two *R*- and two *Q*-branches of the $K = 2–1$ subband detected for the first time in the ground vibrational state of CO ($v_{CO} = 0$). Improved molecular parameters of the Ne–CO complex were obtained which allowed for a sensitive test of the available intermolecular potential energy surfaces of the Ne–CO system.

1. Introduction

Ne–CO is one of the best studied van der Waals complexes containing a rare gas atom (Rg) and the CO molecule. The fundamental interest in such systems is explained by their structural simplicity and low binding energy between Rg and CO leading to large amplitude motions within the complex. Investigating Rg–CO complexes (Rg = He, Ne, Ar, Kr, Xe) from the heavy atom system Xe–CO to the light atom system He–CO one can follow the transition from semi-rigidity to nearly free rotation of the CO molecule within the complex [1]. Ne–CO represents the crucial intermediate case between these two limits which serves as a sensitive testbed of calculated potential energy surfaces (PES).

In the first spectroscopic study Randell et al. [2] analyzed the infrared (IR) spectrum of the Ne–CO complex by combining data from a pulsed supersonic jet probed by a tunable IR laser apparatus with data from a long-path cold cell and a Fourier transform infrared (FTIR) spectrometer. The spectra of ^{20}Ne–CO and ^{22}Ne–CO were recorded in the frequency range of the CO stretching vibration mode between 2130 and 2160 cm^{-1}. The rotational levels with $K = 0$ and 1, and those of the bending state $v_2 = 1$, with $K = 0$, have been assigned (the latter only for the excited state $v_{CO} = 1$). Later pure rotational spectra have been observed applying pulsed beam Fourier transform microwave (FTMW) technique in the range of 6–26 GHz [3]. The *a*-type *R*-branch transitions within $K = 0$ of seven isotopologues of Ne–CO as well as within $K = 1$ of ^{20}Ne–CO were measured. The main isotopologue ^{20}Ne–CO has been studied in more detail in the IR frequency range by using a tunable diode laser source with a long-path low-temperature absorption cell [4]. The location of a number of new energy states of the complex, including those with $K = 2$ and 3 for both $v_{CO} = 0$ and 1, and that with $v_2 = 1$ and $K = 0$ for $v_{CO} = 0$ were determined. This work was followed by millimeter-wave (MMW) measurements of pure rotational *b*-type transitions of the $K = 1–0$ subband using an intracavity jet OROTRON spectrometer in the frequency range of 80–150 GHz [5–7]. These measurements included observation of all three ^{20}Ne, ^{21}Ne, and ^{22}Ne isotopic modifications of the complex.

The performed spectroscopic studies provided most accurate data which have been used for testing of a number of PES of Ne–CO [8–12]. A recent semi-empirical exchange-Coulomb model PES [12] gave significantly better agreement with the observed spectra from Refs. [2–7] as well as with bulk mixture properties and beam scattering data [13] as compared to earlier full *ab initio* surfaces [8–10]. A new high quality three-dimensional PES based on coupled cluster CCSD(T) method also showed good agreement with the IR experimental spectra [11].

In the present paper we extend earlier spectroscopic measurements of ^{20}Ne–CO by reporting the first direct observation of the $K = 2–1$ subband in the $v_{CO} = 0$ state. Lines belonging to *R*- and *Q*-branches between the $K = 1$ and 2 stacks were recorded and analyzed.

2. Experimental details

The supersonic jet spectrometer for terahertz applications (SuJeSTA) [14] has been used to record spectra of Ne–CO in the frequency range from 208 to 230 GHz.

* Corresponding author at: I. Physikalisches Institut, University of Cologne, Zülpicher Str. 77, 50937 Cologne, Germany.
E-mail addresses: potapov@ph1.uni-koeln.de (A.V. Potapov), surin@ph1.uni-koeln.de (L.A. Surin).

0022-2852/$ - see front matter © 2011 Elsevier Inc. All rights reserved.
doi:10.1016/j.jms.2011.09.007

The 13–14.4 GHz output frequency of a synthesizer (Agilent 83650 B) is multiplied by a commercial multiplier chain (Virginia Diodes, Inc.) to obtain output frequencies at 208–230 GHz. The sub-millimeter wave beam intersects a pulsed supersonic jet approximately 5 cm downstream in a perpendicular configuration. A multi-pass optics with 10 paths is used to enhance the signal -to-noise ratio. The absorption signal is detected by a low-noise liquid-He cooled InSb hot electron bolometer of high sensitivity. The frequency of the synthesizer is modulated at 40 kHz and phase sensitive detection of the signal is achieved by a lock-in amplifier in 2*f*-mode operation. In addition to the frequency modulation of the radiation source, an on–off modulation of the jet is used for background subtraction through a pair of boxcar integrators. Data acquisition is taken within a 1 ms time window. The combination of frequency and source modulation (double modulation technique) substantially improves the signal-to-noise ratio and at the same time suppresses standing wave etalon effects.

A gas mixture of 2% of CO in Ne at a backing pressure of 5 bar was used for production of the Ne–CO complex. The gas mixture adiabatically expanded into the multi-pass cell through a 1 mm diameter pulsed pin-hole nozzle at a repetition rate of 30 Hz. The measurements accuracy was estimated to be about 100 kHz.

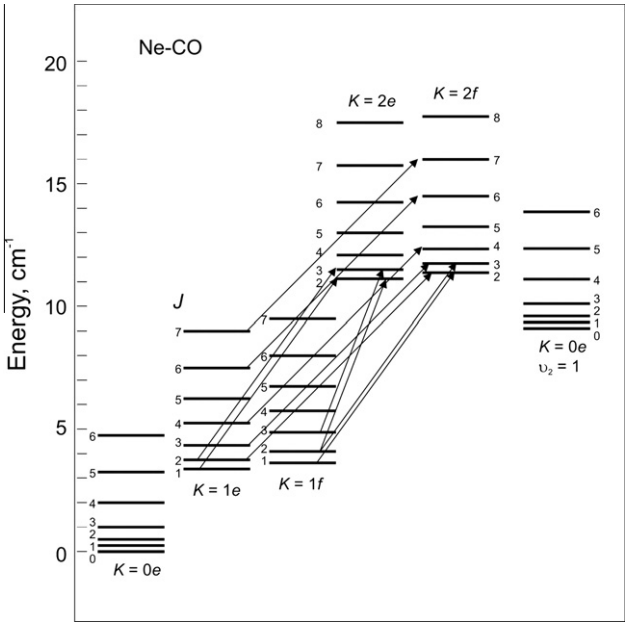

Fig. 1. Low energy level scheme of the Ne–CO complex and measured transitions.

3. Results and analysis

Previous studies have shown that Ne–CO has an approximately T-shaped structure with an effective intermolecular separation of about 3.65 Å. For this configuration, the CO dipole moment lies along the *b*-inertial axis, and thus the strongest rotational transitions have *b*-type (perpendicular) selection rules, with $\Delta K = 1$.

The following quantum numbers of a conventional semi-rigid molecule basis are used here: v_{CO} for the CO stretching vibration, v_2 for the complex bending vibration, J for the total angular momentum, K for the projection of J on the intermolecular axis. Parity labels e (+1) and f (−1) are used to assign the parity p of individual levels according to $p(-1)^J$ symmetry. The stacks of low energy levels with $K = 0$, 1 and 2 in the $v_{CO} = 0$ state of Ne–CO are shown in Fig. 1 and measured transitions are indicated by arrows.

The rotation of CO within Ne–CO is only slightly hindered and thus an alternative way of assigning energy levels of the complex is that of a free rotor basis set with j for the angular momentum of the CO unit, l for the end-over-end rotation of the complex and J for the total angular momentum. The corresponding notation for energy levels shown in Fig. 1 can be interchanged in the following way: $(J,j,l)_{K=0e} = (J,0,J)$; $(J,j,l)_{K=1e} = (J,1,J-1)$; $(J,j,l)_{K=1f} = (J,1,J)$; $(J,j,l)_{K=2e} = (J,2,J-2)$; $(J,j,l)_{K=2f} = (J,2,J-1)$; $(J,j,l)_{K=0e,v2=1} = (J,1,J+1)$.

The rotational transitions of the $K = 2$–1 subband were predicted using the set of molecular constants from the IR study by McKellar and Chan [4]. The largest difference between measured and predicted frequencies was 36 MHz. As an example Fig. 2 shows the $R(1)$ transition of the $K = 2e$–$1e$ subband recorded in second derivative due to 2*f*-mode detection technique. In total, 11 new transitions were measured and assigned, $R(1)$ and $R(2)$ of both the $K = 2e$–$1e$ and the $K = 2f$–$1f$ subband, $Q(2), Q(3), \ldots, Q(7)$ except $Q(5)$ of the $K = 2f$–$1e$ subband and $Q(2)$, $Q(3)$ of the $K = 2e$–$1f$ subband. Higher-J R-branch lines and higher-J Q-branch of $K = 2e$–$1f$ lines lie outside the currently accessible frequency range of the spectrometer. $Q(5)$ of $K = 2f$–$1e$ has not been measured because of a too low output power of the radiation source at this frequency. $Q(8)$ of $K = 2f$–$1e$ was not detected despite an extensive search most probably due to the low population of the $K = 1e$, $J = 8$ level caused by the low rotational temperature in the beam.

The simulated stick spectrum of the $K = 2$–1 subband of Ne–CO is presented in Fig. 3. The frequencies of the newly measured

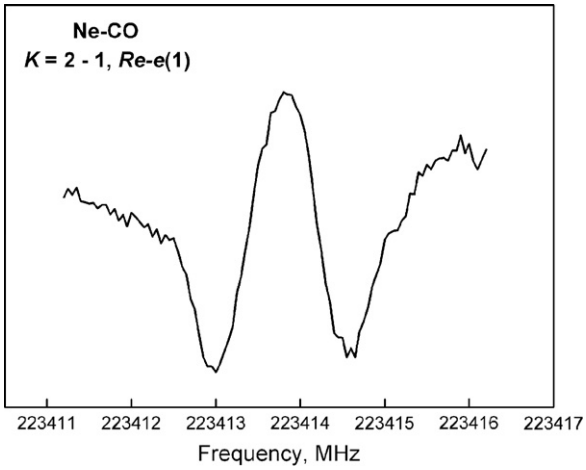

Fig. 2. Line recording of the $R(1)$ $K = 2e$–$1e$ transition of Ne–CO.

submillimeter-wave transitions are given in Table 1. Line positions were fitted together with available millimeter-wave [5–7] and microwave data [3] using the PGOPHER program, which is open to the public [15]. McKellar and Chan [4] concluded that due to very large asymmetry splitting terms for $K = 2$ and 3 it was preferable in case of Ne–CO to represent each individual stack of levels by a band origin σ plus an independent power series in $J(J+1)$ in contrast to the more common way to represent the asymmetry splitting for the $K \geqslant 1$ states by additional power series. The resulting energy expression for each K-stack therefore was extremely simple:

$$E = \sigma + B[J(J+1)] - D[J(J+1)]^2 + H[J(J+1)]^3 + L[J(J+1)]^4,$$

where B, D, H, L is a set of rotational parameters. In the fitting procedure the frequencies of the submillimeter-wave, millimeter-wave and microwave transitions were given with relative statistical weights of 1, 2 and 100 according to the corresponding measurement accuracies. Due to the limited number of observed transitions into the $K = 2e$ stack only the parameters B and D were fitted

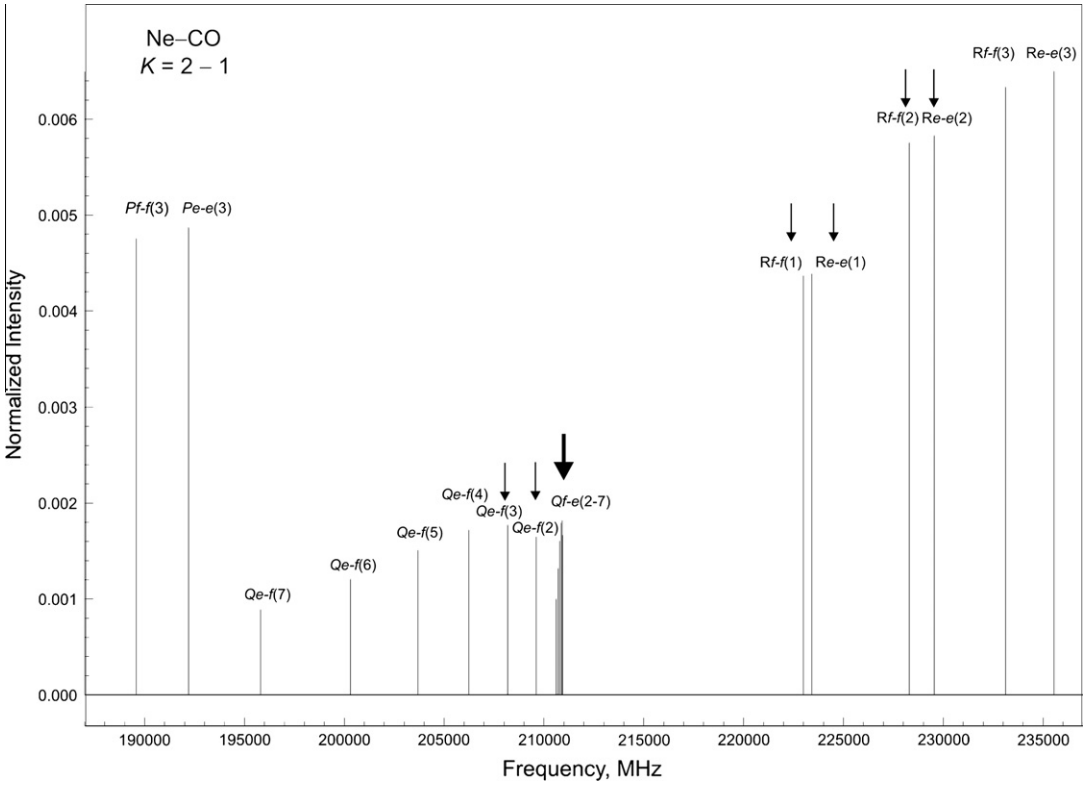

Fig. 3. Simulated stick spectrum of the $K = 2–1$ subband of Ne–CO ($T = 5$ K). Measured transitions are indicated by arrows. Bold arrow indicates closely located $Q[f \leftarrow e]$ lines.

Table 1
Observed $K = 2–1$ ground vibrational state transitions of the Ne–CO complex and comparison to high level *ab initio* results. All values are given in MHz.

J	Obs.	Fit: obs. – calc.[a]	SAPT: obs. – calc.[b]	CCSD(T): obs. – calc.[c]
$R[e \leftarrow e](J)$				
1	223413.769	0.033	578	−1064
2	229540.412	−0.050	349	−979
$R[f \leftarrow f](J)$				
1	222988.203	0.062	602	−1099
2	228298.539	−0.015	456	−1018
$Q[f \leftarrow e](J)$				
2	210937.665	−0.062	693	−1191
3	210905.300	0.015	570	−1167
4	210859.103	0.000	434	−1138
5				
6	210712.353	0.000	78	−1070
7	210604.975	0.000	−89	−1030
$Q[e \leftarrow f](J)$				
2	209601.032	−0.032	705	−1172
3	208183.228	0.051	577	−1144

[a] From molecular parameters obtained in the present work (Table 2).
[b] From energy levels calculated from *ab initio* SAPT potential [8].
[c] From molecular parameters calculated from *ab initio* CCSD(T) potential [11].

whereas σ, H and L were fixed and set to the values from the IR analysis given in Ref. [4].

The obtained set of molecular parameters is given in Table 2. The value of root mean square deviation σ_{fit} is 40 kHz which is within the limits of experimental uncertainty. For comparison the molecular parameters of Ne–CO from earlier IR [4] and MMW [7] studies are also given in Table 2. Newly obtained parameters for the $K = 0$ and 1 states are in good agreement with the previous MMW and IR values but have higher accuracies. For the $K = 2$ state the obtained molecular parameters are substantially improved, especially the D constant for the $K = 2e$ stack.

4. Discussion

In conclusion of results and analysis, the pure rotational spectrum of Ne–CO has been studied using the SuJeSTA setup. Eleven new transitions belonging to the $K = 2–1$ subband in the $v_{CO} = 0$ state were measured and assigned. The sets of molecular parameters for $K = 0$, 1 and 2 rotational states of Ne–CO were determined with high accuracy.

As it was mentioned by McKellar and Chan [4] the fact that such a large number of parameters had to be used indicates that the Ne–CO energy levels are not well determined by the sort of conventional rigid rotor approach and power series expressions for moderate distortion effects. In case of the e stacks a perturbative treatment is indicated. In particular the $K = 0$ levels of the bending excited $v_2 = 1$ state lie energetically close to, and interact with, one asymmetry component (e) of the here presented $v_2 = 0$, $K = 2$ stack (see Fig. 1), which causes an anomalously large asymmetry splitting [4]. Indeed calculated energies for the $K = 2e$ levels from constants obtained in the IR study [4] show that they start to decrease from $J = 14$ and become negative at $J = 18$. The energies for $K = 2e$ levels calculated from the constants obtained in the present work show a reasonable dependence on J values (Fig. 4).

The deviations of frequencies calculated from the obtained molecular parameters from the observed frequencies are shown in Table 1. All differences are in the limits of the experimental uncertainty. It is also interesting to compare our new results with the results of available theoretical calculations. In Table 1 we included comparison to the calculations of frequencies of the $K = 2–1$ subband from the SAPT (symmetry-adapted perturbation theory) potential [8] and from molecular parameters calculated from the most recent

Table 2
Molecular parameters for Ne–CO (all values in cm^{-1}).

		Present	Previous MMW [7]	Previous IR [4]
$j_{CO} = 0$, $K = 0$	σ_e	0	0	0
	B_e	0.108732739(19)	0.108732784(52)	0.10873159(91)
	D_e	$0.1286424(228)\times10^{-4}$	$0.128709(48)\times10^{-4}$	$0.12834(38)\times10^{-4}$
	H_e	$-0.57245(1286)\times10^{-8}$	$-0.546(16)\times10^{-8}$	$-0.379(25)\times10^{-8}$
	L_e	$0.36638(3494)\times10^{-10}$	$0.342(55)\times10^{-10}$	$-0.0376(45)\times10^{-10}$
	M_e	$0.1141(51)\times10^{-13}$	$0.1224(49)\times10^{-13}$	
$j_{CO} = 1$, $K = 1$	σ_e	3.21613936(80)	3.21613820(51)[a]	3.2161(1)[a]
	B_e	0.104259443(31)	0.104259458(66)	0.10426483(107)
	D_e	$0.118604(37)\times10^{-4}$	$0.118631(64)\times10^{-4}$	$0.12338(46)\times10^{-4}$
	H_e	$-0.9248(165)\times10^{-8}$	$-0.912(26)\times10^{-8}$	$-0.160(33)\times10^{-8}$
	L_e	$0.4525(2292)\times10^{-11}$	$0.35(39)\times10^{-11}$	$-4.234(68)\times10^{-11}$
	σ_f	3.21613823(85)	3.21613820(51)[a]	3.2161(1)[a]
	B_f	0.111609823(23)	0.111609830(60)	0.11161397(99)
	D_f	$0.123288(24)\times10^{-4}$	$0.123319(51)\times10^{-4}$	$0.12653(48)\times10^{-4}$
	H_f	$-0.69783(1299)\times10^{-8}$	$-0.678(16)\times10^{-8}$	$-0.1198(30)\times10^{-8}$
	L_f	$0.35348(3528)\times10^{-10}$	$0.334(55)\times10^{-10}$	$-0.1780(50)\times10^{-10}$
$j_{CO} = 2$, $K = 2$	σ_e	10.2548[b]		10.2548(4)[a]
	B_e	0.10372652(59)		0.103737(38)
	D_e	$0.03604(52)\times10^{-4}$		$0.0908(117)\times10^{-4}$
	H_e	-65.40×10^{-8}[b]		$-65.40(133)\times10^{-8}$
	L_e	21.05×10^{-10}[b]		$21.05(49)\times10^{-10}$
	σ_f	10.2532953(21)		10.2548(4)[a]
	B_f	0.1040912(11)		0.104036(15)
	D_f	$0.1239(11)\times10^{-4}$		$0.1206(15)\times10^{-4}$
	H_f	$-2.10(30)\times10^{-8}$		$-1.245(46)\times10^{-8}$
	L_f	$1.08(27)\times10^{-10}$		

[a] Band origin is common for *e* and *f* stacks.
[b] Fixed values from IR work [4].

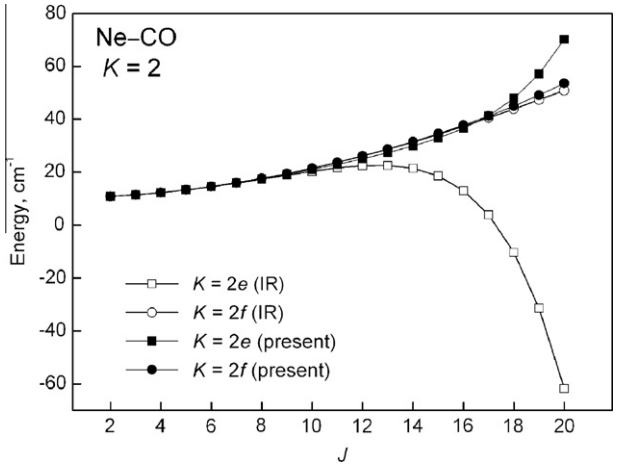

Fig. 4. Dependencies of calculated energies for the $K = 2e$ and $K = 2f$ levels from constants obtained in the IR [4] and present studies on total angular momentum J.

and advanced CCSD(T) potential [11]. The differences between the measured and the SAPT calculated frequencies are of the order of hundreds of megahertz, which is reasonable but spectroscopically significant. Comparison with frequencies derived from the CCSD(T) calculations [11] show a systematic deviation of the order of 1 GHz due to inappropriate theoretical values of band origins for the $K = 1$ and 2 states. Surprisingly the frequencies from the SAPT calculations are in better agreement with our experimental results than the values from the CCSD(T) calculation. This is in opposite to the author's conclusion [11], based on comparison of both methods with the IR experiment [4] for the two $K = 0$–0 subbands.

Acknowledgments

AVP acknowledges financial support from the DAAD (Stipendien für Forschungsaufenthalte für Hochschullehrer und Wissenschaftler). This work was supported in part by the Deutsche Forschungsgemeinschaft (DFG) via Research Grants GI 319/1-3, SCHL 341/10-1, and SU 579/1-2. The support of the Institute of Spectroscopy at Troitsk through Grants of the Russian Foundation for Basic Research (09-02-00813 and 11-02-91342) is gratefully acknowledged by LAS and AVP.

References

[1] B.S. Dumesh, L.A. Surin, Phys. Usp. 49 (11) (2006) 1113.
[2] R.W. Randall, A.J. Cliffe, B.J. Howard, A.R.W. McKellar, Mol. Phys. 79 (1993) 1113.
[3] K.A. Walker, T.O. Ogata, W. Jäger, M.C.L. Gerry, I. Ozier, J. Chem. Phys. 106 (1997) 7519.
[4] A.R.W. McKellar, M.-C. Chan, Mol. Phys. 93 (1998) 253.
[5] G. Winnewisser, B.S. Dumesh, I. Pak, L.A. Surin, F. Lewen, D.A. Roth, F.S. Rusin, J. Mol. Spectrosc. 192 (1998) 243.
[6] D.A. Roth, I. Pak, L.A. Surin, B.S. Dumesh, G. Winnewisser, Z. Naturforsch. 55a (2000) 754.
[7] L.A. Surin, A.V. Potapov, V.A. Panfilov, B.S. Dumesh, G. Winnewisser, J. Mol. Spectrosc. 230 (2005) 149.
[8] R. Moszinski, T. Korona, P.E.S. Wormer, A. Van der Avoird, J. Phys. Chem. A 101 (1997) 4690.
[9] G.C. McBane, S.M. Cybulski, J. Chem. Phys. 110 (1999) 11734.
[10] V. Subramanian, K. Chitra, D. Sivanesan, R. Amutha, S. Sankar, Chem. Phys. Lett. 307 (1999) 493.
[11] Z. Wang, E. Feng, H. Yu, C. Zhang, J. Du, J. Chem. Phys. 134 (2011) 024320.
[12] A.K. Dham, F.R.W. McCourt, W.J. Meath, J. Chem. Phys. 130 (2009) 244310.
[13] A.K. Dham, G.C. McBane, F.R.W. McCourt, W.J. Meath, J. Chem. Phys. 132 (2010) 024308.
[14] M. Caris, T.F. Giesen, C. Duan, H.S.P. Müller, S. Schlemmer, K.M.T. Yamada, J. Mol. Spectrosc. 253 (2009) 99.
[15] PGOPHER, C.M. Western, 2008. <http://pgopher.chm.bris.ac.uk>.

PCCP

PAPER

View Article Online
View Journal | View Issue

Cite this: *Phys. Chem. Chem. Phys.*, 2017, **19**, 17224

Conformational landscape of the SF_6 dimer as revealed by high resolution infrared spectroscopy and complexation with rare gas atoms

Pierre Asselin, *[ab] Alexey Potapov,[c] Andrew C. Turner,[d] Vincent Boudon,[e] Laurent Bruel,[f] Marc-André Gaveau [g] and Michel Mons [g]

Received 18th April 2017,
Accepted 13th June 2017

DOI: 10.1039/c7cp02529g

rsc.li/pccp

Taking advantage of a versatile set-up, combining pulsed pin hole or slit nozzle supersonic expansion with an external cavity quantum cascade laser, the rovibrational absorption spectrum of the SF_6 dimer in the ν_3 mode region has been revisited at high resolution under various experimental conditions in SF_6:He mixtures. Two new rotationally resolved spectral bands have been identified in the range of the parallel band of the dimer spectrum in addition to that previously reported. Among these three spectral features, two of them are assigned to conformations of the dimer (noted #1 and #2), clearly distinguished from their different S–S interatomic distances, *i.e.* 474 and 480 pm respectively. The third one is assigned to a $(SF_6)_2$–He complex, from comparison with additional experiments in which $(SF_6)_2$–Rg heterotrimers (Rg = Ne, Ar, Kr, Xe) are observed. A schematic picture of the potential energy landscape of the SF_6 dimer in terms of a nearly flat surface is proposed to account for the conformational relaxation observed in the expansions and for the structure of the $(SF_6)_2$–Rg heterotrimers, which are exclusively formed from the conformer #2 dimer. Although modelling qualitatively supports this picture, much effort has still to be achieved from a theoretical point of view to reach a quantitative agreement with the present benchmark experimental data both in terms of structure and energetics.

I. Introduction

van der Waals complexes of apolar molecules are challenging species for theoreticians of molecular interactions.[1–3] Owing to the large contribution of dispersive interactions to the energetics of these systems, an accurate theoretical description requires great effort to be done to account for electronic correlation effects, including for systems as simple as the iconic SF_6 dimer. The pioneering work of van Bladel *et al.* using an atom–atom potential predicted two structures of $(SF_6)_2$, of high symmetry, the lowest one of D_{2d} symmetry, more stable by about 0.4 kJ mol^{-1} than the second one of C_{2h} symmetry.[4] Thereafter a more sophisticated intermolecular potential model taking into account atom-atom repulsion, dispersion, electrostatic and induced dipole intermolecular interactions ended up with similar conclusions.[5] More recently, the conformational landscape of $(SF_6)_2$ has been reinvestigated, with a specific focus on the nature of the interaction between the monomers, using MP2 and symmetry-adapted perturbation theory in conjunction with large basis sets and correction for basis set superposition error (BSSE).[6] Both methods indicated the existence of a unique minimum energy structure of C_2 symmetry, surrounded by two saddle point structures, one of C_{2h} symmetry at +0.1–0.2 kJ mol^{-1} and another of D_{2d} symmetry (at +0.4–0.5 kJ mol^{-1} above the minimum). The very small energy difference calculated between these remarkable structures suggests a nearly flat potential energy surface, which questions the stability order computed, considering that (i) the energy difference is probably of the order of the accuracy of the method, (ii) the C_{2h} structure becomes the most stable one once zero-point energy (ZPE) corrections are carried out and (iii) optimizations were performed without counterpoise correction of the BSSE.

From the experimental side, infrared spectroscopy provides an interesting set of data against which the theoretical picture can be assessed. Many spectroscopic infrared data have indeed been collected in the past decades on the dimer, though most of them at a low resolution.[7–12]

Several groups[7–13] used powerful line-tunable cw CO_2 and N_2O lasers to excite the dimers formed in a continuous supersonic

[a] *Sorbonne Universités, UPMC Univ Paris 06, UMR 8233, MONARIS, F-75005, Paris, France. E-mail: pierre.asselin@upmc.fr*
[b] *CNRS, UMR 8233, MONARIS, F-75005, Paris, France*
[c] *Laboratory Astrophysics Group of the Max Planck Institute for Astronomy at the Friedrich Schiller University Jena, Germany*
[d] *Department of Chemistry, University of Florida, Gainesville, Florida, USA*
[e] *Laboratoire Interdisciplinaire Carnot de Bourgogne, UMR 6303 CNRS Université Bourgogne Franche-Comté, 9 Av. A. Savary, BP 47870, F-21078 Dijon, France*
[f] *CEA Marcoule, DEN, Bagnols-sur-Cèze, France*
[g] *LIDYL, CEA, CNRS, Université Paris-Saclay, CEA Saclay, 91191 Gif-sur-Yvette, France*

free jet or solvated in large H_2[13] and Ar[14] clusters and on the surface of large rare gas cluster[14–16] and measured the absorption either from the depletion of a dimer signal or from the detection of dissociation fragments. The spectral region of the triply degenerate ν_3 vibration of the SF_6 monomer at 948 cm^{-1} has been found to exhibit two broad peaks, one blue-shifted and the other red-shifted from the monomer band, interpreted as resulting from a resonant dipole–dipole coupling between the two SF_6 molecules. The first high resolution gas phase measurements using laser diode spectroscopy, by Urban and Takami,[17] provided the most accurate band centers of the parallel and perpendicular bands of the dimer at 934.01 and 956.10 cm^{-1}. The intensity alternation and the existence of a first-order Coriolis interaction observed in the rotational structure of the perpendicular band were interpreted as the most stable structure of $(SF_6)_2$ being of D_{2d} symmetry.[17] The partially resolved rotational structure enabled the authors to report a S–S distance of 475 pm in the dimer. High-resolution laser spectrum of small SF_6 clusters embedded in large He droplets also displays a partially resolved rotational structure proving their nearly free rotation in the helium droplet environment.[18] Such an ultra-low temperature sensitive method enables to study any weakly bound complex but the increase of the moments of inertia due to the proximity of He atoms inhibits to derive structural information related to a free gaseous environment.

Owing to this discordant set of data, the high resolution infrared spectroscopy of the SF_6 dimer has been reinvestigated, taking advantage of an infrared tunable laser spectrometer recently developed in our laboratory, which combines a pulsed supersonic jet with an external cavity quantum cascade laser (EC-QCL) working in the 10.5 μm region. The rapid scanning scheme used for data acquisition provides a much larger detectivity with respect to supersonic expansions coupled to Fourier Transform Infrared (FTIR) spectrometers. Moreover, the two types of nozzle used (pin hole *vs.* slit) offer a variety of experimental conditions suitable to address the issue of the existence of conformers in this system.

II. Experimental details

The vibration–rotation spectra have been recorded thanks to the coupling of an external-cavity quantum cascade laser (EC-QCL) with a pulsed supersonic jet.[19] The SF_6 clusters are generated either in a planar or an axisymmetric supersonic expansion for different dilutions of SF_6 in He, ranging from 0.25 to 4% (in pressure), at backing pressures of Helium (Air Liquide) of 6 bar. The light source is a continuous-wave room-temperature mode-hop-free EC-QCL with a spectral width of 10 MHz, which covers the 930–990 cm^{-1} range (Daylight Solutions). About 8% of the total light is sent through two laser channels for relative and absolute frequency calibrations. Relative frequencies are monitored by measuring the intensity transmitted through a solid germanium etalon with a free spectral range of 490 MHz, to provide a relative frequency scale. Absolute laser frequencies are obtained by measuring the transmission through a 15 cm-length reference cell containing a known reference gas at a pressure of about 5 mbar (ethene in the present work). The remaining light is sent through a multipass optical cavity mounted in the jet chamber, which is evacuated by a 2000 l s^{-1} oil diffusion pump backed by a combination of a 350 m^3 h^{-1} Roots blower and a 40 m^3 h^{-1} rotary pump. For the present study two different optical configurations were successively used: a near-concentric Perry cavity[20] providing 20 passes, with a focal point half way between two spherical mirrors, and an astigmatic cavity composed of two 1.5″ astigmatic mirrors (R = 99.2%, AMAC-36, Aerodyne Research), aligned according to a 182-pass configuration. Three liquid-nitrogen-cooled HgCdTe detectors (Judson J15D12) are used to measure the powers transmitted through the multipass cavity, the etalon and the reference gas cell. The molecular jet is produced from a pulsed nozzle (General Valve Series 9) either in standard configuration with a 0.35 mm diameter (D) pinhole, or by fitting the pin hole nozzle with two modified industrial blades, forming a 30 mm length × 50 μm width (l) slit opening, and serving as the molecular expansion source.[21] Molecular complexes were probed by the infrared laser light at z average distances between 9 and 18 mm from the nozzle exit. The z values are only indicative because the zone Δz probed in the jet by the two optical cavities is relatively large (several mm) and corresponds to a large range of reduced distances z/D (z/l). A good balance between efficient rovibrational cooling (rotational temperature T_R = 1–3 K) and high molecular density was found even at longer distances up to z = 18 mm for slit jet expansions and at shortest distances (z = 12 mm) for pin hole jet expansions. Our rapid scan scheme described in detail elsewhere[22,23] is close to the original designs used for high resolution molecular spectroscopy. Fine tuning of the laser frequency over about 0.8 cm^{-1} at a repetition rate of 100 Hz is obtained by a sine wave generated by a Labview code and delivered to a piezoelectric transducer attached to the diffraction grating that ends the external cavity. The intensities transmitted through the supersonic jet, the etalon and the reference gas cell are digitized and recorded simultaneously as a function of time. A baseline-free transmittance through the multipass cavity is then obtained by taking the ratio of the corresponding signals recorded with and without the jet. The procedure for absolute frequency calibration is achieved *a posteriori* by measuring the deviation between experimental and HITRAN12 database C_2H_4 frequencies to correct the free spectral range value of the etalon fixed at the beginning of each experiment. The accuracy of the frequency calibration is around 0.0001 cm^{-1}.

III. Results

III.1. Evidence for three different features in He:SF_6 mixtures

We started our investigation from the parallel band region (932–935 cm^{-1}) in order to search for other rovibrational signatures than the band detected by Urban and Takami[17] composed of three $^QP(J,K)$ $^QQ(J,K)$ and $^QR(J,K)$ branches, as expected for a parallel transition (ΔJ = 0, ±1 and ΔK = 0).

With respect to this previous study, significant changes in the spectral features could be obtained by changing the SF_6/He

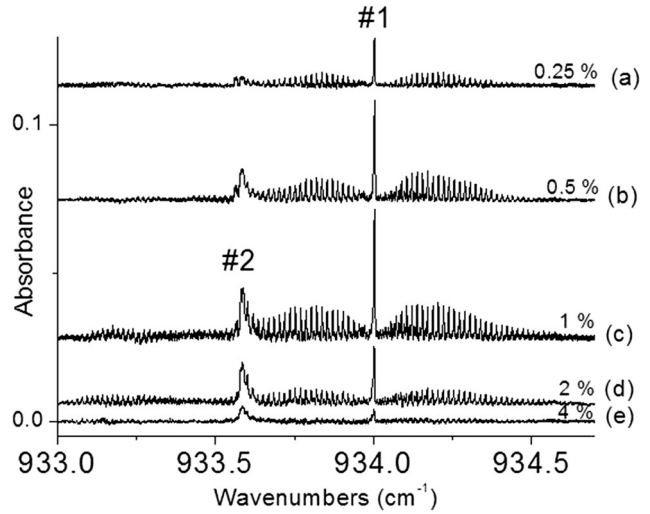

Fig. 1 EC-QCL jet-cooled spectra of the parallel band of $(SF_6)_2$ for (a) 0.25%, (b) 0.5%, (c) 1%, (d) 2%, (e) 4% SF_6 diluted in 6 bar helium at an axial distance z = 9 mm from the slit nozzle.

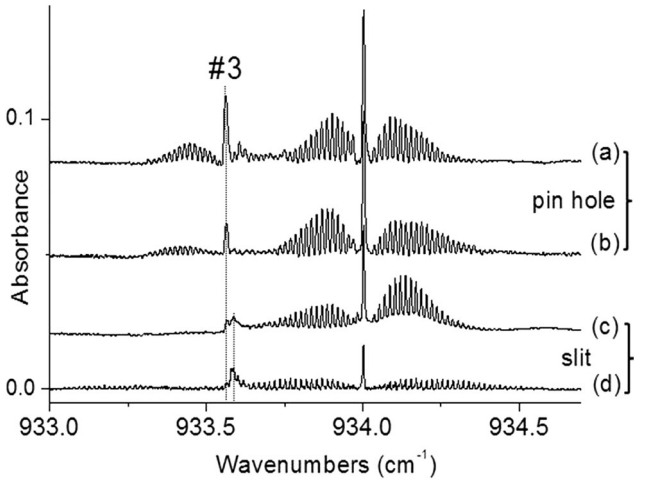

Fig. 2 Spectra of the parallel band of $(SF_6)_2$ for different configurations of nozzle geometry/axial distance z from the nozzle exit and SF_6 concentration in He at a backing pressure of 6 bar: (a) pin hole nozzle at z = 12 mm with 0.25% SF_6; (b) pin hole, z = 12 mm, 0.5% SF_6; (c) slit nozzle, z = 18 mm, 0.5% SF_6 and (d) slit nozzle, z = 9 mm, 0.5% SF_6.

mixture ratio as well as the nozzle geometry. From these different conditions, corresponding to different collision regimes, one expects to gain useful information on relaxation effects in the supersonic expansions, and in fine information about conformational populations, relative stabilities and final temperatures achieved. Fig. 1 displays a series of jet-cooled EC-QCL spectra of the parallel band of $(SF_6)_2$ by expanding SF_6:He mixtures (SF_6 concentrations ranging from 0.25 to 4%) at a pressure of 6 bar through a pulsed slit nozzle (slit width 50 μm). The rotational band contour observed (noted hereafter #1) is composed of an intense $^QQ(J,K)$ branch at 934.0 cm^{-1} accompanied with well J-resolved $^QP(J,K)$ and $^QR(J,K)$ branch lines from J'' = 30 for P to J'' = 37 for R, in agreement with the high resolution spectrum of Urban and Takami.[17] The K substructure is not resolved in our experimental linewidth (100 MHz), limited by residual collisional and Doppler broadenings.

More interestingly, a new spectral feature (noted hereafter #2), not detected in the previously published spectrum, is observed at 933.58 cm^{-1} whatever the concentration. It is composed of a ^QQ branch, accompanied by weaker ^QP and ^QR branch lines (clearly visible in Fig. 1 at 0.5–2% SF_6 concentrations) interleaved between the more intense lines of the #1 band. As shown in Fig. 1, intensities of both #1 and #2 bands begin to increase as the SF_6/He ratio increases, and then drop significantly between 1–2%. However, one notices that the ratio #2/#1 increases monotonically, from close to 0 at small concentration up to 2 at 4%, suggesting a real population reversal between these radically different regimes. Also one notes that at small concentrations, band #2 seems to exhibit a satellite band on its red (low frequency) side.

In a second step, different configurations of nozzle geometry, z axial distance and SF_6 concentration at the same backing pressure of 6 bar have been selected to test differential relaxation effects on the high resolution parallel band spectra of $(SF_6)_2$ (Fig. 2). With respect to the series of spectra in Fig. 1, statistic noise was significantly reduced by a substantial increasing of the number of averaging cycles, as illustrated by the better signal-to-noise ratio obtained for the slit nozzle spectrum (0.5% SF_6 at z = 9 mm) in Fig. 2d compared to that in Fig. 1b. Comparison of the 4 spectra shows that the satellite band to the red of #2 (Fig. 1a and b) turns out to be an additional well-defined feature (hereafter referred to as #3), prominent at low concentrations (Fig. 2a and b) with the pin hole nozzle, but much less abundant with the slit (Fig. 2c and d). This feature, not detected previously, is observed at 933.56 cm^{-1} and is also composed of a ^QQ branch, accompanied by weaker ^QP and ^QR branch lines (clearly visible in Fig. 2 at 0.25–0.5% SF_6 concentrations) interleaved between more intense lines of the #2 band.

From these concentration studies, it appears that the two new features (#2 and #3) reach an absorption intensity, and therefore a population, comparable to that of the previously reported dimer feature (#1). However the expansion conditions that favor them correspond to different ranges of SF_6 concentration and expansion temperatures. #3 appears exclusively at low concentrations and in low temperature expansions (pin hole nozzle), whereas #2 seems to be rather favored by higher temperatures and concentrations. These puzzling properties cast some doubts about the stoichiometry of these species, inasmuch as one the vibrational spectral shifts of #2 and #3 are very close. One could for instance have one of these features being a He complex and the other a SF_6 cluster, *e.g.* a second conformation of the dimer or a trimer, for instance.

III.2 Band contour analysis of the #2 feature

The simulations (Fig. 3 and 4) of the parallel band of the three features #1–3 (Fig. 2a and d) assuming a symmetric top structure allowed us to obtain the best fit molecular parameters $\nu_\parallel$, B'' and B' for each of them (Table 1). Since the K structure is not resolved, K was set to zero and consequently A'' and A' could not be determined. Due to the higher rotational temperature

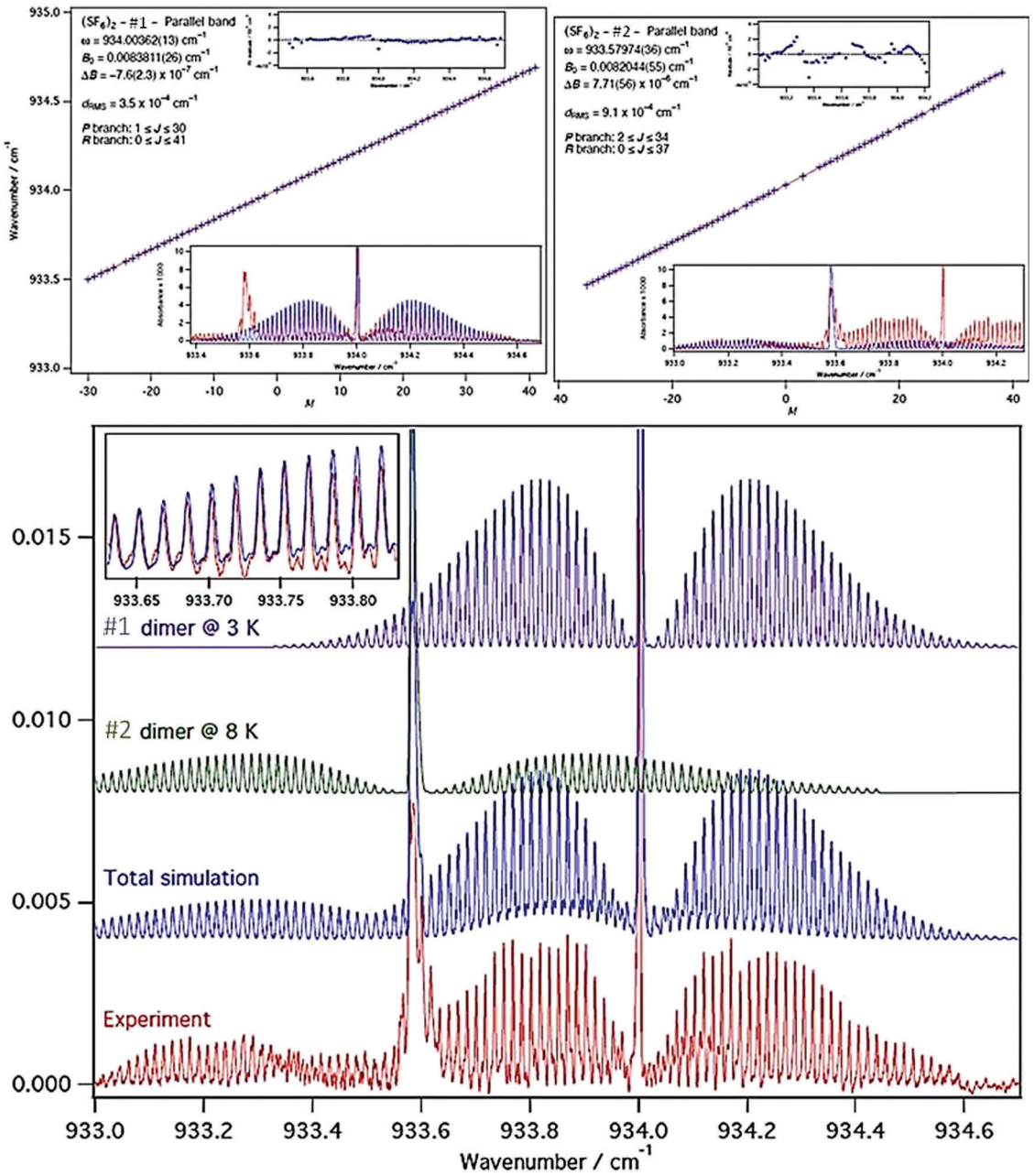

Fig. 3 Bottom panel: Comparison between the "hot slit" nozzle spectrum of the parallel band of $(SF_6)_2$ recorded with 0.5% SF_6 seeded in 6 bar He at z = 9 mm (Fig. 2d) and the rovibrational simulation of two band contours of #1 and #2 spaced from 0.424 cm^{-1} at respective rotational temperatures of 3 and 8 K, top panel: observed (+) and calculated (solid lines) wavenumbers *versus* M ($M = -J$ for the P branch and $J + 1$ for the R branch, respectively), residues for observed minus calculated spectra of #1 and #2 conformers.

achieved with the planar expansion, larger intensities of high J lines with respect to the previous high resolution study enabled us to improve the accuracy for the structure of the band #1. For the first time, molecular parameters were obtained for the bands #2 and #3.

At this stage, the experimental rotational constants of B'' of both #1 and #2 features were used to derive accurate experimental S–S distances (Table 1), assuming that the monomer structure does not change upon dimer formation. The S–S distance obtained for conformer #1 (474 pm) fits well the previous value deduced by Urban and Takami (475 pm[17]). Concerning the band #2, the precision achieved is large enough to assert the presence of a second SF_6 dimer, distinct from #1, and characterized by a S–S distance of 480 pm. Much lower T_R values are attained with the pin hole jet spectrum (Fig. 2a), simulated with the band contours of #1 and #3 structures (Fig. 4) and nearly equal T_R values for both conformers (0.8 K). The fit obtained (Fig. 3) agrees well with the slit jet spectrum (Fig. 2d) provided that overlapping rotational band contours at two different rotational temperatures (T_R = 3 K for #1 and 8 K for #2) are introduced; this point will be discussed below.

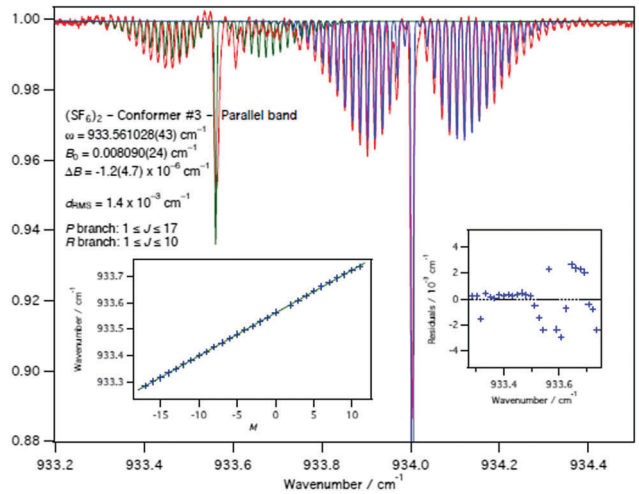

Fig. 4 Top panel: Comparison between the pin hole nozzle spectrum of the parallel band of $(SF_6)_2$ recorded with 0.25% SF_6 seeded in 6 bar He at z = 12 mm (Fig. 2a) and the rovibrational simulation of two band contours of #1 and #3 spaced from 0.402 cm^{-1} at the same rotational temperature of 0.8 K, bottom panel left: observed (+) and calculated (solid lines) wavenumbers *versus* M ($M = -J$ for the P branch and $J + 1$ for the R branch, respectively) of the #3 feature, right: residues for observed minus calculated wavenumbers of the #1 conformer and the #3 feature.

B97D3 calculations (DFT with the D3 dispersive correction[24]) were realized to evaluate the possibility of a SF_6 trimer as band carrier of #2. The theoretical results show that this hypothesis can be ruled out: (i) the computed ground state rotational constants B'' of the SF_6 trimer are smaller than that of the dimer by more than 10%, which is largely incompatible with the results of our contour analysis which yields B'' values #1 and #2 differing by 2.5% only (Table 1), (ii) a blue shift of about 4–5 cm^{-1} is calculated between the band centers of both SF_6 trimer and dimer bands, in agreement with photodissociation experiments[10,12] and force field calculations[4,5] but in disagreement with the red shift observed for band #2 with respect to #1 of SF_6 dimer, (iii) the theoretical splitting in two intense parallel bands to the C_3 axis for the SF_6 trimer contradicts the unique experimental band to be assigned in the parallel band region. These arguments indeed confirm that the #2 feature is a second conformer of SF_6 dimer.

III.3 New spectroscopic data about #3 feature from SF_6:Rg:He mixtures (Rg = rare gas)

In order to provide additional information on the third species observed (#3), in particular about the presence of complexes with the carrier gas such as $(SF_6)_2$–He, additional spectroscopic slit nozzle experiments have been carried out with He expansions containing traces of SF_6 and of a rare gas (Rg = Ne, Ar, Kr, Xe). The corresponding spectra recorded in the parallel band region using very diluted (0.5%) SF_6/Rg equimolar mixtures seeded in 6 bar helium are shown in Fig. 5. They all exhibit rotational band contours of #1 and #2, accompanied by additional features. The most intense of them (identified by an asterisk) is comparable in intensity to #1 or #2; it is located to the red side of the #2 feature, and its position increases with the rare gas mass. Noticeably, no such satellite band is observed in the vicinity of band #1.

These observations bring invaluable information in relation with #3. Indeed, based on band intensity and equimolar mixture considerations, these most intense new bands, located respectively at 933.548, 933.433, 933.345 and 933.185 cm^{-1} when going from Ne to Xe, are tentatively assigned to the respective $(SF_6)_2$–Rg complexes. We will not discuss here the assignment of other weaker bands observed which could correspond either to isomers of $(SF_6)_2$–Rg related to the position of the Rg atom or to larger $(SF_6)_2$–Rg_2 complexes. Further experiments necessary to validate their assignments are beyond the scope of the present study. More enlightening is the dependence of the vibrational shift $\Delta\nu$ of these $(SF_6)_2$–Rg complex bands, relative to the ^QQ

Table 1 Molecular parameters for the two conformers of $(SF_6)_2$ and $(SF_6)_2$He (expressed in cm^{-1}, apart from the S–S distances in pm). Parentheses represent the one standard deviation in units of the last digit. The S–S distance marked by an asterisk corresponds to the rotational analysis of the $(SF_6)_2$–He heterotrimer band, assuming a symmetric top dimer (*cf.* Section III.3)

Experiment			
Parameters	#1 of $(SF_6)_2$	#2 of $(SF_6)_2$	$(SF_6)_2$–He
$\nu_{\parallel}$	934.00362(13)	933.57974(36)	933.561028(43)
B'	0.0083803(28)	0.0082121(61)	0.008089(29)
B''	0.0083811(26)	0.0082044(55)	0.008090(24)
$\nu_{\perp}$	956.09502(37)	—	—
A'	0.04551 (fixed)	—	—
A''	0.04554(6)	—	—
ζ (unitless)	0.66796(70)	—	—
S–S′ (v = 0) (ref. 17)	475.4(1)		
S–S′ (v = 0) (this work)	474.2(1)	480.1(2)	484.4(8)*
Quantum chemistry			
Vazhappilly (MP2)[6]	472.6 (C_2)	473.0 (C_{2h} optimized) 483.6 (D_{2d} optimized)	
This work B97-D3	505.6 (C_i, close to D_{3d}) 500.2 (D_{3d} optimized)	508.3 (C_1, close to C_2)[6] 517.3 (C_1, close to D_{2d}) 522.3 (D_{2d} optimized)	
Force field			
van Bladel[4]	497 (D_{2d})	508 (C_{2h})	
Beu (potential I)[5]	490 (D_{2d})	503 (C_{2h})	

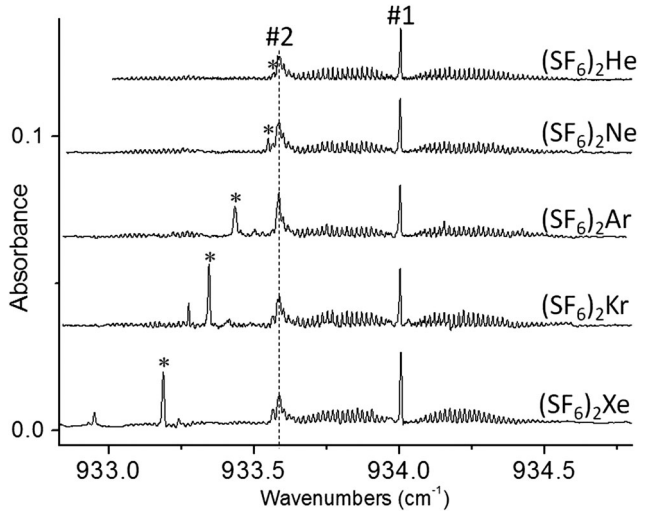

Fig. 5 Spectra of different $(SF_6)_2$–Rg heterotrimers (Rg = He, Ne, Ar, Kr, Xe) in the parallel band region of $(SF_6)_2$ recorded with the slit nozzle at an axial distance z = 9 mm and 0.5% SF_6 concentration in He at a backing pressure of 6 bar: for all spectra except for that with pure helium, a SF_6:Rg equimolar concentration is used. The most intense ^QQ branches marked with an asterisk are assigned to $(SF_6)_2$–Rg complexes and their respective band centers are used to plot the vibrational shift dependence with the polarizability of the rare gas atom.

branch frequency of feature #2 (Fig. 6) as a function of the polarizability α of the rare gas atom. This graph provides evidence for a remarkable linear dependence between $\Delta\nu$ and α, as expected for systems essentially stabilized by dispersive interactions. This correlation suggests that these species are composed of the #2 dimer complexed by a single rare gas atom, whose complexation site does not vary significantly with the rare gas, presumably in the vicinity of the median plan of the SF_6 dimer, perpendicular to the S–S distance. Interestingly, for the #3 feature, its vibrational shift fits well the linear dependence of Fig. 6 if one assumes an helium complexation partner, suggesting that this feature should be assigned to a helium complex of the #2 dimer. The corresponding spectral shift is consistent with the vibrational red shift induced by a He atom ($\sim$0.02 cm^{-1}) expected from previously reported diffusion Monte Carlo computations about SF_6–He_N interactions.[25]

One will also notice a striking point: the fact that whatever the Rg considered, no additional band in the vicinity of the #1 dimer, that could be assign to a #1 dimer complexed by rare gas atom(s), is observed, emphasizing a quite intriguing specificity of #1 compared to #2 in terms of complexation.

Lastly, B97D3 calculations[24] were realized to determine whether the band contour obtained from the rotational constants of a top symmetric band (that of a SF_6 dimer) could be differentiated from the expected top asymmetric band of the $(SF_6)_2$–He heterotrimer. Geometry optimization of the most stable structure of $(SF_6)_2$–He yields a position of the He atom slightly shifted with respect to the symmetry plane of the dimer perpendicular to the S–S axis, as a result of the non symmetric interaction with one fluor atom on one side and two on the other side. Consequently, the trimer is no longer a symmetric top, but the difference between the B'' and C'' constants is not large enough for the spectrum to be distinguished from that of symmetric top, within our experimental widths: the calculated B'' constant of the trimer is only 2% smaller, in agreement with the slightly smaller (1.5%) experimental rotational constants of $(SF_6)_2$–He compared to #2 of SF_6 dimer (Table 1). This result shows that the rotational analysis of the #3 band as consistent with that of a symmetric top does not provide an unambiguous assignment to a symmetric species, in case of complexation by a rather light complexation partner like He.

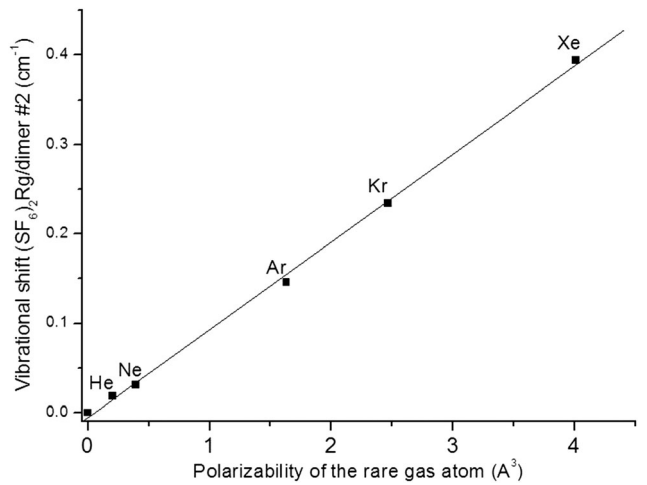

Fig. 6 Graph of the vibrational shift $\Delta\nu$ between the ^QQ branch frequencies of five $(SF_6)_2$Rg hetero trimers and the band center of the conformer #2 of $(SF_6)_2$ *versus* the polarizability α of the corresponding Rg atom. The remarkable dependence between $\Delta\nu$ and α proved by the linear fit inquires about the structure of these hetero trimers formed from the #2 subunit.

IV. Discussion

IV.1 Conformational landscape of the dimer

A systematic study of the dependence of various spectroscopic features as a function of the expansion conditions, *i.e.*, nozzle type, backing pressure, SF_6 concentration and z axial distance, allowed us to provide additional information about the formation of the dimers and the interconversion processes that take place between the #1 and #2 forms of the dimer. The behavior of the $(SF_6)_2$–He trimer band with respect to dimer bands will be also examined.

– In the pin hole expansion, performed at low SF_6 concentration and high backing pressure (Fig. 2a), transient SF_6–SF_6 and SF_6–He complexes can lead to stable dimers either directly from bimolecular (SF_6–SF_6)–He collisions or through (SF_6–He)–SF_6 collisions, the latter process being expected to be competitive because of a substantial population is expected for the SF_6–He complex: its low binding energy being compensated by a large rate of collisions between SF_6 and the carrier gas, at least in the early expansion. The high generating pressures (6 bar) enable to cool down the species formed, namely the dimer #1 accompanied with a significant population of the heterotrimer #3. Low rotational temperatures are eventually

achieved for each of these species (T_R = 0.8 K). As the SF_6 concentration increases (Fig. 2b), the early SF_6–SF_6 collisions are more efficient to form the dimer and its signal increases relative to #3. The temperature is also higher, as indicated by the shift of the maximum of the *R* and *P* branch envelops, due to the larger population of SF_6 monomers in the expansion, making it more difficult to cool down.

– Slit expansions are slower than pin hole ones, meaning that the collision rates are larger at the same reduced distances (z/D for pin hole, z/l for slit).[26] Thus comparison between spectra at different z distances enable us to diagnose effects of collision-induced relaxations taking place in the slit expansion, whereas in pin hole nozzles they would take place too early in the expansion to be efficiently observed. In the early slit expansion, (Fig. 2d; $z \sim 9$, corresponding to a reduced distance $z/l \sim 180$), both dimers #1 and #2 are present in the expansion, with comparable intensities. However, the population ratio #2/#1 drops from ~40% down to ~10%, when one moves away from the nozzle to 18 mm ($z/l \sim 360$; Fig. 2c), demonstrating that an efficient collisional relaxation process occurs and leads to a significantly population conversion from #2 into #1, indicating both a larger stability of #1 as the temperature decreases, together with a relatively low energy #2 → #1 interconversion barrier, that can be overcome under these low temperature conditions.

A second informative point can be derived from the population dependence upon the SF_6 concentration in the slit nozzle (Fig. 1). As the concentration increases, the SF_6–SF_6 and SF_6-dimer collision rates increase as well as the formation of larger complexes/clusters. #2 is strongly favored under these collisions, suggesting a mode of formation in the expansion significantly different from that of #1. Population #2 is consistent with hot complexes formed under early expansion conditions in presence for collisions with SF_6 monomers. The rotational temperatures measured in the slit expansion support this interpretation: they are found to be different for the two conformers ($T_R \sim 3$ K for #1, and 8 K for #2), in agreement with distinct modes of formation and/or different spatial distributions of these species in the expansion, since the near concentric multipass cavity[20] used for the slit measurements actually probes a relatively large range of distances from the nozzle (z = 9–12 mm; $z/l \sim 180$–240). One can note that in these hot expansions, the population of the hetero-trimer #3 remains small, in relation with the low binding energy of the He atom to the dimer. These considerations lead us to tentatively propose the qualitative picture of Fig. 7 for the potential energy surface of the SF_6 dimer. The dimer form #1 observed in both fast/cold and slow/hotter expansions, is formed under cold conditions of homo dimer, and can be assigned to well-defined minima of the surface. In contrast, #2 is favored by hot conditions, suggesting a ''floppy'', entropically stabilized species, compatible with the existence of frequent collisions with other heavy species $(SF_6)_n$ in the expansion, and illustrated by a conformer ''located'' on a flat surface, possibly delocalized over identical minima. Such a qualitative picture is consistent with the larger S–S distance obtained from the rotational analysis (Table 1). It is also consistent with the structure of the $(SF_6)_2$–Rg hetero-trimers, which are shown to be built on a #2 dimer. These trimers

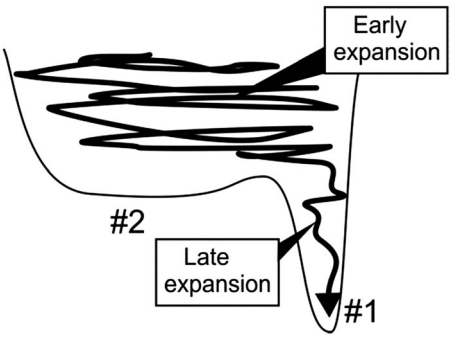

Fig. 7 Scheme of the potential energy surface of the SF_6 dimer, proposed to account for the present observations.

are formed from (SF_6–SF_6)–Rg or (SF_6–Rg)–SF_6 collisions, and require additional collisions with the carrier gas to be stabilized. In this case the interaction of the rare gas with each of the monomers is probably large enough to hamper the formation of the most stable dimer within the complex, which eventually favors the second most stable dimer form #2. Such an interpretation is supported by the high symmetry assumed for dimer #1 (D_{2d}, see below), whose geometry would forbid to the complexation partner to establish identical interactions with each of the SF_6 molecules, which would favor the #1 → #2 interconversion in the complex.

IV.2 Symmetry

The band contours of the perpendicular transitions should be in principle indicative of the existence of high symmetry in the system. This was the origin of the assignment of #1 to a D_{2d} species by Urban and Takami.[17]

Perpendicular band spectra of $(^{32}SF_6)_2$ recorded with slit and pin hole nozzles in the same conditions as the parallel band are displayed in Fig. 8. The ''cold slit'' spectrum recorded at large z (Fig. 8b) resembles to the previous high resolution one,[17] in agreement with large contribution of #1 and the low T_R achieved. The pin hole spectrum (Fig. 8a) exhibits a broad unresolved hump in the red (centered at 955.7 cm^{-1}), that we assign to the perpendicular transition of $(SF_6)_2$–He, expected to be populated under these conditions (Fig. 2a). Similarly, in the ''hot slit'' spectrum recorded at small z (Fig. 8c), additional systems of lines (around 955.75 cm^{-1}) overlap the rotational structure of the ^PQ branches of #1 and to a lesser degree of the ^RQ ones. They are assigned to the cold band of the #2 structure of $(SF_6)_2$, red shifted by about 0.4 cm^{-1} in the parallel band region.

The simulation of the #1 band (Fig. 9) does match well with a first-order Coriolis interaction but not with the intensity alternation expected for a D_{2d} symmetry. Taking into account the very flat potential energy surface of SF_6 dimer, a coupling between low frequency geared rotation motions[4] and the total angular momentum of the ν_3 vibration is quite possible and could influence the rovibrational pattern.

As to the #2 band, the high rovibrational temperature of the ''hot slit'' spectrum makes difficult to bring a reliable proof of a high symmetry, *e.g.* C_{2h}. In such a structure the ν_3 vibration is

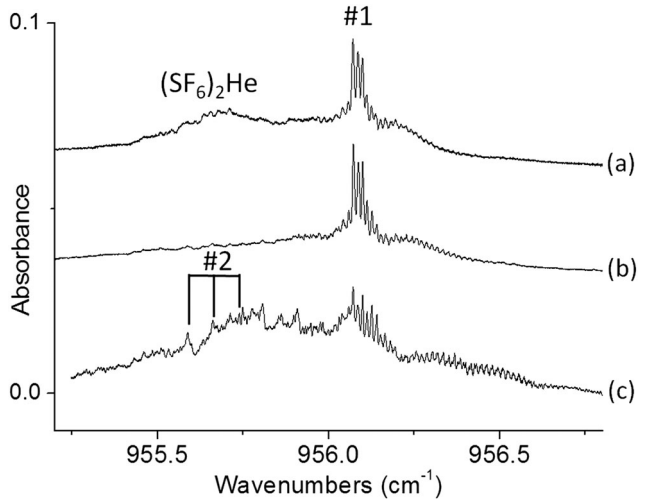

Fig. 8 Spectra of the perpendicular band of $(SF_6)_2$ for a concentration of 0.5% SF_6 in He at a backing pressure of 6 bar, for several nozzle geometries and axial distances z from the nozzle exit: (a) pin hole nozzle at z = 12 mm; (b) slit nozzle at z = 18 mm, and (c) slit nozzle at z = 9 mm (c).

lifted to one redshifted parallel band and two blue shifted perpendicular bands without first-order Coriolis interaction, *i.e.* with a spacing close to $2(A' - B')$ as observed for $(SiF_4)_2$.[27] In the case of $(SF_6)_2$ the spacing between $^{P,R}Q(J,K)$ branches would be equal to about 0.075 cm^{-1}. The first members of this series could belong to the bands at 955.588, 955.663 and 955.739 cm^{-1} on the *P*-branch side (Fig. 8c) but a definite proof of the rovibrational signature of C_{2h} structure cannot be obtained from the present data. About the trimer band #3, the absence of a structured pattern for the perpendicular top asymmetric band of the pin hole spectrum (Fig. 8a) is consistent with the symmetry lowering due to the He atom.

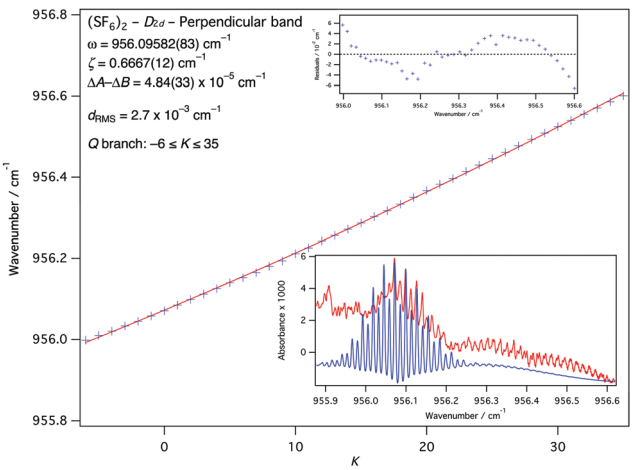

Fig. 9 Observed wavenumbers (+) of the "cold slit" spectrum for the perpendicular band of $(SF_6)_2$ recorded with 0.5% SF_6 seeded in 6 bar He at z = 18 mm and calculated wavenumbers of #1 conformer (solid lines) *versus* K by taking only the frequency positions of $^{P,R}Q_{K''}$ branches up to K'' = 3 (*P*-branch) and K'' = 27 (*R*-branch) adjusted at a rotational temperature of 0.8 K. Top panel: Residues for observed minus calculated wavenumbers of #1 conformer. Bottom panel: Comparison between experimental (top) and calculated (bottom) spectra in the $^{P,R}Q$ branch region.

One should note that the spectral shifts of dimer #2 and of the trimer #3, relative to the monomer, remain similar whatever the transition considered, parallel or perpendicular. This shift being an indicator of the way the ν_3 modes do couple to each other, it confirms that the structure of the $(SF_6)_2$ subunit in the trimer is very similar to that of #2.

IV.3 Experiment-theory comparison

At this stage it is interesting to compare the present experimental set of information, namely the existence of two different dimers, to the theoretical picture of the potential energy surface. The agreement is only qualitative, in the sense that the surface is flat, since admitting several identical minima as well as remarkable points (*e.g.* of high symmetry) of comparable energetics (within a range as low as a few kJ mol^{-1}). Our present calculations (Table 1 and Fig. 10) at the DFT-D level of theory (RI-B97-D3/TZVPP[24] using the TurboMole package[28]), chosen in order to account efficiently for dispersive interactions, confirm the flat surface picture, with at least 3 minima with electronic energies within less than 0.7 kJ mol^{-1}, *i.e.*, far below the precision expected for the calculations. They also confirm that the nature of the remarkable structures (minimum *vs.* saddle points) and their ordering strongly depends on the method used. However, beyond this qualitative agreement, discrepancies between calculations are found as soon as one goes into details, either S–S distances or energetics and symmetry of the most stable forms, and, worse, no agreement is found with experiment. For example, MP2 calculations predict a range of S–S distances very close to

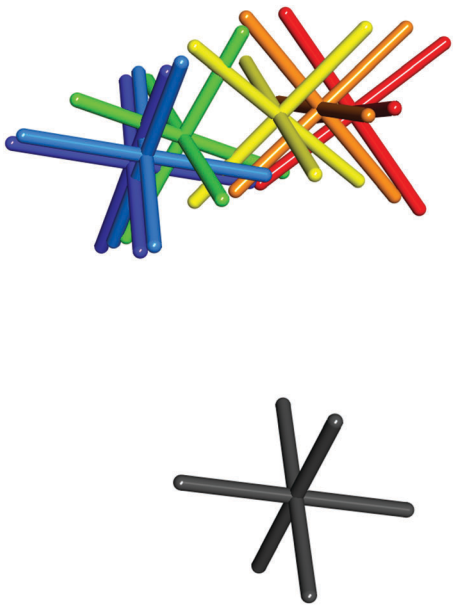

Fig. 10 Minimum structures found for the dimer at the RI-B97-D3/TZVPP level of theory. The picture is obtained by an overlay of one of the monomers (in gray) and by displaying the second one in color: dark blue, D_{3d}-optimized structure; light blue, C_i minimum, close to the D_{3d} structure; green, C_1 structure, close to that of the C_2 minimum of Vazhappilly *et al.*;[6] yellow, lowest C_1 structure; orange, C_1 structure close to a D_{2d} structure; red, D_{2d} optimized structure. The respective relative electronic energies are 16, 0, 28, 1, 56 and 100 cm^{-1} expressed with respect to the C_i minimum.

that of experiment, but the structure that matches the S–S distance of species #1 is the theoretical minimum of C_2 symmetry, inconsistent with the high symmetry suggested by the pattern of the perpendicular band. Semi-empirical potentials provide two minima of D_{2d} and C_{2h} symmetry, that could match both experimental symmetry and distance ordering, but the absolute S–S bond length values are grossly overestimated by 3–4%. Interestingly enough, DFT-D results nevertheless suggest several minima with elongated S–S distances compared to experiment, but with a fair range of dependence upon conformation. No candidate is clearly identified to account for structure #2, and, owing to the unique shallow character of the potential energy surface, the possibility of a vibrational level with a large amplitude motion, possibly delocalized over multiple identical minima, cannot be ruled out.

V. Conclusion

In summary, the versatile tunable infrared laser spectrometer recently developed in our laboratory has been exploited to probe the conformational landscape of the SF_6 dimer by combining different geometries of supersonic expansions, SF_6 concentrations seeded in He and axial probe distances. Two conformers #1 and #2 have been unambiguously identified on the grounds of 2 distinct S–S distances derived from the rovibrational analysis of the parallel band contours of the ν_3 transition. A specific dynamics of formation has been evidenced for each conformer from the evolution of their relative populations in cold/fast and slow/hot expansions. Furthermore a third intense rovibrational band in the pin hole spectrum could be assigned to the $(SF_6)_2$–He trimer, from a series of additional experiments in presence of a rare gas in the He expansion, which provided unambiguous evidence for the formation of $(SF_6)_2$–Rg hetero trimers. The spectroscopic evidence that these hetero trimers are only built upon #2 dimers illustrates the lack of robustness of the #1 dimer, owing to external perturbations, including complexation with a He atom. This result is in agreement with the qualitative picture of a #2 dimer entropically favored, especially in presence of a rare gas collision partner, separated by a low barrier from the most stable #1 form, characterized by a narrow well. Lastly, the poor agreement between experimental observations and existing calculations in terms of number of different minima, S–S distances, energetics and symmetry of the most stable forms, is a strong incentive to apply more sophisticated approaches to the electronic and vibrational degrees of freedom of these systems.

Acknowledgements

We would like to thank one of the reviewers for his/her invaluable comments about the possible involvement of He complexes in the expansions. AP acknowledges COST Action CM1401 ''Our Astro-Chemical History''. ACT thanks NSF IREU grant # 1659782, CNRS, UPMC (Paris VI), University of Florida.

References

1 K. Müller-Dethlefs and P. Hobza, *Chem. Rev.*, 2000, **100**, 143.
2 S. Grimme, J. Antony, T. Schwabe and C. Muck-Lichtenfeld, *Org. Biomol. Chem.*, 2007, **5**, 741.
3 W. Hujo and S. Grimme, *Phys. Chem. Chem. Phys.*, 2011, **13**, 13942.
4 J. W. I. van Bladel and A. van der Avoird, *J. Chem. Phys.*, 1990, **92**, 2837.
5 T. A. Beu and K. Takeuchi, *J. Chem. Phys.*, 1995, **103**, 6394.
6 T. Vazhappilly, A. Marjolin and K. J. Jordan, *J. Phys. Chem. B*, 2016, **120**, 1788.
7 M. Snels and J. Reuss, *Chem. Phys. Lett.*, 1987, **140**, 543.
8 M. Snels and R. Fantoni, *Chem. Phys.*, 1986, **109**, 67.
9 J. Geraedts, S. Setiadi, S. Stolte and J. Reuss, *Chem. Phys. Lett.*, 1981, **78**, 277.
10 J. Geraedts, M. Waayer, S. Stolte and J. Reuss, *Faraday Discuss. Chem. Soc.*, 1982, **73**, 375.
11 T. E. Gough, D. G. Knight, P. A. Rowntree and G. Scoles, *J. Phys. Chem.*, 1986, **90**, 4026.
12 B. Heijmen, A. Bizzarri, S. Stolte and J. Reuss, *Chem. Phys.*, 1989, **132**, 331.
13 S. Goyal, D. L. Schutt, G. Scoles and G. N. Robinson, *Chem. Phys. Lett.*, 1992, **196**, 123.
14 T. E. Gough, M. Mengel, P. A. Rowntree and G. Scoles, *J. Chem. Phys.*, 1985, **83**, 4958.
15 S. Goyal, D. L. Schutt and G. Scoles, *Phys. Rev. Lett.*, 1992, **69**, 933.
16 S. Goyal, D. L. Schutt and G. Scoles, *J. Phys. Chem.*, 1993, **97**, 2236.
17 R.-D. Urban and M. Takami, *J. Chem. Phys.*, 1995, **103**, 9132.
18 M. Hartmann, R. E. Miller, J. P. Toennies and A. F. Vilesov, *Science*, 1996, **272**, 1631.
19 P. Asselin, Y. Berger, T. R. Huet, R. Motiyenko, L. Margulès, R. J. Hendricks, M. R. Tarbutt, S. Tokunaga and B. Darquié, *Phys. Chem. Chem. Phys.*, 2017, **19**, 4576.
20 D. Kaur, A. M. Souza, J. Wanna, S. A. Hammad, L. Mercorelli and D. S. Perry, *Appl. Opt.*, 1990, **29**, 119.
21 Z. Su, S. Tam and Y. Xu, *J. Chem. Phys.*, 2006, **124**, 024311.
22 M. D. Brookes, C. Xia, J. A. Anstey, B. G. Fulsom, K.-X. Au Yong, J. M. King and A. R. W. McKellar, *Spectrochim. Acta, Part A*, 2004, **60**, 3235.
23 X. Liu, Y. Xu, Z. Su, W. S. Tam and I. Leonov, *Appl. Phys. B: Lasers Opt.*, 2011, **102**, 629.
24 S. Grimme, *J. Comput. Chem.*, 2006, **27**, 1787.
25 R. N. Barnett and K. B. Whaley, *J. Chem. Phys.*, 1993, **99**, 9730.
26 D. R. Miller, in *Atomic and Molecular Beam Methods*, ed. G. Scoles, Oxford University Press, New-York, 1988, vol. 1, p. 14.
27 R.-D. Urban and M. Takami, *J. Chem. Phys.*, 1995, **102**, 3017.
28 TURBOMOLE V6.4 2012, a development of University of Karlsruhe and Forschungszentrum Karlsruhe GmbH, 1989–2007, TURBOMOLE GmbH, since 2007; available from http://www.turbomole.com.

The Astrophysical Journal, 846:131 (5pp), 2017 September 10 https://doi.org/10.3847/1538-4357/aa85e8

The Formation of Formaldehyde on Interstellar Carbonaceous Grain Analogs by O/H Atom Addition

Alexey Potapov[1], Cornelia Jäger[1], Thomas Henning[2], Mindaugas Jonusas[3,4], and Lahouari Krim[3,4]
[1] Laboratory Astrophysics Group of the Max Planck Institute for Astronomy at the Friedrich Schiller University Jena, Institute of Solid State Physics, Helmholtzweg 3, D-07743 Jena, Germany; alexey.potapov@uni-jena.de
[2] Max Planck Institute for Astronomy, Königstuhl 17, D-69117 Heidelberg, Germany
[3] Department of Chemistry, Sorbonne Universités, UPMC Univ Paris 06, UMR 8233, MONARIS, Paris F-75005, France
[4] CNRS, UMR 8233, MONARIS, Paris F-75005, France
Received 2017 May 23; revised 2017 August 9; accepted 2017 August 9; published 2017 September 11

Abstract

An understanding of possible scenarios for the formation of astrophysically relevant molecules, particularly complex organic molecules, will bring us one step closer to the understanding of our astrochemical heritage. In this context, formaldehyde is an important molecule as a precursor of methanol, which in turn is a starting point for the formation of more complex organic species. In the present experiments, for the first time, following the synthesis of CO, formaldehyde has been produced on the surface of interstellar grain analogs, hydrogenated fullerene-like carbon grains, by O and H atom bombardment. The formation of H_2CO is an indication for a possible methanol formation route in such systems.

Key words: astrochemistry – dust, extinction – ISM: molecules – methods: laboratory: solid state – molecular processes – techniques: spectroscopic

1. Introduction

Chemical processes leading to the formation of molecules in the interstellar medium (ISM) can be divided into two groups, gas phase and grain surface reactions. These two formation routes interact with each other due to the adsorption of gas phase molecules on the surface of grains and the desorption of "solid" molecules to the gas phase. Interstellar dust grains are mainly amorphous carbon- or silicate-based particles (Dorschner & Henning 1995; Draine 2003). In regions of low temperature and high density they are covered by molecular ices. Interstellar ices covering dust grains are known to be a source of complex organic molecules (COMs) detected in the ISM (Herbst & van Dishoeck 2009). An alternative route of COM formation could be grain surface processes in regions where the grains are not covered by ices.

The main triggers of grain surface chemistry in the ISM are UV irradiation, cosmic rays, thermal processing, reactions with radicals, and atom addition. The last process is very important in all cold ISM phases. Among the atom addition reactions, hydrogenation and oxygenation are the two most important cases. H and O, due to their mobility, can diffuse across the surface of grains and react with other species on the surface (Congiu et al. 2014). Hydrogen is the most abundant element in the universe, and thus is the main trigger of the ice chemistry, responsible for the formation of key molecules, such as H_2, H_2O, NH_3, and CH_3OH. Oxygen is the third most abundant element in the universe. It was found that several times more gaseous O than CO has to be present in cold molecular clouds (Vastel et al. 2000; Lis et al. 2001; Hollenbach et al. 2009). The uptake of elemental oxygen on interstellar siliceous and carbonaceous grains was quantified for diffuse and dense molecular clouds, providing presumptive evidence for an organic refractory component of interstellar grains with significant oxygen content (Whittet 2010). A substantial amount of interstellar oxygen may freeze out on interstellar grains in the form of molecular oxygen, a process that may explain the low abundance of O_2 in the gas phase of molecular clouds (Acharyya et al. 2007; Goldsmith et al. 2011; Chen et al. 2014). A surprisingly high amount of O_2 was detected in the coma of comet 67P/Churyumov–Gerasimenko and was found to be associated with water (Bieler et al. 2015), suggesting that molecular oxygen was incorporated into water ice. In fact, studies show that O_2 may have been incorporated in H_2O ice in the prestellar phase and then entered the disk intact and formed comets (Mousis et al. 2016).

Thus, O atoms on grains in interstellar clouds can directly come from the gas phase or from dissociated solid O_2 molecules. The latter process is definitely more efficient in diffuse molecular clouds and photon-dominated regions, where photodissociation takes place. Atomic oxygen interacting with solid hydrocarbons can trigger an active surface chemistry (Jones 2016). It was shown, for example, that oxygen atoms can readily add to carbon–carbon double bonds on a graphite surface at temperatures of interstellar clouds to produce epoxide rings (Ward & Price 2011), which can be a basis for further interstellar chemistry. For protoplanetary disks a selective erosion of carbonaceous materials by free oxygen atoms has been investigated (Lee et al. 2010; Anderson et al. 2016). It was found that given sufficient turbulence to lift small grains into the oxidative surface regions of the disk, carbon grains are rapidly converted into CO. This could also happen in the inner part of disks (Finocchi et al. 1997).

Many laboratory experiments have been performed on the formation of simple and complex molecules, including amino acids, in interstellar ice analogs using the main triggers mentioned above (for a review see Theule et al. 2013; Linnartz et al. 2015; Öberg 2016). A major part of the laboratory work deals with molecular ices covering standard substrates not related to the ISM, such as metals, KBr, or HOPG. The grain surface can participate in ice chemistry and can alter the efficiency of molecule formation. A different COM formation route is grain surface chemistry. In pioneering experiments on the formation of molecules in grain-ice systems, CO and CO_2 were produced by irradiation of hydrogenated carbon grains

covered by water ice with He^+ ions (Mennella et al. 2004) and by Lya photons (Mennella et al. 2006). These experiments were followed by the synthesis of CO_2 in H_2O ice covering amorphous carbon foil by irradiation with protons (Raut et al. 2012), and in O_2 ice covering amorphous carbon foil by ultraviolet irradiation (Fulvio et al. 2012). Finally, the formation of CO and CO_2 in H_2O and O_2 ices on hydrogenated fullerene-like carbon grains after proton bombardment (Sabri et al. 2015), and in H_2O ice on graphite films by Lyα irradiation (Shi et al. 2015), were demonstrated.

It is well known that "non-energetic" hydrogenation of CO leads to the formation of formaldehyde and methanol in molecular ices (Hiraoka et al. 1994, 2002; Watanabe & Kouchi 2002; Chuang et al. 2017) following a simple reaction chain:

$$CO \rightarrow HCO \rightarrow H_2CO \rightarrow H_3CO \rightarrow CH_3CO. \quad (1)$$

Most of the CO ice in the ISM is considered to be formed through accretion of CO molecules from the gas phase on the surface of grains at low cloud temperatures (Tielens et al. 1991; Boogert et al. 2015). However, one more possible mechanism for CO formation is an O atom addition reaction on a carbonaceous surface, which can be quite efficient in interstellar clouds, as was discussed above.

In the context of an alternative route of COM formation—grain surface processes—the purpose of the present work is to synthesize H_2CO and CH_3OH molecules by bombardment of the surface of hydrogenated fullerene-like carbon grains (interstellar grains analogs) by O and H atoms without a pre-existing ice layer.

2. Experimental Part

2.1. Hydrogenated Fullerene-like Carbon Grains

A 40 nm thick layer of hydrogenated fullerene-like carbon grains was formed by pulsed laser ablation of a graphite target, produced by mixing ^{13}C powder (carbon-^{13}C, sigma aldrich, 99.2 atom% ^{13}C) with polyethylene, heating, and pressing. The target contained ^{13}C:^{12}C in a ratio of 8:1, but, as was further obtained from the IR spectra, the deposited grains contained only about 10% of ^{13}C. There can be a number of explanations for this result, such as, for example, that ^{12}C included in polyethylene desorbs more efficiently from the target surface than ^{13}C powder. The ablation was followed by subsequent condensation of evaporated species in a quenching atmosphere of He:H_2, with a mixing ratio of 5:2 in volume at a pressure of 4 mbar and final deposition on a KBr substrate. The particles in the condensation zone are characterized by very small diameters between 1 and 4 nm and the deposited material represents a very early stage of particle aggregation. The details of this experiment can be found elsewhere (Jäger et al. 2008, 2009).

The grains are composed of small, strongly bent graphene layers with varying lengths and distances between these layers (see Figure 1). The grain structure can be described as amorphous, showing a typical structureless halo in the Fourier-transformed bright field images. The individual particles are very small (less than 3–4 nm) and the largest particle agglomerates are in a range of 15 nm. The morphology of the dust particle agglomerates on the substrate can be understood as a porous layer of rather fractal agglomerates. The density of the grains was determined to be about 1.7 g cm^{-3} and the porosity of the deposited dust is very high and was found to be about 90% (Sabri et al. 2015). The surface of the dust is very large, but the area cannot be measured exactly. We note here that bent graphene layers are very reactive and may easily adsorb molecules.

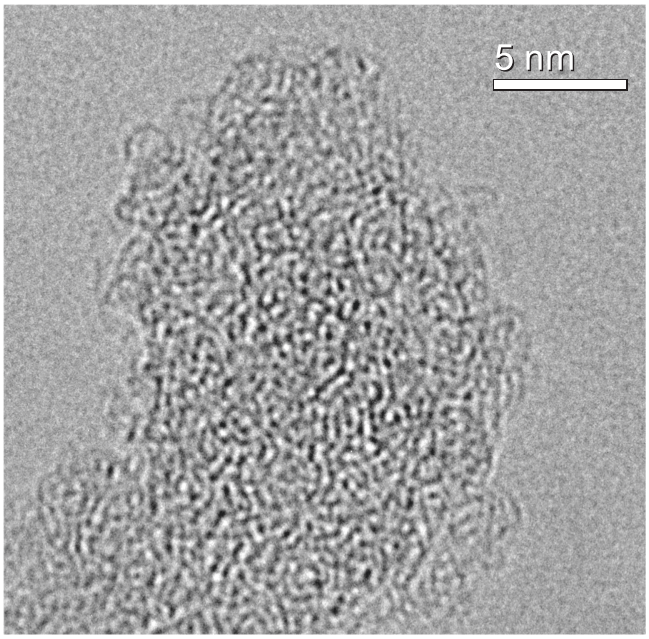

Figure 1. High-resolution transmission electron microscopy image of the deposited hydrogenated carbon grains.

2.2. Atom Addition Experiment

The sample was fixed on a cryogenic polished copper mirror. The experiment was performed in a high vacuum chamber with a base pressure of 10^{-8} mbar. The temperature of the mirror was 10 K. The IR spectra were recorded in the transmission-reflection mode between 5000 and 500 cm^{-1} with a resolution of 0.5 cm^{-1}, using a Bruker Vertex 80v FTIR spectrometer equipped with a liquid-N_2-cooled narrowband HgCdTe photoconductor. Spectra recorded prior to the bombardment of the sample were used as background spectra in the treatment of the final sample spectra.

Atoms were generated from molecular dissociations using a microwave-driven atomic source (SPECS, PCS-ECR), where inside the plasma chamber, the electron cyclotron resonance (ECR) method is used to achieve massive dissociation of molecules. Our ECR atomic source has a specially designed aperture that inhibits the release of ions from the plasma while allowing neutral atoms and molecules to effuse out (Pirim & Krim 2011). An additional tube has been added after the plasma aperture to eliminate UV photons, a known problem of atom sources (Hiraoka et al. 2002). The source is schematized in Figure 2. The atomic flux has been estimated from the amount of molecular species injected during the bombardment, while the molecular dissociation yield has been measured using a quadrupole mass spectrometer (QMS—Hidden Analytical). The atomic flux was assessed to be about 10^{17} atoms cm^{-2} s^{-1} and arrives onto the substrate thermally cooled, due to numerous atom–molecule collisions in the expansion. In our experiments, gas mixtures of O_2:H_2 1:60 or 10:70 (in pressure) were injected at 0.5 bar into the plasma chamber. The gas expanding from the plasma chamber is a combination of both

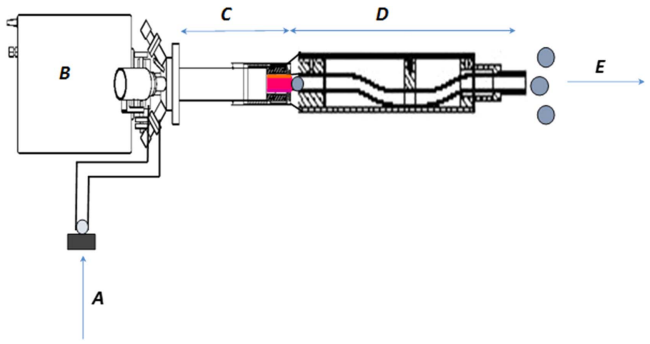

Figure 2. PCS-ECR atomic source with a tube added after the plasma apertures to eliminate UV photons. A—molecular gas input, B—Microwave generator, C—Plasma discharge zone, D—Teflon tube, E—Atomic beam exit.

atomic and molecular species with dissociation yields of 15% and 40% for H_2 and O_2, respectively. The bombardment was performed for 30 minutes with the final fluence of 1.8×10^{20} atoms cm^{-2}.

3. Results

Figure 3(a) shows the IR signatures of the carbon grains on a KBr substrate at 10 K, characterized by peaks at around 2900 cm^{-1} corresponding to the saturated $-CH_3$ and $-CH_2$ groups and two narrow peaks at 3486.8 and 3446.8 cm^{-1}, which are temperature-dependent (more intense at lower temperature) and are due to impurities or inclusions in the KBr substrate. The absorption signals due to carbon grains located between 1800 and 600 cm^{-1} are also observable. We can assign the band at 1735 cm^{-1} to the C=O vibration (the presence of a small amount of O in the carbon grains was demonstrated earlier (Jäger et al. 2008)). The 1620 and 1468 cm^{-1} bands are caused by the C=C vibration and C–H deformation, respectively. The bands between 1000 and 700 cm^{-1} are in the range where many vibrations of functional groups are merged together and it is difficult to distinguish between individual vibrations. Figure 3(b) shows the result of H bombardment of carbon grains where no new signal has been detected. However, an increase of C–H bands at around 2900 cm^{-1} can be observed that can be related to an incorporation of hydrogen into the carbon grains. Figure 3(c) shows the result of the O/H bombardment of carbon grains using a low amount of oxygen in the discharged mixture ($[O_2]/[H_2] = 1/60$), whereas Figure 3(d) shows the result of the O/H bombardment with a higher O fraction in the mixture ($[O_2]/[H_2] = 10/70$) discharged.

In addition, pure O bombardment has also been realized (see Figure 4). In this case, mainly CO_2 and O_3 were formed on the top of the carbon grains. All the ν modes in Figure 4 are fundamental, harmonic, and combination modes of O_3.

Figure 5 shows the corresponding difference spectra before and after the atom bombardment presented in Figure 3. From Figures 5(a) and (b) we note that a number of reaction products are formed after O/H bombardment: CO, CO_2, H_2CO, H_2O, and H_2O_2. However, the relative amounts of these products depend strongly on the composition of the O_2–H_2 mixtures discharged. In the inset of Figure 5, which zooms in on the 3300–1000 cm^{-1} spectral range, one can observe that with a low amount of oxygen atoms, mainly CO, CO_2, H_2CO, and H_2O were formed, while the increase of the oxygen fraction in the O_2–H_2 mixture considerably increases the amount of CO_2,

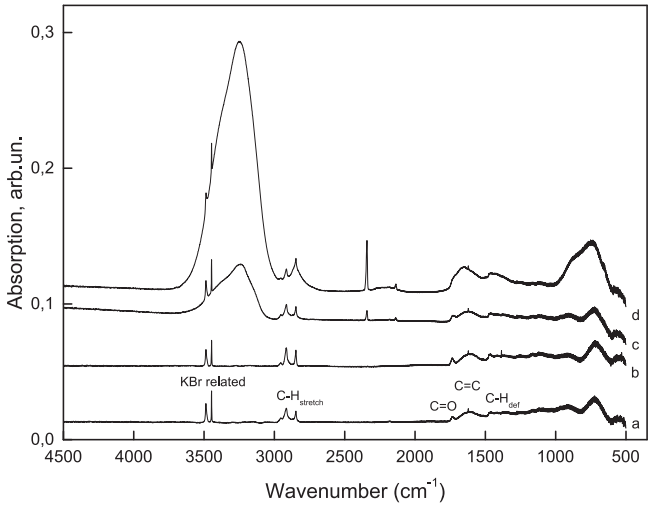

Figure 3. IR spectra recorded at 10 K (a) of carbon grains, (b) after H bombardment of carbon grains, (c) after O/H bombardment of carbon grains using a low amount of atomic oxygen ($[O_2]/[H_2] = 1/60$), and (d) after O/H bombardment of carbon grains using a high amount of atomic oxygen ($[O_2]/[H_2] = 10/70$).

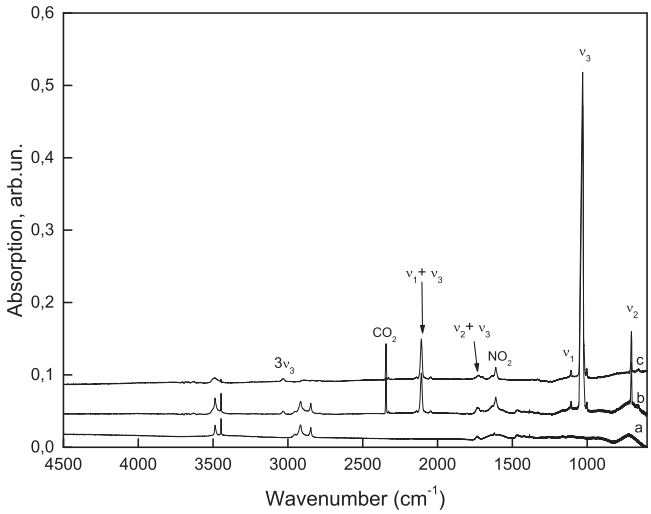

Figure 4. IR spectra recorded at 10 K (a) of carbon grains, (b) after O bombardment of carbon grains, and (c) difference spectrum.

H_2O, and H_2O_2, and moderately increases those of CO and H_2CO. This is mainly caused by two factors. The increase of the oxygen amount in the O_2–H_2 mixture promotes the formation of H_2O and H_2O_2. A higher fraction of oxygen promotes the formation of CO via the C + O reaction but also induces the CO-oxidation to form CO_2, competing with the CO-hydrogenation.

The H_2O and H_2O_2 ices are formed through reactions involving dissociated and non-dissociated molecular oxygen and hydrogen derived from the plasma discharge, as follows (Tielens 2005):

$$H + O \rightarrow HO,$$

$$H + O_2 \rightarrow HO_2,$$

$$OH + O \rightarrow HO_2.$$

As the OH and HO_2 radical species are very reactive, they lead in solid phase to stable species through radical–radical

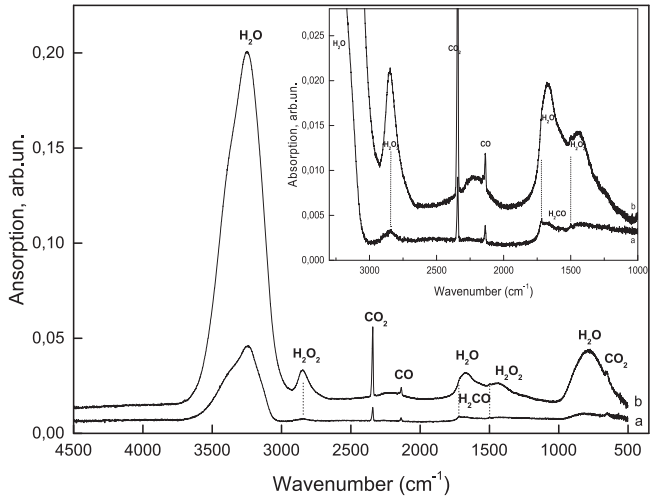

Figure 5. Difference spectra before and after O/H bombardment of carbon grains: (a) $[O_2]/[H_2] = 1/60$, (b) $[O_2]/[H_2] = 10/70$. Inset: zoom-in of Figure 5 in the 3300–1000 cm^{-1} spectral range.

recombination:

$$OH + H \rightarrow H_2O,$$

$$HO_2 + H \rightarrow H_2O_2.$$

The O/H bombardment of carbon grains leads to the appearance of two absorption signals at 1716.4 and 1499.7 cm^{-1}, corresponding to H_2CO molecules (Watanabe & Kouchi 2002; Pirim & Krim 2014). There are seven vibrational IR bands of formaldehyde, and in our spectra the strongest two are observed (Watanabe & Kouchi 2002).

The obtained frequency of the $H_2CO_{C=O}$ vibrational mode of 1716.4 cm^{-1} is redshifted in comparison with the ones in the Ne matrix, 1740.5 cm^{-1} (Pirim & Krim 2011), and in the water matrix, 1723 cm^{-1} (Pirim & Krim 2014). The redshift of 17 cm^{-1} measured in water ices as compared to the Ne matrix reflects the hydrogen bounding between H_2CO and H_2O molecules, while that of 24 cm^{-1}, measured for the grains, gathers both the interaction of H_2CO molecules with H_2O and H_2O_2 ices and the interaction with the surface of carbon grains.

The column densities N_{CO2}, N_{CO}, and N_{H2CO} normalized to the column density of carbon N_C (3×10^{17} molecule cm^{-2}) were used to evaluate the conversion factors of C atoms of the grains to CO_2, CO, and H_2CO molecules. The values were derived using the band strengths of 7.6×10^{-17} and 1.1×10^{-17} cm $molecule^{-1}$ for the CO_2 and CO vibrational stretching modes (Gerakines et al. 1995) and a band strength of 4×10^{-18} cm $molecule^{-1}$ for the 1499.7 cm^{-1} formaldehyde band (Schutte et al. 1993). We obtained conversion factors of 0.005 ± 0.001 for the C atoms to CO_2, 0.009 ± 0.003 for the C atoms to CO, and 0.003 ± 0.001 for the C atoms to H_2CO.

4. Discussion

To form "new" molecules, such as CO, CO_2, and H_2CO on hydrogenated carbon grains (already containing C and H), one needs to add oxygen from an external source or cover grains with oxygen-containing ice, such as O_2 or H_2O, with subsequent dissociation of the ice molecules. The last process requires relatively high energy. For example, it was shown that replacing oxygen with water ice on the surface of carbon grains irradiated by 6.41 eV photons did not produce CO_2, since H_2O does not dissociate at this photon energy (Fulvio et al. 2012). In the case of the atom bombardment presented here, the atoms arrive thermally cooled onto the substrate. Such an addition of O/H atoms cannot be compared to an energetic bombardment or UV irradiation able to break molecular bonds. H_2O and H_2O_2 ices are side products of the bombardment, where the main reactive species are O and H atoms.

Thus, the experiments demonstrate a new route to COMs. The bombardment of carbon grains by O/H atoms leads to an efficient formation of formaldehyde. The conversion factor of the C atoms from the grains to H_2CO is less than that to CO and the amount of synthesized molecules is small, as can be seen in Figure 5. This could be the reason that we do not yet observe methanol, the next stable species in the reaction chain (1). The band strength of the most intense methanol transition at 1026 cm^{-1} is 1.8×10^{-17} cm $molecule^{-1}$ (Hudgins et al. 1993), which is three times greater than that of formaldehyde; thus one could in principle expect a detectable IR signal for CH_3OH. The formation of CH_3OH through the CO + H reaction depends strongly both on the flux of atomic hydrogen and the amount of H_2CO formed as a reaction intermediate during the hydrogenation process. Previous CO-hydrogenation studies have shown that a threshold amount of H_2CO should be reached in order to promote the formation of methanol in the next step (Hidaka et al. 2007). However, the formation of methanol below the experimental detection limit cannot be discounted, since in ices the transition $H_2CO \rightarrow CH_3CO$ is rather barrier-less (Pirim & Krim 2011, 2014).

For the formation of molecules on the surfaces of grains under O/H atom bombardment, we propose the following scenario. The hydrogenated fullerene-like carbon grains have strongly bent graphene layers and many defects that can easily form bonds. Such defects are susceptible to chemisorption of oxygen (Zacharia 2004). It has been demonstrated that hydrogen atoms adsorbed on a graphite surface show an adsorption barrier of 0.2 eV (Areou et al. 2011), while atomic oxygen chemisorbs on a graphite surface (Barber et al. 1973) at three favorable adsorption sites, namely the two top sites and the bridge site, and that O binds the strongest at the bridge site (Incze et al. 2003). Thus, the first reaction occurring during the H/O bombardment of the grains should involve atomic oxygen:

$$\text{surface-C} + O \rightarrow \text{surface-CO}. \quad (2)$$

Surface-CO can be transferred into free CO by further bombardment, so both CO forms can participate in the following reactions with either atomic O or H:

$$CO + O \rightarrow CO_2, \quad (3)$$

$$CO + H \rightarrow HCO;\ HCO + H \rightarrow H_2CO, \quad (4)$$

$$CO + H + H \rightarrow H_2CO. \quad (5)$$

Since we did not detect HCO as an intermediate under our experimental conditions, we might then conclude that H_2CO is formed on the surface of grains through reaction (5), which involves a simultaneous interaction with two hydrogen atoms, rather than through the two-step reaction seen in (4). The reactions of O and H atoms with the grain surface should mainly occur at the beginning of the bombardment, before the grains are covered by H_2O and H_2O_2 ices. The penetration depth of H atoms into mixed H_2O/CO ices was shown to be a few tens of monolayers (Watanabe et al. 2003; Fuchs et al. 2009) and the penetration depth into H_2O and H_2O_2 ices was shown to be several monolayers (Ioppolo et al. 2010).

5. Conclusion

An alternative route of COM formation—grain surface processes—is discussed and probed experimentally. Hydrogenation and oxygenation are two important cases in the grain surface chemistry due to the mobility of H and O atoms. Our results demonstrate, for the first time, that the bombardment of interstellar carbon grain analogs by O and H atoms at low temperatures causes the formation of CO molecules, with their further hydrogenation leading to the formation of solid formaldehyde. Formaldehyde in turn can be converted into solid methanol under further bombardment or another triggering process—a goal for our next set of experiments.

We would like to thank the anonymous reviewer for very useful questions, suggestions, and corrections. The work was supported by Deutsche Forschungsgemeinschaft (grant FOR2285, sub-project P8). A.P. acknowledges COST Action CM1401 “Our Astro-Chemical History.”

References

Acharyya, K., Fuchs, G. W., Fraser, H. J., van Dishoeck, E. F., & Linnartz, H. 2007, A&A, 466, 1005
Anderson, D., Bergin, E. A., Blake, G. A., et al. 2016, AAS Meeting, 227 228.01
Areou, E., Cartry, G., Layet, J. M., & Angot, T. 2011, JChPh, 134, 014701
Barber, M., Evans, E. L., & Thomas, J. M. 1973, CPL, 18, 423
Bieler, A., Altwegg, K., Balsiger, H., et al. 2015, Natur, 526, 678
Boogert, A. C. A., Gerakines, P. A., & Whittet, D. C. B. 2015, A&ARv, 53, 541
Chen, J. H., Goldsmith, P. F., Viti, S., et al. 2014, ApJ, 793, 111
Chuang, K.-J., Fedoseev, G., Qasim, D., et al. 2017, MNRAS, 467, 2552
Congiu, E., Minissale, M., Baouche, S., et al. 2014, FaDi, 168, 151
Dorschner, J., & Henning, T. 1995, A&ARv, 6, 271
Draine, B. T. 2003, A&ARv, 41, 241
Finocchi, F., Gail, H. P., & Duschl, W. J. 1997, A&A, 325, 1264
Fuchs, G. W., Cuppen, H. M., Ioppolo, S., et al. 2009, A&A, 505, 629
Fulvio, D., Raut, U., & Baragiola, R. A. 2012, ApJL, 752, L33
Gerakines, P. A., Schutte, W. A., Greenberg, J. M., & Vandishoeck, E. F. 1995, A&A, 296, 810
Goldsmith, P. F., Liseau, R., Bell, T. A., et al. 2011, ApJ, 737, 96
Herbst, E., & van Dishoeck, E. F. 2009, A&ARv, 47, 427
Hidaka, H., Kouchi, A., & Watanabe, N. 2007, JChPh, 126, 204707
Hiraoka, K., Ohashi, N., Kihara, Y., et al. 1994, CPL, 229, 408
Hiraoka, K., Sato, T., Sato, S., et al. 2002, ApJ, 577, 265
Hollenbach, D., Kaufman, M. J., Bergin, E. A., & Melnick, G. J. 2009, ApJ, 690, 1497
Hudgins, D. M., Sandford, S. A., Allamandola, L. J., & Tielens, A. G. G. M. 1993, ApJS, 86, 713
Incze, A., Pasturel, A., & Chatillon, C. 2003, SurSc, 537, 55
Ioppolo, S., Cuppen, H. M., Romanzin, C., van Dishoeck, E. F., & Linnartz, H. 2010, PCCP, 12, 12065
Jäger, C., Huisken, F., Mutschke, H., Jansa, I. L., & Henning, T. H. 2009, ApJ, 696, 706
Jäger, C., Mutschke, H., Henning, T., & Huisken, F. 2008, ApJ, 689, 249
Jones, A. P. 2016, R. Soc. Open Sci., 3, 160224
Lee, J. E., Bergin, E. A., & Nomura, H. 2010, ApJL, 710, L21
Linnartz, H., Ioppolo, S., & Fedoseev, G. 2015, IRPC, 34, 205
Lis, D. C., Keene, J., Phillips, T. G., et al. 2001, ApJ, 561, 823
Mennella, V., Baratta, G. A., Palumbo, M. E., & Bergin, E. A. 2006, ApJ, 643, 923
Mennella, V., Palumbo, M. E., & Baratta, G. A. 2004, ApJ, 615, 1073
Mousis, O., Ronnet, T., Brugger, B., et al. 2016, ApJL, 823, L41
Öberg, K. I. 2016, ChRv, 116, 9631
Pirim, C., & Krim, L. 2011, PCCP, 13, 19454
Pirim, C., & Krim, L. 2014, RSC Adv., 4, 15419
Raut, U., Fulvio, D., Loeffler, M. J., & Baragiola, R. A. 2012, ApJ, 752, 159
Sabri, T., Baratta, G. A., Jäger, C., et al. 2015, A&A, 575, A76
Schutte, W. A., Allamandola, L. J., & Sandford, S. A. 1993, Icar, 104, 118
Shi, J., Grieves, G. A., & Orlando, T. M. 2015, ApJ, 804, 24
Theule, P., Duvernay, F., Danger, G., et al. 2013, AdSpR, 52, 1567
Tielens, A. G. G. M. 2005, The Physics and Chemistry of the Interstellar Medium (Cambridge: Cambridge Univ. Press)
Tielens, A. G. G. M., Tokunaga, A. T., Geballe, T. R., & Baas, F. 1991, ApJ, 381, 181
Vastel, C., Caux, E., Ceccarelli, C., et al. 2000, A&A, 357, 994
Ward, M. D., & Price, S. D. 2011, ApJ, 741, 121
Watanabe, N., & Kouchi, A. 2002, ApJL, 571, L173
Watanabe, N., Shiraki, T., & Kouchi, A. 2003, ApJL, 588, L121
Whittet, D. C. B. 2010, ApJ, 710, 1009
Zacharia, R. 2004, PhD, Free Univ. Berlin

The Astrophysical Journal, 861:84 (9pp), 2018 July 10 https://doi.org/10.3847/1538-4357/aac6d3

Low-temperature Optical Properties of Interstellar and Circumstellar Icy Silicate Grain Analogs in the Mid-infrared Spectral Region

Alexey Potapov[1], Harald Mutschke[2], Phillip Seeber[1], Thomas Henning[3], and Cornelia Jäger[1]
[1] Laboratory Astrophysics Group of the Max Planck Institute for Astronomy at the Friedrich Schiller University Jena, Institute of Solid State Physics, Helmholtzweg 3, D-07743 Jena, Germany; alexey.potapov@uni-jena.de
[2] Astrophysical Institute and University Observatory, Friedrich Schiller University, Schillergässchen 2-3, D-07745 Jena, Germany
[3] Max Planck Institute for Astronomy, Königstuhl 17, D-69117 Heidelberg, Germany
Received 2018 March 9; revised 2018 May 7; accepted 2018 May 17; published 2018 July 6

Abstract

Two different silicate/water ice mixtures representing laboratory analogs of interstellar and circumstellar icy grains were produced in the laboratory. For the first time, optical constants, the real and imaginary parts of the complex refractive index, of such silicate/water ice mixtures were experimentally determined in the mid-infrared (IR) spectral region at low temperatures. In addition, optical constants of pure water ice and pure silicates were derived in the laboratory. Two sets of constants were compared, namely, "measured" constants calculated from the transmission spectra of silicate/ice samples, and "effective" constants calculated from the optical constants of pure silicates and pure water ice samples using different mixing rules (effective medium approaches). Differences between measured and effective constants show that a mixing (averaging) of the optical constants of water ice and silicates for the determination of the optical properties of silicate/ice mixtures can lead to incorrect results. Also, it is shown that a part of the water ice molecules is trapped in/on silicate grains and does not desorb up to 200 K. Our unique data are well-timed with respect to the new and challenging space mission, *James Webb Space Telescope* (*JWST*), which will be able to provide novel and detailed information on interstellar and circumstellar grains. Suitable laboratory data are extremely important for the decoding of astronomical spectra.

Key words: dust, extinction – methods: laboratory: solid state – techniques: spectroscopic

1. Introduction

Dust grains play a central role in the physics and chemistry of practically all astrophysical environments. They influence the thermodynamic properties of the medium and provide a surface for very efficient chemical reactions that are responsible for the synthesis of a major part of important astronomical molecules. Interstellar and circumstellar dust grains are of great interest, as they are the building blocks of planets and remnants of protoplanetary disks. Knowing the properties of grains, we can follow their pathways to larger astronomical bodies and trace back the history of planetary systems.

Dust grains are typically nanometer- to micrometer-sized aggregates of carbonaceous or siliceous particles (Henning & Salama 1998; Draine 2003). In cold cosmic environments, such as dense molecular clouds and the outer parts of circumstellar shells, including the envelopes of evolved stars, protoplanetary disks, and debris disks, dust grains are mixed with molecular ices. Observations and dedicated laboratory experiments have shown that the main constituent of interstellar and circumstellar ices is H_2O, with lower fractions of other volatile species (Allamandola et al. 1999; Burke & Brown 2010; van Dishoeck 2014; Boogert et al. 2015).

Dust grains absorb and scatter stellar light and re-emit the absorbed energy. To interpret the astronomical spectra of dust grains, the spectral data on laboratory dust grain analogs are required. The optical properties of grains in different frequency regions are important for the modeling and understanding of the physics in astrophysical environments. The opacity of grains is the basis for the estimation of important astrophysical parameters, such as dust temperatures, mass-loss rates of evolved stars, and the total dust mass in circumstellar shells or molecular clouds.

The infrared (IR) range (wavelength from 700 nm to 1 mm) is one of the most important spectral regions with respect to dust grains because it provides information on the vibrational modes of dust-building structural units; also, it is the range, which is mainly far-IR (wavelength from 0.1 mm to 1 mm), where the emission from interstellar dust is detected. Thus, infrared spectroscopy is the best astronomical and laboratory tool for studying the composition and properties of the cosmic dust and its laboratory analogs.

The optical properties of pure water ice, silicate, and carbon grains have been intensively investigated in the laboratory (Hagen et al. 1981; Kitta & Krätschmer 1983; Smith et al. 1994; Dorschner et al. 1995; Henning & Mutschke 1997; Jäger et al. 1998, 2003; Curtis et al. 2005; Jäger et al. 2008; Mastrapa et al. 2008, 2009; Allodi et al. 2014; Sabri et al. 2014; Reinert et al. 2015). The real astronomical grains in cold environments are mixtures of dust and ice, which explains why there is a strong need to study the experimentally optical properties of such mixtures, which are not yet known. One can try to obtain the optical constants of dust/ice mixtures by mixing known pure dust and ice constants using a number of mixing rules, as has been done in a number of works (Mukai & Mukai 1984; Maron & Maron 2008; Min et al. 2016), but the reliability of such approaches is questionable.

The main purpose of this work is to present unique sets of experimental optical data for silicate/water ice mixtures in the mid-IR spectral region at low temperatures, and to check the reliability of different mixing rules for the production of optical data for such mixtures from the optical data of its components, silicates and water ice. The new optical constants of silicate/water ice mixtures published here can be used in models describing molecular clouds and circumstellar shells and in predictions of observable IR features.

2. Experimental Procedure

Amorphous silicate $MgSiO_3$/water ice mixtures were produced in a device consisting of a laser ablation setup combined with a cryogenic chamber, which is able to condense solid carbonaceous and siliceous grains and gases at temperatures down to 8 K. The setup (without the cryostat) is described in detail elsewhere (Jäger et al. 2008). The gas-phase deposition of nanometer-sized amorphous $MgSiO_3$ grains was achieved by pulsed laser ablation of a MgSi 1:1 target and subsequent condensation of the evaporated species in a quenching atmosphere of 4 mbar O_2. Condensed grains were extracted adiabatically from the ablation chamber through a nozzle into a second low-pressure chamber (10^{-3} mbar) to decouple the grains from the gas. A second extraction through a skimmer into a third chamber (10^{-6} mbar) generated a particle beam that was directed into a fourth, cryogenic, chamber, where the grains were deposited onto a cold CsI substrate. Water was deposited simultaneously with the grains from a water reservoir through a leakage valve and a capillary tube. All of the depositions were performed in a high vacuum chamber with a base pressure of 9×10^{-8} mbar at the temperature of the substrate of 8 K. Such relatively poor vacuum conditions due to the combination of a laser ablation system with the cryogenic chamber led to a deposition of CO_2 from the chamber atmosphere. A CO_2 stretching band is visible in the IR spectra that were recorded. However, the amount of CO_2 is small compared to the amount of the main deposits and cannot influence the optical properties discussed in this study. The deposition time was 20 minutes for all samples. The water deposition rate was a few tens of nm minutes^{-1} depending on the ice thickness. Such a low deposition rate corresponds to the formation of high-density amorphous water ice (Mastrapa et al. 2009).

The thickness of the silicate grain deposit was measured by a quartz crystal resonator microbalance (sensitivity 0.1 nm) using known values for the deposit area and density. The particle beam was divided by an aperture to simultaneously deposit the grains on the microbalance and the substrate. Due to a slight tilt of the beam, the microbalance may not have been completely covered. The uncertainty related to the determination of the area of the deposit on the microbalance is estimated to be about 5%. The thickness of the water matrix was estimated from the 3.1 μm water band area using the band strength of 2×10^{-16} cm molecule^{-1} (Hudgins et al. 1993) with an uncertainty of 2%. A 280 nm $MgSiO_3$ layer and a 640 nm H_2O layer, and two silicate/water ice mixtures with the $MgSiO_3/H_2O$ mass ratios of 0.8 and 2.7, were deposited and studied. Additional measurements were also done for mixtures with the mass ratios of 0.3 and 1.5 to establish the mass-ratio dependence of water trapped at 200 K. The mass ratio was calculated from the thicknesses of the deposits and densities of 1.1 g cm^{-3} for high-density amorphous water ice (Narten 1976) and 2.5 g cm^{-3} for amorphous silicates. For glassy silicates the density of 2.71 was measured (http://www.astro.uni-jena.de/Laboratory/OCDB/index.html). $MgSiO_3$ grains produced by laser ablation are characterized by less dense structures and show slightly lower values of 2.6–2.5. The thicknesses corresponding to the silicate/ice samples were 280 nm for $MgSiO_3$ and 800 nm for H_2O (sample with the mass ratio of 0.8) and 180 nm for $MgSiO_3$ and 170 nm for H_2O (sample with the mass ratio of 2.7).

IR spectra at four temperatures, namely 8, 100, 150, and 200 K, were measured in the transmission mode using a Fourier transform infrared (FTIR) spectrometer (Vertex 80v, Bruker) in the spectral range of 6000–200 cm^{-1} with a resolution of 0.5 cm^{-1}, but will be presented further in the 4500–400 cm^{-1} range because of the noisy low- and high-frequency edges. Due to slight instrumental instabilities of the baseline of the transmission spectra and possible multiple reflections on the silicate/ice layers, there can be artifacts affecting k-values in the ranges, where the k-values are supposed to be close to zero. Each higher temperature (100, 150, and 200 K) was achieved by heating the sample with the rate of 1 K minutes^{-1}. Before taking spectra at 100, 150, and 200 K the samples were allowed to stabilize for 30 minutes. The spectra of CsI substrates recorded before depositions at 8 K were used as reference spectra.

3. Data Proceeding and Calculation of Optical Constants

There are two sets of quantities that are typically used to describe the optical properties: the real and imaginary parts of the complex refractive index $n_1 = n + ik$, and the real and imaginary parts of the complex dielectric function (or relative permittivity) $\varepsilon = \varepsilon' + i\varepsilon''$ (Bohren & Huffman 2004). The relations between these two sets are as follows:

$$\varepsilon' = n^2 - k^2,\ \varepsilon'' = 2nk. \tag{1}$$

Two sets of the n and k constants have been obtained; these are "measured" constants calculated directly from the transmission spectra of the silicate/ice samples, and "effective" constants calculated from the n- and k-values of pure silicate and ice layers using different mixing rules. In both cases the n- and k-values were determined from Kramers–Kronig analysis of the transmission spectra. The reflection and interference losses were taken into account using an iterative procedure described in Hagen et al. (1981):

$$\alpha \equiv 4\pi k\nu = \frac{1}{d}\left(-\ln\left(\frac{I}{I_0}\right) + \ln\left|\frac{t_{01}t_{12}/t_{02}}{1 + r_{01}r_{12}e^{2ix}}\right|^2\right) \tag{2}$$

$$n(\nu) = n_1^o + \frac{1}{2\pi^2}\int_0^\infty \frac{\alpha(\nu')}{\nu'^2 - \nu^2}d\nu' \tag{3}$$

where α is the absorption coefficient, I/I_0 is the transmission spectrum, d is the thickness of the sample, ν is the wavenumber, ν' is a running wavenumber in the integral, r_{pq} and t_{pq} are the complex reflection and transmission coefficients of the pq boundary, $x = 2\pi\nu dn_1$, and n_1^0 is a seed value for the real part of the index of refraction. For water ice, n_1^o is 1.29 for amorphous H_2O ice (in our case 8 K and 100 K) and 1.32 for crystalline H_2O ice (in our case 150 K and 200 K; Mastrapa et al. 2009). Assuming a starting value for n_1, the absorption coefficient and the imaginary part of the refractive index were calculated from the transmission spectrum according to Equation (2). Then, n, the real part of the refractive index, was calculated by taking the integral in Equation (3) over the measured range because the denominator in Equation (3) gives little weight to contributions to the integral, which are far from ν. With this new refractive index, $n_1 = n + ik$, we calculated the transmission spectrum and compared it with the measured one. The procedure was repeated until a 0.1% agreement

between the measured and calculated transmission spectra was achieved.

For the silicate and silicate/ice samples, these calculations were complicated by the porosity introduced by the layer of $MgSiO_3$ particles. Silicate grains are known to be very porous, with a porosity that can be as high as 90% (Sabri et al. 2014). Fortunately, from the interference structures in the IR spectra due to the standing waves arising in the sample, we were able to estimate the total film thicknesses of the porous layers to be 1460 nm for the silicate sample and 2200 and 1200 nm for the silicate/ice samples, with the mass ratios of 0.8 and 2.7, respectively. The thicknesses were determined from the distance between fringes in the spectra. Using these values, Equations (2) and (3) delivered optical constants for the porous layer. Then, we calculated the constants for the inclusions, $MgSiO_3$ or $MgSiO_3/H_2O$, in a vacuum using the inverted Maxwell–Garnett formula (see below) and the inverted volume fraction of the inclusions. This procedure delivered k and n for the silicate and silicate/ice samples. In these computations, n_1^o was chosen in a such a way that the real parts of the measured optical constants came close to the effective ones after the correction of the porosity.

The effective optical constants were calculated from the k and n spectra of the $MgSiO_3$ and H_2O samples using different mixing rules (often called effective medium approaches) for a two-component mixture composed of inclusions (silicate grains) embedded in a matrix (water ice). In the next section we present the results of the application of the Maxwell–Garnett mixing rule working with the following approximations: (i) a mixture that is composed of inclusions embedded in an otherwise homogeneous matrix, (ii) inclusions that are identical in composition but may be different in volume, (iii) inclusions that are separated by distances greater than their characteristic size, and (iv) inclusions that are spherical and small compared to λ. In this case, the dielectric function of the effective medium can be calculated by the following equation (Bohren & Huffman 2004):

$$\varepsilon_{av} = \varepsilon_m \left(1 + \frac{3f\left(\frac{\varepsilon_i - \varepsilon_m}{\varepsilon_i + 2\varepsilon_m}\right)}{1 - f\left(\frac{\varepsilon_i - \varepsilon_m}{\varepsilon_i + 2\varepsilon_m}\right)} \right) \quad (4)$$

where ε_{av} is average dielectric function, ε_m and ε_i are dielectric functions of matrix and inclusions, and f is the volume fraction of inclusions. The effective n- and k-values were obtained from ε_{av} using relation 1. The other mixing rules tried were Bruggeman, Lichtenecker, and Looyenga (Maron & Maron 2008).

Thus, for each silicate/ice ratio two sets of optical constants have been obtained: measured constants, calculated from the transmission spectra of the corresponding silicate/ice sample, and effective constants, calculated by mixing the n- and k-values obtained from the transmission spectra of the $MgSiO_3$ and H_2O samples. The measured constants will be published in the Heidelberg-Jena-St.Petersburg Database of Optical Constants (http://www.mpia.de/HJPDOC/) and can be used in astrochemical models and for the decoding of astronomical spectra.

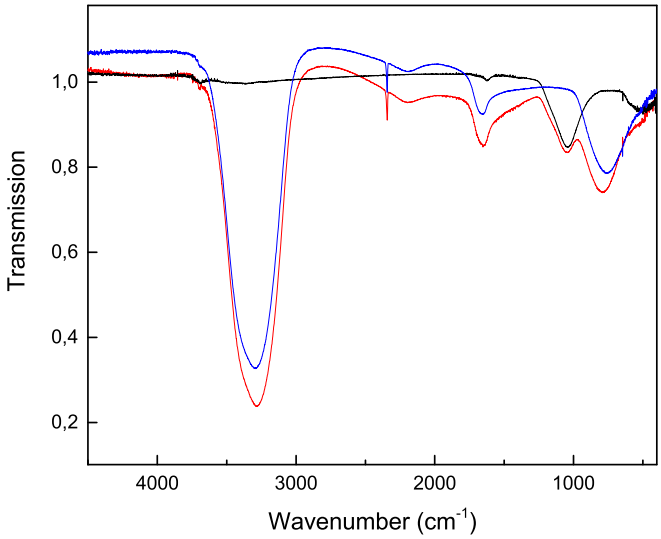

Figure 1. Transmission spectra of the $MgSiO_3/H_2O$ sample with the mass ratio of 0.8 (red curve), $MgSiO_3$ sample (black curve), and H_2O sample (blue curve) at 8 K.

4. Results

The chosen temperatures of 8, 100, and 150 K correspond to different structures of water ice, namely high-density amorphous ice, low-density amorphous ice, and crystalline ice (Hagen et al. 1981; Jenniskens et al. 1995). At a temperature of 200 K, pure water ice (deposited without silicate grains) is completely desorbed from the substrate.

The observed vibrational bands in the spectra are as follows: 3300 cm^{-1} involving symmetric and asymmetric H_2O stretching vibrations, 2347 cm^{-1} – CO_2 stretching, 2200 cm^{-1} – H_2O combination mode, 1640 cm^{-1} – H_2O bending, 1040 cm^{-1} – Si–O stretching, 770 cm^{-1} – H_2O librational motion, and 520 cm^{-1} – O–Si–O bending. As an example of the measured spectra, transmission spectra of the silicate/ice sample with the mass ratio of 0.8, of the pure $MgSiO_3$ sample, and a pure H_2O ice sample at 8 K, can be seen in Figure 1.

The optical constants of pure water ice and pure silicates obtained in this work were compared with the optical constants of amorphous and crystalline water ice (Mastrapa et al. 2009) and amorphous, sol-gel $MgSiO_3$ (Jäger et al. 2003) available in the Heidelberg-Jena-St.Petersburg Database of Optical Constants (http://www.mpia.de/HJPDOC/). There is a very good agreement between the optical constants of water ice derived in this study and the database ones. For silicates, the observed differences are not striking. The k- and n-values in the range of the stretching and bending vibrations of $MgSiO_3$ are comparable. Slight differences in the ranges where the k-values are supposed to be close to zero are related to baseline instabilities and multi-reflection problem mentioned at the end of the experimental section.

The effective medium approaches discussed in the previous section were applied to silicate and water ice optical constants to obtain the effective optical constants for the silicate/ice mixtures. These effective constants were compared with the measured constants obtained directly from the transmission spectra of the silicate/ice samples. An example is presented in Figure 2. As one can see, the mixing rules applied bring very similar spectra with small deviations in the regions of the water

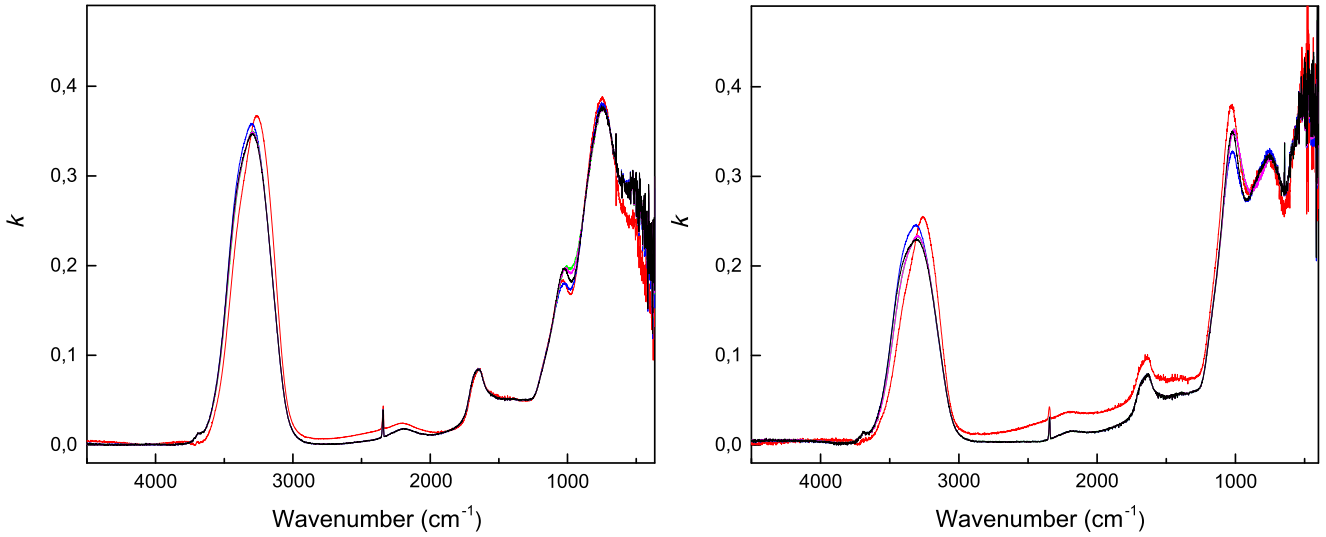

Figure 2. Measured (red curve) and effective k spectra at 8 K: Maxwell–Garnett approach (black), Bruggeman approach (violet), Lichtenecker approach (blue), and Looyenga approach (green). $MgSiO_3/H_2O$ mass ratio of 0.8 (left) and 2.7 (right). The effective curves practically coincide and the differences are visible only with the enlargement of the figure.

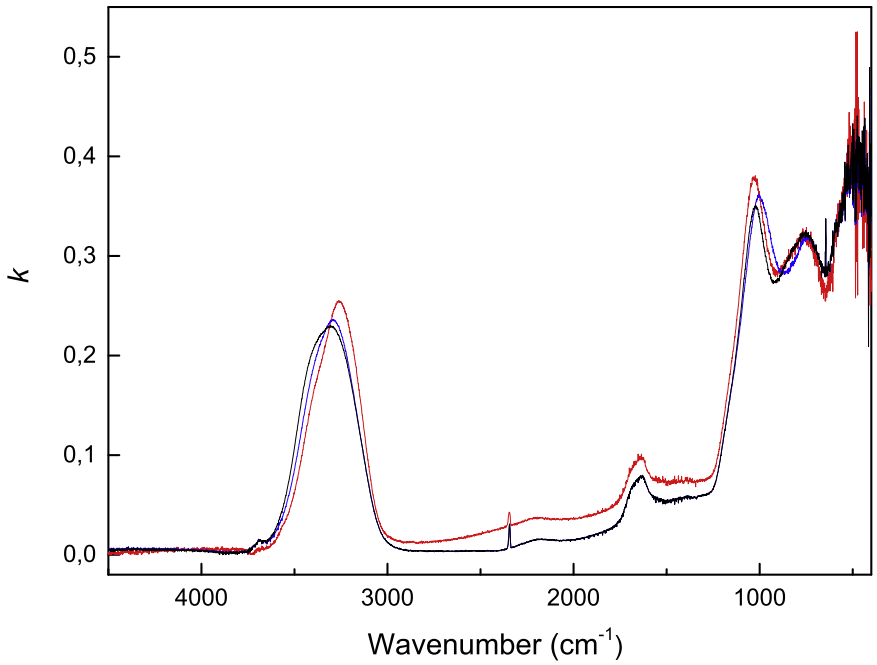

Figure 3. Measured (red curve) and effective k spectra of the sample with the $MgSiO_3/H_2O$ mass ratio of 2.7 at 8 K.: water ice as matrix (black), silicate grains as matrix (blue).

stretching vibration and librational motion, and the silicate stretching vibration.

The case of the silicate/ice mixture with the mass ratio of 2.7 is a bit more complicated because of the higher mass and volume fraction of silicates with respect to water ice. One can consider the sample to be silicate inclusions in a water ice matrix (as in the case of the silicate/ice sample with the mass ratio of 0.8), as well as water ice inclusions in a silicate matrix. Bruggeman, Lichtenecker, and Looyenga rules are symmetrical; i.e., the dielectric functions of matrix and inclusions can be exchanged. We have applied the asymmetrical Maxwell–Garnett mixing rules for both silicate/ice mixtures. An example is shown in Figure 3. The differences between the spectra "silicates in ice" and "ice in silicates" are small, but a homogeneous water ice matrix is considered to be more appropriate for the Maxwell–Garnett approach, which requires a homogeneous matrix.

A comparison of the measured k and n constants of the silicate/ice samples with mass ratios of 0.8 and 2.7 with the effective k and n values is presented for different temperatures. The effective constants were obtained by using the Maxwell–Garnett rule for the case of silicate grain inclusions in water ice matrix. Figure 4 presents the optical constants at 8 K for the two silicate/ice mixtures studied. A number of differences between the measured and effective spectra can be observed, namely a redshift, a slight narrowing, and an intensity increase of the stretching vibration of H_2O in the measured spectra as compared to the effective ones. One can also observe an

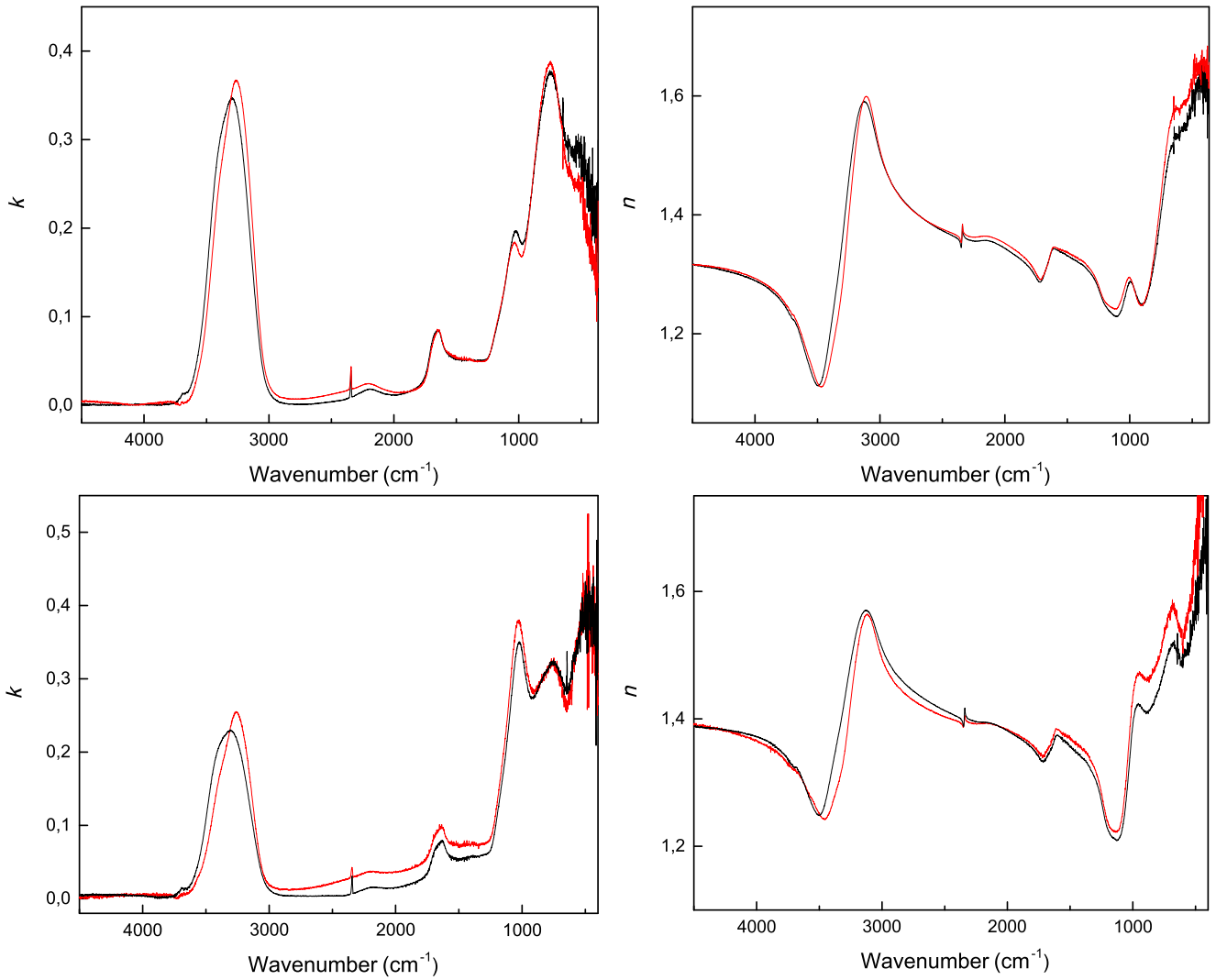

Figure 4. Effective (black curve) and measured (red curve) k and n spectra of the $MgSiO_3/H_2O$ mixtures at 8 K with the mass ratio of 0.8 (top) and 2.7 (bottom).

increased absorption on the low-frequency (long wavelength) side of the band, which is much more noticeable for the mixture with the mass ratios of 2.7.

The first structural transformation of the ice from high- to low-density amorphous ice expected in the temperature range between 8 and 100 K leads to the typical redshift, narrowing, and intensity increase of the 3300 cm^{-1} and 1640 cm^{-1} water bands, a blueshift of the 2200 cm^{-1} and 770 cm^{-1} bands, and a decrease of the intensity of the stretching vibration of H_2O in the measured spectra with respect to the effective ones. This effect is again more noticeable for the sample with mass ratios of 2.7. The optical constants at 100 K are shown in Figure 5.

The conversion of the amorphous into crystalline ice around 140 K leads to the typical redshift, narrowing, intensity increase, and appearance of a substructure in the 3300 cm^{-1} water band. In addition, a suppression of the stretching vibration band of H_2O in the measured spectra with respect to the effective ones can be observed. Optical constants of the silicate/ice mixtures at 150 K are presented in Figure 6.

At 200 K we observe water absorption bands in the spectra of all silicate/ice samples, while water ice in the pure H_2O sample is completely desorbed. An example is presented in Figure 7. The water stretching band observed for the silicate/ice samples is very broad, which could be related to the morphology of the sample as well as to an insufficient baseline correction. A small positive bump in the water spectrum is due to the presence of a low amount of water ice in the reference sample (CsI substrate at 8 K before the deposition). The dependence of the relative (to deposited) remaining amount of water in the silicate/ice samples at a temperature of 200 K on the silicate/ice mass ratio is presented in Figure 8.

5. Discussion

With the approximations of the Maxwell–Garnett mixing rule we can assume that the scattering on the grains is small and the extinction is the same as the absorption. In this case, a useful magnitude for the comparison of astronomical and laboratory measurements is the total absorption cross section (or absorption efficiency Q_a) of grains (Ossenkopf et al. 1992). It can be taken per unit volume of grains or normalized to the particle radius. A comparison between the absorption efficiencies divided by particle radius, Q_a/a, calculated for small spherical particles in the Rayleigh limit from the measured optical constants is presented in Figure 9. Q_a was defined as

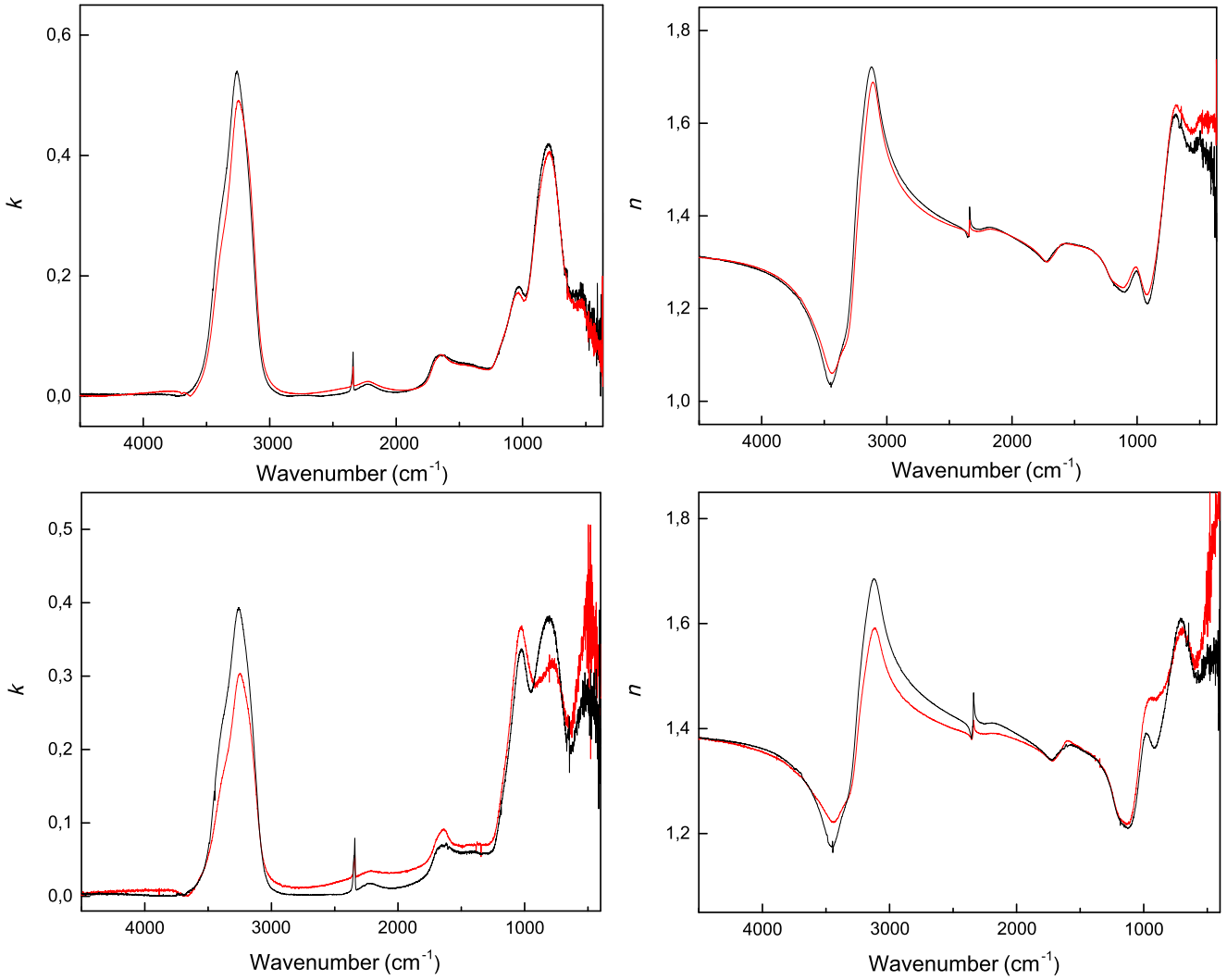

Figure 5. Effective (black curve) and measured (red curve) k and n spectra of the $MgSiO_3/H_2O$ mixtures at 100 K with the mass ratio of 0.8 (top) and 2.7 (bottom).

follows (Fabian et al. 2001):

$$Q_a = 2kVIm\left(\frac{\varepsilon}{\varepsilon - \varepsilon_m} ln\frac{\varepsilon}{\varepsilon_m}\right) \quad (5)$$

where k is the wave vector, V is the volume, ε is the measured complex dielectric function, and ε_m is the dielectric function of vacuum.

For the two different silicate/ice composites with dust fractions of 0.8 and 2.7, the ratio between the OH stretching band at $\sim$3 μm and the Si–O stretching band of silicates at about 9.7 μm is clearly changing. With increasing temperature, the sample characterized by the lower dust-to-ice ratio of 0.8 shows distinct shifts of the H_2O stretching band at 3.1 μm to longer wavelengths and of the libration band at $\sim$13 μm to shorter wavelengths. In addition, both bands are getting stronger. The position of the H_2O stretching band at the maximum shifts from 3.05 μm at 8 K to 3.07 μm and 3.10 μm at 100 K and 150 K, respectively. In contrast, the libration bands show a short-wavelength drift from 12.78 μm to 12.34 μm and 12.01 μm, for 8 K, 100 K, and 150 K, respectively. With a higher dust fraction of 2.7, the 3.1 μm band is shifted comparably due to the modification of the ice structure with the temperature, whereas the libration mode is unaffected by the temperature rise. The stretching band position varies from 3.06 μm, to 3.07 μm, and 3.10 μm for the temperatures of 8 K, 100 K, and 150 K, respectively. Consequently, the temperature-related band shift of the H_2O stretching band at around 3.1 μm seems to be independent of the silicate/ice ratio of the sample. The Si–O stretching vibrations shows only negligible changes with the temperature but a weak long wavelength shift of $\sim$0.1 μm for the sample having a higher dust/ice ratio.

Experiments on various deposition rates of water at 10 K demonstrated that a decrease in the deposition rate shifts the peak frequency to lower frequencies while the bandwidth decreases (Hagen et al. 1981). It was later shown in a number of experiments that a lower deposition rate leads to a denser ice (Berland et al. 1995; Jenniskens et al. 1995). High condensation rates limit the time for lateral diffusion following adsorption, thus producing a lower density film (Berland et al. 1995). Summarizing the results of these studies, we can conclude that the denser the deposited ice, the lower the band frequency and the narrower the band. Thus, in our case, the observed redshift and narrowing of the measured spectra can be linked to the denser water ice in the case of simultaneous deposition of water and silicate grains. The transformation from high-density to low-density ice also shifts the peak frequency to

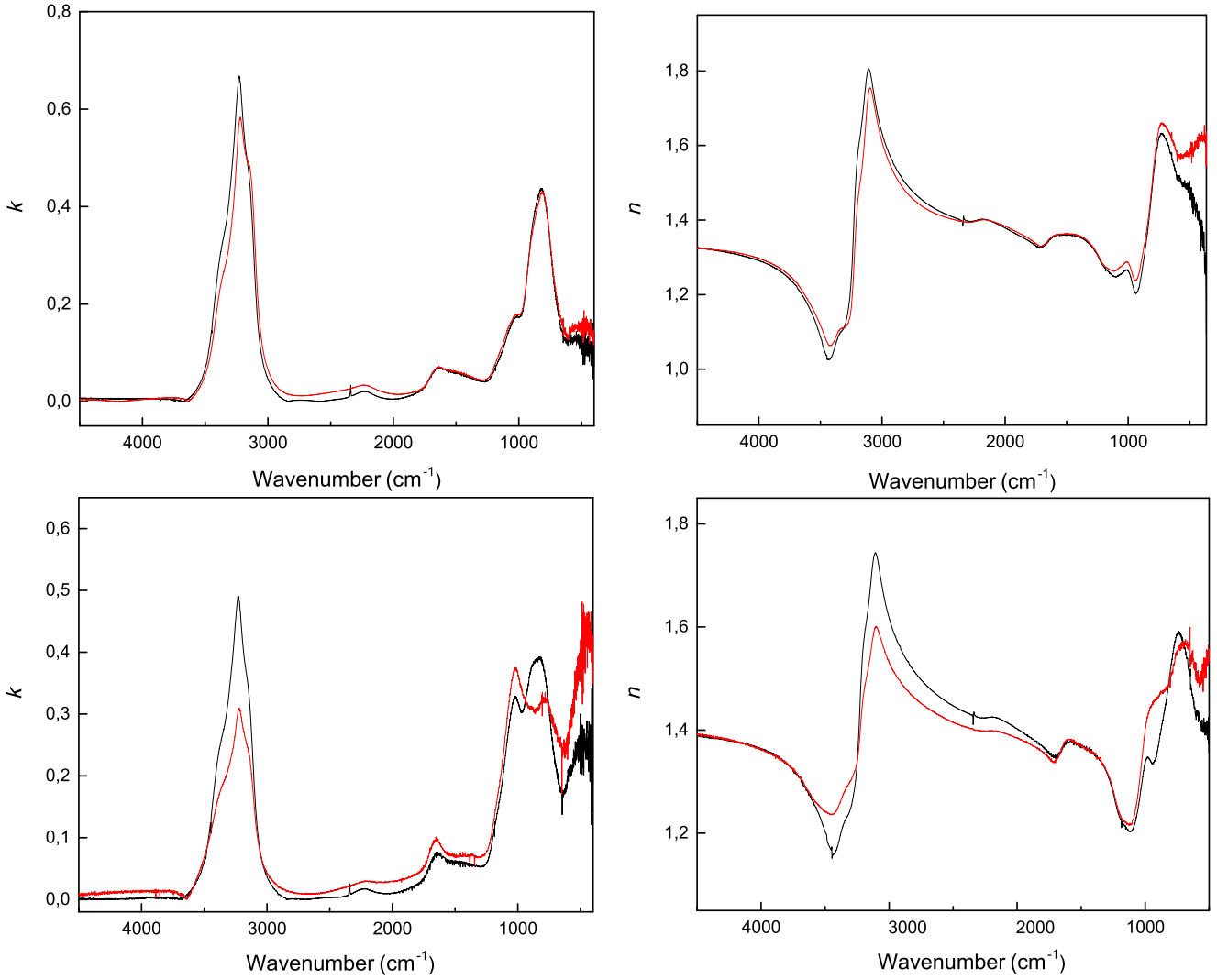

Figure 6. Effective (black curve) and measured (red curve) k and n spectra of the $MgSiO_3/H_2O$ mixtures at 150 K with the mass ratio of 0.8 (top) and 2.7 (bottom).

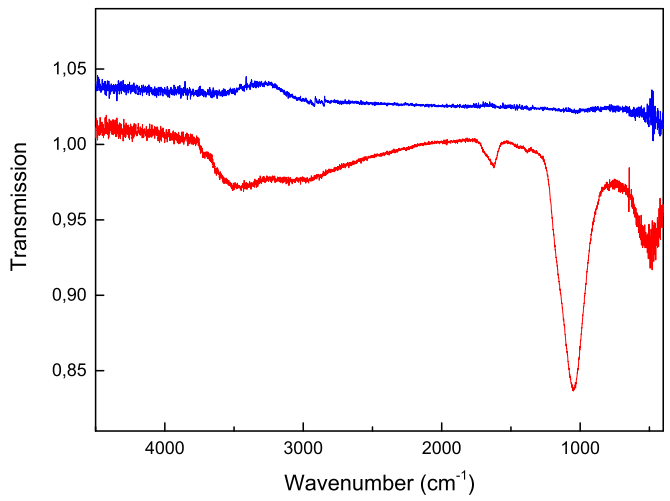

Figure 7. Transmission spectra at 200 K of the $MgSiO_3/H_2O$ sample with the mass ratio of 0.8 (red curve) and H_2O sample (blue curve).

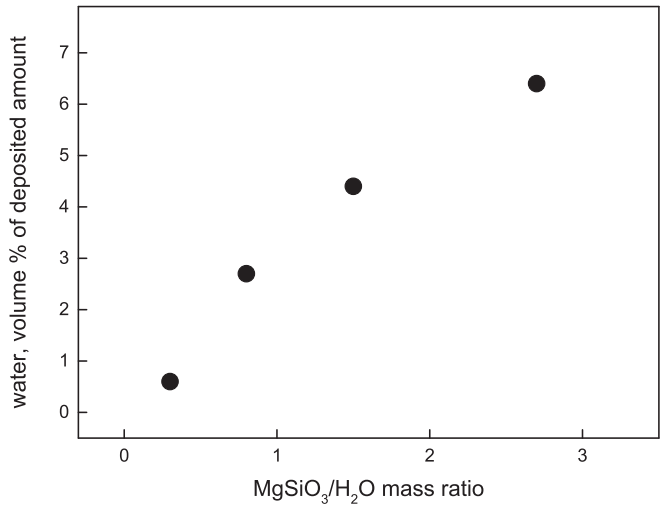

Figure 8. Dependence of the volume percentage of remaining water in the $MgSiO_3/H_2O$ samples at 200 K on the $MgSiO_3/H_2O$ mass ratio.

lower frequencies and narrows the band. It was supposed that this transformation requires the breaking of, on average, one hydrogen bond per molecule in the high-density ice structure (Jenniskens et al. 1995), which leads to a strengthening of the rest hydrogen bonds. One more explanation for the observed redshift and narrowing of the measured spectra can be the strengthening of hydrogen bonds due to the interaction with silicate molecules.

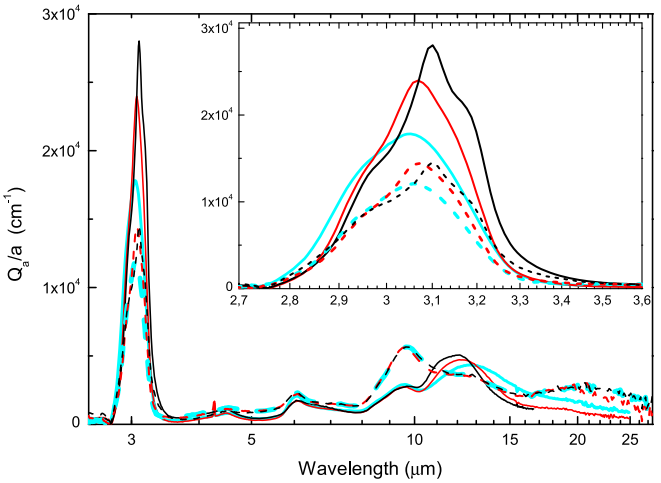

Figure 9. Normalized absorption efficiencies of silicate/ice composites with the mass ratios 0.8 (solid lines) and 2.7 (dashed lines) for 8 K (cyan), 100 K (red), and 150 K (black) calculated from the measured optical constants for a continuous distribution of ellipsoids.

The astronomically observed increased absorption on the long wavelength side of the H_2O stretching band was partly explained by the scattering of large water grains (hundreds of nanometers; Boogert et al. 2015). In our case, the scattering by nanometer-sized grains covered by water ice may contribute to the increased absorption observed. However, this effect is much less noticeable for the laboratory grains as compared to cosmic grains mentioned by Boogert et al., probably due to their much smaller radius. As one can see from Figures 4–6, the effect is more noticeable for the sample with the silicate/ice mass ratio of 2.7, where the grains can be bigger due to a larger amount of material.

The suppression of the water stretching vibrations can be explained by the different morphology of pure water ice and ice mixed with silicate grains. The transformation of the ice structure from high-density to low-density ice below 100 K and from amorphous to crystalline ice below 150 K leads to an intensity increase of the water stretching band. We assume that the ice in silicate/ice mixtures converts incompletely and that there is a noticeable fraction of high-density ice at 100 K and of amorphous ice at 150 K. A change of the hydrogen bond strength due to the interaction with silicates can also play a role in the observed phenomenon.

All of the mixing rules applied fit the measured constants with comparable accuracy. The effective optical constants of silicate/water ice mixtures can be calculated by mixing the optical constants of the individual components, such as silicate grains and water ice. However, the position, width, and intensity, as well as the increased absorption at long wavelengths of the water stretching vibration of the silicate/ice samples, are not reproduced by the effective spectra. Thus, the mixing of the optical data of the icy silicate grain components to describe the optical properties of grains in the temperature range between 8 and 200 K can lead to incorrect results and complicate the analysis of astronomical data.

At 200 K, the water ice in the sample should be completely desorbed, but residual water is clearly detected in all silicate/ice samples. This is probably due to interactions between water molecules and the silicate surface. It is possible that a part of H_2O molecule is chemisorbed on the surface of grains. Obviously, only molecules from the first monolayer of water ice can have stronger bonds to silicate grains or chemisorb on the grain surface. Also, water molecules can be trapped in pores of silicate grains. From our results in Figure 8, we can conclude that the higher the silicate/ice mass ratio, the greater the number of binding sites or pores allowing more water molecules stay bound/trapped in silicates at 200 K.

The trapping of water ice in/on silicate grains is very important with respect to the presence of icy grains in protoplanetary disks, where grains are generally taken to be a starting point toward the formation of planets. Ice-coated grains are expected to stick together much more efficiently. The increase of the mass of solid material in the region where there is ice, compared to where there is no ice, has been estimated to range from a factor of 1.6 (Min et al. 2011) to a factor of 4.2 (Thommes & Duncan 2006). Crystalline water ice in protoplanetary disks was tentatively detected (McClure et al. 2012, 2015). Recently, it was unambiguously detected in a disk around the Herbig star HD 142527 (Min et al. 2016). It was shown there that the disk contains a large reservoir of water ice, comparable to the water ice abundance in the outer solar system, comets, and dense interstellar clouds. The silicate/water ice mass ratio in the disk was determined to be ~0.63. This ratio was reproduced by one of our silicate/ice samples with the $MgSiO_3/H_2O$ mass ratio of 0.8. Water ice that was trapped in/on silicate grains and, therefore survived the transition from a dense molecular cloud to a protoplanetary disk, can partly explain large amounts of H_2O ice in disks around young stars.

6. Conclusions

We have presented new sets of experimental optical data of silicate/water ice mixtures with the $MgSiO_3/H_2O$ mass ratios of 0.8 and 2.7 in the mid-IR spectral region at temperatures of 8, 100, and 150 K. The optical constants were obtained from the transmission spectra of the silicate/ice mixtures and compared with the effective constants calculated from the optical constants of pure silicate grains and pure water ice using the Maxwell–Garnett mixing rule. Differences between measured and effective constants demonstrate that the determination of the optical properties of interstellar and circumstellar icy silicate grains by a mixing of optical constants of water ice and silicates can lead to incorrect results, and underline the importance of conducting further investigations of optical and structural properties of grain/ice mixtures. A trapping of a part of water ice in/on silicate grains at 200 K is detected, and this can improve our understanding of the abundance and desorption properties of interstellar and circumstellar ices and help to develop a link between the dust/ice ratio in a cosmic body and the cosmic environment, from where the body originates. The new optical constants of silicate/water ice mixtures published here can be used in models describing molecular clouds and circumstellar shells and for predictions of observables.

This work was supported by the Deutsche Forschungsgemeinschaft, Research Unit FOR 2285 (grants MU 1164/9-1 and JA 2107/3-1).

References

Allamandola, L. J., Bernstein, M. P., Sandford, S. A., & Walker, R. L. 1999, SSRv, 90, 219
Allodi, M. A., Ioppolo, S., Kelley, M. J., McGuire, B. A., & Blake, G. A. 2014, PCCP, 16, 3442
Berland, B. S., Brown, D. E., Tolbert, M. A., & George, S. M. 1995, GeoRL, 22, 3493

Bohren, C. F., & Huffman, D. R. 2004, Absorption and Scattering of Light by Small Particles (Weinheim: Wiley-VCH)
Boogert, A. C. A., Gerakines, P. A., & Whittet, D. C. B. 2015, ARA&A, 53, 541
Burke, D. J., & Brown, W. A. 2010, PCCP, 12, 5947
Curtis, D. B., Rajaram, B., Toon, O. B., & Tolbert, M. A. 2005, ApOpt, 44, 4102
Dorschner, J., Begemann, B., Henning, T., Jager, C., & Mutschke, H. 1995, A&A, 300, 503
Draine, B. T. 2003, ARA&A, 41, 241
Fabian, D., Henning, T., Jager, C., et al. 2001, A&A, 378, 228
Hagen, W., Tielens, A. G. G. M., & Greenberg, J. M. 1981, CP, 56, 367
Henning, T., & Mutschke, H. 1997, A&A, 327, 743
Henning, T., & Salama, F. 1998, Sci, 282, 2204
Hudgins, D. M., Sandford, S. A., Allamandola, L. J., & Tielens, A. G. G. M. 1993, ApJS, 86, 713
Jäger, C., Dorschner, J., Mutschke, H., Posch, T., & Henning, T. 2003, A&A, 408, 193
Jäger, C., Mutschke, H., & Henning, T. 1998, A&A, 332, 291
Jäger, C., Mutschke, H., Henning, T., & Huisken, F. 2008, ApJ, 689, 249
Jenniskens, P., Blake, D. F., Wilson, M. A., & Pohorille, A. 1995, ApJ, 455, 389
Kitta, K., & Krätschmer, W. 1983, A&A, 122, 105
Maron, N., & Maron, O. 2008, MNRAS, 391, 738
Mastrapa, R. M., Bernstein, M. P., Sandford, S. A., et al. 2008, Icar, 197, 307
Mastrapa, R. M., Sandford, S. A., Roush, T. L., Cruikshank, D. P., & Ore, C. M. D. 2009, ApJ, 701, 1347
McClure, M. K., Espaillat, C., Calvet, N., et al. 2015, ApJ, 799, 162
McClure, M. K., Manoj, P., Calvet, N., et al. 2012, ApJL, 759, L10
Min, M., Dullemond, C. P., Kama, M., & Dominik, C. 2011, Icar, 212, 416
Min, M., Bouwman, J., Dominik, C., et al. 2016, A&A, 593, A11
Mukai, T., & Mukai, S. 1984, AdSpR, 4, 207
Narten, A. H. 1976, JChPh, 64, 1106
Ossenkopf, V., Henning, T., & Mathis, J. S. 1992, A&A, 261, 567
Reinert, C., Mutschke, H., Krivov, A. V., Lohne, T., & Mohr, P. 2015, A&A, 573, A29
Sabri, T., Gavilan, L., Jager, C., et al. 2014, ApJ, 780, 180
Smith, R. G., Robinson, G., Hyland, A. R., & Carpenter, G. L. 1994, MNRAS, 271, 481
Thommes, E. W., & Duncan, M. J. 2006, in Planet Formation, The Accretion of Giant-planet Cores, ed. H. Klahr & W. Brandner (Cambridge: Cambridge Univ. Press), 129
van Dishoeck, E. F. 2014, FaDi, 168, 9

The Astrophysical Journal, 865:58 (7pp), 2018 September 20 https://doi.org/10.3847/1538-4357/aad803

Temperature Programmed Desorption of Water Ice from the Surface of Amorphous Carbon and Silicate Grains as Related to Planet-forming Disks

Alexey Potapov[1], Cornelia Jäger[1], and Thomas Henning[2]
[1] Laboratory Astrophysics Group of the Max Planck Institute for Astronomy at the Friedrich Schiller University Jena, Institute of Solid State Physics, Helmholtzweg 3, D-07743 Jena, Germany; alexey.potapov@uni-jena.de
[2] Max Planck Institute for Astronomy, Königstuhl 17, D-69117 Heidelberg, Germany
Received 2018 June 20; revised 2018 July 19; accepted 2018 August 1; published 2018 September 20

Abstract

Understanding the history and evolution of small bodies, such as dust grains and comets, in planet-forming disks is very important to reveal the architectural laws responsible for the creation of planetary systems. These small bodies in cold regions of the disks are typically considered to be mixtures of dust particles with molecular ices, where ices cover the surface of a dust core or are actually physically mixed with dust. While the first case, *ice-on-dust*, has been intensively studied in the laboratory in recent decades, the second case, *ice-mixed-with-dust*, presents uncharted territory. This work is the first laboratory study of the temperature-programmed desorption of water ice *mixed with* amorphous carbon and silicate grains. We show that the kinetics of desorption of H_2O ice depends strongly on the dust/ice mass ratio, probably due to the desorption of water molecules from a large surface of fractal clusters composed of carbon or silicate grains. In addition, it is shown that water ice molecules are differently bound to silicate grains in contrast to carbon. The results provide a link between the structure and morphology of small cosmic bodies and the kinetics of desorption of water ice included in them.

Key words: astrochemistry – dust, extinction – methods: laboratory: solid state – molecular processes – protoplanetary disks – techniques: spectroscopic

1. Introduction

Interstellar and circumstellar ices are considered to be possible sources of organic molecules responsible for the origin and early evolution of life on Earth (Oro 1961; Cronin & Chang 1993; Brack 1999; Pearce et al. 2017). A number of amino acids have been found in comets and meteorites (Cronin & Chang 1993; Elsila et al. 2009; Altwegg et al. 2016) and have been produced in interstellar ice analogs in the laboratory (Bernstein et al. 2002; Muñoz Caro et al. 2002; Nuevo et al. 2006; Elsila et al. 2007). On this background, there has been increasing interest in studying the chemistry, the structure, and the dynamical properties of laboratory cosmic ice analogs in the last decades.

In the interstellar medium (ISM), ices form a mantle around a dust core (Allamandola et al. 1999) through condensation of gaseous species onto cold dust grains. Dust grains (ice-covered or not), which are mainly carbon or silicate based particles (Henning & Salama 1998; Draine 2003), represent the most pristine starting material for planetary systems. Ice plays an important role in the grain growth. According to coagulation models (Wada et al. 2009; Wettlaufer 2010) and collisional experiments (Gundlach & Blum 2015), ice-coated grains are expected to stick together much more efficiently. After a coagulation of dust grain monomers covered by ice in dense regions, such as dense molecular clouds and planet-forming disks, ice can be trapped inside grain aggregates. Laboratory experiments on dust particle aggregation by collisions (see, for example, Wurm & Blum 1998; Krause & Blum 2004, and a recent review by Blum 2018) and an analysis of the fractal dust particles observed by Rosetta (Fulle & Blum 2017) have shown that final dust aggregates are highly porous. Ice can cover the surface of grains and grain aggregates and can fill the pores of the aggregates via adsorption of volatile molecules from the gas phase. As was shown by the examination of the samples returned by the Stardust mission, there are indications that the dust and water–ice agglomerates were mixed before cometesimals formed in the outer solar system (Brownlee et al. 2006). The results of the Rosetta mission demonstrated that the nucleus of the comet 67P/Churyumov–Gerasimenko is characterized by an average dust-to-ices mass ratio of 7.5, which is consistent with a mixture of ices, Fe-sulfides, silicates, and hydrocarbons (Fulle et al. 2017). It was also recently shown in laboratory experiments that a part of water ice molecules mixed with silicate grains at 8 K is trapped in silicate agglomerates and does not desorb up to 200 K (Potapov et al. 2018). This trapped ice can survive the transfer from a dense molecular cloud into a protoplanetary disk, even at high temperatures. Thus, it is very probable that dust grains and comets in planet-forming disks present, as a rule, physical mixtures of ice and dust.

Observations and dedicated laboratory experiments have shown that the main constituent of interstellar and circumstellar ice is H_2O with lower fractions of other volatile molecules such as CO, CO_2, NH_3, CH_4, and CH_3OH (for reviews, see Allamandola et al. 1999; Burke & Brown 2010; van Dishoeck 2014). The first stage of molecular ice formation on cold grain surfaces is dominated by H_2O ice and mixtures with H_2O in all Galactic and extragalactic environments (Boogert et al. 2015). Water ice plays an important role in the chemistry of the ISM, acting as a catalyst for chemical reactions and for the sticking of small dust particles. Concerning the role of water in space, we refer the reader to the following reviews (Bergin & van Dishoeck 2012; van Dishoeck et al. 2014).

Desorption of molecular ices increases the molecular diversity of the gas phase in different astrophysical environments, including dense molecular clouds, protoplanetary and debris disks, envelopes of evolved stars, and surfaces and atmospheres of planets. It has been shown that for multi-component ices based on water ice matrices, the desorption of

all species in the ice is controlled by the behavior of water (Collings et al. 2004; Martin-Doménech et al. 2014), thus, the desorption of water ice triggers the release of other molecules, which play an active role in the gas phase chemistry. In addition, the desorption properties of water ice are directly related to the observed amounts of gaseous and solid H_2O in protoplanetary disks (Dominik et al. 2005; Min et al. 2016).

Thus, the study of the desorption of H_2O ice mixed with dust particles is critical for our understanding of ice–dust interactions, the structure and morphology of dust grains and comets, the chemical diversity of the gas phase and thereby the physics and chemistry of different cosmic environments. A number of laboratory experiments studying the desorption of ices *from* dust surfaces have been performed. Here, we refer the reader to a review paper (Burke & Brown 2010) and recent studies (Noble et al. 2012; Dawley et al. 2014; Shi et al. 2015; Suhasaria et al. 2017). However, as was discussed above, dust in dense molecular clouds, planet-forming disks, and comets is mixed with molecular ices. Therefore, real astronomical dust aggregates are better modeled by ice *mixed with* dust rather than ice *layered* on dust. To our knowledge, the desorption of ices *mixed with* dust grains has not yet been reported. In the present study, we aim to provide results on the temperature-programmed desorption (TPD) of water ice mixed with laboratory analogs of interstellar and circumstellar amorphous carbon or silicate particles. The results are relevant for planet-forming disks, where a central star can trigger the thermal desorption of molecular ices.

2. Experimental Part

Dust/ice mixtures were produced in a setup combining a laser ablation experiment with a cryogenic chamber. In this setup, solid carbonaceous and siliceous grains can be condensed together with relevant gas molecules at temperatures down to 8 K. The setup (without the cryostat) is described in detail elsewhere (Jäger et al. 2008).

In our experiments simulating the formation of cosmic dust, the deposition of nanometer-sized hydrogenated fullerene-like amorphous carbon and amorphous silicate ($MgSiO_3$ and $MgFeSiO_4$) particles was performed by pulsed laser ablation of graphite, MgSi, and MgFeSi targets and subsequent condensation of the evaporated species in a quenching atmosphere of either He/H_2 (volume ratio of 5/2) for carbon grains or O_2 for silicate grains. The pressure in the ablation chamber was kept at 4 mbar. The low pressure regime applied is comparable to the pressure conditions for dust condensation in AGB stars (Lodders & Fegley 1999). The condensed dust grains were extracted adiabatically from the ablation chamber through a nozzle into a second chamber that was held at a pressure of around 10^{-3} mbar. During such an expansion, the particles decouple from the gas. Consequently, further particle growth due to reactions with reactive gas molecules and agglomeration processes are prevented. A second extraction was performed through a skimmer into a third chamber with a pressure of 10^{-6} mbar. The generated particle beam was directed into a fourth, cryogenic chamber, where the dust grains were deposited onto a KBr substrate cooled down to 8 K. Water ice molecules evaporated from a water reservoir and introduced through a leakage valve and a capillary tube were simultaneously deposited with grains. The deposition rate was varied from 2 to 10 nm minutes^{-1} in order to adjust the ice and grain deposition. Ice deposited at such low rates and low temperatures, forms high-density amorphous solid water (ASW; Hagen et al. 1981; Berland et al. 1995; Jenniskens et al. 1995). All depositions were performed in a vacuum chamber with a base pressure of 10^{-7} mbar. Such relatively poor vacuum conditions due to the combination of a laser ablation system with the cryogenic chamber lead to a deposition of CO_2 from the chamber atmosphere (CO_2 stretching band is visible in the IR spectra recorded). However, the amount of CO_2 is small compared to the amount of H_2O and cannot influence the kinetics of desorption of water ice discussed in this study.

Table 1
Dust and Ice Thicknesses and Dust/Ice Mass Ratios

Sample Number, N	Sample Description	Dust/Ice Mass Ratio
1	Pure H_2O ice, 450 nm	...
2	Pure H_2O ice, 40 nm	...
3	Carbon grains, 35 nm + H_2O ice, 670 nm	0.1
4	Carbon grains, 35 nm + H_2O ice, 320 nm	0.2
5	Carbon grains, 35 nm + H_2O ice, 130 nm	0.5
6	Carbon grains, 30 nm + H_2O ice, 40 nm	1.3
7	$MgSiO_3$, 150 nm + H_2O ice, 40 nm	9.4
8	$MgFeSiO_4$, 75 nm + H_2O ice, 20 nm	13.8

The thickness of the grain deposits was controlled by a quartz crystal resonator microbalance (sensitivity 0.1 nm) using known values for the deposit area and density. The thickness of the water ice was calculated for all depositions from the 3.07 μm water band area using a band strength of 2×10^{-16} cm molecule^{-1} (Hudgins et al. 1993). The carbon/ice mass ratio was varied between 0.1 and 1.3. The silicate/ice mass ratios were 9.4 for the $MgSiO_3$ and 13.8 for the $MgFeSiO_4$ samples. The mass ratios were calculated from the thicknesses of the deposits using densities of 1.1 g cm^{-3} for high-density amorphous water ice (Narten 1976), 1.7 g cm^{-3} for amorphous carbon (Sabri et al. 2015), 2.5 g cm^{-3} for amorphous $MgSiO_3$ silicates (slightly lower value, such as 2.7 g cm^{-3}, measured for glassy silicates, http://www.astro.uni-jena.de/Laboratory/OCDB/index.html), and 3.7 g cm^{-3} for amorphous $MgFeSiO_4$ silicates (Jäger et al. 2016). The thicknesses and mass ratios used are presented in Table 1.

TPD experiments were performed by linear ramping of the substrate temperature with a rate of 1 K minutes^{-1} in the temperature range between 8 and 200 K. The error of the temperature measurements was determined to be ± 1 K. Infrared spectra during the warming-up were measured using a Fourier transform infrared (FTIR) spectrometer (Vertex 80v, Bruker) in the spectral range from 6000 to 400 cm^{-1} with a resolution of 1 cm^{-1}. 16 scans were taken for one spectrum, which was equivalent to 40 s of the scanning time.

3. Results

The obtained vibrational spectra of H_2O ice are dominated by a broad band around 3300 cm^{-1}, which involves symmetric and antisymmetric OH stretching vibrations. IR spectra of a H_2O ice and a carbon/ice mixture are presented in Figure 1. One can see five water bands related to the stretching and bending vibrations at 3300 cm^{-1} and 1660 cm^{-1}, to the librational motion at 750 cm^{-1}, to a combination mode at 2200 cm^{-1}, and to the presence of free H_2O molecules at

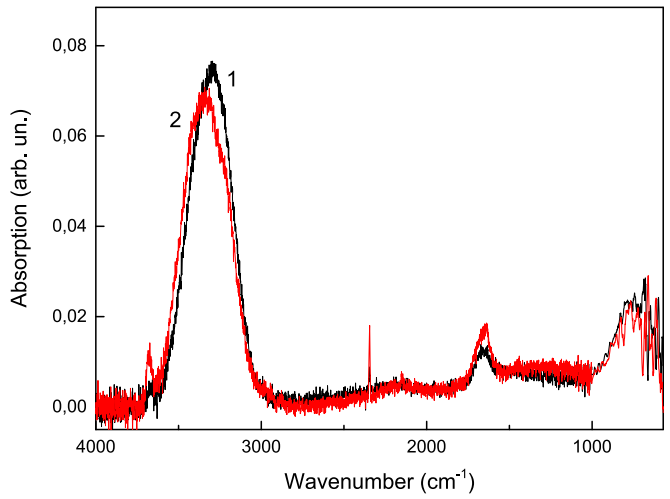

Figure 1. IR spectra at 8 K: 1—H_2O ice (40 nm, N2 in Tables 1 and 2) and 2—carbon grains/H_2O ice (30 nm/40 nm, N6 in Tables 1 and 2). The spectra were smoothed in the range below 1000 cm^{-1}.

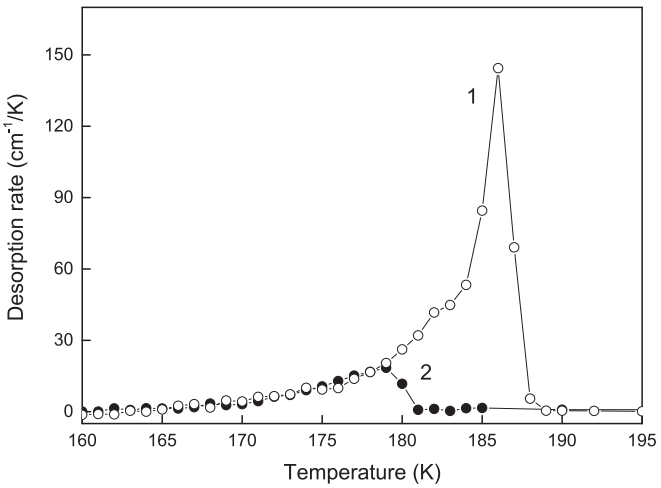

Figure 2. TPD curves for H_2O ice: 1—450 nm (N1 in Tables 1 and 2) and 2—40 nm (N2 in Tables 1 and 2).

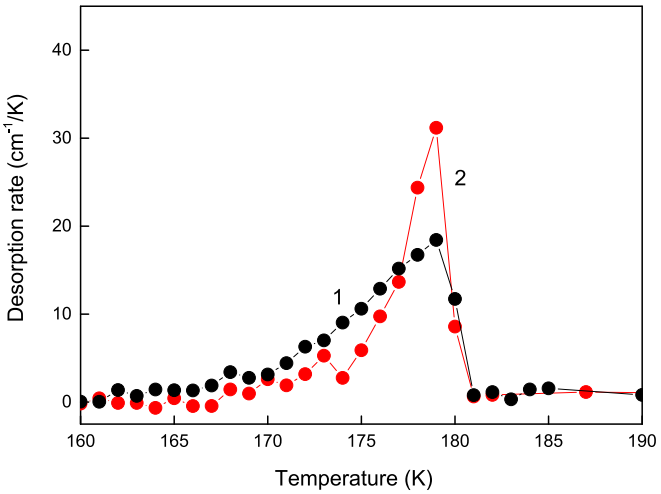

Figure 3. TPD curves: 1—H_2O ice (40 nm, N2 in Tables 1 and 2) and 2—carbon/ice (30 nm/40 nm, N6 in Tables 1 and 2).

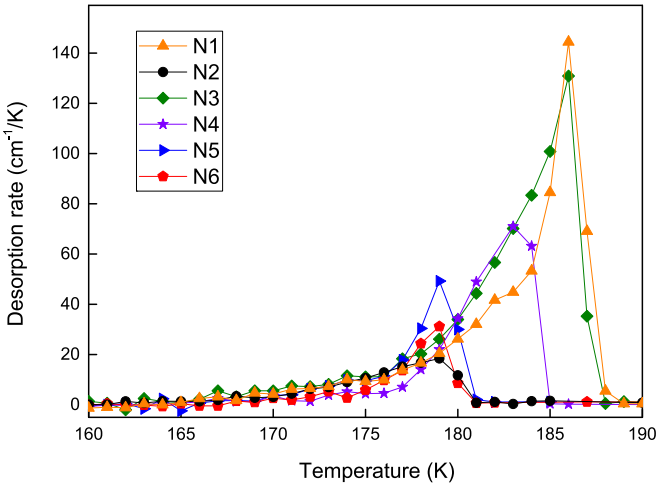

Figure 4. TPD curves for the samples N1–N6 (see Tables 1 and 2).

3680 cm^{-1}. In addition, the stretching band of CO_2 at 2344.9 cm^{-1} is visible due to the relatively poor vacuum conditions used.

A number of differences between the spectrum of the carbon/ice mixture and the spectrum of pure water ice presented in Figure 1 can be observed. The spectral properties of dust/ice mixtures at different temperatures are outside of the scope of the present paper. The optical properties of silicate/water ice mixtures have recently been published (Potapov et al. 2018) and a study of the optical properties of carbon/water ice mixtures is in progress.

The high-density ASW converts into the low-density ASW in the temperature range between 30 and 80 K and then into crystalline ice (CI), typically, in the temperature range between 130 and 150 K (Hagen et al. 1981; Jenniskens et al. 1995; Fraser et al. 2001; Bolina et al. 2005a). Both transformations lead to changes in the water band positions, shapes, and intensities (Hagen et al. 1981; Jenniskens et al. 1995). Following the evolution of the 3300 cm^{-1} water ice band with the temperature, we observed the spectral changes corresponding to both structural transformations, specifically, a redshift, a narrowing, an intensity increase, and the appearance of a substructure of the band.

TPD curves were obtained by heating the samples with a heating rate of 1 K $minutes^{-1}$ and taking the first temperature derivative of the integrated intensity of the OH stretching band. In Figure 2, TPD curves for pure water ices of two different thicknesses are shown. Figure 3 presents a TPD curve for pure H_2O ice together with a TPD curve for the carbon grains/water ice sample with the same amount of water. The TPD curves of all carbon/ice samples are shown in Figure 4.

Following a number of studies (Acharyya et al. 2007; Noble et al. 2012; Martin-Doménech et al. 2014), we fitted the leading edges of the TPD curves with the Polanyi–Wigner equation (Polanyi & Wigner 1928):

$$\frac{dA}{dT} = \nu_0 \frac{1}{b} N^i e^{\frac{-E}{RT}}, \quad (1)$$

where A corresponds to the integrated band intensity, T is the temperature, ν_0 is the pre-exponential factor of 10^{12} s^{-1}, which is a standard value for physisorbed species (Sandford & Allamandola 1988; Biham et al. 2001; Fayolle et al. 2011), and b is the heating rate of 1 K $minutes^{-1}$. N and i correspond to the number of molecules and to the desorption order, respectively.

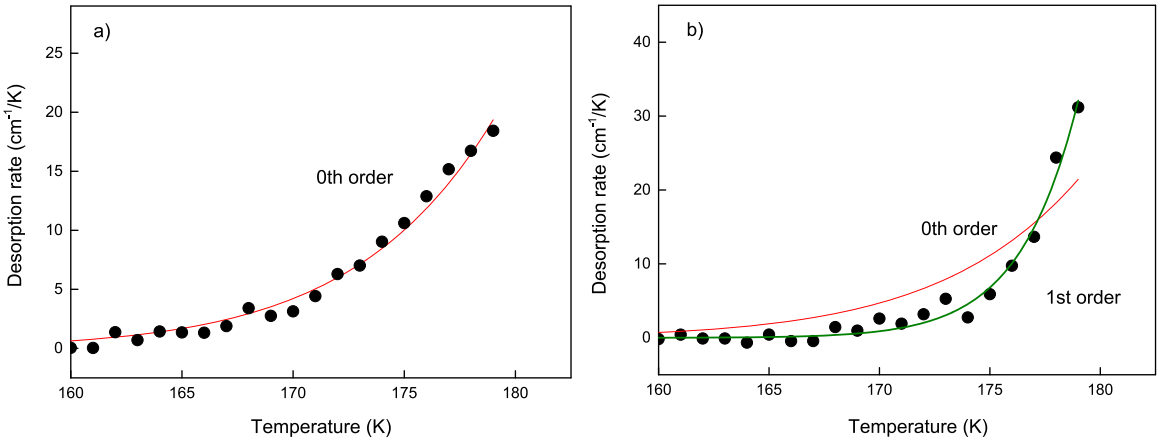

Figure 5. Leading edges of the TPD curves: (a) pure H_2O ice (N2 in Tables 1 and 2) and (b) carbon/ice sample (N6 in Tables 1 and 2) and their fits using zeroth and first desorption orders.

E represents the desorption energy and R the gas constant. The pre-exponential factor depends on the ice thickness, but this dependence is not strong, even for nonzero desorption orders (Bisschop et al. 2006; Martin-Doménech et al. 2014). As was shown, an effect of altering the desorption energy on the pre-exponential factor for water ice is very small (Bolina et al. 2005a). Therefore, the pre-exponential factor was kept constant for all the studied samples. The results of the fits of the TPD curves presented in Figure 3 are shown in Figures 5(a) and (b).

For the pure water ice multilayer (40 nm of water ice is more than 100 monolayers), we obtained zeroth-order desorption in agreement with the literature (Fraser et al. 2001; Bolina et al. 2005a). In addition, an alternative approach for the determination of the desorption order proposed in Bolina et al. (2005a), from the gradient of the plot of the natural logarithm of the TPD peak versus the relative ice coverage at a fixed temperature, was used. The zeroth desorption order of the pure water ice was confirmed.

For the carbon/ice sample N6, the result is different. In order to fit the leading edge of the TPD curve, we had to use first-order desorption kinetics (see Figure 5(b)). A series of experiments using different carbon/ice mass ratios was performed. Variations of these ratios lead to a transformation of the TPD curve, which can be fitted with the Polanyi–Wigner equation using fractional desorption orders. Such an approach was used to describe TPD curves for H_2O, NH_3, and CH_3OH ices (Bolina et al. 2005a, 2005b; Brown & Bolina 2007). The desorption order increases with an increase of the carbon/ice mass ratio as shown in Table 2.

The desorption energy obtained for the pure water ice using Equation (1) is 48.7 ± 0.3 kJ mol^{-1} in agreement with literature data (Fraser et al. 2001; Collings et al. 2004). Redhead's peak maximum method (Redhead 1962) valid for the first-order desorption gave us a value for the desorption energy E of 49.7 ± 0.5 kJ mol^{-1} for the carbon/ice samples N5 and N6. All desorption energies determined are presented in Table 2.

In addition, we present our first experimental data on silicate/ice mixtures. TPD curves of the $MgSiO_3/H_2O$ (N7) and $MgFeSiO_4/H_2O$ (N8) samples are shown in Figure 6.

As one can see, there is a principal difference between the silicate/ice and carbon/ice TPD curves, namely the presence of a second peak in the silicate/ice measurements. In addition, we observed slightly increased desorption rates beyond the second desorption maxima indicating a rest of water ice in the samples up to 200 K. This result is in agreement with our recent study,

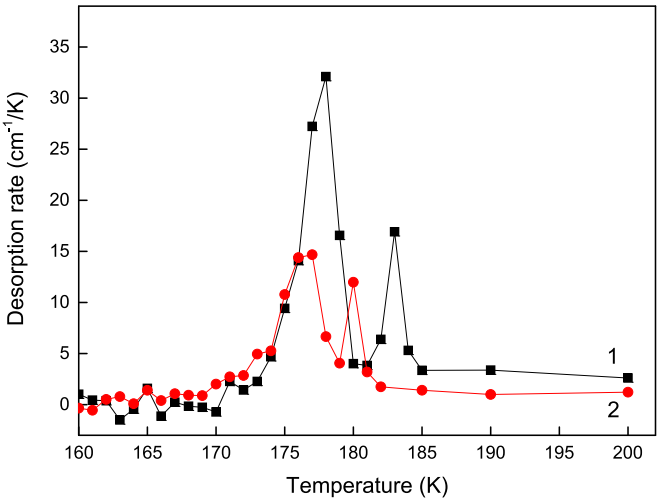

Figure 6. TPD curves: 1—$MgSiO_3/H_2O$ sample (N7 in Tables 1 and 2) and 2—$MgFeSiO_4/H_2O$ sample (N8 in Tables 1 and 2).

Table 2
Dust/ice Mass Ratios, Desorption Orders Used to Fit the TPD Curves, Peak Desorption Temperatures, and Desorption Energies

N	Dust/Ice Mass Ratio	Desorption Order	Desorption Temperature (K)	Desorption Energy (kJ mol^{-1})
1	…	0	186	48.7 ± 0.3
2	…	0	179	48.7 ± 0.3
3	0.1[a]	0.3	186	…
4	0.2[a]	0.7	183	…
5	0.5[a]	1.0	179	49.7 ± 0.5
6	1.3[a]	1.0	179	49.7 ± 0.5
7	9.4[b]	1.0	178, 183	49.4 ± 0.5, 50.9 ± 0.5
8	13.8[b]	1.0	177, 180	49.1 ± 0.5, 50.0 ± 0.5

Notes. N1, N2: Pure water ice.
[a] Carbon/ice mixtures.
[b] Silicate/ice mixtures.

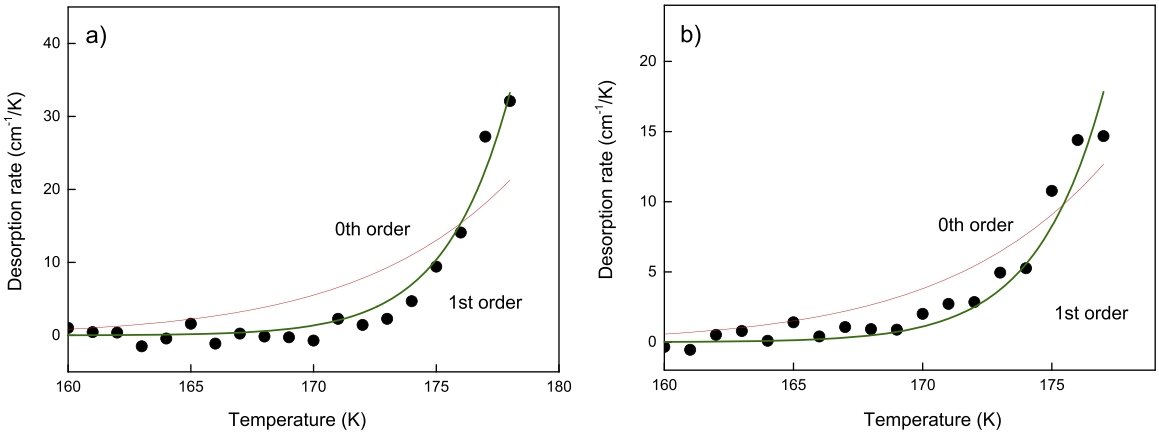

Figure 7. Leading edges of the TPD curves: (a) $MgSiO_3/H_2O$ sample (N7 in Tables 1 and 2) and (b) $MgFeSiO_4/H_2O$ sample (N8 in Tables 1 and 2) and their fits using zeroth and 1first desorption orders.

which showed a trapping of water ice molecules in silicate grains (Potapov et al. 2018). For both silicate/ice samples, first-order kinetics of desorption was determined (Figures 7(a), (b)). The desorption energies obtained using the Readhead's method are presented in Table 2.

4. Discussion

4.1. Kinetics of Desorption. Desorption of Water Ice Molecules from the Surface of Fractal Clusters of Dust Grains

Why water ice mixed with dust grains shows different kinetics of desorption in comparison with the same amount of pure ice? This result has not been obtained in previous experiments on the thermal desorption of ices *from* carbon and silicate surfaces. In the following, we will try to answer the question stated above.

Fractional desorption orders in molecular ices, such as H_2O, NH_3, and CH_3OH, has been attributed to the hydrogen-bonded network, which results in a strong interaction between adjacent molecules. Therefore, the desorption of one molecule is not independent of the desorption of neighboring molecules, as would be expected for zero-order desorption (Bolina et al. 2005a, 2005b; Brown & Bolina 2007). Similarly, the formation of molecular clusters in glycolaldehyde and acetic acid ices has been shown to influence their kinetics of desorption (Burke et al. 2015) due to the intermolecular hydrogen bonds formed between the ice molecules, even at the lowest surface coverage. However, the desorption orders of all of these ices in the multilayer regime were determined to be close to zero. In our case, the desorption order rises up to 1, so hydrogen-bonded network between water molecules is probably not an appropriate answer.

Another answer could be an influence of the structure of water ice deposited with or without grains on the desorption behavior. It was observed that a part of the desorption of water ice after the ASW—CI phase transition occurs from the residual amorphous phase showing a shoulder in the leading edge of a TPD curve (Fraser et al. 2001). The authors showed that the weak TPD peak related to the desorption of ASW is at a lower temperature than the main TPD peak related to the desorption of CI, due to the higher vapor pressure of the amorphous ice, and does not noticeably alter the curve behavior. In the same study, a comparison between TPD dependencies of high and low-density ASW was performed and the curves were found to be essentially equivalent. Thus, the structure of ice is also not an answer that we are looking for.

Typically, zeroth-order desorption relates to a desorption of ice multilayers and the desorption rate does not depend on the number of adsorbed molecules. First-order desorption arises from a monolayer and submonolayer desorption and the desorption rate depends linearly on the number of molecules on the surface. Second-order desorption refers to a desorption of chemically formed species or to a specific distribution of binding sites on the surface when the desorption of one molecule causes a desorption of another one. In this case, the desorption rate depends quadratically on the number of adsorbed molecules. The first-order desorption of water ice in the dust/ice mixtures could be explained by the large surface area of dust clusters that form during the dust deposition. H_2O molecules occupy this surface forming monolayer or submonolayer rather than the thick water ice multilayer as in the case of pure water ice covering a flat substrate. The monolayer desorbs directly from the surface of dust grains following the first-order kinetics. When the concentration of the dust in the ice is decreased, the ice coverage exceeds the dust surface and forms, probably, a monolayer with multilayer islands. Such an island structure can explain the fractal desorption orders related to the desorption of a monolayer and multilayers of ice in this case. The desorption order decreases with the increasing area of multilayer islands and approaches the desorption order of pure H_2O ice. A link between a fractional order desorption kinetics and an island growth on the surface was also proposed elsewhere (Suhasaria et al. 2017).

We have measured the structural characteristics of the deposited hydrogenated carbon grains by using high-resolution transmission electron microscopy (HRTEM; Jäger et al. 2008, 2009). As an example, Figure 8 shows an HRTEM image of grains produced by laser ablation in 3.3 mbar He/H_2 quenching gas atmospheres. The particles are composed of small, strongly bent graphene layers with varying lengths and distances between these layers. The individual particles are very small (less than 3–4 nm) and the largest particle agglomerates are in the range of 15 nm. The morphology of the deposit can be understood as a porous layer of rather fractal agglomerates. The measurements showed that the surface of the dust is very large, but the area cannot be measured exactly. This surface defines the thickness of the coverage of dust grains by water ice molecules.

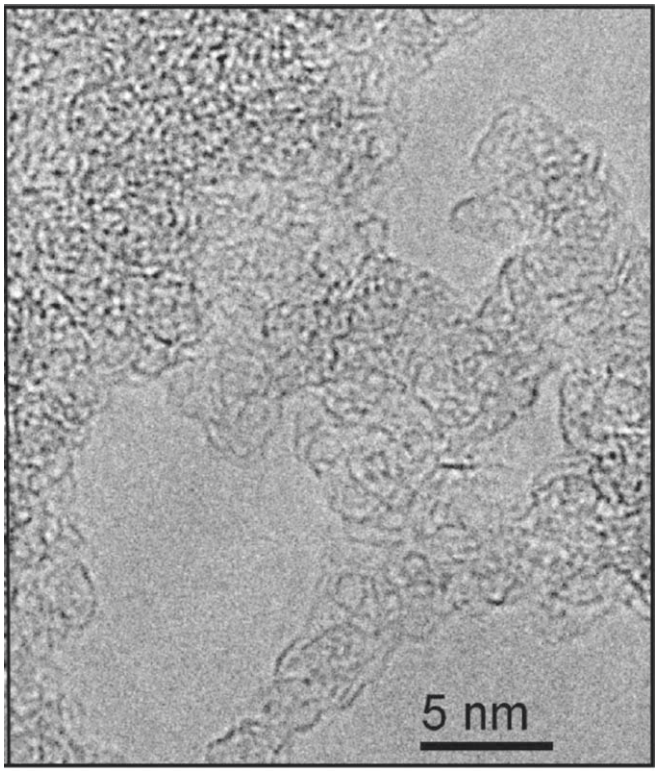

Figure 8. HRTEM image of carbon grains produced by laser ablation in 3.3 mbar He/H_2 quenching gas atmospheres (Jäger et al. 2008).

Numerical simulations of the structure of cometary grain aggregates showed that they are fractals with low densities and irregular shapes (see Fulle & Blum 2017 and references therein). The fractal dimension of about 2 for small cometary grain aggregates was proposed in a number of studies (Donn & Hughes 1986; Samson et al. 1987; Meakin & Donn 1988; Meakin et al. 1989; Donn 1990; Weidenschilling 1997; Kataoka et al. 2013; Tazaki et al. 2016) and as a result of collisional experiments (Wurm & Blum 1998; Krause & Blum 2004). A fractal dimension of 2 in 3D space means that physical and chemical processes occur on the *surface* of fractal aggregates supporting our suggestion about the desorption of ice from the surface of dust grains.

4.2. Desorption Temperature and Energy. Trapping of Water Ice Molecules in Silicates

As one can see from Table 2, the desorption energies for dust/ice mixtures are only slightly higher than the one for pure water ice. The peak desorption temperature depends on the amount of ice deposited. It is the same for the samples N2, N6, and N7 (first peak) containing the same amount of water (see Table 1). The results indicate that ice molecules are equivalently bound to neighboring ice molecules and to the carbon surface. This is also true for the major part of water molecules interacting with the silicates. However, in the TPD curves of the silicate/ice samples, additional peaks at 183 and 180 K point to differently bound ice molecules to the silicate surface. The presence of two desorption maxima was registered for CO, N_2, O_2, and CH_4 ices (Collings et al. 2004; Suhasaria et al. 2017). This finding was explained by the multilayer and monolayer desorption of ice, which can be discussed with stronger bonds between the species and the surface of the substrate compared to the bonds in the ice matrix. In contrast, H_2O, NH_3, CH_3OH, and HCOOH ices were found to show only a single TPD peak (Collings et al. 2004). According to the discussion in the previous section, a multilayer desorption of water ice from the silicate samples can be excluded. Thus, in our study, the two peaks do not correspond to the multilayer and monolayer desorption as in the case of CO, N_2, O_2, and CH_4 ices, but to water molecules differently bound to silicate grains.

The residual desorption beyond the TPD maxima shows that a small part of ice molecules might be physically trapped in small pores of silicate aggregates even at temperatures beyond the desorption temperature of pure water ice. In addition, it can correspond to the release of chemically trapped OH groups from the surface of the silicates. The trapping of water ice at temperatures up to 200 K was also observed in our recent study (Potapov et al. 2018). The trapping of ice molecules was not detected for carbon/ice mixtures, although carbon grains are also very porous.

The difference between carbon and silicate grains can point to the hydrophobic and hydrophilic properties of their surfaces. The transition from hydrophobic to hydrophilic behavior of carbon surfaces due to the formation of oxygenated sites has been simulated (Müller & Gubbins 1998). Hydrophobic-to-hydrophilic conversion by oxidation applied to carbonaceous aerosol (Petters et al. 2006) and carbon nanowalls (Watanabe et al. 2012) is discussed in the literature. The fullerene-like carbon grains used in the present study are characterized by strongly bent graphene layers linked by aliphatic chains and therefore they are typically considered to be hydrophobic material. In our experiments, oxygenation of the carbon surface did not occur. On the other hand, silica (SiO_2) as well as silicates are known to have hydrophilic and hydrophobic surface groups (Klier et al. 1973; Lee & Rossky 1994; Yu et al. 2018). The structure of silicates is characterized by SiO_4 tetrahedra, which can be isolated or linked with adjacent tetrahedra by oxygen bridges. The polymerization degree of the tetrahedra depends on the stoichiometry of the material. At the surface of silicates, either hydrophilic silanol groups (Si–OH) or hydrophobic Si–O–Si groups are present. The ratio of these groups depends on the production process, the thermal treatment of the silicates, and on a possible processing of silicate surfaces. In silicates produced by laser ablation, the amount of Si–OH groups is small. However, reactions between water molecules and grains have probably increased the number of silanol groups on the surface of the grains. Consequently, the number of hydrophilic surface sites was increased.

Thus, with our results, we demonstrate a principal difference between the surface properties of two classes of interstellar grains, namely, the finding of differently bound water ice molecules to silicate grains in contrast to fullerene-like carbon grains. However, this is not a general statement for carbon because carbon surfaces can be very different. For example, oxygenation of C-atoms can produce hydrophilic surface sites.

4.3. Astrophysical Implication

The knowledge of the desorption properties of water ice mixed with dust is very important for the understanding of astronomical observations of water vapor in planet-forming regions and for the revealing of the architecture and evolution of planet-forming disks. The desorption of water ice triggering the release of other volatiles trapped in the ice influences the chemistry of the gas phase of disks by feeding it with

molecules. In addition, the formation efficiency of larger bodies depends on the ice coverage of dust grains.

Knowing the amount of ice relative to dust in a planet-forming disk and the kinetics of desorption of the ice, the structure and morphology of grains and larger bodies can be modeled. It will help to trace back the thermal history of the disk. Conversely, knowing the thermal history of a cosmic body seeded with molecular ice and the kinetics of desorption of ice, the abundance of molecules stayed in the ice and released into the gas phase can be estimated. It will improve our understanding of astrochemical processes in the gas phase and on surfaces. However, more systematic studies on the thermal desorption of molecular ices mixed with different dust analogs are needed. This work represents the first small step in this challenging direction.

5. Summary

We measured the TPD of water ice, which had been premixed with amorphous carbon or silicate dust grains, and demonstrate the dependence of the kinetics of desorption of water ice on the dust/ice ratio. The desorption order increases with an increase of the dust/ice mass ratio and reaches 1, indicating the desorption of ice molecules from the large surface of dust grains. This result shows an important link between the structure and morphology of icy dust grains in planet-forming disks and the amount and the desorption properties of seeded ice. If more information on the thermal history of dust grains was known, more information about the structure and morphology of these grains in the ISM and planet-forming disks could be derived. Moreover, a principal difference between the surface properties of two classes of interstellar grains, namely, the finding of differently bound water ice molecules to silicate grains in contrast to fullerene-like carbon grains is demonstrated.

This study has greatly benefitted from discussions with Guillermo Muñoz Caro and Patrice Theulé. It was supported by the Research Unit FOR 2285 "Debris Disks in Planetary Systems" of the Deutsche Forschungsgemeinschaft (grant JA 2107/3-1).

References

Acharyya, K., Fuchs, G. W., Fraser, H. J., van Dishoeck, E. F., & Linnartz, H. 2007, A&A, 466, 1005
Allamandola, L. J., Bernstein, M. P., Sandford, S. A., & Walker, R. L. 1999, SSRv, 90, 219
Altwegg, K., Balsiger, H., Bar-Nun, A., et al. 2016, SciA, 2, e1600285
Bergin, E. A., & van Dishoeck, E. F. 2012, RSPTA, 370, 2778
Berland, B. S., Brown, D. E., Tolbert, M. A., & George, S. M. 1995, GeoRL, 22, 3493
Bernstein, M. P., Dworkin, J. P., Sandford, S. A., Cooper, G. W., & Allamandola, L. J. 2002, Natur, 416, 401
Biham, O., Furman, I., Pirronello, V., & Vidali, G. 2001, ApJ, 553, 595
Bisschop, S. E., Fraser, H. J., Oberg, K. I., van Dishoeck, E. F., & Schlemmer, S. 2006, A&A, 449, 1297
Blum, J. 2018, SSRv, 214, 52
Bolina, A. S., Wolff, A. J., & Brown, W. A. 2005a, J. Phys. Chem. B., 109, 16836
Bolina, A. S., Wolff, A. J., & Brown, W. A. 2005b, JChPh, 122, 044713
Boogert, A. C. A., Gerakines, P. A., & Whittet, D. C. B. 2015, ARA&A, 53, 541
Brack, A. 1999, AdSpR, 24, 417
Brown, W. A., & Bolina, A. S. 2007, MNRAS, 374, 1006
Brownlee, D., Tsou, P., Aléon, J., et al. 2006, Sci, 314, 1711
Burke, D. J., & Brown, W. A. 2010, PCCP, 12, 5947
Burke, D. J., Puletti, F., Woods, P. M., et al. 2015, JPCA, 119, 6837
Collings, M. P., Anderson, M. A., Chen, R., et al. 2004, MNRAS, 354, 1133
Cronin, J. R., & Chang, S. 1993, in NATO ASI Ser. 416, The Chemistry of Life's Origins, ed. J. M. Greenberg, C. X. Mendoza-Gomez, & V. Pirronello (Dordrecht: Kluwer), 209
Dawley, M. M., Pirim, C., & Orlando, T. M. 2014, JPCA, 118, 1220
Dominik, C., Ceccarelli, C., Hollenbach, D., & Kaufman, M. 2005, ApJL, 635, L85
Donn, B., & Hughes, D. 1986, in ESA Proc. 20th ESLAB Symp. Exploration of Halley's Comet 3, ed. B. Battrick (Heidelberg: ESA), 523
Donn, B. D. 1990, A&A, 235, 441
Draine, B. T. 2003, ARA&A, 41, 241
Elsila, J. E., Dworkin, J. P., Bernstein, M. P., Martin, M. P., & Sandford, S. A. 2007, ApJ, 660, 911
Elsila, J. E., Glavin, D. P., & Dworkin, J. P. 2009, M&PS, 44, 1323
Fayolle, E. C., Oberg, K. I., Cuppen, H. M., Visser, R., & Linnartz, H. 2011, A&A, 529, A74
Fraser, H. J., Collings, M. P., McCoustra, M. R. S., & Williams, D. A. 2001, MNRAS, 327, 1165
Fulle, M., & Blum, J. 2017, MNRAS, 469, S39
Fulle, M., Della Corte, V., Rotundi, A., et al. 2017, MNRAS, 469, S45
Gundlach, B., & Blum, J. 2015, ApJ, 798, 34
Hagen, W., Tielens, A. G. G. M., & Greenberg, J. M. 1981, CP, 56, 367
Henning, T., & Salama, F. 1998, Sci, 282, 2204
Hudgins, D. M., Sandford, S. A., Allamandola, L. J., & Tielens, A. G. G. M. 1993, ApJS, 86, 713
Jäger, C., Huisken, F., Mutschke, H., Jansa, I. L., & Henning, T. H. 2009, ApJ, 696, 706
Jäger, C., Mutschke, H., Henning, T., & Huisken, F. 2008, ApJ, 689, 249
Jäger, C., Sabri, T., Wendler, E., & Henning, T. 2016, ApJ, 831, 66
Jenniskens, P., Blake, D. F., Wilson, M. A., & Pohorille, A. 1995, ApJ, 455, 389
Kataoka, A., Tanaka, H., Okuzumi, S., & Wada, K. 2013, A&A, 554, L4
Klier, K., Shen, J. H., & Zettlemo, A. 1973, J. Phys. Chem., 77, 1458
Krause, M., & Blum, J. 2004, PhRvL, 93, 021103
Lee, S. H., & Rossky, P. J. 1994, JChPh, 100, 3334
Lodders, K., & Fegley, B. 1999, in IAU Symp. 191, Asymptotic Giant Branch Stars, ed. T. Le Bertre, A. Lebre, & C. Waelkens (St Louis, MO: Washington Univ.), 279
Martin-Doménech, R., Muñoz Caro, G. M., Bueno, J., & Goesmann, F. 2014, A&A, 564, A8
Meakin, P., & Donn, B. 1988, ApJL, 329, L39
Meakin, P., Donn, B., & Mulholland, G. W. 1989, Langm, 5, 510
Min, M., Bouwman, J., Dominik, C., et al. 2016, A&A, 593, A11
Müller, E. A., & Gubbins, K. E. 1998, Carbon, 36, 1433
Muñoz Caro, G. M., Meierhenrich, U. J., Schutte, W. A., et al. 2002, Natur, 416, 403
Narten, A. H. 1976, JChPh, 64, 1106
Noble, J. A., Theule, P., Mispelaer, F., et al. 2012, A&A, 543, A5
Nuevo, M., Meierhenrich, U. J., Muñoz Caro, G. M., et al. 2006, A&A, 457, 741
Oro, J. 1961, Natur, 190, 389
Pearce, B. K. D., Pudritz, R. E., Semenov, D. A., & Henning, T. K. 2017, PNAS, 114, 11327
Petters, M. D., Prenni, A. J., Kreidenweis, S. M., et al. 2006, GeoRL, 33, L2480
Polanyi, M., & Wigner, E. 1928, Z. Phys. Chem., Abt. A, 139, 439
Potapov, A., Mutschke, H., Seeber, P., Henning, T., & Jäger, C. 2018, ApJ, 861, 84
Redhead, P. A. 1962, Vacuu, 12, 203
Sabri, T., Baratta, G. A., Jäger, C., et al. 2015, A&A, 575, A76
Samson, R. J., Mulholland, G. W., & Gentry, J. W. 1987, Langm, 3, 272
Sandford, S. A., & Allamandola, L. J. 1988, Icar, 76, 201
Shi, J., Grieves, G. A., & Orlando, T. M. 2015, ApJ, 804, 24
Suhasaria, T., Thrower, J. D., & Zacharias, H. 2017, MNRAS, 472, 389
Tazaki, R., Tanaka, H., Okuzumi, S., Kataoka, A., & Nomura, H. 2016, ApJ, 823, 70
van Dishoeck, E. F. 2014, FaDi, 168, 9
van Dishoeck, E. F., Bergin, E. A., Lis, D. C., & Lunine, J. I. 2014, in Protostars and Planets VI, ed. H. Beuther et al. (Tucson, AZ: Univ. Arizona Press), 835
Wada, K., Tanaka, H., Suyama, T., Kimura, H., & Yamamoto, T. 2009, ApJ, 702, 1490
Watanabe, H., Kondo, H., Sekine, M., Hiramatsu, M., & Hori, M. 2012, JaJAP, 51, 10ND18
Weidenschilling, S. J. 1997, Icar, 127, 290
Wettlaufer, J. S. 2010, ApJ, 719, 540
Wurm, G., & Blum, J. 1998, Icar, 132, 125
Yu, Y. T., Krishnan, N. M. A., Smedskjaer, M. M., Sant, G., & Bauchy, M. 2018, JChPh, 148, 074503

AIP | Review of Scientific Instruments

Total power millimeter-wave spectrometer for measurements of dust opacity at cryogenic temperatures

Alexey Potapov, Frank Lewen, Harald Mutschke, Pierre Mohr, and Stephan Schlemmer

Citation: Review of Scientific Instruments **85**, 073102 (2014); doi: 10.1063/1.4887416
View online: http://dx.doi.org/10.1063/1.4887416
View Table of Contents: http://scitation.aip.org/content/aip/journal/rsi/85/7?ver=pdfcov
Published by the AIP Publishing

Total power millimeter-wave spectrometer for measurements of dust opacity at cryogenic temperatures

Alexey Potapov,[1,a)] Frank Lewen,[1,b)] Harald Mutschke,[2,c)] Pierre Mohr,[2,d)] and Stephan Schlemmer[1,e)]
[1]*I. Physikalisches Institut, University of Cologne, Zülpicher Str. 77, 50937 Cologne, Germany*
[2]*Astrophysical Institute and University Observatory, Friedrich-Schiller-University Jena, Schillergaesschen 3, 07745 Jena, Germany*

(Received 25 March 2014; accepted 25 June 2014; published online 16 July 2014)

A highly sensitive total power millimeter-wave spectrometer has been built to investigate the opacity of important interstellar-dust analogues in the 10–300 K temperature range. The key elements of the spectrometer are a frequency agile synthesizer followed by a microwave amplifie and a subsequent frequency multiplier. In a f rst step, the frequency range of 72–120 GHz is covered by the spectrometer, and a room temperature Schottky detector is employed as a detector. A newly developed two channel (sample/reference) copper sample holder is cryogenically cooled for the 10–300 K range. Here we present the technical details of the spectrometer including examples of the obtained results. The analysis of these results will be published elsewhere. © *2014 AIP Publishing LLC*. [http://dx.doi.org/10.1063/1.4887416]

I. INTRODUCTION

In this article we present a detailed description of a newly developed total power millimeter-wave spectrometer currently working at 72–120 GHz frequencies (4–2.5 mm wavelength) with high sensitivity, frequency accuracy, and equipped with a temperature controlled (10–300 K) sample/matrix holder. The spectrometer is currently in use in the Cologne laboratory. It has been employed to detect the millimeter-wave absorption of various interstellar-dust analogues, such as amorphous silicates with different iron contents and of mixtures, e.g., of silicate and carbon- or iron-based materials which are all composed in the Jena laboratory.

The necessity of the millimeter wave (MMW) and submillimeter wave or far infrared (FIR) measurements is explained by the importance of these spectral ranges as a source of information for studies on the spatial distribution of the interstellar medium. The spectral continuum observed in the MMW and FIR is dominated by the thermal emission of cold dust particles. Consequently, the continuum dust opacity influence strongly the interpretation of astronomical observations, provided by recent major observatories, such as Herschel and Planck.[1,2] For instance, the determination of the dust mass, which is also essential for interpreting the dynamics of the interstellar medium, depends on the exact knowledge of the dust opacity.

Data on the emission properties of the cold interstellar dust particles in the MMW and FIR are scarce, thus, power-law extrapolations from shorter wavelengths are usually applied in models. However, even the exponent β (λ, T), which is used for an extrapolation, is poorly known, because the amorphous solids dominating the interstellar dust possess low-energetic transitions, which depend on the precise nature of their disorder,[3] and show strong temperature dependence. The T-beta anti-correlation that is predicted by solid-state physics for the temperature range above 10 K has also been found by astronomical observations of interstellar-dust emission.[4] The available opacity data are based on relatively small number of laboratory measurements. Most of the measurements have been done in the FIR region,[5–10] and only a few studies have been carried out in the MMW,[9,10] all demonstrating a strong temperature dependence of the absorption coefficient The relation of the absorption coefficien with the structure of the materials remains unclear and the studies are restricted to the simplest compounds, underlining the neediness of further systematic and extended investigations.

The most common laboratory method of dust opacity measurements is the IR/FIR Fourier transform (FT) spectroscopy, but at longer wavelengths (>1 mm) the signal to noise of the FT spectrometers is limited due to the low power density of the globar source at mm-waves. Even if a FT spectrometer is equipped with a liquid helium cooled bolometer detector, conventional FT spectroscopy becomes ineffi cient. In principle, a synchrotron radiation source can be used for reaching wavelengths above 1 mm, like it was done in Ref. 8, but it complicates the experiment considerably. Additionally, the discrete FT procedure becomes problematic at low frequencies because of the poor spectral resolution.

In the last years coherent, broadband tunable, and powerful solid state THz sources became available. State of the art THz broadband emitters for laser mixing experiments either for time domain[11] or frequency domain[12] measurements are now commonly in use for THz spectroscopy. These techniques replace the thermal emitter by a more powerful

[a)]Author to whom correspondence should be addressed. Electronic mail: potapov@ph1.uni-koeln.de. Tel.: +492214703560.
[b)]E-mail: lewen@ph1.uni-koeln.de
[c)]E-mail: harald.mutschke@uni-jena.de
[d)]E-mail: pierre.mohr@uni-jena.de
[e)]E-mail: schlemmer@ph1.uni-koeln.de

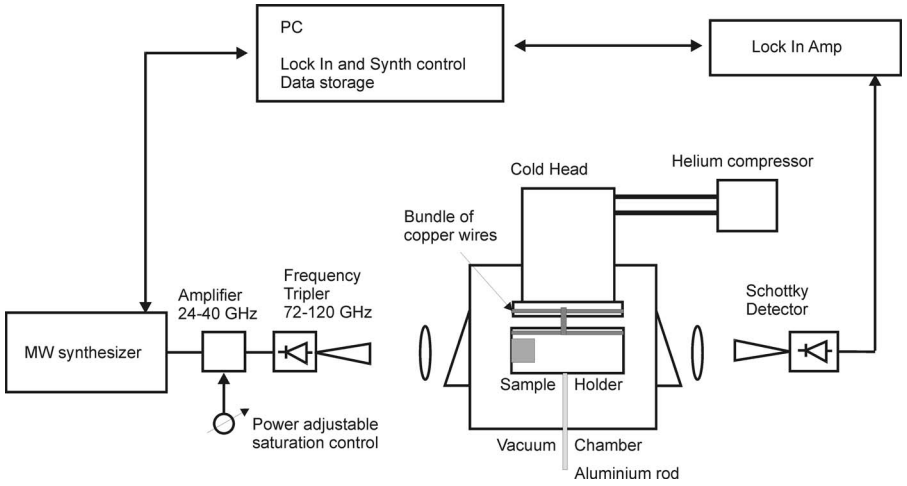

FIG. 1. Block scheme of the total power millimeter-wave spectrometer.

semiconductor radiation source. We decided to employ frequency multiplying techniques, which allows also setting up a spectrometer with highest resolution necessary for molecular gas spectroscopy. In the course of this work we developed a broadband tunable Schottky multiplier based total power spectrometer.

II. SPECTROMETER

The block scheme of the spectrometer is presented in Fig. 1 and a more detailed scheme of the optical setup is shown in Fig. 2. In contrast to FT spectrometer, the radiation source is frequency controlled by a microwave synthesizer, which output is frequency multiplied, as it is used in high-resolution setups for spectroscopy of gaseous species.[12–15] For the dust opacity measurements we choose the internal pulse modulation, which changes fast the amplitude of the synthesizer between 0 and 100%. This operational mode is also referred as a total power modulation.

The 24–40 GHz output frequency of a synthesizer (Agilent83650B) is amplifie and then multiplied by a commercial tripler (Virginia Diodes Inc., VDI) to obtain output frequencies at 72–120 GHz. The multiplier is based on planar GaAs Schottky diode technology. The amplifie has three stages, and the tripler output power is adjustable and stabilized with a saturation control circuit of the last active amplifie stage. The saturation diagram (the dependences of output signal on synthesizer power level at different amplifie voltages) is presented in Fig. 3.

In our experiments we used a f xed amplifie voltage of 3 V, and synthesizer power level of −3 dBm. As presented in the inset of Fig. 3 the power stability is significantl enhanced by the saturation circuit. An input level change from −5 to 0 dBm (5 dB change) leads to the tripler output power change of less or equal to 0.01 dB. Also the AM noise (amplitude instability) of the synthesizer and power amplifie is suppressed by the circuit, increasing the whole system signal-to-noise ratio.

The dependence of the tripler output power over frequency measured by the manufacturer (VDI) and the Schottky detector output signal measured by us are shown in Fig. 4. The difference between these two measurements can be explained by the influenc of the antenna characteristic; by the optical system, define by the two lenses and two windows, and their mechanical adjustment; by the spectral response of the detector; and by weak standing waves between the source and the detector, creating fringes.

The millimeter wave beam, created by a conical standard gain horn antenna, is focused with the help of two biconvex polyethylene (HDPE) lenses with a focal length of 100 mm.

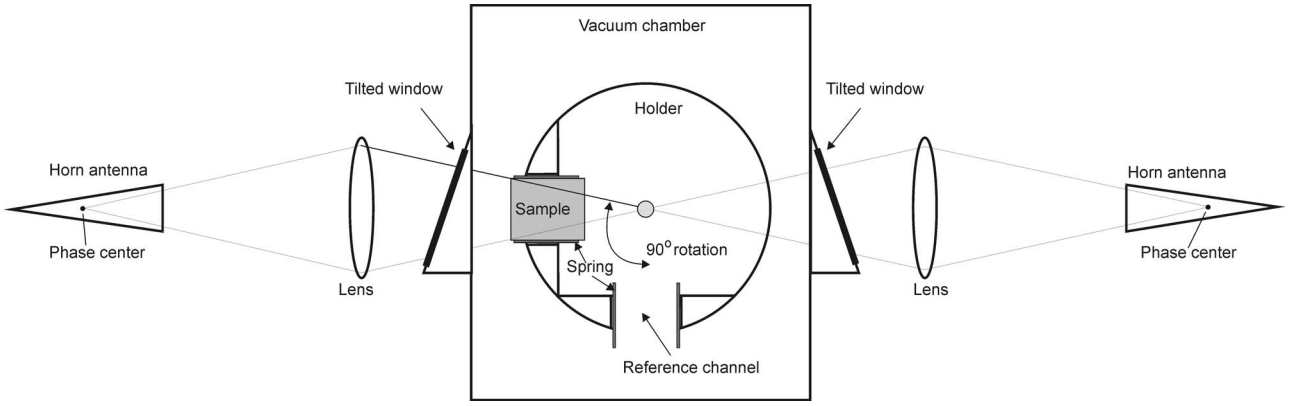

FIG. 2. Optical scheme of the total power millimeter-wave spectrometer.

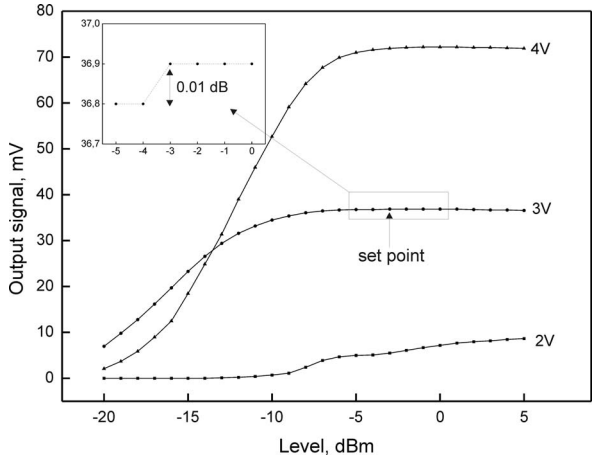

FIG. 3. Tripler output signal versus the synthesizer power level at different amplifie voltages.

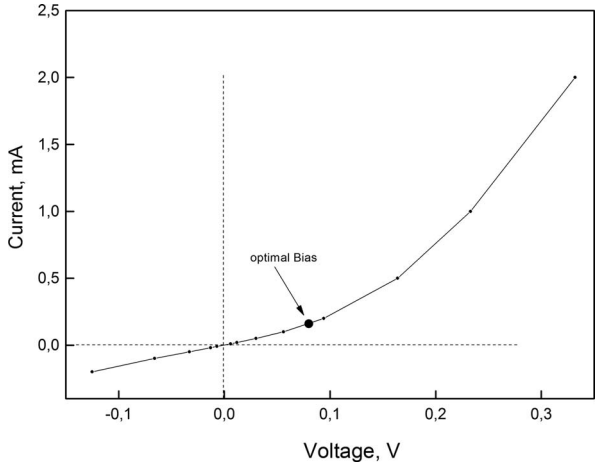

FIG. 5. Bias point and I/V characteristic of the room temperature Schottky detector. The optimal bias point is +80 mV, +160 μA.

The second lens guides the beam into the Schottky detector (see Fig. 2). To realize a small beam width at the position of the sample we decided to create a minimal beam waist in the center of the vacuum chamber. In this case the optical beam has the same size at both chamber windows. As a drawback, the beam is not minimized at the sample position, but the sample center is only 20 mm off the chamber center, so that the beam size is smaller than the sample diameter. The distances between the phase centers of the horn antennas and the lenses and between the lenses and the vacuum chamber center are equal to 200 mm. The optical coupling depends quite critical on small displacements, therefore a micrometer translation stage for the tripler as well as for the detector is incorporated to allow fin adjustment and optimization of the beam coupling.

The samples have been prepared in the form of powders of magnesium/iron silicate glass, which are mixed with polyethylene in a ratio of 2.4 g silicate to 0.3 g polyethylene and pressed at slightly elevated temperature to pellets of 13 mm diameter and about 1 cm thickness, thus, that the silicate particles are distributed homogeneously in the matrix. For this reason no corrections of a spectrum due to the sample composition are needed. Details of the sample production process are given in Ref. 7. The samples are placed in the vacuum chamber evacuated to pressures lower than 10^{-4} mbar. The chamber is equipped with two HDPE windows. Both windows are tilted by 33° in order to reduce the reflectio losses and to take reflectin power out of the optical center line.

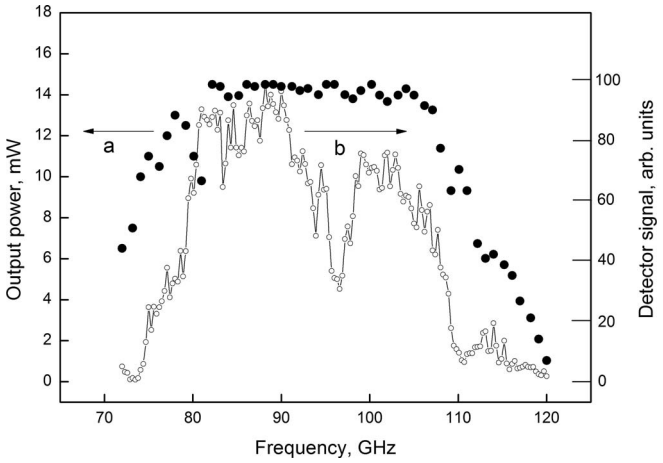

FIG. 4. Bandpass characteristics: (a) Power/frequency characteristic of the tripler given by VDI Inc. in mW (full circles, left scale); (b) Schottky detector output signal given in arbitrary units representing the whole bandpass of the spectrometer (open circles, right scale).

The upper part of the specially designed 90° rotatable copper sample holder is fi ed by a center screw on the cold-head. The lower part of the holder is connected by four bundles of thin copper wires to the upper part to ensure high thermal conductivity and free to a ±45° rotation. The wires are pressed inside the both holder parts. The sample is placed in a cylindrical beryllium-copper spring, and this spring is placed in the holder (see Fig. 2). The size of the sample decreases with cooling and the spring prevents losing a contact between the sample and the holder. The lower part of the holder can be switched to two positions to allow the consequent measurements of the sample and reference channel. The rotation is being done by the rotation of the aluminum rod screwed to the fibe glass plate fi ed on the bottom of the lower holder part (Fig. 1). Thus, this part rotates together with the rod, and the reference channel is placed into the radiation beam instead of the sample (Fig. 2).

The radiation is received by the second standard gain horn antenna coupled with the room temperature Schottky detector in waveguide technique with fi ed back short. The I/V curve of the "zero bias" detector (manufacturer AEG) is given in Fig. 5.

The optimal bias point has been found to be +80 mV and +160 μA, the bias electronics works with constant voltage control. The optimal bias was adjusted by monitoring the response of the detector at 90 GHz. Compared to zero bias operation the response could be doubled. For more detailed characterization of the detector we have checked its linearity by comparison with a millimeter wave pyro detector, which is self-developed and incorporates black PE IR filter to remove IR sensitivity. Since the pyro detector is a large aperture thermal detector, it is linear within the given power range.

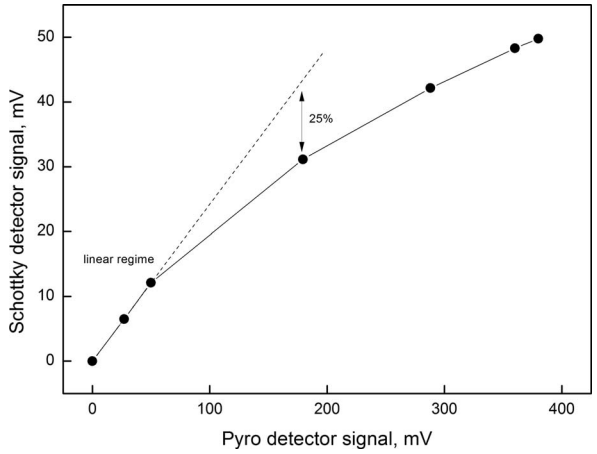

FIG. 6. Saturation behavior of the Schottky detector at f xed frequency of 90 GHz and 113 Hz modulation frequency.

By recording the signal of both detectors at a modulation frequency of 113 Hz (Fig. 6) the linear regime and the saturation characteristics of the Schottky detector were determined.

Up to about 15 mV the Schottky detector signal is linear with respect to the pyro detector signal. As one can see the signal saturates at high input power levels, therefore a power control is crucial. At a pyro detector signal of 200 mV the signal compression reached 25% (1 dB compression point). The advantages of the Schottky detector are a much lower noise level and a much faster detection.

To lower the 1/f noise contribution and to increase the measuring speed we finall chose a pulse modulation of 97.3 kHz frequency instead of 113 Hz. Phase sensitive rectifi cation of the signal is achieved at the modulation frequency (1f detection) by a digital lock-in amplifie with free adjustable integration time.

Since the spectrometer works in total power mode, high and known power stability is of up most interest. Stability limiting drifts have been measured as the evolution of the difference of two reference measurements, $((I_t - I_0)/I_0) \times 100\%$, with time. The result is shown in Fig. 7 and represents changes by drifts. The values are about 0.1% (0.005 dB) in 5 min up to 0.5% (0.02 dB) in 30 min, which allows the consequent sample and reference measurements without any additional recalibration. The total integration time in the sample/reference measurements was subdivided into 80 ms delay (to allow frequency setting of the synthesizer) and into 12 individual data points with 5 ms of integration time each. A typical forward and backward scan of 45 GHz with 1000 data points amounts to about 10 min (taking into account the time needed for data communication). Thus, the time of a sample + reference measurement at a f xed temperature was about 20 min.

III. MEASUREMENTS AND DISCUSSION

A number of samples containing important interstellar-dust materials have been measured by using the new spectrometer. We present the evolution of the absorption spectra of the iron-free silicate sample (STW25, composition $MgSiO_3$) with temperature increase from 10 to 300 K in the 75–120 GHz range in Fig. 8. The absorption coefficien κ was obtained as a logarithm of the ratio of reference measurements to sample measurements normalized to the sample mass and surface square according to Beer–Lambert's law. The periodical structure of the spectra is due to the standing waves arising in the sample. With the sample length of 1 cm and effective refractive index of 2.1, we have a periodicity of about 7 GHz.

One can see the increase of the absorption coefficien with temperature, especially in the range of 50–300 *K*. The same increase has been obtained for all measured samples, confirmin previous MMW and our recent FIR measurements (see Fig. 9).

The minima of the spectra correspond to the 11th (~75 GHz at room temperature) to 17th (~116 GHz) interference orders of the multiple reflection within the sample pellet. With cooling to 10 K, these interference fringes shift by about 3 GHz (or 3%) to larger frequencies, which corresponds to the thermal contraction of the pellets (about 10^{-4}/K).

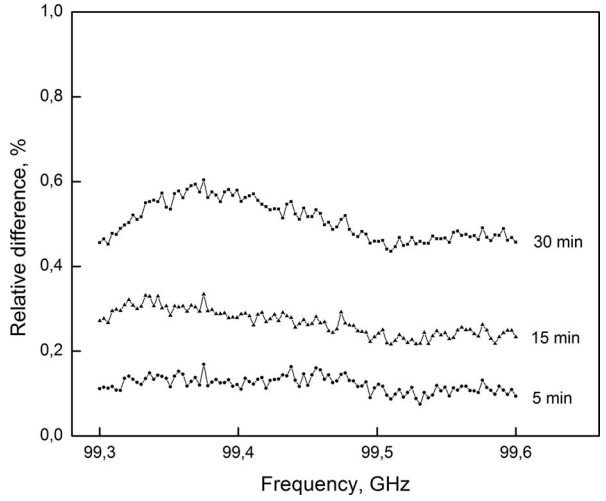

FIG. 7. Stability test of the reference signal for different time offsets. The total scan time was adjusted to less than 20 s (drifts during the time of this order can be neglected). The scan width is 300 MHz.

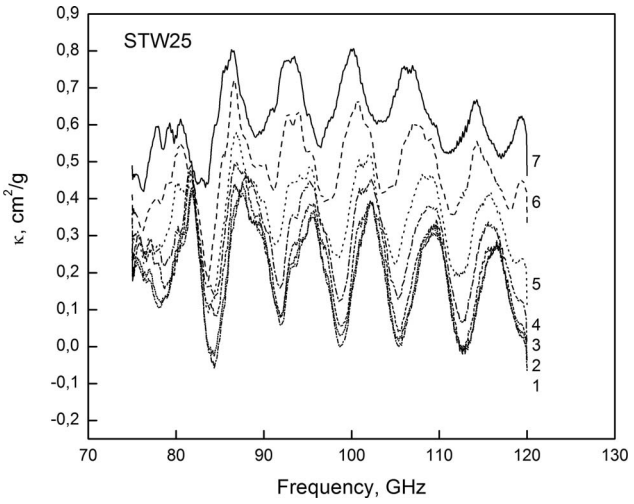

FIG. 8. Evolution of the absorption spectra of the sample STW25 with temperature: 1–10 K, 2–15 K, 3–20 K, 4–50 K, 5–100 K, 6–200 K, and 7–300 K.

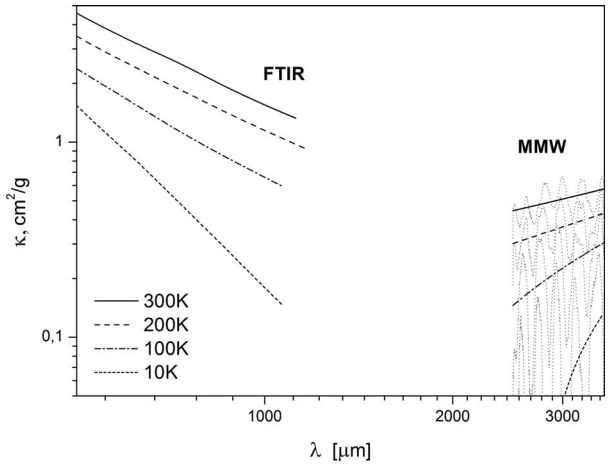

FIG. 9. Evolution of the absorption spectra of the sample STW25 with temperature in the FIR and MMW ranges.

For evaluation of the absorption coefficien spectrum, we applied a simple linear fittin function to derive average spectra free of interference fringes. Note that a certain constant value (0.15 cm^2/g for the pellet of Fig. 8), calculated from the effective refractive index, in these average spectra is due to the mean reflectio losses. In other words, absorption at 10 *K* is negligible at 120 GHz (2500 μm) in Fig. 8, which is consistent with the fringe minima reaching zero at these frequencies. The result of this procedure is shown in Fig. 9 together with our unpublished IR data.

It could be a better way to eliminate the interference fringes than a simple linear fit but we leave this discussion for the future publication concerning obtained FIR and MMW results.

The extension of the frequency range of the present spectrometer up to 400 GHz would allow closing the existing gap between the far infrared and millimeter-wave regions.

IV. CONCLUSIONS

In this article we have described a millimeter-wave spectrometer, which was developed for recording sensitive spectra of PE dust samples. The spectrometer is optimized for high total power stability, and the corresponding parameters have been measured. Extended efforts have been taken to minimize the influenc of amplitude instabilities of the fundamental frequency source. Two different detectors have been employed to optimize the linear response of the system. We demonstrate that the system is capable to record spectra with freely define frequency step sizes and integration times.

The signal-to-noise ratio is more than sufficien to record spectra of interstellar-dust analogues. By assuming a detector noise equivalent power (NEP) of approximately 10 pW/$\sqrt{}$Hz and a power level of 1 mW of the tripler, the dynamic range is expected to be in the order of 80 dB for 1 Hz bandwidth (=160 ms integration time per step). The beryllium-copper spring enforced holder is working reliable and allows simple switching between reference and sample channels. Spectra of the samples containing important interstellar-dust materials have been recorded demonstrating the temperature dependences, which are in agreement with the previous MMW and our recent FIR results.

ACKNOWLEDGMENTS

The work was supported by Deutsche Forschungsgemeinschaft through grant ISM-SPP 1573 (LE 1217/1-1 and MU 1164/8-1).

[1]D. Paradis, R. Paladini, A. Noriega-Crespo, C. Mény, F. Piacentini, M. A. Thompson, D. J. Marshall, M. Veneziani, J.-P. Bernard, and S. Molinari, Astron. Astrophys. **537**, A113 (2012).
[2]Planck Collaboration, P. A. R. Ade, N. Aghanim, M. Arnaud, M. Ashdown, J. Aumont, C. Baccigalupi, A. Balbi, A. J. Banday, R. B. Barreiro *et al.*, Astron. Astrophys. **536**, A19 (2011).
[3]C. Meny, V. Gromov, N. Boudet, J.-Ph. Bernard, D. Paradis, and C. Nayral, Astron. Astrophys. **468**, 171 (2007).
[4]F.-X. Désert, J. F. Macías-Pérez, F. Mayet, G. Giardino, C. Renault, J. Aumont, A. Benoît, J.-Ph. Bernard, N. Ponthieu, and M. Tristram, Astron. Astrophys. **481**, 411 (2008).
[5]V. Mennella, J. R. Brucato, L. Colangeli, P. Palumbo, A. Rotundi, and E. Bussoletti, Astrophys. J. **496**, 1058 (1998).
[6]N. Boudet, H. Mutschke, C. Nayral, C. Jäger, J.-P. Bernard, T. Henning, and C. Meny, Astrophys. J. **633**, 272 (2005).
[7]P. Mohr, H. Mutschke, and F. Lewen, in "The life cycle of dust in the Universe: Observations, theory, and laboratory experiments," edited by C. Kemper *et al.* Proceedings of Science, SISSA, Trieste, 140 (2014).
[8]A. Coupeaud, K. Demyk, C. Meny, C. Nayral, F. Delpech, H. Leroux, C. Depecker, G. Creff, J.-B. Brubach, and P. Roy, Astron. Astrophys. **535**, A124 (2011).
[9]M. A. Bösch, Phys. Rev. Lett. **40**, 879 (1978).
[10]N. I. Agladze, A. J. Sievers, S. A. Jones, J. M. Burlitch, and S. V. W. Beckwith, Astrophys. J. **462**, 1026 (1996).
[11]D. M. Mittleman, R. H. Jacobsen, R. Neelamani, R. G. Baraniuk, and M. C. Nuss, Appl. Phys. B **67**, 379 (1998).
[12]C. P. Endres, H. S. P. Müller, S. Brünken, D. G. Paveliev, T. F. Giesen, S. Schlemmer, and F. Lewen, J. Mol. Struct. **795**, 242 (2006).
[13]K. A. Walker, and A. R. W. McKellar, J. Mol. Spectrosc. **205**, 331 (2001).
[14]K. Harada, K. Tanaka, T. Tanaka, S. Nanbu, and M. Aoyagi, J. Chem. Phys. **117**, 7041 (2002).
[15]A. V. Potapov, L. A. Surin, S. Schlemmer, and T. F. Giesen, J. Mol. Spectrosc. **270**, 116 (2011).

Ehrenwörtliche Erklärung

Ich erkläre hiermit ehrenwörtlich, dass ich die vorliegende Arbeit selbständig, ohne unzulässige Hilfe Dritter und ohne Benutzung anderer als der angegebenen Hilfsmittel und Literatur angefertigt habe. Die aus anderen Quellen direkt oder indirekt übernommenen Daten und Konzepte sind unter Angabe der Quelle gekennzeichnet.

Bei der Auswahl und Auswertung folgenden Materials haben mir die nachstehend aufgeführten Personen in der jeweils beschriebenen Weise entgeltlich/unentgeltlich geholfen:

6.1.1 The rotational analysis was done together with V.A. Panfilov. The microwave spectra were measured by P.L. Raston
6.1.2 The infrared spectra were measured by A.R.W. McKellar. The interaction potential was developed by P. Jankowski and K. Szalewicz. The paper was written by L.A. Surin
6.1.4 The program of the observations was prepared together with A. Sanchez-Monge. Synthetic spectra were created by Th. Möller.
6.1.6 The spectrometer was built together with P. Asselin at the MONARIS laboratory in Paris. The rovibrational analysis was done by V. Boudon. The experiments were done together with A. Turner and L. Bruel
6.2.1 The experiments were done at the MONARIS laboratory in Paris. M. Jonusas helped with the experiments.
6.2.2 P. Seeber did a few experiments. The analysis and interpretation was done together with H. Mutschke.
6.2.4 P. Mohr and H. Mutschke provided the samples.

Weitere Personen waren an der inhaltlich-materiellen Erstellung der vorliegenden Arbeit nicht beteiligt. Insbesondere habe ich hierfür nicht die entgeltliche Hilfe von Vermittlungs- bzw. Beratungsdiensten in Anspruch genommen. Niemand hat von mir unmittelbar oder mittelbar geldwerte Leistungen für Arbeiten erhalten, die im Zusammenhang mit dem Inhalt der vorgelegten Habilitationsschrift stehen.

Die Arbeit wurde bisher weder im In- noch im Ausland in gleicher oder ähnlicher Form einer anderen Prüfungsbehörde vorgelegt.

Die geltende Habilitationsordnung der Friedrich-Schiller-Universität ist mir bekannt.

Ich versichere ehrenwörtlich, dass ich nach bestem Wissen die reine Wahrheit gesagt und nichts verschwiegen habe.

Jena, den 18.06.2018